Science

13 May 2011 $10

AAAS

EDITORIAL
767 The Birth of the Operon
François Jacob

NEWS OF THE WEEK
772 A roundup of the week's top stories

NEWS & ANALYSIS
776 Cholera Linked to U.N. Forces, But Questions Remain
777 Scientific Link-Up Yields 'Control Panel' for Networks
778 Did Neandertals Linger in Russia's Far North?
>> Report p. 841
779 Feedback From Frontal Cortex May Be a Signature of Consciousness
>> Report p. 858
781 Loosing the Louse on Europe's Largest Invasive Pest
782 Is It Time to Declutter the Dinosaur Roster?
783 Homeland Security Science Chief Aims to Put House in Order

NEWS FOCUS
784 The Emerging Race to Cure HIV Infections
Understanding HIV Latency to Undo It
>> *Science* Podcast

LETTERS
791 Counting India's Wild Tigers Reliably
K. U. Karanth et al.
Practical Implications of Test Anxiety Tools
J. W. B. Lang and J. Lang
Response
S. L. Beilock and G. Ramirez
792 CORRECTIONS AND CLARIFICATIONS

BOOKS *ET AL.*
793 Braintrust
P. S. Churchland, reviewed by R. S. Mathis
794 Brainwave 2011
T. McHenry, Producer, reviewed by T. Requarth and M. Crist

POLICY FORUM
795 Toward the Second Commitment Period of the Kyoto Protocol
A. J. Weaver

PERSPECTIVES
797 Cold-Trapping Mars' Atmosphere
P. C. Thomas
>> Report p. 838
798 The Cost of Being Male
J. Parsch
>> Report p. 845
799 Planarian Pluripotency
J. M. W. Slack
>> Research Article p. 811; Report p. 852
801 From Computational Design to a Protein That Binds
B. S. Der and B. Kuhlman
>> Report p. 816
802 Brownian Motion Goes Ballistic
P. N. Pusey
804 Retrospective: Walter M. Fitch (1929–2011)
W. R. Atchley

REVIEW
805 Comparing Photosynthetic and Photovoltaic Efficiencies and Recognizing the Potential for Improvement
R. E. Blankenship et al.
>> *Science* Podcast

CONTENTS continued >>

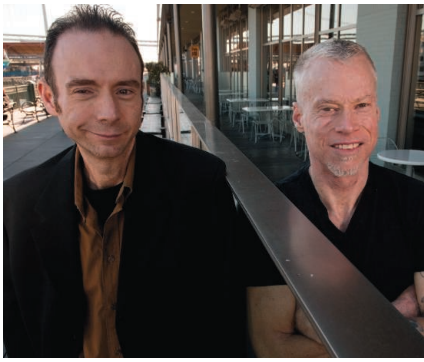

page 784

page 794

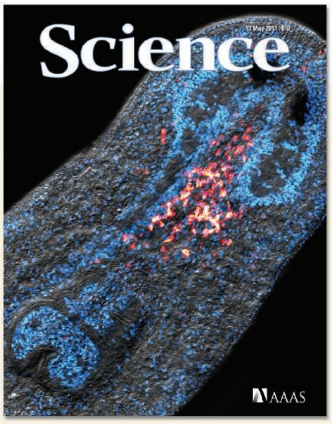

COVER
Composite confocal image of an adult planarian (*Schmidtea mediterranea*) showing a growing colony of dividing cells (red) that initiated from a single, pluripotent stem cell called a clonogenic neoblast (cNeoblast). The ~1-millimeter-long animal is visualized with differential interference contrast microscopy and nuclear staining (blue). The colony is just posterior to the animal brain (nuclei-rich, bi-lobed structure) and eyes (two dark pigmented areas). See page 811.

Credit: Daniel E. Wagner, Irving E. Wang, Peter W. Reddien/Department of Biology, Massachusetts Institute of Technology, Whitehead Institute for Biomedical Research

DEPARTMENTS

763 This Week in *Science*
768 Editors' Choice
770 *Science* Staff
865 New Products
866 *Science* Careers

RESEARCH ARTICLES

811 Clonogenic Neoblasts Are Pluripotent Adult Stem Cells That Underlie Planarian Regeneration
D. E. Wagner et al.
A pluripotent adult stem cell underlies flatworms' amazing regenerative ability.
>> Perspective p. 799; Report p. 852

816 Computational Design of Proteins Targeting the Conserved Stem Region of Influenza Hemagglutinin
S. J. Fleishman et al.
Proteins can be designed that bind to specific patches on target proteins to alter their subsequent interactions.
>> Perspective p. 801; Science *Podcast*

REPORTS

821 Interplay of Rotational, Relaxational, and Shear Dynamics in Solid ^{4}He
E. J. Pratt et al.
Comprehensive measurements argue against the existence of the exotic supersolid quantum state of frozen helium.

825 Very Large Capacitance Enhancement in a Two-Dimensional Electron System
L. Li et al.
Electron correlation effects at the interface of two metal oxides lead to a lower chemical potential and enhance capacitance.

828 Beating Crystallization in Glass-Forming Metals by Millisecond Heating and Processing
W. L. Johnson et al.
Resistive heating can be used to rapidly heat a bulk metallic glass without inducing crystallization.

833 Three-Dimensional Orientation Mapping in the Transmission Electron Microscope
H. H. Liu et al.
Electron microscopy is used to nondestructively map the three-dimensional grain orientations in nanocrystalline aluminum.

835 Silver-Catalyzed C-C Bond Formation Between Methane and Ethyl Diazoacetate in Supercritical CO_2
A. Caballero et al.
Supercritical carbon dioxide solvent facilitates transformation of the generally inert carbon-hydrogen bonds in methane.

838 Massive CO_2 Ice Deposits Sequestered in the South Polar Layered Deposits of Mars
R. J. Phillips et al.
Radar measurements reveal a substantial buried deposit of carbon dioxide in the south pole of Mars.
>> Perspective p. 797

841 Late Mousterian Persistence near the Arctic Circle
L. Slimak et al.
Artefacts at a site in the northern Urals dating to about 33,000 years ago suggest a last northern refuge of Neandertals.
>> News & Analysis story p. 778

845 Experimental Evidence Supports a Sex-Specific Selective Sieve in Mitochondrial Genome Evolution
P. Innocenti et al.
Polymorphisms in the organelle genome have little effect in female flies but do alter gene expression in males.
>> Perspective p. 798

848 Role for piRNAs and Noncoding RNA in de Novo DNA Methylation of the Imprinted Mouse *Rasgrf1* Locus
T. Watanabe et al.
Small, noncoding PIWI-interacting RNAs regulate the imprinting of a mouse gene.

852 Polarized *notum* Activation at Wounds Inhibits Wnt Function to Promote Planarian Head Regeneration
C. P. Petersen and P. W. Reddien
Local detection of tissue polarity results in selective feedback inhibition of signaling at posterior-facing wounds.
>> Perspective p. 799; Research Article p. 811

855 Natural Microbe-Mediated Refractoriness to *Plasmodium* Infection in *Anopheles gambiae*
C. M. Cirimotich et al.
Insect midgut-dwelling bacteria generate reactive oxygen species that inhibit malaria parasite development.

858 Preserved Feedforward But Impaired Top-Down Processes in the Vegetative State
M. Boly et al.
Discerning the neural correlates of (un)consciousness sheds light on the mechanisms underlying vegetative states.
>> News & Analysis story p. 779

862 Improved Learning in a Large-Enrollment Physics Class
L. Deslauriers et al.
Encouraging active engagement results in enhanced learning.

CONTENTS continued >>

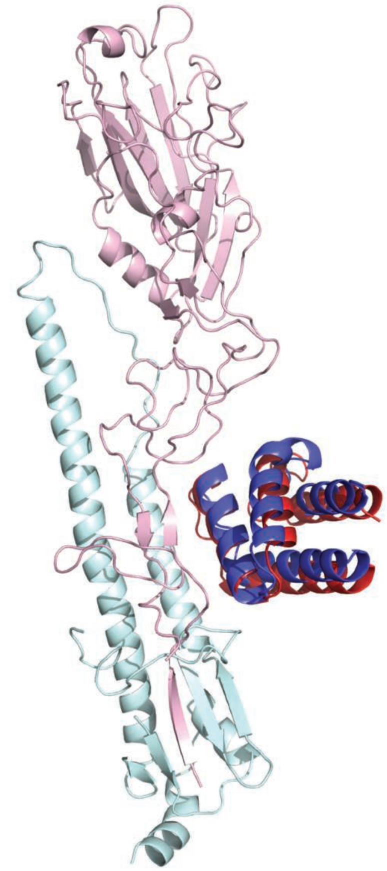

pages 801 & 816

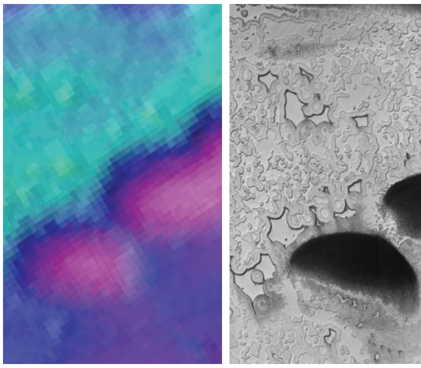

pages 797 & 838

SCIENCEONLINE

SCIENCEXPRESS
www.sciencexpress.org

Evidence of a Global Magma Ocean in Io's Interior
K. K. Khurana et al.
Magnetic field measurements made near Jupiter's moon Io strengthen the evidence for a magma ocean in its interior.
10.1126/science.1201425

Carbon-Based Supercapacitors Produced by Activation of Graphene
Y. Zhu et al.
Activated microwave-exfoliated graphite oxide combined with an ionic liquid can be used to make an enhanced capacitor.
10.1126/science.1200770

Disorder-Enhanced Transport in Photonic Quasicrystals
L. Levi et al.
Optical interference in a photorefractive crystal is used to study light propagation in a controlled disordered system.
10.1126/science.1202977

Local Macrophage Proliferation, Rather than Recruitment from the Blood, Is a Signature of T_H2 Inflammation
S. J. Jenkins et al.
Proliferation in situ, rather than immune cell recruitment, drives macrophage expansion in response to parasitic infection.
10.1126/science.1204351

Crystal Structure of the Maltose Transporter in a Pretranslocation Intermediate State
M. L. Oldham and J. Chen
An intermediate structure provides insight into how a transport substrate allosterically activates adenosine triphosphatase activity.
10.1126/science.1200767

SCIENCENOW
www.sciencenow.org
Highlights From Our Daily News Coverage

Study: High-Tech Gas Drilling Is Fouling Drinking Water
Fracking for deep stores of methane may be contaminating nearby wells.
http://scim.ag/deep-drilling

Titan's Atmosphere Spawned by Impacts?
Ancient bombardments may have transformed ammonia-rich ices into gaseous nitrogen.
http://scim.ag/titan-impacts

Earliest American Dogs May Have Been Dinner
A bone found in 9000-year-old human excrement may be the first definitive evidence of dogs in the New World and of dogs being eaten by people.
http://scim.ag/dog-dinner

SCIENCESIGNALING
www.sciencesignaling.org
The Signal Transduction Knowledge Environment
10 May issue: http://scim.ag/ss051011

RESEARCH ARTICLE: Methylation of a Phosphatase Specifies Dephosphorylation and Degradation of Activated Brassinosteroid Receptors
G. Wu et al.

PERSPECTIVE: PP2A Phosphatases—The "On-Off" Regulatory Switches of Brassinosteroid Signaling
S. Di Rubbo et al.
The abundance of brassinosteroid receptors and thus the intensity of brassinosteroid signaling are set by methylation of a protein phosphatase.

RESEARCH ARTICLE: A Peptide-Based Target Screen Implicates the Protein Kinase CK2 in the Global Regulation of Caspase Signaling
J. S. Duncan et al.

PERSPECTIVE: Protein Kinases Curb Cell Death
O. Filhol and C. Cochet
Phosphorylation of caspase substrates by the protein kinase CK2 may underlie its role in tumorigenesis.

GLOSSARY
Find out what AAM, BFA, and cSMAC mean in the world of cell signaling.

SCIENCECAREERS
www.sciencecareers.org/career_magazine
Free Career Resources for Scientists

An Interdisciplinary Approach to Successful Aging
E. Pain
Social and behavioral scientist Nardi Steverink studies the psychological well-being of older people to help them stay well and happy longer.
http://scim.ag/steverink

On Kidney Stones and Qualifying Exams
A. Marnett
Both can be painful and hard to pass, but proper preparation can make it easier—for the qualifying exam, at least.
http://scim.ag/qualifying_exam

SCIENCETRANSLATIONAL MEDICINE
www.sciencetranslationalmedicine.org
Integrating Medicine and Science
11 May issue: http://scim.ag/stm051111

COMMENTARY: Universal Design of Research—Inclusion of Persons with Disabilities in Mainstream Biomedical Studies
A. S. Williams and S. M. Moore
Simple changes in clinical study design allow individuals with disabilities to participate in and contribute to research.

PERSPECTIVE: Diagnosing the Individual to Control the Epidemic
G. F. Medley
Infection experiments help to elucidate how epidemics propagate through individuals.

RESEARCH ARTICLE: Losartan Restores Skeletal Muscle Remodeling and Protects Against Disuse Atrophy in Sarcopenia
T. N. Burks et al.

PODCAST
R. D. Cohn and A. Colmone
Losartan improves muscle remodeling and protects against immobilization atrophy by mediating pathways critical for muscle homeostasis.

RESEARCH ARTICLE: Cytosolic DNA Triggers Inflammasome Activation in Keratinocytes in Psoriatic Lesions
Y. Dombrowski et al.
In psoriasis, cytosolic DNA in keratinocytes triggers maturation of the cytokine IL-1β via the AIM2 inflammasome.

RESEARCH ARTICLE: In Vivo Liver Regeneration Potential of Human Induced Pluripotent Stem Cells from Diverse Origins
H. Liu et al.
Hepatic cells derived from human induced pluripotent stem cells of various origins contribute to liver regeneration in vivo.

SCIENCEPODCAST
www.sciencemag.org/multimedia/podcast
Free Weekly Show

On the 13 May *Science* Podcast: protein interactions by design, curing HIV infection, comparing photosynthetic and photovoltaic efficiencies, and more.

SCIENCEINSIDER
news.sciencemag.org/scienceinsider
Science Policy News and Analysis

SCIENCE (ISSN 0036-8075) is published weekly on Friday, except the last week in December, by the American Association for the Advancement of Science, 1200 New York Avenue, NW, Washington, DC 20005. Periodicals Mail postage (publication No. 484460) paid at Washington, DC, and additional mailing offices. Domestic individual membership and subscription (51 issues): $149 ($74 allocated to subscription). Domestic institutional subscription (51 issues): $990; Foreign postage extra: Mexico, Caribbean (surface mail) $55; other countries (air assist delivery) $85. First class, airmail, student, and emeritus rates on request. Canadian rates with GST available upon request, GST #1254 88122. Publications Mail Agreement Number 1069624. **Printed in the U.S.A.**

Change of address: Allow 4 weeks, giving old and new addresses and 8-digit account number. **Postmaster:** Send change of address to AAAS, P.O. Box 96178, Washington, DC 20090–6178. **Single-copy sales:** $10.00 current issue, $15.00 back issue prepaid includes surface postage; bulk rates on request. The identification code for *Science* is 0036-8075. *Science* is indexed in the *Reader's Guide to Periodical Literature* and in several specialized indexes.

AAAS
ADVANCING SCIENCE, SERVING SOCIETY

Published by AAAS

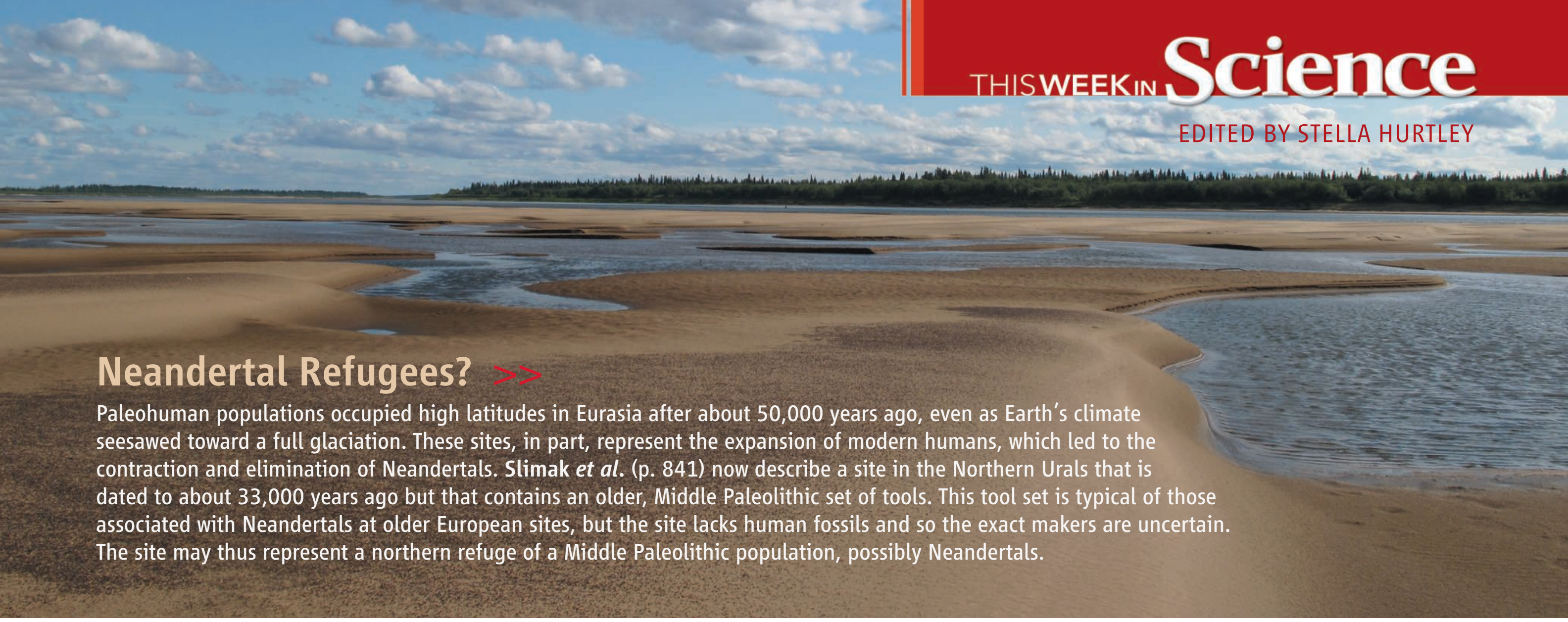

EDITED BY STELLA HURTLEY

Neandertal Refugees? >>

Paleohuman populations occupied high latitudes in Eurasia after about 50,000 years ago, even as Earth's climate seesawed toward a full glaciation. These sites, in part, represent the expansion of modern humans, which led to the contraction and elimination of Neandertals. **Slimak *et al.*** (p. 841) now describe a site in the Northern Urals that is dated to about 33,000 years ago but that contains an older, Middle Paleolithic set of tools. This tool set is typical of those associated with Neandertals at older European sites, but the site lacks human fossils and so the exact makers are uncertain. The site may thus represent a northern refuge of a Middle Paleolithic population, possibly Neandertals.

Heads or Tails?

Planarian flatworms are famous for their ability to regenerate any missing body part (see the Perspective by **Slack**). **Petersen and Reddien** (p. 852) studied the mechanism by which planaria know what body part to regenerate, whether head or tail. The secreted Wnt inhibitor *notum* was selectively activated at anterior-facing wounds to throw a regeneration polarity switch. When *notum* was inhibited using RNA interference, a two-tailed planarian was produced. Thus, local responses to tissue orientation at wounds can determine the regeneration outcome. **Wagner *et al.*** (p. 811; see the cover) examined whether regeneration is made possible by neoblasts (adult proliferative cells) that are pluripotent or whether multiple, lineage-restricted cells are needed. Pluripotent clonogenic neoblasts were able to regenerate lethally irradiated animals otherwise lacking dividing cells, ultimately transforming host animals into genetic clones of the donor. Thus, the remarkable regenerative abilities of planarians require persistence of pluripotent cells into adulthood.

Partners by Design

Proteins such as antibodies that bind with high affinity to targets are valuable in diagnostics and therapeutics. Computational design could complement high-throughput screening methods; however, designing high-affinity interaction partners to chosen targets remains a challenge. **Fleishman *et al.*** (p. 816; see the Perspective by **Der and Kuhlman**) engineered proteins that target a conserved region on the influenza hemagglutinin (HA) protein from the 1918 H1N1 virus, using a computational method aimed to design high shape complementarity and core residue interactions. Two designed proteins exhibited low-nanomolar affinity binding to HA after affinity maturation and the actual binding interface was confirmed by structural analysis to be nearly identical to the designed model.

Nanoimaging Nanocrystals

Analysis of the three-dimensional grain structure in a nanocrystalline metal usually requires destruction of the specimen through repeated removal of the surface layers, or through slicing into multiple specimens. While x-ray techniques can be used nondestructively, the resolution is limited to features larger than 100 nanometers in size. **Liu *et al.*** (p. 833) acquired a series of dark-field electron microscopy images over all beam and sample tilt positions, and determined the grain orientation in each voxel. Analysis of over 100,000 images provided a resolution down to 1 nanometer in a specimen of nanocrystalline aluminum.

He Not So Super After All

Lowering the temperature of a rotating ring of frozen helium to temperatures below 250 millikelvin gives rise to an increase of the rotational frequency. One interpretation of the effect was the formation of an exotic supersolid quantum phase, whereby the atoms within the frozen sample decouple and "flow" akin to that seen for a normal to superfluid transition. Since the initial report, however, the interpretation has been controversial. **Pratt *et al.*** (p. 821) revisited the effect using an ultrasensitive torsional oscillator to comprehensively map out the temperature and mechanical dependence of the frozen helium's behavior. The results favor a scenario involving the shearing of the frozen helium at impurity and defect sites and did not reveal a phase transition associated with a quantum supersolid.

Enhancing Capacitance

Typically, the capacitance of a flat interface is limited by geometrical properties, but electron correlation effects can allow more electrons to be confined. These enhancements are often on the order of a few percent, but **Li *et al.*** (p. 825) observed enhancements of up to 40% at the interface between $LaAlO_3$ and $SrTiO_3$ that arise from a "negative compressibility" effect. These enhancements, which occur at low electron densities when top-gate electrodes deplete most of the electrons from the interface, could prove useful in increasing the speed and power consumption of field-effect transistors.

Rapid Heating

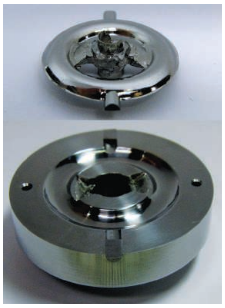

Metallic glasses need very high cooling rates to prevent crystallization. If one wants to process a supercooled metallic glass, even faster heating rates are needed. **Johnson *et al.*** (p. 828) used the discharge of a critically damped capacitor to induce an intense millisecond current pulse to achieve uniform, quantifiable, Ohmic heating, which could be used to measure the temperature-dependent enthalpy of the metallic systems.

Martian CO_2 Store

Mars' CO_2-dominated atmosphere is believed to have been denser in the ancient past. Using radar measurements from the Mars Reconnaissance Orbiter, **Phillips *et al.*** (p. 838,

Continued on page 765

CREDITS (TOP TO BOTTOM): L. SLIMAK ET AL.; W. L. JOHNSON ET AL.

Continued from page 763

published online 21 April; see the Perspective by **Thomas**) found that large quantities of the ancient atmospheric CO_2 could be stored in solid deposits within the Mars South Polar region. If released completely into the atmosphere, which might occur during a period of high obliquity, these deposits would almost double the atmospheric CO_2 content of Mars and could instigate major changes in the red planet's climate.

Light-Harvesting Benchmarks

Plants and a variety of autotrophic microbes use the energy in sunlight to oxidize water, ultimately channeling the electrons into carbon dioxide reduction to form sugars and more complex organic compounds. Artificial solar cells, or photovoltaics, also harvest the energy in sunlight to liberate electrons, but, rather than driving chemical transformations, these electrons often simply loop around a circuit before returning to their starting place. **Blankenship *et al.*** (p. 805) review the fundamental efficiency of photovoltaic-driven water splitting in an effort to make as clear a comparison as possible with the fundamental parameters of natural photosynthesis and assess the prospects for improving the efficiencies of each process, an endeavor crucial to ensuring a sustainable societal energy supply in the long term.

Consciousness and Feedback

The vegetative state is defined by preserved arousal, in the absence of any behavioral signs of awareness. Earlier investigations of patients and healthy volunteers suggested that, in addition to activity in low-level specialized brain regions, the conscious perception of external stimuli requires activation of fronto-parietal cortices. **Boly *et al.*** (p. 858) compared dynamic causal modeling of event-related potentials during auditory processing in healthy subjects and in patients in a minimally conscious state or a vegetative state. Although the frontal cortex was still involved in the generation of event-related potentials in the patients, recurrent processing between higher-order cortices was highly abnormal because of impaired backward connections from frontal to temporal cortices. Thus, the integrity of backward connections is required for conscious perception.

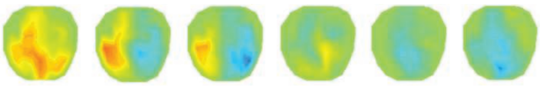

Mother's Curse

Because mitochondria, which contain their own genome, are primarily inherited from the mother, males are an evolutionary dead end for mitochondria. **Innocenti *et al.*** (p. 845; see the Perspective by **Parsch**) compared the genomic transcripts of male and female fruit fly with varying mitochondrial types but the same nuclear background. In females, exchanging mitochondrial genomes altered the expression of only a handful of nuclear genes; in contrast, in males, more than a thousand genes showed a significant change in expression and more than 10% of transcripts exhibited male-biased expression. Because changes in gene expression are generally deleterious, males will exhibit a much greater mutational load than females.

Mosquito Malaria Defenses

Despite the challenges of a complex life cycle, the malaria parasite is terrifyingly successful. Most parasites picked up by the blood-feeding insects fail to develop into transmission stages in the salivary glands because of both mosquito-immune responses and the effects of midgut microflora. **Cirimotich *et al.*** (p. 855) isolated bacteria from wild-caught Zambian *Anopheles arabiensis* and monitored their effect on *Plasmodium* oocyst development in several anopheline species. One enterobacter-like isolate, called *Esp_Z*, was able to almost eliminate the malaria parasite in vitro via the production of reactive oxygen species.

Active Learning

Teaching large groups of undergraduate students often involves lectures. **Deslauriers *et al.*** (p. 862) found that more active teaching formats improved student attention, engagement, and learning. Two sections of a large physics class, one taught by lecture, and one taught with active formats were compared. Students offered clicker response questions, small group tasks, and opportunities for student discussion within the class demonstrated better learning outcomes.

CREDIT: M. BOLY *ET AL.*

François Jacob is an emeritus professor at the Institut Pasteur and Collège de France. François Jacob, André Lwoff, and Jacques Monod won the Nobel Prize in Physiology or Medicine in 1965.

The Birth of the Operon

WHAT IS THE OPERON, WHOSE 50TH ANNIVERSARY IS BEING CELEBRATED THIS WEEK? THE WORD heralded the discovery of how genes are turned on and off, and it launched the now-immense field of gene regulation. The idea was born in André Lwoff's laboratory at the Institut Pasteur. At one end of a long corridor in the loft of a building devoted to research on bacteria were Lwoff, Elie Wollman, and myself. At the other end were Jacques Monod and his group. Lwoff studied lysogenic *Eschericia coli* bacteria capable of producing bacteriophage without infection. Monod was analyzing the properties of the β-galactosidase enzyme in the same bacterium: an enzyme required for the metabolism of lactose that was produced only when the culture medium contained galactosides. To all and sundry the two systems appeared mechanistically miles apart. But their juxtaposition would produce a critical breakthrough for our understanding of life, demonstrating that we cannot presume to know how new ideas will arise and where scientific research will lead.

Toward the end of the 1940s, after 2 years of hospital care for my wounds from the war and a rather slapdash end to my medical studies, I wandered aimlessly in Paris. Unable to realize my dream of becoming a surgeon, I was persuaded by a cousin to launch out into the newly hatching science of biology, and I decided to join a laboratory. After several unsuccessful attempts, no doubt due to my notorious incompetence, I was kindly received by Professor Tréfouel, the director of the Institut Pasteur. He quizzed me on my wartime escapades; explained the importance of sulphamides, of which he was one of the fathers; described the wartime horrors at the Institut; and finally offered me a research bursary.

I spent the first year taking the "Grand Cours," learning bacteriology, immunology, and virology, and then sought a lab in which to use my newfound talents. There were two exceptional labs in Paris: that of Boris Ephrussi and that of André Lwoff. After several fruitless visits, I returned to see Lwoff again. His eyes seemed bluer, the turn of his head more dignified, and his manner warmer. Without giving me time to either display ignorance or express my wishes, he said "We've just discovered how to induce the prophage." I didn't know what a prophage was, let alone what it meant to induce it. Nevertheless, I retorted immediately "That's exactly what I'd like to work on." And Lwoff agreed.

Much later came a day in 1958 when, my mind wandering on a lazy July evening, I sensed in a flash that there were important analogies between the systems studied at the two ends of our corridor: In both cases, the expression of a cluster of structural genes directed the synthesis of several proteins, and this expression was modulated by a "repressor" encoded by an adjacent regulatory gene. Monod and I baptized this structural gene–regulatory gene ensemble an "operon" (from "to operate"), and we quickly recognized that the operon-repressor system could be combined ad infinitum to produce circuits of increasing complexity, adapting to the demands of the cell. Thus did we discover a "mechanism fundamental to all living beings from their very beginnings, and that would persist as long as they exist . . . More than ever, research seemed to be identified with human nature . . . It was by far the best means found by man to face the chaos of the universe."*

Our breakthrough was the result of "night science": a stumbling, wandering exploration of the natural world that relies on intuition as much as it does on the cold, orderly logic of "day science."** In today's vastly expanded scientific enterprise, obsessed with impact factors and competition, we will need much more night science to unveil the many mysteries that remain about the workings of organisms.

– François Jacob

10.1126/science.1207943

*F. Jacob, J. Monod, *J. Mol. Biol.* **3**, 318 (1961). **F. Jacob, *The Statue Within: An Autobiography* (Unwin Hyman, London, 1988).

EDITED BY KRISTEN MUELLER AND JAKE YESTON

BIOMEDICINE

Multitasking Drugs

The escalating cost of developing new drugs has reinvigorated interest in "drug repositioning," the idea that a drug with a good track record for clinical safety and efficacy in treating one disease might have broader clinical applications, some of which would not easily be predicted from the drug's mechanism of action. This concept is illustrated by two recent studies that propose that drugs developed for cardiovascular disease might offer beneficial effects in the setting of prostate cancer.

Farwell *et al.* suggest that statins (cholesterol-lowering drugs) merit serious consideration as a possible preventive strategy for prostate cancer. Building on earlier work on this topic, they found in a study of medical files of over 55,000 men that those who had been prescribed statins were 31% less likely to be diagnosed with prostate cancer than those who had been prescribed another type of medication (antihypertensives). In independent work, Platz *et al*. screened for agents that inhibit the growth of prostate cancer cells and found that one of the most effective was digoxin, a drug used to treat heart failure and arrhythmia. A complementary epidemiological analysis of about 48,000 men revealed that digoxin use was associated with a 25% lower risk of prostate cancer, leading the authors to suggest that this drug be further studied as a possible therapeutic for the disease. — PAK

J. Natl. Cancer Inst. **103**, 1 (2011); *Cancer Discovery* **1**, OF66 (2011).

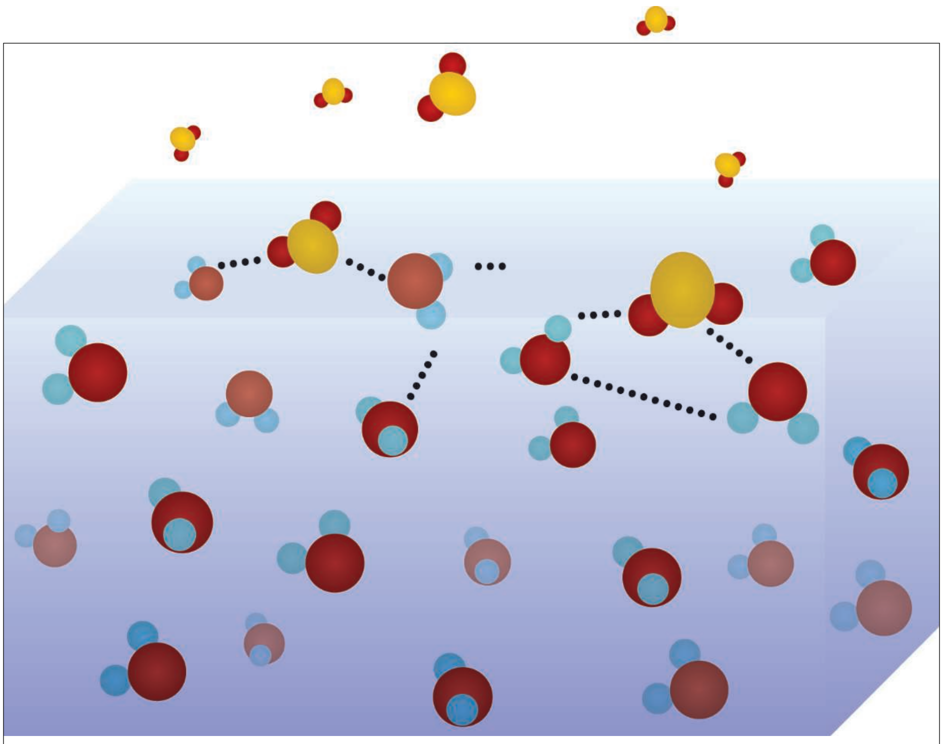

CHEMISTRY

Accumulating SO_2

Once in the atmosphere, SO_2 (a byproduct of coal combustion) can be oxidized further in the gas phase by radicals or undergo a more complex sequence of events within the aqueous phase of aerosol droplets, where (among other things) it may contribute to acid rain. The initial step in the latter process, the surface adsorption of SO_2, probably depends on temperature and droplet composition. Ota and Richmond used vibrational sum-frequency generation—a technique highly sensitive to surface phenomena—to look at the adsorption of SO_2 on water surfaces between the freezing point and room temperature. They found that at the coldest temperatures, almost all of the water molecules formed a surface complex with an adsorbed SO_2 molecule, unlike the much lower surface coverage near room temperature. They also found that changing pH had little effect on adsorption, demarcating a clear division between the surface and internal chemistry of the droplets. — PDS

J. Am. Chem Soc. **133**, 10.1021/ja201027k (2011).

ECOLOGY

Community Shares

Climate change impacts are often assessed by tracking single species' responses. Species exist as part of larger biological communities, however, and environmental changes can influence how species interact and allocate resources. One approach for assessing community-level change is to look at "aggregate properties," the physical and energetic components of a community produced by the contribution and consumption of all its members. These include total abundance, biomass, and energy use. Community aggregate properties are typically thought to be more resistant to disturbance than are single species because of compensatory dynamics among community members.

According to Rowe *et al.*, however, these properties do indeed respond to persistent environmental changes, and such responses may be important indicators of the large-scale ecological impacts of climate change. The estimated total abundance, biomass, and energy use of a small mammal community, consisting of over 20 species, sampled 80 years ago in the Ruby Mountains of Utah, was compared to the same properties measured in the modern community. All properties showed marked declines and a shift in allocation away from diet and habitat specialists to generalists. These findings suggest that climate warming and increased variability in precipitation have reduced primary productivity, resulting in not only a decrease in small mammal biomass but also an increased prevalence of ecological generalists better able to respond to an idiosyncratic fluctuation in resources. — SNV

Ecology **92**, 10.1890/10-1634.1 (2011).

CHEMISTRY

Accumulating CO_2

Even a milliliter of water contains so many trillions upon trillions of molecules that a proton concentration range spanning 14 orders of magnitude (the standard pH scale) is rather easily sampled and measured. What happens, though, when water droplets shrink down to a few thousand molecules or less? At that point, it's hard to even define the pH range, let alone measure it. Levinger *et al.* confronted this dilemma in exploring the potential of CO_2 to penetrate and react within reverse micelles—nanometer-scale pools of water bounded by surfactants within a hydrophobic solvent. They relied on tracking the extent to which vanadium oxide ions dissolved in the

CREDIT (TOP TO BOTTOM): OTA AND RICHMOND, J. AM. CHEM SOC. **133**, 10.1021/JA201027K (2011)

Published by AAAS

water pools linked up with one another after CO_2 was introduced (^{51}V nuclear magnetic resonance spectroscopy can clearly distinguish and quantify the different metal clusters). The known pH dependence of this oligomerization equilibrium in more conventional environments then allowed them to estimate the effective acidity within the micelles before and after CO_2 absorption. The results indicated significant absorption of CO_2 into the water pools, even under ambient conditions, with concomitant acidification presumably associated with carbonic acid formation. The study implies that analogous acidification of atmospheric aerosols by CO_2 may be a more important process than previously appreciated. — JSY

J. Am. Chem. Soc. **133**, 7205 (2011).

CELL BIOLOGY

Splicing Limits the Damage

When plants encounter stresses such as extreme heat and drought, they induce signaling systems to minimize potential damage. Yeast and mammalian cells also engage similar signaling cascades in response to stress. In plant, yeast, and mammalian cells, stress-induced cellular damage is induced by the accumulation of unfolded proteins in the endoplasmic reticulum (ER), and this drives the expression of genes that promote proper protein folding or sequestration of misfolded proteins. Proteolytic processing and splicing of transcription factor mRNA are major mechanisms of generating transcription factors capable of inducing stress-related genes. In plants, two members of the bZIP family of transcription factors are activated by proteolytic processing, but bZIP60, although truncated in its active form, is not activated in this manner. Deng *et al*. now show that in response to stress, mRNA that encodes the transcription factor bZIP60 is spliced to exclude a transmembrane domain and to implement a putative nuclear targeting signal. After splicing and translation, the bZIP60 protein translocates to the nucleus (above; top row: unspliced bZIP60 (green) localized to the cytoplasm; bottom row: spliced bZIP60 localized to the nucleus), where it is able to activate downstream stress-response genes. These results show that stress-induced signaling mechanisms are highly conserved. — PJH

Proc. Natl. Acad. Sci. U.S.A. **108**, 7247 (2011).

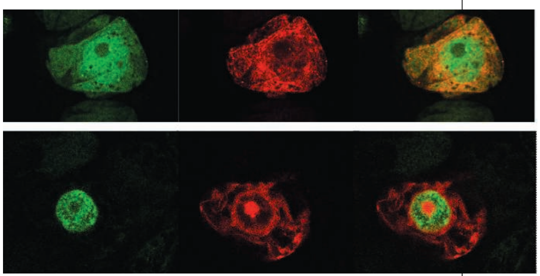

CREDIT (TOP TO BOTTOM):DENG *ET AL., PROC. NATL. ACAD. SCI. U.S.A.* 108, 7247 (2011)

MOLECULAR BIOLOGY

Precision RNA Measurements

Total RNA content within a cell depends on the rates of production of RNA transcripts, their processing, and the degradation of mature transcripts. Rabani *et al*. sought to determine how each of these processes contributes to the total RNA levels within a cell by using metabolic RNA labeling, RNA quantification, and computer modeling. Changes in RNA levels depended most on the rate of transcription; however, this was variable across genes. Degradation rates were also variable across genes, and alterations in degradation rates were important for achieving sharp peaks in RNA amounts. Furthermore, RNA processing rates also varied across genes. These studies comprehensively show that RNA amounts within the cells are determined by complex interactions between all three processes, whose rates may be linked to the biological functions of these transcripts. — LMZ

Nat. Biotechnol. **29**, 10.1038/nbt.1861 (2011).

GEOLOGY

When It's Cold Down South

Earth's climate cooled markedly over the past 65 million years, changing from a world with forests and dinosaurs near the poles to one with huge ice sheets in Antarctica and much lower sea levels. A marked decrease in atmospheric CO_2 levels probably drove this cooling; a further important change was that plate motions isolated Antarctica from the other continents. Temperature records have been available from the oceans and other continents, where a variety of biological records can be tapped, but not from Antarctica for comparison. Dallai and Burgess have now constructed an initial temperature record using hydrogen isotopes in minerals in Antarctic igneous rocks altered by hydrothermal fluids at specific dated times in the past. These fluids tap surface waters where the isotopic ratio in part reflects temperature, and hydrogen is regularly exchanged between fluids and OH-bearing minerals. The record, although rough and in some cases supported with limited data, shows cooling after about 40 to 45 million years ago by more than 10°C and a suggestion of some significant oscillations. — BH

Geology **39**, 423 (2011).

www.sciencemag.org

Science

1200 New York Avenue, NW
Washington, DC 20005
Editorial: 202-326-6550, FAX 202-289-7562
News: 202-326-6581, FAX 202-371-9227
Bateman House, 82-88 Hills Road
Cambridge, UK CB2 1LQ
+44 (0) 1223 326500, FAX +44 (0) 1223 326501

Subscription Services For change of address, missing issues, new orders and renewals, and payment questions: 866-434-AAAS (2227) or 202-326-6417, FAX 202-842-1065. Mailing addresses: AAAS, P.O. Box 96178, Washington, DC 20090-6178 or AAAS Member Services, 1200 New York Avenue, NW, Washington, DC 20005

Institutional Site Licenses please call 202-326-6755 for any questions or information

Reprints: Author Inquiries 800-635-7181
Commercial Inquiries 803-359-4578

Permissions 202-326-7074, FAX 202-682-0816

Member Benefits AAAS/Barnes&Noble.com bookstore www.aaas.org/bn; AAAS Online Store www.apisource.com/aaas/ code MKB6; AAAS Travels: Betchart Expeditions 800-252-4910; Apple Store www.apple.com/eppstore/aaas; Bank of America MasterCard 1-800-833-6262 priority code FAA3YU; Cold Spring Harbor Laboratory Press Publications www.cshlpress.com/affiliates/aaas.htm; GEICO Auto Insurance www.geico.com/landingpage/go51.htm?logo=17624; Hertz 800-654-2200 CDP#343457; Office Depot https://bsd.officedepot.com/portalLogin.do; Seabury & Smith Life Insurance 800-424-9883; Subaru VIP Program 202-326-6417; VIP Moving Services www.vipmayflower.com/domestic/index.html; Other Benefits: AAAS Member Services 202-326-6417 or www.aaasmember.org.

science_editors@aaas.org (for general editorial queries)
science_letters@aaas.org (for queries about letters)
science_reviews@aaas.org (for returning manuscript reviews)
science_bookrevs@aaas.org (for book review queries)

Published by the American Association for the Advancement of Science (AAAS), *Science* serves its readers as a forum for the presentation and discussion of important issues related to the advancement of science, including the presentation of minority or conflicting points of view, rather than by publishing only material on which a consensus has been reached. Accordingly, all articles published in *Science*—including editorials, news and comment, and book reviews—are signed and reflect the individual views of the authors and not official points of view adopted by AAAS or the institutions with which the authors are affiliated.

AAAS was founded in 1848 and incorporated in 1874. Its mission is to advance science, engineering, and innovation throughout the world for the benefit of all people. The goals of the association are to: enhance communication among scientists, engineers, and the public; promote and defend the integrity of science and its use; strengthen support for the science and technology enterprise; provide a voice for science on societal issues; promote the responsible use of science in public policy; strengthen and diversify the science and technology workforce; foster education in science and technology for everyone; increase public engagement with science and technology; and advance international cooperation in science.

Information for Authors
See pages 784 and 785 of the 11 February 2011 issue or access www.sciencemag.org/about/authors

AROUND THE WORLD

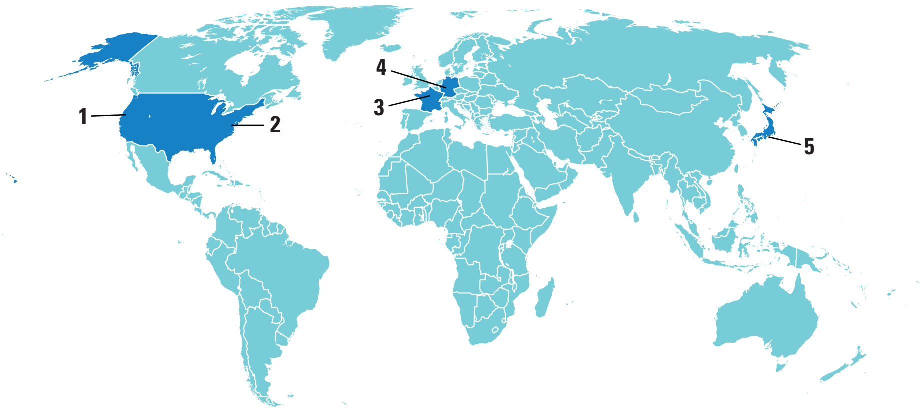

Northern California **1**

Science Is Lacking in California Bay Delta Conservation Plan

A draft plan to restore the California Bay delta east of San Francisco contains major scientific gaps, according to a new report from the National Research Council (NRC).

The delta provides drinking water to about 25 million people and irrigation to the Central Valley, a major agricultural zone. But pumping the water out has helped drive down the estuary's fish populations; at the same time, water demand is increasing.

In search of a sustainable solution, members from interest groups—such as wildlife agencies and irrigation districts—in 2006 began work on the Bay Delta Conservation Plan (BDCP). Its centerpiece is a 65-km-long tunnel designed to ferry water from the Sacramento River north of the delta directly to consumers, thus avoiding the destructive pumping of water from the estuary.

But the draft BDCP fails to scientifically evaluate the consequences for the region's ecosystem, the NRC panel concluded. This analysis is now under way, but the plan has other problems, the report says. Among them: fragmented science and a lack of detail, such as how much water would be channeled through the tunnel. The nearly $150 million endeavor will have to fill in these blanks by the end of 2013, when the final plan is due. **http://scim.ag/ca-water**

Washington, D.C. **2**

White House Tempers Impact of China Ban

The Obama Administration has interpreted a congressionally imposed ban on scientific collaboration with China in a way that may limit its impact. At a hearing last week, John Holdren, the president's science adviser, argued that it doesn't apply to any diplomatic agreements between the two countries. The ban, which applies to activities involving NASA or the White House Office of Science and Technology Policy, is part of the recently passed budget for the rest of fiscal year 2011 (*Science*, 29 April, p. 521). Holdren told Representative Frank Wolf (R–VA), chair of a House of Representatives spending panel and author of the language, that "the prohibition should not be read as prohibiting interactions that are part of the president's constitutional authority to conduct negotiations. But we will be looking at that on a case-by-case basis." After the hearing, Holdren noted that "my assumption is that there will be some activities that will be precluded."

Wolf is unlikely to let the matter rest, however. Don't be surprised if an expanded version of the ban shows up in next year's spending bill.

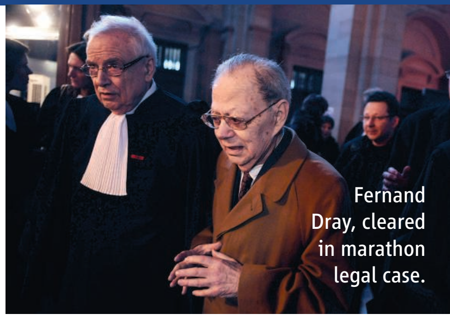

Fernand Dray, cleared in marathon legal case.

Paris **3**

Scientists in Growth Hormone Scandal Found Blameless

A French appeals court last week threw out charges of involuntary manslaughter and other crimes against two scientists involved in a growth hormone scandal that has led to the deaths of 125 children from Creutzfeldt-Jakob disease (CJD), a fatal brain illness. The case has dragged on since the early 1990s, and two of the original defendants have died. But the lawyers for the victims' families say they intend to take the case to France's highest court of appeal.

From 1959 to 1988, France treated 1698 growth-deficient children with hormone derived from pituitary glands taken from human cadavers, a practice that has been linked to the transmission of CJD, a prion disease. Prosecutors faulted the scientists involved for not doing enough to prevent the infections, and for switching to the much safer synthetic growth hormone later than other countries.

But the appeals court confirmed a lower court's 2009 ruling that "no fault" had been committed by biochemist Fernand Dray (pictured), who was in charge of purifying the material at the Pasteur Institute, and pediatrician Elisabeth Mugnier, who was in charge of collecting the pituitary glands and monitoring treatment. The verdict noted that no one could have detected the contamination at the time. **http://scim.ag/CJD-case**

Frankfurt, Germany **4**

European Science Foundation Members Fumble Merger Plans

A plan to create a new body that would provide a powerful voice for science policy across Europe was thrown into disarray last week. The idea was to merge two existing organizations—the European Science Foundation (ESF) and an informal body with the unfortunate acronym EuroHORCs (European Heads of Research Councils)—into a single outfit that would help develop European science strategy, coordinate national research activities, and lobby on behalf of national

CREDITS (TOP TO BOTTOM): OLIVIER LABAN-MATTEI/AFP/GETTY IMAGES; CALIFORNIA DEPARTMENT OF WATER RESOURCES

funding agencies. The new organization, with the working title Science Europe, was planned as something of a counterweight to the European Union, which funds around 5% of the continent's research but is the dominant body in European science policymaking.

But some objected to the exclusion from Science Europe of societies that are now part of ESF; others complained that current ESF funding programs would be scrapped. Last week, the planned merger failed to gain enough votes at ESF's general assembly. ESF is now discussing how to proceed. "Everyone will have to take a deep breath," says ESF President Ian Halliday.
http://scim.ag/merger-fail

THEY SAID IT

"The Q'ero Nation knows its history, its past, present and future is our Inca culture and we don't need any so-called genetic study to know who we are. We are Incas, we always have been and always will be!"

—Benito Machacca Apaza, president of the Community of Hatun Q'eros, in a letter objecting to plans to collect DNA from the remote tribe in Peru as part of the National Geographic Society's Genographic Project. **http://scim.ag/qeros-dna**

Tokyo **5**

Japan Scraps Nuclear Plan

In the wake of the Fukushima nuclear disaster, Japan's prime minister, Naoto Kan, announced this week that his government is abandoning its plan to build 14 new reactors and generate half the country's electricity from nuclear power. Instead, Kan said, Japan will emphasize renewable energy production and conservation. Nuclear plants now produce 30% of Japan's electricity.

The move came 4 days after Kan urged the operators of the Hamaoka nuclear power plant to cease operations for "the safety and security of the Japanese people." The plant, which sits near a fault line in a high-risk seismic area 200 kilometers southwest of Tokyo, is protected from tsunamis only by sand dunes. The Chubu Electric Power Co. complied on 9 May. The shutdown will add to Japan's electricity-generating woes; the country is already facing potential shortages this summer.

NEWSMAKERS

Three Q's

As the head of Howard Hughes Medical Institute's (HHMI's) new documentary film unit, **Michael Rosenfeld** hopes to team up with researchers around the world to bring the excitement of scientific discovery to a broader audience.
HHMI has committed $60 million over 5 years to finance film projects. Rosenfeld, a television journalist who produced the popular *Explorer* series during more than 2 decades at National Geographic, begins his job in July.

Q: Why has HHMI launched this initiative?
Both public and cable TV have had a lot of pressure on their financial budgets. The initiative will make it possible to produce high-end, ambitious projects. A good film can provide clarity about scientific discoveries and what they mean. That's especially crucial in the areas that are often debated … like vaccines or nuclear power.

Q: How do you balance substance and entertainment?
Make the scientific process really engaging. It's the job of the film to make people understand why the process is so important and what makes it so interesting and what the stakes are. A great producer can take an intellectual puzzle and turn it into a mystery story and get the person hooked.

Q: What's an adventure that you've had?
[Volcanologists and I] took a chopper up to the edge of the lava lake in Hawaii. We went out and collected lava samples, and … my [rubber-bottomed] shoes melted out under me. Suddenly I'm essentially standing in my bare socks. But the only injury was to my pride!

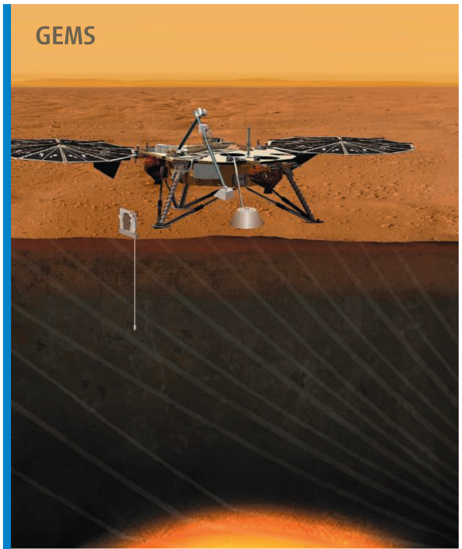

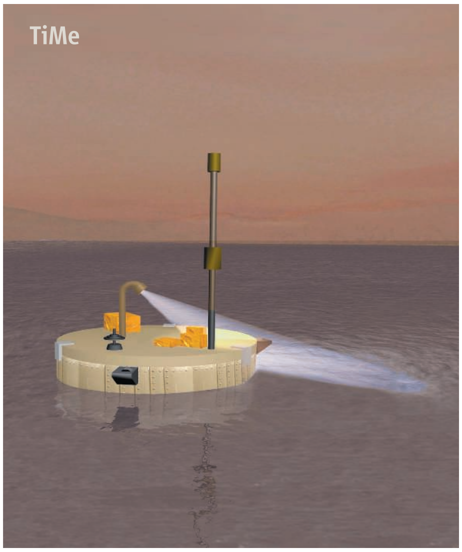

CREDITS (LEFT TO RIGHT): NASA/JPL-CALTECH; OPFM/JPL/NASA; JAMES KEGLEY

Hoping for a Ticket to Ride

Care for a cruise on a hydrocarbon lake? Or a journey beneath the surface of Mars? How about hopping on and off a comet? NASA selected those three possibilities last week as candidates for its next Discovery mission, to be launched in 2016.

The Titan Mare Explorer (TiMe, right) would splash down on a large methane-ethane lake on Saturn's moon Titan, float there for 3 months, and send back data on the lake's composition and its role in Titan's methane cycle. The Geophysical Monitoring Station (GEMS, left) would monitor seismic activity on Mars, probe heat flow from the interior, and track variations in the planet's wobble. The third mission, Comet Hopper, would land on a comet several times and monitor changes as the comet interacts with the sun.

The three competing groups have each been awarded $3 million to flesh out their proposals; NASA will pick the winner next year. The cost: no more than $425 million.

Published by AAAS

FINDINGS

Another Blow to Putative Cause Of Chronic Fatigue Syndrome

An exhaustive hunt for a mouse retrovirus known as XMRV in people who have chronic fatigue syndrome (CFS)—including patients who tested positive for the virus in other labs—has come up dry, further deflating hopes that a cause for this baffling disease has been found. "I'd urge people to move on rather than to keep their hopes hanging on the link between XMRV and CFS," says Ila Singh, a virologist at the University of Utah in Salt Lake City, who led the new study.

The link between XMRV and CFS has sparked debate since it was first reported (*Science*, 23 October 2009, p. 585). Singh's analysis is the latest of several that have failed to find XMRV in CFS patients, but the first to test samples from patients involved in the original study. As Singh and her colleagues reported online 4 May in the *Journal of Virology*, they used several tests for XMRV, including fishing for viral sequences with the ultrasensitive PCR assay, trying to grow the virus in cell cultures, and scouring the blood for antibodies to viral proteins. All 100 samples, including those from 14 patients from the original study, were negative. **http://scim.ag/_XMRV**

Vaccine Thwarts SIV in Monkeys

AIDS vaccine research received a much-needed booster shot this week. An experiment published online in *Nature*, led by immunologist Louis Picker of the Oregon Health & Science University in Beaverton, showed that an unusual approach to outwit SIV (a simian cousin of HIV) protected 12 of 24 vaccinated monkeys from a "challenge" with a particularly virulent strain of that virus. The protected monkeys became infected, but their immune systems drove the virus down to undetectable levels for more than a year. "It's the best result I've seen against the worst SIV known," says David Watkins of the University of Wisconsin, Madison, who was not involved with the work. "I'm very excited by this approach."

The vaccine contains SIV genes stitched into a harmless cytomegalovirus (CMV) vector. AIDS vaccines usually use vectors that quickly die out after delivering the AIDS virus genes, but the CMV stays alive indefinitely and constantly confronts the immune system with the mock version of the enemy. As a result, Picker contends, the immune system stays on high alert and can respond to an attack by the real virus much more quickly. "The whole game changes when you talk about early interception of the virus," Picker says. **http://scim.ag/_SIV**

Ship in Bottle, Meet Rogue Wave in Tub

Toy boats beware! For the first time, physicists have created a rogue wave in a laboratory tank, supporting the idea that a simplified theory can explain the freakishly tall ship sinkers.

Researchers have proposed describing anomalous water waves with a simple differential equation called the nonlinear Schrödinger equation. One of its solutions consists of an isolated peak that emerges out of a steady wave train (a so-called sine wave) then fades back into it, just like a rogue wave. Now, mathematician Amin Chabchoub at the Hamburg University of Technology and colleagues have produced that "Peregrine solution" in a 15-meter-by-1.6-meter tank filled with water to a depth of 1 meter. Using a computer-controlled paddle, they generated a sine wave with an amplitude of 1 centimeter. They then briefly increased the size of the paddle's motion to trigger a rogue wave that grows to three times the sine wave's height and moves at half its speed, exactly as predicted by the Peregrine solution, the researchers report in a paper in press at *Physical Review Letters*.

Demonstrating the Peregrine solution in water waves is a "big step" toward proving that the nonlinear Schrödinger equation can describe real-world ocean waves, says Al Osborne, a physicist at the University of Turin in Italy. Next up: creating rogue waves in water that's more chaotic. http://scim.ag/_rogue

Even Robots Can Be Heroes

Evolutionary biologists have struggled to explain self-sacrificing behavior, which seems to defy survival of the fittest. Simulations of "evolving" robots have now confirmed an explanation posed by biologist W. D. Hamilton in the 1960s: We tend to

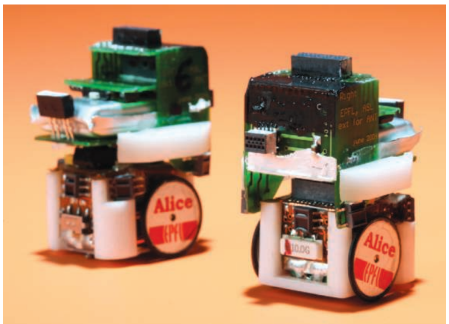

CREDITS (TOP TO BOTTOM): FOTOSEARCH; RICHARD BEHN, NOAA CORPS/NOAA PHOTO LIBRARY; EPFL/ALAIN HERZOG

Published by AAAS

BY THE NUMBERS

10.1 Billion The world population by 2100, according to new projections by the United Nations. It had previously forecasted the population peaking in the low 9 billions, then declining. **http://scim.ag/_worldpop**

8.2% The percentage of Americans with asthma as of 2009, according to the U.S. Centers for Disease Control and Prevention. That's up from 7.3% in 2001.

2.6% The prevalence of autism among children aged 7 to 14 in Goyang, South Korea. That's more than twice the estimated rate in the United States, according to an online paper in *The American Journal of Psychiatry*.

help those who are more closely related to us because they can pass on more of our genes.

To test Hamilton's idea, scientists need to watch organisms evolve over many generations. So Laurent Keller of the University of Lausanne in Switzerland and his colleagues created an evolutionary computer simulation starring tiny robots (pictured). To simulate mutations, the computer randomly tweaked the connections in the robots' "nervous systems," making them better or worse at retrieving small discs—a stand-in for food.

The simulations ran for hundreds of rounds, each time selecting and cloning the best food gatherers and culling the others. Sharing evolved most quickly in more closely related robots, as Hamilton predicted, the researchers reported online 3 May in *PLoS Biology*.

Some researchers are leery of drawing conclusions about organisms from virtual robots, but others say the work shows how robust Hamilton's rule is.
http://scim.ag/robot-heroes

Random Sample

Missing in Action

Who won the 1916 Nobel Prize in physics? Trick question: The Nobel Committee, harried by World War I, left it vacant. But a petition circulating to dozens of U.S. universities aims to fill that gap with Henry Moseley, an x-ray specialist.

In 1913, Moseley, just 25 and then at the University of Manchester in the United Kingdom, determined that each element's spot on the periodic table equaled the proton count in its nucleus, uniting chemistry and atomic physics and giving the table a sound theoretical basis. Moseley likely would have won a Nobel but died serving with the British Army at Gallipoli in 1915.

Nobels cannot be awarded posthumously. But as the centennial of Moseley's death approaches, David Harder, a science enthusiast and former UPS warehouse worker living in California, wants the Nobel Committee to take this unprecedented step. Others, notably Isaac Asimov, suggested the idea before, Harder says, "but since nothing was getting done, I decided I'd take care of it."

So on 1 April ("terrible date to postmark them," he admits), Harder mailed petitions to 104 top chemistry and physics departments in 28 states, asking scientists for support. So far he's gotten no response: "It's really bummed me out."

Harder knew he might struggle to enlist people, partly because one could argue that Nikola Tesla, Lise Meitner, or others deserve vacant prizes, too. But Moseley's "fantastic leap forward" stands above all, Harder argues. "We are not talking about rewriting history," his letter pleads, "merely correcting an error."

High-Tech Gas Drilling Fouling Drinking Water

A study, published this week in the *Proceedings of the National Academy of Sciences*, is the first systematic, peer-reviewed analysis to build a credible link between extraction of natural gas locked deep in shale and the contamination of nearby water wells. The analysis gives few clues, however, to how pervasive such contamination might be.

Injecting high-pressure fluids into deep shale frees methane.

The Oscar-nominated documentary film *Gasland* dramatized the debate over shale gas extraction by showing a homeowner setting fire to well water gushing from a faucet. The supposed culprit was nearby "fracking," pumping fluids into a wellbore until the shale shatters, releasing the tightly bound gas.

Duke University environmental scientists sampled well water across 175 kilometers of far northeast Pennsylvania. Methane was at background levels more than a kilometer from an active gas well. But methane levels shot up closer to fracking operations, in some cases to flammable levels. Chemical and isotopic analyses clinched the case, tying the gas from close-in water wells to the deep shale. The new study will no doubt be on the reading list of a blue-ribbon panel announced last week by Energy Secretary Steven Chu that will recommend ways to improve shale gas fracking.
http://scim.ag/methane-water

CREDITS (TOP TO BOTTOM): UNIVERSITY OF OXFORD, MUSEUM OF THE HISTORY OF SCIENCE, COURTESY AIP EMILIO SEGRÈ VISUAL ARCHIVES, PHYSICS TODAY COLLECTION; ROBERT JACKSON

Unsanitary. A Haitian contractor dumped waste from three Nepalese camps at an open pit.

HAITI'S CHOLERA OUTBREAK

Cholera Linked to U.N. Forces, But Questions Remain

They came to the island with the best of intentions—only to sow disease and death.

An eagerly awaited report from an independent panel leaves little doubt that United Nations peacekeeping forces from Nepal inadvertently introduced cholera to Haiti last fall, triggering an epidemic that has killed almost 5000 and whose end is not yet in sight. The four-member committee, which presented its findings to U.N. Secretary-General Ban Ki-moon in New York City on 3 May, dispatches with the theory that *Vibrio cholerae* had been lurking in local waters and emerged as a result of favorable ecological or environmental circumstances.

Although the study finds fault with the sanitation at three camps of the United Nations Stabilization Mission in Haiti (MINUSTAH), it is careful not to apportion blame; it also says there is no evidence that anyone within the camps ever suffered from cholera. The entire catastrophe may have started with a single carrier: an infected person who wasn't sick himself but shed the bacteria in his stool, says the panel's chair, Alejandro Cravioto, who heads the International Centre for Diarrhoeal Disease Research, Bangladesh, in Dhaka.

This puts the panel's report starkly at odds with another study by French epidemiologist Renaud Piarroux that was published online last weekend by the journal *Emerging Infectious Diseases* (*EID*). Based on data gathered in Haiti early in the epidemic, Piarroux concludes that a Nepalese camp near the town of Mirebalais, in Haiti's Centre department, had a major outbreak of cholera among its men and dumped up to 1000 liters of contaminated feces into local waters, despite telling the world all was fine.

The U.N. panel reviewed a series of genetic studies, some not yet published, which strongly suggested that the *V. cholerae* strain wreaking havoc in Haiti originated in South Asia and was released in Haiti from a single point. A weeklong investigation on the ground in Haiti convinced the group that the outbreak started in Mirebalais and in a matter of days spread along the Artibonite, Haiti's biggest river, which is used widely for collecting drinking water, bathing, washing clothes, playing, and irrigation.

An inspection of the Mirebalais camp further showed that MINUSTAH had failed at a cornerstone of cholera prevention: keeping feces and drinking water apart. Waste from toilets was collected in big fiberglass tanks,

Leaky system. The camp at Mirebalais had "broken pipes and poor pipe connections," a U.N. report says.

but the pipes leading to the tanks were shoddily constructed, and waste may have leaked into an open ditch running through the camp. Moreover, a Haitian contractor who came to empty the tanks twice a week simply trucked the waste to an open disposal pit on a nearby hilltop, which overflowed during rainfall. Panel members also saw children playing and animals roaming near the pit. (Two other Nepalese camps nearby had their waste dumped at the pit as well.)

Piarroux—who investigated the outbreak with other scientists in November at the request of the Haitian government—also blamed unsanitary conditions at the camp, but his paper in *EID* goes much further. The Artibonite delta saw a wave of thousands of cases in the first few days, followed by a sharp drop. Only a massive, one-time release of contaminated feces racing down the river could explain that pattern, he writes.

A back-of-the-envelope calculation that takes into account the number of bacteria one needs to ingest to contract a serious case of cholera, the water volume of the river, and other factors leads Piarroux to conclude that more than 100 trillion *V. cholerae* microbes may have been released—which means that dozens or even hundreds of soldiers were sick. "What happened in this river is something I have never seen in all of my experience with cholera," Piarroux says.

Cravioto says he has no reason to doubt MINUSTAH's claim that it had no diarrhea cases at the camp. The medical records were silent, he says, and "we didn't see any pages that were torn out." Another panel member, Harvard University water and sanitation engineer Daniele Lantagne, says other mechanisms could explain the initial spike in cases, such as *V. cholerae* replication inside the first Haitian victims or in the disposal pit.

CDC epidemiologist Scott Dowell, who wrote a commentary to Piarroux's paper in *EID*, praises Piarroux's "careful field investigations" but says he sees no reason to question MINUSTAH's version either. But Harvard cholera scientist Matthew Waldor says the panel's report doesn't fully address what happened during the early stages of the outbreak. "There are still scientific questions about how the spread happened so rapidly," he says. Waldor says he'd like to see a comparison of the whole-genome sequence of the Haitian strain with one from the cholera outbreak in the Nepalese capital Kath-

CREDITS: RAMON ESPINOSA/AP PHOTO (2)

mandu in September 2010, right before the U.N. forces left home.

Suspicions of a U.N. link to the epidemic have incited protests and violence in Haiti, and the panel does not fan those flames. It says that the outbreak "was not the fault of, or deliberate action of, a group or individual," and that the introduction would never have evolved into disaster without what Lantagne calls a "perfect storm" of other factors, including Haiti's poor infrastructure and the salinity of the Artibonite delta, which favors *V. cholerae*'s growth.

Nevertheless, it proposes a series of measures to prevent such introductions in the future. U.N. installations around the world should get their own waste-treatment facilities so they're independent of questionable local contractors, and U.N. staff coming from cholera-endemic countries should be screened for the disease before leaving home or given a prophylactic dose of antibiotics.

Some scientists have called such measures ineffective or impractical (*Science*, 28 January, p. 388), and Waldor says *The New England Journal of Medicine* made him strike similar recommendations, deemed "inflammatory," from a January paper presenting evidence for an Asian connection. But Cravioto says the measures are not that difficult to implement. Ban Ki-moon has said a new panel will study how to put the advice into practice.

–MARTIN ENSERINK

PHYSICS

Scientific Link-Up Yields 'Control Panel' for Networks

In principle, scientists could control the worm *Caenorhabditis elegans* as if it were a robot by tapping into the creature's 297 nerve cells—as some are trying to do. The neurons switch one another on or off, and, making 2345 connections among themselves, they form a network that stretches through the nematode's millimeter-long body. How many neurons would you have to commandeer to control the network with complete precision? The answer is 49. And the algorithm that made that tally marks a key advance in the young field of "network science," researchers say.

Taking a connect-the-dots approach, researchers have modeled groups of friends, stock markets, the Internet, and countless other systems as networks of points, or "nodes," linked by their interactions. Most research has focused on characterizing different types of networks and their behavior. But physicists Yang-Yu Liu and Albert-László Barabási of Northeastern University in Boston, and engineer Jean-Jacques Slotine of the Massachusetts Institute of Technology in Cambridge, have gone further, taking a step toward manipulating networks.

The trio has found a way to determine the smallest number of nodes that must be externally controlled to force a given network from any initial state to any desired final state. That number can be calculated by brute force, but the size of the computation grows exponentially with the number of nodes. So the researchers take a more efficient tack, as they report this week in *Nature*. For each node in a network, they randomly erase all but one outgoing link and all but one incoming link to create a skeleton called a "matching." They apply a simple technique to make sure the matching contains as many links as possible. In the end, some nodes are left disconnected. And those nodes form a set that can control the original network.

The researchers counted the number of control nodes in 37 real-world networks, including social networks among prison inmates and wiring diagrams of electronic chips, and unearthed some surprises. The number of control nodes doesn't depend on how a network is wired, for example, and the nature of the interactions isn't very important, either. What matters most is a statistical measure of how many nodes have different numbers of incoming and outgoing links, the "degree distribution."

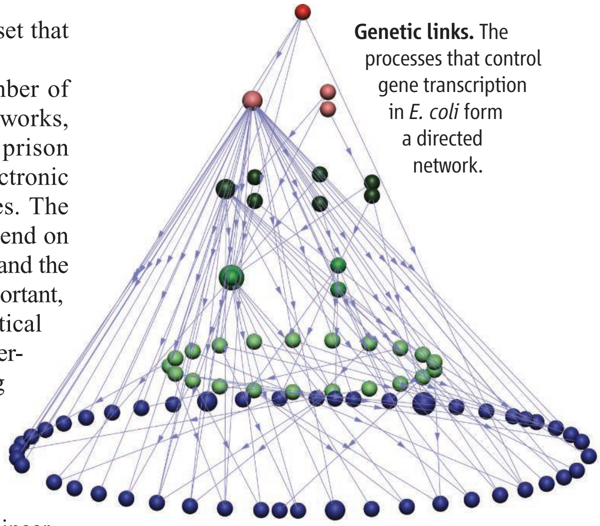

Genetic links. The processes that control gene transcription in *E. coli* form a directed network.

CREDIT: CREATED BY YANG-YU LIU

The work is both more general and more practical than earlier efforts to apply control theory to networks, says Guanrong Chen, an electrical engineer at City University of Hong Kong. Previous studies, he says, dealt only with "undirected" networks: special cases in which if node A influences node B, then node B must influence node A in the same way. The new work treats the more-common case of directed networks, in which A can influence B without B influencing A. Also, Chen says, the algorithm for finding a set of control nodes "is very important because it's useful."

The algorithm might help decipher the networks of biochemical interactions within cells, says Rune Linding, a biologist at the Technical University of Denmark in Lyngby. In kinase phosphorylation networks, proteins called kinases attach phosphate groups to one another to alter their functions. Human cells contain more than 500 kinases with more than 200,000 phosphorylation sites. Biologists have traced those interaction networks but don't know how to control them, Linding says. "We've really been lacking a framework with which to derive this from data and not from wishful thinking," he says. "This paper gives us a framework to go forward."

Even so, the paper has its limitations. For example, it doesn't explain how to manipulate the control nodes to get from one state to another. That likely *would* depend on the details of connections and interactions in the network, says Steven Strogatz, an applied mathematician at Cornell University. "I feel that there is a lot missing between 'controllable in principle' and 'controllable in practice,' " he says.

Still, the paper is important, Strogatz says, and so is the collaboration that produced the results. Twenty years ago, physicists and control theorists locked horns over the study of chaos, he says, as the two groups sometimes ignored or dismissed each other's contributions. "What's really appealing about this paper is that Jean-Jacques Slotine is a topflight control theorist, and [in Barabási] he's teamed up with one of the leading network theorists," Strogatz says. In other words, the paper itself has forged a network among fields.

–ADRIAN CHO

Published by AAAS

ARCHAEOLOGY

Did Neandertals Linger in Russia's Far North?

For more than 150,000 years, Neandertals had Europe's lush river valleys to themselves. Then, beginning about 40,000 years ago, modern humans swept in from Africa and the Near East, spreading rapidly from east to west. Soon, the archaeological evidence suggests, the Neandertals retreated to "refugia" in southern Europe, such as Spain and Portugal—their last holdouts before going extinct.

Or were they? On page 841, a research team claims that some of the last Neandertals may have taken refuge in the dark Arctic north rather than the sunny south. At the 32,000-year-old site of Byzovaya in Russia's Polar Ural Mountains, which at 65 degrees latitude is as far north as Iceland, archaeologists found stone tools they argue are typical of those long associated with Neandertals in Europe.

Tools of contention. Archaeologists argue that tools in Byzovaya Cave (*top*) were left by some of the last Neandertals.

If Neandertals did make the tools, it would be a "very big thing," says archaeologist Wil Roebroeks of Leiden University in the Netherlands. Byzovaya would push Neandertals' range northward by 1000 kilometers, and the site would be one of the youngest claimed for Neandertals, especially since recent redating has moved many Neandertal sites earlier in time (http://scim.ag/Neandertals). It would also show that the cold-adapted Neandertals could survive the rigors of the Arctic.

But because the new evidence is tools rather than the bones of Neandertals themselves, the Byzovaya team appears to have walked into the whirling blades of one of archaeology's sharpest debates: Can a hominin species be identified solely by the stone tools it left behind?

Archaeologists working in Europe have been identifying Neandertals by their characteristic stone tool culture, called the Mousterian, "for 150 years of research," notes archaeologist Ludovic Slimak of the University of Toulouse in France, lead author on the new Byzovaya paper. But a growing number of researchers take issue with the practice, arguing that modern humans in Africa and the Near East often made Mousterian-like tools. "There is no basis for concluding that the simple-looking tools at Byzovaya were made by Neandertals," says archaeologist John Hoffecker of the University of Colorado, Boulder. He says the mammoth hunters of Byzovaya may have been modern humans rather than Neandertals.

Byzovaya has been excavated by several teams since the 1960s, yielding more than 300 stone artifacts and about 4000 animal bones, nearly all from mammoths. Slimak and his colleagues found that the tools were made from stone cores carefully prepared to maximize the number and quality of flakes that could be struck from them with a hammer of stone or bone. That kind of preparation is typical of Mousterian tools, which are associated with Neandertal bones across Europe. (They are named after the site of Le Moustier in southern France, where they were first identified.) The Byzovaya hominins also apparently did not use "blades": long, slender, finely worked tools that in Europe are typical of modern human sites. So Slimak's team concludes that Neandertals probably made the Byzovaya tools.

If the tools are Mousterian, it is a "good bet" that Neandertals made them, archaeologist Harold Dibble of the University of Pennsylvania says. "In Europe, there has never been an exception to [Mousterian] tools being associated with Neandertals," he says.

But others say such a conclusion is premature at best. Artifacts similar to those found at Byzovaya were used by both Neandertals and modern humans throughout western Asia, including the Near East, where both species lived about 100,000 years ago, argues archaeologist John Shea of Stony Brook University in New York. Shea adds that "Mousterian-like" tools are also found in Africa. "They are no more uniquely associated with Neandertals than is a big brain or an opposable thumb," he says.

And Hoffecker says modern humans apparently used Mousterian-like tools if they suited their purposes. Tools similar to those found at Byzovaya are sometimes found at sites associated with modern humans, he says. At Kostenki in Russia, Hoffecker and colleagues have found that such tools were used to butcher horses and other large mammals, even though there is fossil evidence that modern humans occupied Kostenki.

In the *Science* paper, Slimak and his colleagues acknowledge that modern humans could have made the tools at Byzovaya, although they think it unlikely. "Byzovaya is in Arctic Europe, not in the [Near East] or in Africa," Slimak told *Science*, "and in Europe, the equation 'Mousterian equals Neandertal' " has always been "absolutely true." Slimak argues that the less-sophisticated tools found at sites like Kostenki, which he has studied, are not truly Mousterian because they were not fashioned in the same way from prepared cores, even if they look similar. And at sites where modern humans left artifacts that resemble Mousterian tools, they also left behind more sophisticated artifacts that "reveal their cultural affiliation," he says. No such characteristically modern tools turn up at Byzovaya, Slimak insists.

Both camps agree that the debate cannot be definitively resolved without finding hominin bones or DNA at Byzovaya or nearby. Until that happens, says Jean-Jacques Hublin of the Max Planck Institute for Evolutionary Anthropology in Leipzig, Germany, the suggestion that Neandertals ranged so far north would be "an overinterpretation of the archaeological evidence."

–MICHAEL BALTER

CREDITS (TOP TO BOTTOM): JOHN-INGE SVENDSEN; L. SLIMAK *ET AL.*, *SCIENCE* (2)

Not responding. A new EEG technique (*above*) might one day help doctors assess vegetative-state patients for any glimmer of consciousness.

CREDITS (LEFT TO RIGHT): CAROL GUZY/THE WASHINGTON POST/GETTY IMAGES; COURTESY OF STEVEN LAUREYS

NEUROSCIENCE

Feedback From Frontal Cortex May Be a Signature of Consciousness

In recent years, researchers working with people who've suffered massive brain injuries due to accidents, hemorrhages, or other causes have found evidence that some patients who show few outward signs of awareness can experience pain and may even have a degree of consciousness. Better methods for assessing consciousness in these patients might help doctors calibrate pain medication and predict their prognoses, and they might help give comfort or closure to families desperate to know whether a loved one can understand their words or feel their touch.

In this week's issue of *Science* (p. 858), researchers describe a potential step in that direction. By feeding electroencephalographic (EEG) recordings of brain activity into a sophisticated mathematical model, they say they have identified a neural signature of consciousness that is present in healthy people and brain-damaged patients who retain some awareness, but not in people who are truly in a vegetative state. Other researchers say the method is innovative but not ready for clinical use. In the meantime, however, the study may provide insights into the mystery of how consciousness is embodied in the human brain.

Researchers led by Melanie Boly and Steven Laureys of the Coma Science Group at the University of Liège in Belgium collected EEG recordings in 22 healthy volunteers and 21 brain-damaged patients. (Their families gave permission.) Eight patients were diagnosed as being in a vegetative state, characterized by only reflexive responses, and 13 were in a minimally conscious state, a less profound impairment in which patients have occasional flashes of responsiveness, such as following an object with their eyes or squeezing someone's hand on command.

The researchers made the EEG recordings while subjects listened to a series of tones. Previous studies with healthy people have found a characteristic pattern of ups and downs in the EEG trace that lasts several hundred milliseconds after the pitch of the tones suddenly changes—a sign that the brain has noticed. These blips diminish during sleep and under anesthesia, suggesting to some researchers that they may be an indicator of consciousness. Boly and colleagues found that in the vegetative-state patients, the response to changing pitch was diminished and fleeting, lasting less than 100 milliseconds.

To investigate why, the Belgian team collaborated with neuroscientist Karl Friston and colleagues at University College London, who have developed mathematical models that enable researchers to infer the network of brain regions that gives rise to a specific EEG signal. This modeling showed that in all of the study subjects, including those in a vegetative state, the tones stimulated activity in parts of the temporal cortex specialized for processing sounds.

Neuroscientists generally agree that the brain processes sounds and other stimuli in a hierarchical fashion: Signals flow up from the brainstem to areas of the temporal cortex that analyze the frequency, timing, and location of sounds, and then on to "higher" areas of the parietal and frontal cortex thought to contribute to conscious awareness ("That's my cell phone ringing,") and decision-making (a looming deadline or "no time to talk"). In healthy subjects and minimally conscious patients, the modeling indicated, the frontal and parietal cortex send signals back down to the temporal cortex, completing a feedback loop. In vegetative-state patients, this feedback signal was absent, which explains their truncated EEG responses to the changing tones. "What we've shown is that it's this top-down communication from these frontal and parietal networks that is necessary for you to be conscious," Laureys says.

The findings give experimental support to a model of consciousness advocated by Lionel Naccache, a neurologist and cognitive neuroscientist at the French biomedical research agency INSERM in Paris, and colleagues. "We've proposed from a theoretical point of view that the first stages of perception are not conscious, and that conscious perception arises from a long-range conversation across cortical regions," Naccache says. He thinks the new EEG method has "a lot of potential" for improving the clinical diagnoses of unresponsive patients.

One caveat is that the method has only been shown to distinguish groups of people, says Adrian Owen, a neuroscientist at the University of Western Ontario in London, Canada. "In a clinical setting, you want to look at an individual and say whether that person is conscious or not," Owen says. In 2006, Owen and colleagues reported such a method, using functional magnetic resonance imaging (fMRI) to reveal surprisingly robust activity in the brain of one unresponsive subject after she'd been instructed to imagine herself engaging in specific activities such as walking through her house (*Science*, 8 September 2006, p. 1402). His group is working on adapting that method for use with EEG, which is cheaper and more portable than fMRI. "It's obvious that for something to be clinically viable, it's going to have to be EEG-based," Owen says.

It remains to be seen which tool—or more likely, combination of tools—will be most useful for distinguishing vegetative-state patients from those with some level of awareness, says Nicholas Schiff, a neurologist at Weill Cornell Medical College in New York City. But such tools are sorely needed, Schiff says: "What you risk is too great a medical error to be tolerated."

–GREG MILLER

Published by AAAS

Weed whacker. In the United Kingdom, a little louse (*lower right*) is about to be set loose against invasive Japanese knotweed.

BIOCONTROL

Loosing the Louse on Europe's Largest Invasive Pest

Don't be duped by its delicate pale flowers; Japanese knotweed can be a sinister plant. Native to eastern Asia, *Fallopia japonica* was intentionally introduced into gardens in Europe 200 years ago by fans of its attractive blooms; from there it spread to North America. What makes this invasive weed so menacing is its ability to grow through solid concrete foundations, forcing contractors to abandon infested building sites. In England alone, about a half-million homes are uninsurable, and in the United Kingdom, damages and removal cost $288 million a year.

Now the British government has taken a bold step to solve this knotty problem, and North American researchers might not be far behind. Last week, after more than 5 years of research into the matter and an initial pilot trial, the United Kingdom approved the widespread release of one of the plant's natural enemies. While there are dozens of biological controls already in use against insect pests, this is the first officially sanctioned release of one against a weed in the European Union. "This is an extremely important step. … If this is successful, it will really open the doors and open the minds of people for this control method in Europe," says weed biocontrol specialist Hariet Hinz of CABI Europe in Delemont, Switzerland, a nonprofit agricultural research organization.

The weapon against this goliath of the weed world—Japanese knotweed grows into 3-meter-high thickets—is a 2-millimeter-long plant louse, or psyllid, *Aphalara itadori*, whose release at eight sites across England and Wales has been approved by the U.K. Food and Environment Research Agency and the Welsh Assembly Government. Researchers hope the winged insect will reproduce and gradually spread throughout the country, sucking the life out of knotweed. "We want to start an invasion," says ecologist Richard Shaw, who leads the psyllid project at CABI's outpost in Surrey, U.K.

Finding a useful enemy of the weed was a long process—and getting approval to release it was even more arduous. After all, what comes to most people's minds when one mentions biological control are high-profile ecological disasters, such as the release of the cane toad in Australia. Rather than sticking to their target insect, the cane beetle *Dermolepida albohirtum*, cane toads wound up gobbling everything in sight. But events like this are rare, Shaw says; over the past 100 years, more than 1400 organisms—mostly insects and fungi—have been released against 380 target weeds worldwide, and only 1% of them have been found to feed on plants other than their targets.

Identifying a natural enemy that, unlike the generalist-feeding cane toad, only attacks Japanese knotweed was Shaw's goal. In Japan, Japanese knotweed is common but rarely grows big enough to cause problems thanks to 168 insects and 40 fungi that keep it in check. Four years ago, Shaw and his team brought about 40 potential biocontrol agents back to the United Kingdom for further testing.

A literature search of each species' diet pinpointed nine potential knotweed specialists: a sawfly, two weevils, two beetles, an aphid, a couple of rust fungi, and the psyllid. The team then tested those dietary preferences in the lab. They tried to grow each weed eater on 90 other plant species, including important crops, native U.K. plants, and close cousins of the Japanese knotweed, such as bindweeds. The psyllid proved the most host-specific. It was also the easiest to rear in huge numbers, which is vital for raising enough individuals to release as a biocontrol agent.

In 2010, the U.K. government gave the cautious go-ahead to a limited field trial at two isolated stands of knotweed. After 3 months, the knotweed was still infected with the psyllid. Although it was too early to assess the louse's impact on knotweed, the trials confirmed that it had not spread to close knotweed relatives planted among the knotweed.

Coming up with this biocontrol agent has taken "a tremendous effort to identify and risk-assess," says ecologist Jeffrey Bale of the University of Birmingham in the United Kingdom. Later this month, the researchers will release an estimated 100,000 lab-raised lice at eight sites. At each site, they will monitor that the psyllid continues to be selective about its culinary decisions.

In parallel with these efforts, the psyllid may be released in the northeastern United States and Canada in 2012, says Fritzi Grevstad, an ecologist at Oregon State University, Corvallis, and one of the researchers on the project.

Even critics of biological control are impressed with the evidence Shaw's team has amassed. "It looks like these guys are right on track," says Peter Stilling, an ecologist at the University of South Florida, Tampa. "They appear to have done their homework" with respect to finding a knotweed specialist, he says. However, Stilling remains worried about unforeseen consequences of the release on the whole ecosystem. He cites the example of a fly species that was introduced into the western United States in the 1970s to control knapweed. The fly didn't kill the weed but instead caused it to form hundreds of galls, which provided an enriched food source for mice. These mice carried hantavirus, which causes serious respiratory problems in humans if contracted. As the mice population grew, the rates of hantavirus infection in humans at a study site in western Montana went up.

Equally important, it remains to be seen if the psyllid can control the knotweed, Stilling says. Shaw agrees: "We are very good at saying what [the psyllid] won't eat … but not whether it will establish," or how effective it will be. Even so, if it reduces the impact of Japanese knotweed by even 1%, it will have paid for its release within a year, Shaw says.

–JENNIFER CARPENTER

CREDITS: WIKIMEDIA COMMONS; (INSET) RICHARD SHAW, CABI

Published by AAAS

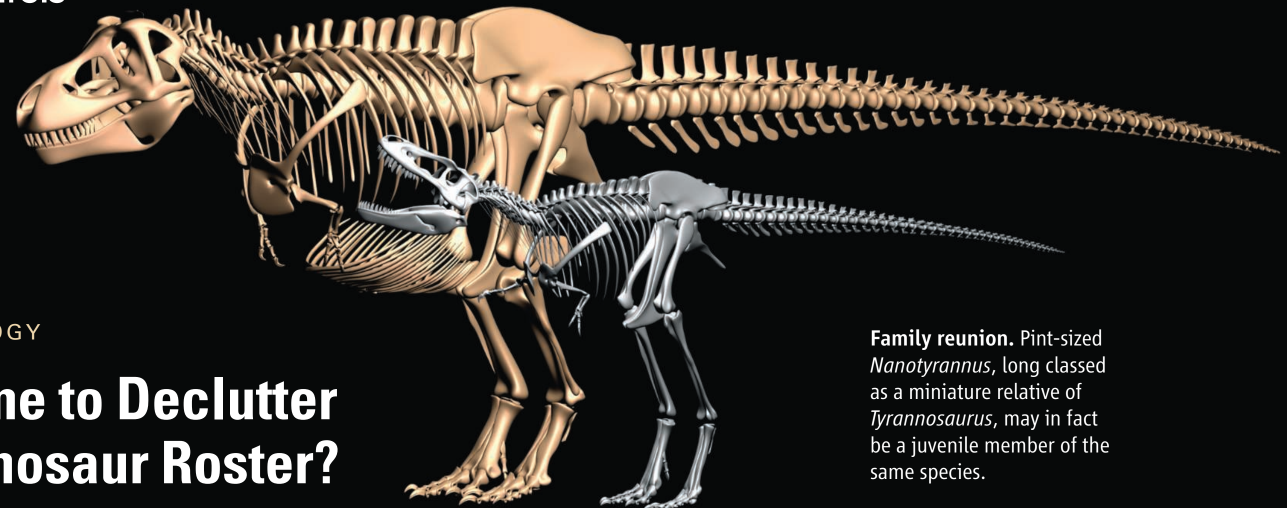

PALEONTOLOGY

Is It Time to Declutter The Dinosaur Roster?

Family reunion. Pint-sized *Nanotyrannus*, long classed as a miniature relative of *Tyrannosaurus*, may in fact be a juvenile member of the same species.

BOLOGNA, ITALY—There are too many dinosaurs in the world, and John Horner says it's time to start culling the herd.

Horner has nothing against the ancient reptiles; as a paleontologist at Montana State University, Bozeman, he has discovered several new species of them himself and even has two named after him. But he worries that—with almost 1000 types of dinosaurs on record and a new species being named somewhere in the world every 2 weeks—too many supposedly new discoveries are actually duplicates of animals already on the books.

Horner wants to set the record straight. At a conference in his honor here last month,* Horner gave colleagues a preview of his plan for doing that: a rigorous set of procedures for studying dinosaur fossils that he calls the Unified Frame of Reference (UFR). "To take Einstein's word, it is a kind of geobiological unified field theory," Horner told *Science*. If implemented worldwide, he says, UFR will eliminate at least 50 dinosaur species in a few years by revealing that those animals were actually other known dinosaurs at different stages of growth.

Other researchers who have studied the "alias problem" share his concern. Michael J. Benton, a paleontologist at the University of Bristol in the United Kingdom, says his analyses of fossil data indicate that 51.7% of dinosaur species are miscategorized. That's a "frightening figure," he says. "This means that more than half the species of dinosaurs ever named were in error."

Part of the problem, Horner says, is that scientists are sometimes too keen on finding and naming new dinosaurs. Philip Currie of the University of Alberta in Edmonton, Canada, president of the U.S. Society of Vertebrate Paleontology (SVP), agrees. "Paleontologists are still more concerned about establishing new species than they are of assessing the … variation of an already established species," Currie says. "Both researchers and journals consider a paper establishing a new species' name as more interesting and publishable." Researchers also tend to study the external characteristics of fossils, such as the size of a leg bone, the shape of a skull, or the number of teeth in a jaw, Horner says, and to focus too much on their differences rather than their similarities. Yet paleontologists are coming to realize that the bones of an adult dinosaur can be very different from those of a juvenile animal of the same species and can easily mislead scientists into thinking they are two different species.

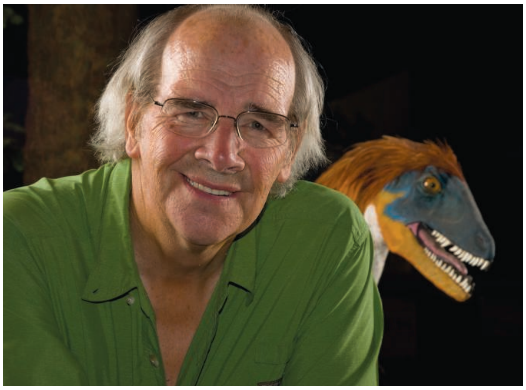

Hit man. John Horner urges his fellow paleontologists to winnow out misidentified dinosaurs.

Thus, Horner's UFR urges researchers to determine as early as possible whether a fossil represents a juvenile animal or an adult. "Being able to decipher the development of various stages of growth of a dinosaur is as important as having discovered a new one," Horner says. In particular, he says, paleontologists must look at the bones from the inside, using microscopic histological analysis to distinguish the spongier bone tissue of young animals from the denser bones of older ones. Features similar to the growth rings in tree trunks can also highlight whether a dinosaur was a juvenile or an adult. Many researchers have shied away from bone histology to avoid spoiling specimens, Currie says, but modern techniques that use minute samples make such fears unfounded.

UFR also calls for rigorous analysis to establish both the place and the age of the rocks in which a fossil was found. Early in their development, Horner explains, the skulls of young dinosaurs may resemble the relatively unspecialized skulls of primitive ancestral species. To avoid confusion, paleontologists must know precisely where a specimen came from, how it appeared while still encased in rock, and which level it occupied in a geologic formation.

Using this painstaking approach, Horner and other researchers have concluded that several dinosaurs long considered to represent different species could be the same animal. *Nanotyrannus*, whose first fossils were unearthed in the 1940s, could be a young *Tyrannosaurus rex*; *Dracorex* and *Stygimoloch* could be the same beast as *Pachycephalosaurus*; *Torosaurus* may be an adult *Triceratops*. Not everyone accepts all of those reclassifications, but they are gaining attention. And many more are likely to follow after Horner unveils his complete UFR program. He hopes to present it at SVP's annual meeting this November. "The proposals by Horner are very important as a reminder of a problem paleontologists are aware of," Benton says, "but we still don't know if it will provide a 100% watertight solution that means we will never make mistakes about dinosaur species ever again."

–LAURA MARGOTTINI

Laura Margottini is a freelance writer based in Rome.

*La settimana di Jack Horner, 11–15 April 2011.

NEWSMAKER INTERVIEW: TARA O'TOOLE

Homeland Security Science Chief Aims to Put House in Order

When Tara O'Toole took over as undersecretary of science and technology at the U.S. Department of Homeland Security (DHS) in November 2009, she knew it was among the least enviable jobs in federal science administration.

Since its inception in 2002, the department's science and technology directorate has been something of a black sheep among government science agencies. Congress has repeatedly criticized it for failing to set priorities for itself and failing to provide adequate support and tools for border protection, cargo screening, airport security, and other homeland security missions. University researchers have complained that the directorate has given short shrift to basic research. The budget for the directorate's Office of University Programs, through which DHS funds 13 research centers at universities and national labs, has declined steadily from $70 million in 2004 to $40 million in 2011, reflecting an antipathy toward basic research among agency officials and congressional overseers. The directorate's overall budget is $686 million.

A physician and public health expert who worked in government before founding the Center for Biosecurity at the University of Pittsburgh in 2003, O'Toole is the first academic to lead the directorate; previous heads were former military and industry officials. O'Toole spoke to *Science* recently about her efforts to boost S&T's role in making the country more secure. The questions and remarks have been edited for brevity and clarity.

—YUDHIJIT BHATTACHARJEE

Q: The directorate has come under a lot of criticism from Congress over the years. How are you responding?

T.O'T.: We're putting a very fierce focus on getting technologies into the field in the next couple of years [to help the different branches of DHS such as Customs and Border Protection and the Transportation Security Administration (TSA)]. We are going to go looking at technologies that are already in late-stage development, whether it's in the private sector or universities. … We're going to do this in a much more efficient, turbocharged way than before.

Q: DHS's support for university research has declined. Does basic research have a role in your scheme?

T.O'T.: Absolutely. We are going to do basic research in some fields that are unique to DHS, like the detection of very small amounts of homemade explosives that terrorists want to use. … But our big emphasis is on transitioning technologies to use.

CREDIT: DHS

"But I do think that a lot of the complaints from the scientific community about the proliferation of [biosecurity] labs is really rice bowl politics."

—TARA O'TOOLE, DHS

Q: You've stated that you want to enhance the directorate's analytic function. Can you give me an example of what you're doing?

T.O'T.: Last spring, Customs and Border Protection wanted to know how to proceed with technologies that they were deploying across the southern border [to prevent illegal immigration]. And we helped them think through what worked and what didn't. You couldn't have a one-size-fits-all technology for the whole southern border, which varies tremendously geographically. Our analysis factored heavily into their decision not to go forward with an electronic fence but instead use that in certain segments and be more flexible elsewhere.

Q: There have been questions about the scientific validity of TSA's behavioral screening program at airports [known as Screening of Passengers by Observation Techniques or SPOT]. Has the directorate evaluated it?

T.O'T.: We have tested it, and yes, it was validated. There's no question that using the SPOT program compared to randomized screening of people is more effective. We picked up more illegal contraband, more false documents, and there were more law-enforcement arrests.

Q: What other changes are you making to make the directorate more effective?

T.O'T.: We're already active in testing and evaluations at the back end of acquisitions: cargo scanners, Coast Guard boats, sensors, lots of stuff. But the testing is only as good as the requirements set in the first instance. If those aren't rigorous enough, you won't get what you're hoping for. What we want to do is help our [branches] think through what they might do in developing technical requirements so that we don't get all the way down this long acquisition process and find out that what we got didn't fit, doesn't work, isn't what we needed in the first place.

Q: Has that been a problem?

T.O'T.: Yes. One of the old examples is the puffers that TSA bought, which worked great in the lab trying to detect explosives via trace detection. When you got them in an airport, they required a lot of maintenance, largely because they were sucking in dirty air which was messing up the mechanisms.

Q: You've said biological threats are a priority. What's your response to those who accuse you and other biodefense advocates of fear mongering?

T.O'T.: I strongly disagree. There's absolutely no doubt that Al-Qaeda has pursued biological weapons and said they'll use them. There's absolutely no doubt on a scientific, analytical basis that a biological weapon could have very bad consequences. The threat and our need to defend against it is going to grow as the science advances.

I think asking whether we need x or y number of biodefense labs is perfectly legitimate. But I do think that a lot of the complaints from the scientific community about the proliferation of BSL-4 [biosecurity level 4] labs is really rice bowl politics. I think there have been erroneous myths propagated that biodefense took away money from basic research at the NIH. That is not true.

Proof negative. The apparent cure of Timothy Ray Brown (*left*) has given momentum to novel interventions like the gene therapy that Matt Sharp (*right*) received.

The Emerging Race To Cure HIV Infections

Timothy Ray Brown's startling fate has pushed to the front a daunting research challenge that long seemed a fool's errand

IN MAY 1995, AFTER LEARNING THAT A FORMER PARTNER HAD become infected with HIV, Timothy Ray Brown, then 29, decided he should take the test himself. Brown, an American living in Berlin and working as a translator, felt perfectly healthy, had not had sex with his former partner in years, and 5 years earlier had tested negative. "It was a bit of a shock," Brown says, when he found he was infected.

At the time, HIV was seen as a death sentence. AZT and two other antiretroviral drugs (ARVs) had come to market, but the pills typically delayed death from AIDS for only a few years. The damage to Brown's immune system wasn't yet life-threatening: His CD4 count, which refers to the white blood cells that HIV destroys, had dropped to under 400 cells per microliter. (Normal is 600 to 1200.) But his doctor recommended immediate treatment, and Brown started taking AZT.

Within a year, cocktails of new ARVs proved so effective that an HIV infection became a chronic disease. Brown changed regimens repeatedly to take advantage of the advances, but he suffered from many side effects, from headaches and night sweats to diarrhea and vomiting. In 2000, his doctor suggested he take a break and stop all medication.

By 2002, Brown's CD4 level had plummeted to 250, 50 shy of an AIDS diagnosis, which indicates that a person's immune system can no longer contain otherwise harmless opportunistic infections. He started treatment again, easily tolerating a cocktail of new-generation ARVs. The amount of virus in his blood, the so-called viral load, dropped to an undetectable level on the most sensitive test available.

Four years later, Brown, then 40, received a second devastating diagnosis: He had developed acute myeloid leukemia, a highly lethal cancer, unrelated to HIV. Because of the complexity of treating leukemia in an HIV-infected patient, his doctor referred him to Campus Benjamin Franklin, a large clinic affiliated with the Free University of Berlin. Gero Hütter, an oncologist and hematologist, took the case.

Three rounds of chemotherapy caused liver and kidney failure and high fevers; Brown became so ill that the hospital put him in the intensive care unit and induced a coma. "While I was in the coma for 16 hours, they thought I was going to die and told my boyfriend they didn't know if I would make it," Brown says. But he fully recovered. In September 2006, Brown took a monthlong trip to Italy and upon his return started working out at the gym again. "I was doing fine," he recalls.

Online
sciencemag.org
Podcast interview with author Jon Cohen, and *Science*LIVE chat with NIH's Anthony Fauci and UCSF's Steven Deeks.

Hütter, who has since moved to the University of Heidelberg, warned his patient that leukemia often returns, and that if it did, the next line of treatment was a bone marrow transplant to replace his stem cells. Then Hütter, who had never treated an HIV-infected patient before, proposed a radical idea: What if a stem cell transplant could eliminate both the leukemia and HIV?

Hütter knew from reading the literature that some rare individuals were highly resistant to becoming infected with HIV because of a mutation in their CD4 cells. HIV establishes an infection by attaching to both the CD4 receptor and a second one on the cell known as CCR5. A mutation in the *CCR5* gene known as δ32, which causes no obvious harm, bars the cellular doors to HIV. Hütter suggested to Brown

CREDIT: BLOOMBERG/GETTY IMAGES

that if they had to do a transplant, they might as well try to find a δ32 donor. "I told him we don't know what will happen, but there might be a chance we'll get rid of the HIV," Hütter says.

Brown at first wasn't interested. "I thought I had got rid of the leukemia because the chemotherapy had worked," Brown says. "And I figured that I always had the medication to fall back on for HIV, and I could probably take it for 50 years and do OK." But in early 2007, his leukemia relapsed, and he gave Hütter the green light to look for a δ32 donor. After screening 62 possibilities for a genetic match that Brown's immune system would tolerate, Hütter found a German man living in the United States who had inherited the δ32 mutation from both parents. They transplanted Brown in February 2007, a procedure that required first destroying his immune system with drugs. He stopped taking his ARVs.

Eleven months later, his leukemia returned again, but his HIV remained undetectable. Brown received a second transplant from the same donor, this time first ablating his immune system with drugs and whole-body irradiation.

Today, Brown remains free of leukemia. And although he has not taken ARVs for more than 4 years, the most sophisticated labs in the world cannot find any HIV in his body

Audacity of hope. At a press conference in November 2008, Hütter described his patient's promising prognosis.

CREDIT: JOHANNES EISELE/REUTERS

Proof of concept

The AIDS epidemic surfaced in June 1981, and the virus has since infected more than 60 million people, killing half of them. Brown, who became widely known in the media as the "Berlin patient" after Hütter publicly described the case in 2008, is the only living human, a growing consensus contends, to be cured.

Since 2008, there's been widespread leeriness about oversimplifying Brown's case and hyping the prospect of an AIDS cure. And Brown's treatment clearly does not offer a road map for many others. After all, the expensive, complex, and risky transplant only made sense because Brown was dying from leukemia. Nor is it clear exactly which components of the extensive transplant regimen cleared the virus from his body.

But Brown's case has moved the much-ridiculed cure idea onto the most scientifically solid ground it has yet occupied, say leading AIDS researchers. Brown's case showed for the first time that it is possible to rid the body of the virus—even from the minuscule reservoirs where the virus can hide out for years, evading both the immune system and ARVs. His astonishing turnaround also raised hopes that other, more practical drugs and immune system modulators might find and destroy every last bit of virus—or at least reduce it to such low levels that people no longer need ARVs.

There are skeptics who say Brown's virus may still come back. At first, even Hütter would not say Brown had been cured, pointing out that a cancer patient has to be free of disease for 5 years before an oncologist will use that term. But he is increasingly willing to use the "c" word, as are other leading researchers.

"Some people pooh-pooh it, but I think it's a game changer," says James Hoxie, a virologist at the University of Pennsylvania. "It's put the word 'cure' in the vocabulary. I don't care if it's $n = 1$. It shows that it's possible." Steven Deeks, an HIV/AIDS clinician at the University of California (UC), San Francisco, who has put efforts to cure the disease on the front burner, says, "A lot of people were interested in cure research before the Berlin patient, but he is a proof of concept. That had a big impact on the field."

Millions of new dollars are being devoted to what some call "a race" to find a cure. The U.S. National Institutes of Health (NIH) last November solicited proposals for an $8.5-million-a-year collaborative grant to search for a cure, and several high-powered consortia applied. NIH last month added another $4.5 million to the cure research pot with the announcement of new grants to develop therapies that will allow people to stop taking ARVs for prolonged periods. The Bill and Melinda Gates Foundation, the California Institute for Regenerative Medicine, and the Foundation for AIDS Research has each issued cure-related grants. The push for a cure is further intensified by limitations of even the best ARVs and the extraordinary cost of providing them to everyone in need for decades on end.

Christine Katlama, who heads the AIDS clinical research unit at the Pitié-Salpêtrière Hospital in Paris, said she hasn't felt this buoyed about the prospects of helping HIV-infected people since the arrival of powerful ARVs—"highly active antiretroviral treatment," or HAART—15 years ago. "For many of us who were for a long time in the field of HIV, it's a very exciting time," she told the 200 attendees at the International AIDS Society's first-ever meeting devoted to cure research, which was held in Vienna last July.

Purging reservoirs

In 1996, *Time* named AIDS researcher David Ho its "Man of the Year," in no small part because he had dared to proclaim that HAART might eliminate HIV from a person's body. Ho, head of the Aaron Diamond AIDS Research Center in New York City, calculated that given the half-life of immune cells, if HAART completely suppressed the virus for 3.2 years, eradication would likely occur. But in the spring of 1997, Robert Siliciano's group at Johns Hopkins University in Baltimore, Maryland, reported a pivotal discovery that torpedoed Ho's simple cure idea. It also introduced a formidable challenge to curing the disease that continues to this day.

Siliciano's group identified the existence of pools of "resting" CD4 cells that harbor HIV in their chromosomes but do not produce new viruses unless they are called into action. These latently infected cells serve as the immune system's memory and can live for years. Siliciano and Ho together published a study in the 14 November 1997 issue of *Science* (p. 1295) showing that people on HAART who had "undetectable" levels of HIV on standard tests for up to 30 months all had reservoirs of about 1 million latently infected cells. Siliciano, his wife Janet, who is also at Johns Hopkins, and co-workers later estimated that it would require 72 years of HAART to clear those stubborn reservoirs.

As bleak as his assessment was, Siliciano's discovery pointed the way to a new strategy for curing AIDS. He and other investigators reasoned that if they could wake up those resting cells, they

Published by AAAS

would start to divide and force HIV out of hiding. This, theoretically, would "purge" the reservoir as the production of HIV would either kill the cells directly or mark them for immune attack. ARVs would mop up any new HIVs before they could infect virgin cells.

A few groups, including Ho's, soon tried to purge reservoirs by jolting the immune system with agents like the chemical messenger interleukin-2 and a monoclonal antibody. Virologist Douglas Richman of UC San Diego says this strategy caused the equivalent of toxic shock syndrome. "They almost killed their patients," Richman says.

They almost killed cure research, too. But with Brown's success and a more refined understanding of reservoirs, efforts to purge them are again the cornerstone of cure strategies. Several prominent research groups have begun experimenting with a variety of different approaches, including using drugs already on the market to treat other diseases, tweaking immune systems, and engineering gene therapies to mimic Brown's transplant.

All these early trials are big gambles, and no one is expecting to discover a cure anytime soon. But with the field's momentum and better funding, hopes are high that progress—which at this point would mean simply showing that an intervention reduced a latent reservoir by any amount—could surface in the next year or two. And luckily for the field, there are plenty of HIV-infected people willing to join these cure studies, which often means agreeing to highly unusual experimental interventions and the extremely invasive tests needed to assess whether they have had an impact.

"It's not like you can take a little blood from someone's arm and know something. … To measure a rare event you need a lot of cells."

—DAVID MARGOLIS, UNIVERSITY OF NORTH CAROLINA, CHAPEL HILL

Acute angles

At 8 a.m. one October morning in 2010, a researcher dressed in a coat and tie entered the apheresis room at the memorial hospital run by the University of North Carolina (UNC), Chapel Hill. But the man, who is in his mid-50s, had not come to study the patients in this room—he was one of them. Over the next 4 hours, a machine would drain the blood from his body two times, 10 liters in all, and replace it, separating out billions of his white blood cells for later analysis. The researcher, who asked that his name not be used, had joined a unique study at the university led by UNC molecular virologist David Margolis that hopes to shrink the HIV reservoir.

Four years earlier, the researcher had gone to see his doctor after repeated night sweats and a fever spiking to 40°C. "I told him I'd been involved in risky behavior and should be tested for HIV," recalls the man, who is married and has children. The antibody test came back negative.

The researcher knew that an HIV infection could take several weeks to trigger a detectable antibody response used in the stock test, but that the polymerase chain reaction could pluck out the viral genetic material itself. He requested a PCR test, which confirmed that an acute HIV infection explained his flulike symptoms. "The first thing I thought about was suicide, the second thing I thought about was suicide, and the third thing I thought about was suicide," he says.

Within a month, the man joined a trial at UNC to assess whether HAART offered extra benefits if people started treatment during acute infection. In particular, HIV destroys CD4s in the gut during the first few weeks of infection, and evidence suggests that when people wait to start HAART—which is standard care—those cells never completely return. This in turn causes a chronic state of inflammation that leads to long-term health problems such as cardiovascular disease and diabetes, even in people who have undetectable levels of virus while on HAART.

The UNC team is now following 80 people who started ARVs during acute infection, and from that cohort, they have recruited 20 volunteers, including this man, to take part in a cure trial that began in March. Margolis and his team reasoned that people treated during the acute phase should have smaller pools of latently infected cells than those who start HAART later, and the smaller the reservoir, the easier it should be to drain.

The UNC study adds to standard HAART a Merck drug, SAHA, already on the market to treat cutaneous T-cell lymphoma. In addition to its cancer-fighting abilities, SAHA tinkers with the structure of chromosomes and kick-starts transcription of DNA (see sidebar), which Margolis and others are hoping will flush latent HIV out of hiding, leading those cells down the road to ruin.

Determining whether SAHA works requires an extraordinary commitment from the infected researcher and the 19 other participants: These otherwise healthy people must repeatedly undergo the grueling, time-consuming apheresis procedure to quantify their minuscule reservoirs and assess whether they have shrunk. "It's a big hassle," Margolis says. "It's not like you can take a little blood from someone's arm and know something. … We're trying to measure a rare event, and to measure a rare event you need a lot of cells."

Daria Hazuda, vice president of virus and cell biology at Merck Research Laboratories in West Point, Pennsylvania, shares Margolis's enthusiasm that SAHA might shrink reservoirs. But Hazuda, who is part of a collaboration led by Margolis that's bidding for the new NIH cure money, also urges people to keep hope in check. "From an experimental medicine point of view, that's a great approach," Hazuda says. "Is that going to be the answer by itself? Having worked so many years on HIV therapy, it would seem to me a single molecule to address reservoirs is a bit naïve."

Multipronged attack

Don Howard, a 47-year-old management consultant in San Francisco, started on HAART the day after he tested positive in 1996. "At some level, I'm a control freak," says Howard, who is so fit and radiant he could be in advertisements for energy drinks. "The notion that I could take something to make it all better was extremely appealing." Now he's first in line for one of the cure studies getting under way at San Francisco General Hospital, where he has been Deeks's patient for 15 years.

Like the UNC group, Deeks and his collaborators hope to purge reservoirs with drugs that trigger transcription, but they have several other strategies in the works that hit the virus from other angles. The trial participants again will come from a group of patients who started treatment during acute infection, and no one has been on HAART longer than Howard. "It suggests he's closer to eradication than anyone in our cohort," Deeks says.

CREDIT: J. COHEN

Howard's motivation to join the study has more to do with curiosity and a desire to contribute than concern about long-term damage from the virus or drugs. "It's more intellectually interesting than it is practically compelling," he says. Nonetheless, he, too, is willing to undergo deep probes of his body to quantify his reservoir. One of the most difficult challenges researchers face is that reservoirs can pool in tissues that are difficult to access. Howard has already had lymph nodes excised and bone marrow extracted, and he may undergo biopsies of his gut, which is home to an estimated 80% of the body's CD4 cells.

Deeks and his collaborators contend that reservoirs persist by different mechanisms, which will require different strategies to deplete them. One possibility is that even in people like Howard who have undetectable virus on HAART, HIV constantly replicates at low levels, creating new latently infected cells and perpetually refilling reservoirs. Adding another powerful ARV to the HAART cocktail, then, might shut down that production.

"You can't cure people by getting rid of low-level replication, but if you want to cure people, you have to get rid of it."

—STEVEN DEEKS, UNIVERSITY OF CALIFORNIA, SAN FRANCISCO

Although several "intensification" studies have failed to detect any impact on HIV, Deeks remains convinced that the approach shows promise. "You can't cure people by getting rid of low-level replication, but if you want to cure people, you have to get rid of it," Deeks says. He also points to an intensification study reported in the April 2010 issue of *Nature Medicine* that found hints of an effect. Led by Maria Buzón of the Autonomous University of Barcelona in Spain, the study has sparked debate and divided Deeks and his like-minded colleagues from Margolis, Siliciano, Richman, and many others who are convinced that standard HAART has reached the limits of what ARVs can do.

After upping the subjects' ARVs, Deeks's team plans to begin testing the drug disulfiram, also known as Antabuse, which is on the market to treat alcoholism. Siliciano's lab recently discovered in test-tube experiments that disulfiram, like SAHA that Margolis is testing, turns on HIV transcription in latently infected cells, although the mechanism is not clear.

Triggering transcription with drugs like disulfiram or SAHA carries risks, especially when tested in healthy people like Howard. On top of the direct toxicities of the drugs, Eric Verdin, a virologist at the Gladstone Institute of Virology and Immunology and one of Deeks's collaborators, cautions that inducing transcription could stir endogenous retroviruses from their slumber. These remnants of ancient infections constitute 8% of the human genome, and no one knows what havoc they might wreak. "A lot of mechanisms used to suppress endogenous retroviruses are the same mechanisms that suppress HIV," Verdin says.

In a completely different tack, Deeks's group wants to tweak the immune system to help cure people. One strategy aims to purge reservoirs by hijacking an immune actor with the macabre name programmed death 1 (PD-1). This receptor on the surface of CD4 cells helps slam the brakes on cell division, maintaining the latent state. A test-tube study presented at the 2011 Conference on Retroviruses and Opportunistic Infections (CROI) by two of Deeks's collaborators, virologist Nicolas Chomont and immunologist Rafick-Pierre Sékaly of the Vaccine & Gene Therapy Institute of Florida in Port St. Lucie, showed that when they blocked the PD-1 receptor with an antibody, the cells coughed up gobs of HIV.

Another approach assumes that purge strategies will not eradicate HIV but that shrinking reservoirs in combination with fortifying the immune system could lead to a "functional" cure that allows people to stop ARVs. "There might be a threshold level where the immune system is able to contain the virus," Verdin says. To that end, the group has joined the multisite Eramune trial (see table, p. 789), which pairs intensification with an HIV vaccine made by NIH.

Designer genes

In a clinical sense, Matt Sharp differs in several ways from Howard and the HIV-infected researcher in North Carolina. "I've been through the ringer and knocked on death's door," says Sharp, 54, an HIV/AIDS educator who lives in Brisbane, near San Francisco. His face is sunken from lipodystrophy, a side effect of the first-generation anti-HIV drugs. For many years, HIV outwitted his drugs and the virus battered his immune system. He has had two hospital stays because of severe pneumonia and has also battled bouts of tuberculosis (TB) and wasting disease. But he, too, is taking part in pathbreaking cure studies.

Sharp, who works with the San Francisco–based advocacy group Project Inform, learned of his HIV infection in October 1988 when he was a ballet dancer in Oklahoma City. "Who knows when I was infected," he says. "We all were having unsafe sex because we didn't know any better. Those were back in the days you'd get a sexually transmitted disease and get a shot and you were back into the mix of things the next few days. There wasn't any consideration of death, so we didn't take it that seriously." His initial CD4 count: 409. "It scared the hell out of me," he says.

Despite starting treatment a year after he tested positive, in 1991 Sharp developed extrapulmonary TB, a dangerous form of the disease linked to HIV. He moved to San Francisco and plugged in with activist groups that kept him abreast of treatment advances, and as new ARVs became available, he changed his regimen repeatedly. Yet by the mid-1990s, his 6-foot-tall frame had withered from 185 pounds to 155. In 1996, Sharp's CD4 cells dropped to as low as 15. After quickly developing resistance to the protease inhibitors that then formed the cornerstone of HAART, he joined a highly unconventional trial and received a thymus transplant, which putatively would rebuild his immune system. "It wasn't anything that probably helped," he says.

In 2001, Sharp became one of a small group of people to take injections of Fuzeon, the first drug to come to market that jams the HIV entry process. "It was very painful, but I was willing to do it because I had no options," he says. His viral load became undetectable for the first time. His good fortune lasted all of 1 week. Five years ago, he added raltegravir to his regimen, and his HIV has subsequently remained undetectable with a CD4 count hovering around 300. "It isn't great, but it got me out of the danger zone," he says.

Last June, Sharp joined one of two gene therapy studies now under way that tries to mimic Brown's success in relatively healthy HIV-infected people. The small trial, led by Jacob Lalezari of Quest Clinical

CREDIT: BILL BERRY

Published by AAAS

Research in San Francisco and Ronald Mitsuyasu at UC Los Angeles, sidesteps the need to find an immunologically matched donor who has the *CCR5* mutant and does not use ablation. Sharp, known as patient 01-203, and eight other participants first went through leukapheresis to remove about 10 million of their CD4 cells, which the researchers then modified with adenoviruses engineered to contain what are known as zinc-finger nucleases. Developed by Sangamo BioScience in Richmond, California, the zinc-finger nucleases clip out a specific small sequence of DNA in the *CCR5* gene, rendering cells incapable of producing a functioning version of the receptor.

After expanding the cells in culture, the researchers in September infused Sharp with about 2 billion of his own rejiggered CD4s. Sharp sat in the audience at the 2011 CROI when Lalezari revealed early results from patient 01-203 and five others. "There are a lot of unanswered questions, obviously, but it was incredibly exciting to see my data points," Sharp says.

As Lalezari explained, the gene therapy modified only about 25% of the cells that they infused, but the *CCR5* mutants persisted in Sharp and four of the others for more than 3 months. Rectal biopsies showed that the modified cells had trafficked to the gut, indicating that they had spread to this critical viral hangout. CD4 counts jumped an average of 100 cells. There were no serious, lasting side effects.

This does not come close to a cure. As Lalezari noted, the fraction of modified CD4s eventually dropped to just over 5%, in contrast to Brown, who had 100% of his CD4 cells destroyed and replaced with *CCR5* mutants. Lalezari cautiously concluded that the therapy ultimately "offers the hope of providing a protected reservoir of CD4+ T cells that are resistant to HIV infection."

In a best case scenario, the modified cells will copy themselves indefinitely and evolve into the predominant group. If HIV does replicate in people like Sharp after they have received the gene therapy, the virus should selectively infect and kill the normal CCR5+ cells, and the population of CCR5– mutants would steadily rise. A report in the August 2010 issue of *Nature Biotechnology* showed that just such a selection occurred in mice engineered to contain a humanlike immune system. Led by Paula Cannon of the University of Southern California in Los Angeles, the experiment used the same Sangamo zinc fingers to cripple CCR5. The transplanted mice then received injections of HIV, and 12 weeks later, the CCR5– mutants almost completely replaced the CCR5+ cells. "And guess what: The virus goes away," says Cannon, who in October 2009 won a $14.5 million grant from the California Institute for Regenerative Medicine to take a similar approach into the clinic with collaborators at the City of Hope in Duarte, California.

Ultimately, transfused patients will have to stop taking ARVs to see whether their modified immune systems are strong enough to contain the virus. "The great news is we can always put people back on ARVs if the gene therapy fails," Cannon says. "It's a no harm, no foul strategy."

In a small trial, similar to the Quest study, that's run by Carl June of the University of Pennsylvania, two patients who received the zinc-finger gene therapy went off ARVs, with intriguing results. As June reported at the 2011 CROI, HIV returned in both patients, but in one, the virus took 10 weeks to surface, a signal that the modified cells made life more difficult for HIV.

Sharp has no interest in going off his medication. The infusion has boosted his CD4s from the dangerously low 281 to the 600 range—the highest they have been since he was diagnosed 23 years ago. He's quick to point out that it's unclear whether the CD4s are functional and improving his health, but he is convinced that, come what may, his contribution will help advance this "very sexy area of research." "Those of us who have survived this long with HIV are able to look back and say, 'Why shouldn't there be a cure?'" Sharp says. "I'm so passionate about this because I want to see a cure before I die."

Cure-Related Clinical Trials Recruiting Patients

Principal Investigators	Sponsors	Intervention
Christine Katlama and Eramune 01 team	ORVACS, Cytheris, Merck, Pfizer	IL-7 + HIV vaccine + intensification
Robert Murphy and Eramune 02 team	Northwestern University, ORVACS, NIAID, Pfizer, Merck	HIV vaccine + intensification
Steve Deeks, Adriana Andrade	UCSF, Johns Hopkins Univ.	Dilsulfiram
David Margolis	University of North Carolina, NIH, Merck	SAHA
Sharon Lewin	Merck, Alfred Hospital in Melbourne, Australia	SAHA
Joseph Alvarnas, Richard Ambinder	NHLBI	Cytoablative therapy for lymphoma
John Mellors	University of Pittsburgh, NCI	Chemotherapy for lymphoma
Joseph Lalezari, Ronald Mitsuyasu, Isabela Sierra, Ana Sizesmore, Winson Tang	Quest Clin. Res., UCLA, Kinder Med. Grp., Orlando Imm. Ctr., Sangamo Biosciences	Autologous CD4s w/*CCR5*- gene
Pablo Tebas, David Stein, Carl June	University of Pennsylvania, Sangamo	Autologous CD4s w/*CCR5*- gene
Amrita Krishnan	Beckman Res. Inst., City of Hope (Duarte, CA), NCI	Autologous stem cells w/*CCR5*- and anti-HIV genes
Frank Maldarelli	NIAID, NCI	Interferon α2B

NIH, NCI, NIAID, NHLBI = U.S. National Institutes of Health and branches
ORVACS = Objectif Recherche Vaccin SIDA

SOURCE: COMPILED BY J. COHEN

Beginning of the end

If researchers do eventually find a widely applicable cure for HIV, the process likely will resemble Brown's rough-and-tumble life, which has seen a remarkable success set against a backdrop of dramatic setbacks. "We are really at the very rudimentary stages," says UC San Diego's Douglas Richman. "If there is going to be success—and I'm optimistic—it's going to be 1 to 2 decades."

The field will receive a big boost in July with NIH injecting millions of new dollars to up to two collaboratory groups working on cure research. There's also a high-profile campaign led by the International AIDS Society and its president-elect, Françoise Barré-Sinoussi—who won the Nobel Prize for co-discovering HIV—to organize the research agenda and then seek more funding. "We are in a period of economic crisis, but if we work together, we can do a lot," Barré-Sinoussi says. On the advocacy front, the Philadelphia-based AIDS Policy Project is aggressively pushing the agenda, lobbying the U.S. Congress and NIH to make cure research a top priority.

Brown, who recently moved to San Francisco, says he initially did not imagine his transplant of CCR5 mutant cells would have much impact on others. "At first, I was like, nobody can get this, it's not very practical, and I don't think anybody could use it for curing HIV." But he now sees his singular triumph as having played a catalytic role in advancing the once-laughable idea that research could discover a cure for this intractable infection, and he's grateful for the chance to give back. "I'd like to be able to continue to tell people about my situation," says Brown, who hopes to write a memoir. "It's a feeling that I'm doing some good for the world."

–JON COHEN

Understanding HIV Latency to Undo It

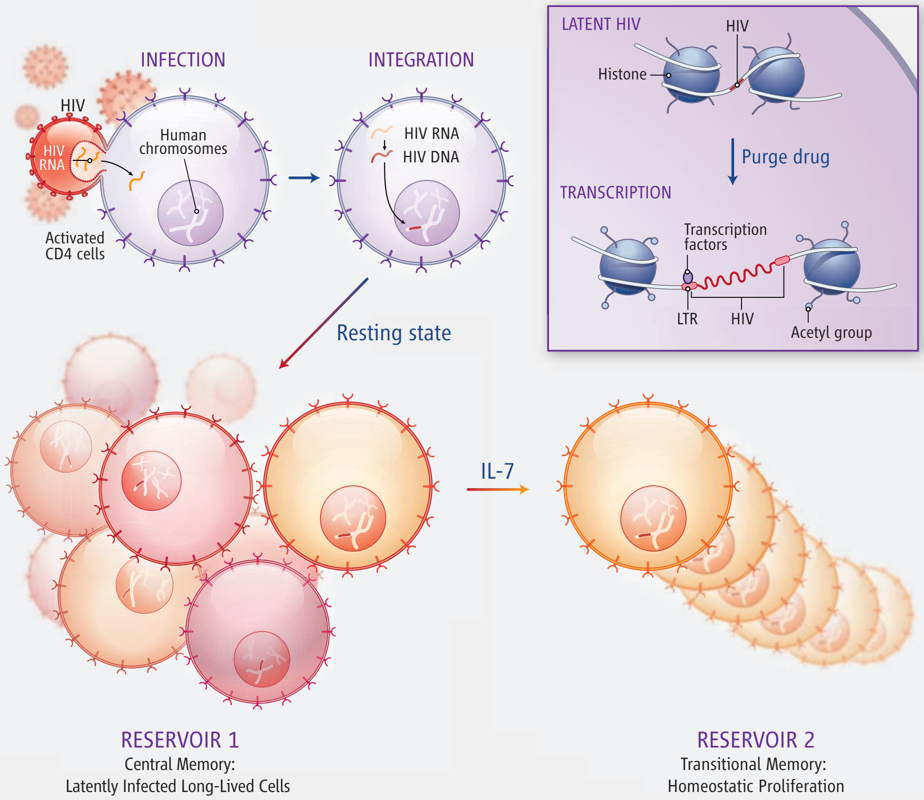

Deep sleep. When HIV infects activated CD4s and integrates with chromosomes, some cells enter a resting state. These latently infected central memory cells can live for years. Interleukin-7 can also transform them into transitional memory cells that persist by cloning themselves. Purge drugs will likely have to attack these reservoirs with different strategies. One approach (*inset*) aims to kick-start transcription, waking up latently infected cells and triggering their demise.

Twenty-five years ago, when HIV still went by the names of HTLV-III and LAV, researchers recognized that the AIDS virus could lie dormant inside human chromosomes, which they erroneously suggested might explain the time lag between infection and disease. Today, with reservoirs of latently infected cells in the spotlight as the central obstacle to a cure (see main text, p. 784), attention is focusing on the fine details of how HIV does this deep dive and stays submerged. "We really need to understand what maintains latency in order to figure out how to reverse it," says Douglas Richman, a virologist at the University of California, San Diego. "Right now, it's sort of coarse guesses."

HIV, unlike herpesviruses, carries no gene that pushes cells into a narcoleptic state. "Latency is not a biological property of the virus," says Eric Verdin, who studies HIV dormancy at the Gladstone Institute of Virology and Immunology in San Francisco, California. "Latency only becomes relevant because drugs can now suppress 99% of HIV replication, and that's what is left."

HIV typically stumbles into a latent state when it infects an actively dividing CD4 white blood cell that then downshifts into a "resting" gear. These resting CD4s can lounge around for years until they are called into action and start dividing, at which point the HIV genes will be expressed along with the CD4 cell's own genes. Much effort has gone into characterizing the specific subsets of memory cells that make up the reservoir, as the distinction could prove critical to purging them.

Virologist Nicolas Chomont and immunologist Rafick-Pierre Sékaly of the Vaccine & Gene Therapy Institute of Florida in Port St. Lucie reported in the August 2009 issue of *Nature Medicine* that 85% of the reservoir consists of two distinct lineages of CD4s known as "transitional" or "central" memory cells. This finding was hugely influential, as it showed that the reservoirs of each lineage persist by different mechanisms: Central memory cells live for decades, and infected transitional memory cells persist by cloning themselves through a process called homeostatic proliferation. "As we try to get rid of them, we'll have to use different strategies," Chomont says.

Other researchers have probed the interior of cells to better understand how proteins, enzymes, and both human and viral DNA all work together to keep HIV silent. Chromosomes tightly pack DNA, wrapping it around proteins called histones. Expression of genes, including those inserted by trespassers like HIV, takes place when these complexes uncoil (see illustration). Specifically, as DNA unspools from histones, protein sherpas guide a suite of transcription factors to genes, which then make the amino acids that form proteins. The most popular purge strategies today aim to selectively induce HIV DNA to uncoil.

One potential way to massage histones so they let loose and allow transcription to begin: protect the acetyl groups that bind to them. Enzymes known as histone deacetylases (HDACs) constantly remove these acetyl groups, which helps keep HIV latent. SAHA, a purge drug now in clinical studies (see table), inhibits HDACs.

A half-dozen other molecular mechanisms that contribute to latency are also possible targets to purge reservoirs. DNA methylation gums up histones, so blocking that process may unspool virus. Human protein complexes sequester critical transcription factors in different parts of the cell, and drugs might free the factors from bondage, allowing them to reach the viral DNA. After transcription begins, several other proteins elongate the new HIV being expressed, and spurring them along could help flush latent virus from cells, too.

Recent advances in laboratory models of latency, including artificial infection of memory CD4 cells and "humanized" mice, are clarifying finer points of how HIV stays quiescent and identifying novel purge drugs. "We have incredible tools now, and these technologies were not available 10 years ago," says Vicente Planelles, a virologist at the University of Utah in Salt Lake City, who developed a new latent cell system.

Just as antiretroviral drugs had little impact against HIV until several compounds simultaneously attacked the virus at different stages of its life cycle, purging reservoirs may ultimately require a cocktail of interventions that undoes latency from multiple angles. "We have to find some combination to tickle the cell and the virus such that the virus can be expressed without vastly affecting all of the other uninfected cells in the body, and that's going to be tricky," says David Margolis, a virologist at the University of North Carolina, Chapel Hill, who has done pioneering studies with HDAC inhibitors. "This is going to be a long, difficult thing to figure out." **–J.C.**

CREDIT: M. TWOMBLY/SCIENCE

Published by AAAS

COMMENTARY

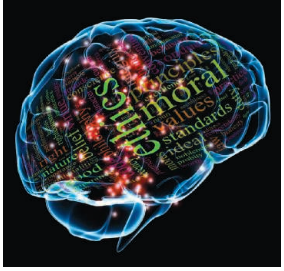

Of neurons and ethics

793

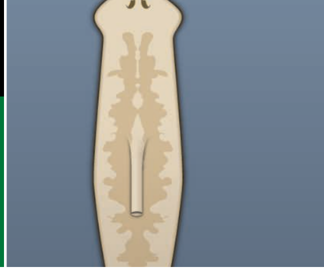

Regeneration

799

LETTERS I BOOKS I POLICY FORUM I EDUCATION FORUM I PERSPECTIVES

LETTERS

edited by Jennifer Sills

Counting India's Wild Tigers Reliably

THE INDIAN GOVERNMENT REPORTED A 16% increase in tiger numbers over the past 4 years (News of the Week, Around the World item "Tiger numbers up? Maybe," 1 April, p. 18). This implies an average increase of 49% in local tiger densities, despite the reported range contraction of 22%. Yet these assertions cannot be verified because details of tiger photo-captures at sampled locations, as well as of spatial extrapolations from these data, are incomplete (*1*–*3*).

Reported tiger numbers were based on calibrations of tiger sign encounter rates against estimated local tiger densities (*2*), but the recently released values of correlation coefficients were much higher than have been reported previously (*4*, *5*). Moreover, the extrapolation of tiger numbers to wider regions is reportedly based on standard methods of sampling and estimation (*1*), but it is not clear from reports (*1*–*3*) whether the survey protocols used actually match these standard practices (*6*, *7*).

A recent global analysis (*8*) showed that 70% of wild tigers survive in 42 "source populations" that occupy a mere 6% of remaining habitat. Although such source populations may suffer annual losses of more than 20%, studies of tiger population dynamics show that high recruitment rates compensate for these losses when there is adequate prey and protection (*9*, *10*). Therefore, future efforts to reverse tiger declines must focus on reliably monitoring tiger numbers, as well as survival and recruitment rates, in these threatened source populations. There is a scientific consensus that monitoring should be conducted annually—within 30 to 45 days to avoid population fluctuations—and cover an area of more than 500 km^2, at intensities of more than 500 trap-nights per 100 km^2 (*11*).

The monitoring protocol for India's national animal requires a major overhaul if it is to generate transparent, reliable measures of tiger conservation successes (or failures) in the future. **K. ULLAS KARANTH,[1,2]* ARJUN M. GOPALASWAMY,[1,3] N. SAMBA KUMAR,[1,4] MOHAN DELAMPADY,[5] JAMES D. NICHOLS,[6] JOHN SEIDENSTICKER,[7] BARRY R. NOON,[8] STUART L. PIMM[9]**

[1]Centre for Wildlife Studies, Bangalore, 560042, India. [2]Wildlife Conservation Society–Global Conservation Program, Bronx, NY 10460–1099, USA. [3]Wildlife Conservation Research Unit (WildCRU), The Recanati-Kaplan Centre, Department of Zoology, University of Oxford, Tubney, Abingdon, OX13 5QL, UK. [4]Wildlife Conservation Society–India Program, Bangalore, 560 070, India. [5]Statistics and Mathematics Unit, Indian Statistical Institute, Bangalore Centre, Bangalore, 560059, India. [6]Patuxent Wildlife Research Center, U.S. Geological Survey, Laurel, MD 20708–4017, USA. [7]Smithsonian Conservation Biology Institute, National Zoological Park, Washington, DC 20013–7012, USA. [8]Department of Fish, Wildlife, and Conservation Biology, Colorado State University, Fort Collins, CO 80521–1474, USA. [9]Nicholas School of the Environment, Duke University, Durham, NC 27708, USA.

*To whom correspondence should be addressed. E-mail: ukaranth@gmail.com

References

1. Y. V. Jhala, R. Gopal, Q. Qureshi, "Status of the tigers, co-predators, and prey in India" (National Tiger Conservation Authority, Government of India, New Delhi, and Wildlife Institute of India, Dehradun, 2008).
2. Y. V. Jhala, Q. Qureshi, R. Gopal, *J. Appl. Ecol.* **48**, 14 (2011).
3. Ministry of Environment and Forests, "India tiger estimate 2010" (Government of India, National Tiger Conservation Authority and Wildlife Institute of India, 2011).
4. J. E. Hines *et al.*, *Ecol. Appl.* **20**, 1456 (2010).
5. K. U. Karanth *et al.*, *J. Appl. Ecol.*, 10.1111/j.1365-2664.2011.02002.x (2011).
6. K. H. Pollock *et al.*, *Environmetrics* **13**, 105 (2002).
7. D. I. MacKenzie *et al.*, *Occupancy Estimation and Modeling: Inferring Patterns and Dynamics of Species Occurrence* (Elsevier, San Diego, CA, 2006).
8. J. Walston *et al.*, *PLoS Biol.* **8**, e1000485 (2010).
9. K. U. Karanth, J. D. Nichols, N. S. Kumar, W. A. Link, J. E. Hines, *Proc. Nat. Acad. Sci. U.S.A.* **101**, 4854 (2004).
10. K. U. Karanth, J. D. Nichols, N. S. Kumar, J. E. Hines, *Ecology* **87**, 2925 (2006).
11. A. F. O'Connell *et al.*, *Camera Traps in Animal Ecology: Methods and Analyses* (Springer, Tokyo, 2011).

Practical Implications of Test Anxiety Tools

IN THEIR REPORT "WRITING ABOUT TESTING worries boosts exam performance in the classroom" (Reports, 14 January, p. 211), G. Ramirez and S. L. Beilock showed that letting students write about their worries for 10 minutes before an exam substantially diminishes the link between test anxiety and test performance. Their second study replicates and extends our previous work, in which we showed that letting students write down attributes of successful problem-solvers for 10 minutes diminishes the relationship between cognitive test anxiety and test performance (*1*).

We differ regarding the theoretical interpretation of the relationship and the resulting practical implications. Although Ramirez and Beilock's intervention is not identical to ours, the fundamental mechanisms are similar. Ramirez and Beilock argue that the effect is mediated by a state of worry during the test situation, but they did not test this proposition. In one of our investigations, we tested this idea and found no support. Instead, we found cognitive test anxiety to affect situational task engagement: Students who have high cognitive test anxiety do not engage in the task because they underestimate their probability for success and consequently do not fully engage in solving the problems at hand. This idea

Published by AAAS

is in line with engagement-disengagement theories (*2*). An implication of applying engagement-disengagement theories is that the performance of students with low cognitive test anxiety should suffer from priming/writing interventions.

We found empirical support for this idea (*1*). Our studies were larger and consequently had more statistical power for detecting an effect than the study by Ramirez and Beilock. In addition, Ramirez and Beilock's Fig. 3 provides some descriptive indication that the interaction effect in the study partly resulted from students with low test anxiety performing worse in the expressive writing group.

We therefore recommend that priming/writing interventions should only be used after screening recipients for cognitive test anxiety. Students with low test anxiety should not be the recipients of interventions of this type because there is theoretical and empirical evidence that their performance will suffer.

JONAS W. B. LANG[1]* AND JESSICA LANG[2]

[1]Department of Work and Social Psychology, Maastricht University, 6200 MD Maastricht, Netherlands. [2]Institute for Occupational Medicine, RWTH Aachen University, Pauwelsstraße 30, 52074 Aachen, Germany.

*To whom correspondence should be addressed. E-mail: jonas.lang@maastrichtuniversity.nl

References

1. J. W. B. Lang, J. Lang, *Psychol. Sci*. **21**, 811 (2010).
2. C. S. Carver, M. F. Scheier, *On the Self-Regulation of Behavior* (Cambridge Univ. Press, New York, 1998).

Response

CONTRARY TO LANG AND LANG'S ASSERTION that the performance of students lower in test anxiety was harmed by expressive writing, students with lower test anxiety performed just as well on their final exams in the writing and control conditions (Experiments 3 and 4 in our Report).

Lang and Lang showed that having students imagine a person successful at solving scientific problems and write about the qualities of this person (i.e., priming competence) improved test performance of those higher in test anxiety, but harmed test performance of those lower in test anxiety (*1*).

Although both our expressive writing and Lang and Lang's competence exercise are designed to enhance test performance, they are very different interventions. In expressive writing, students write about their feelings regarding the upcoming test. In the competence exercise, students write about the qualities of a successful test taker. In their study, task engagement explains the impact of the competence intervention on the test performance of students lower and higher in test anxiety. In contrast, we show that the extent to which one writes about negative thoughts and worries accounts for the benefits of expressive writing (our Experiment 2).

Given the different mechanisms, it is not surprising that the two interventions affect students with lower test anxiety differently. Whereas Lang and Lang's exercise primes competence and thus leads to less engagement for these students, our writing exercise need not relate to competence or engagement in this way. In support of this idea, in Experiment 1, we had some students expressively write before taking a low-pressure math test. If expressive writing primes competence, which in turn alters task engagement, then writing should hurt students' performance in a low-pressure situation. This is because students should approach a low-pressure test with high self-perceived competence (especially after succeeding on a similar pretest). Thus, priming competence further should lead to less effort and worse performance. However, we found that writing had no impact on low-pressure test performance.

We suggest that writing allows students to express their negative thoughts and worries, which reduces the tendency to ruminate during the test. This expression is not necessary for those in a low-pressure situation or for students with lower test anxiety; thus, their performance is neither enhanced nor harmed by expressive writing.

Lang and Lang do correctly point out that we do not provide direct evidence that expressive writing alleviated negative thoughts and worries during test performance. However, our intervention was guided by previous research showing that performance drops in high-pressure situations are accounted for by negative thoughts and worries (*2*) and that writing about worries alleviates the tendency to ruminate (*3*). If worries lead to poor test performance and writing helps alleviate these worries, then giving students the opportunity to express themselves should enhance test performance—especially for those highest in test anxiety. This is exactly what we found.

Our evidence supports the counterintuitive idea that writing about worries benefits the performance of the most test-anxious students without compromising the performance of students lower in test anxiety. Thus, we see no need to screen people for test anxiety before they engage in expressive writing.

SIAN L. BEILOCK AND GERARDO RAMIREZ

Department of Psychology and Committee on Education, University of Chicago, Chicago, IL 60637, USA.

*To whom correspondence should be addressed. E-mail: beilock@uchicago.edu

References

1. J. W. B. Lang, J. Lang, *Psychol. Sci*. **21**, 811 (2010).
2. M. S. DeCaro, K. E. Rotar, M. S. Kendra, S. L. Beilock, *Q. J. Exp. Psychol.* **63**, 8 (2010).
3. K. Klein, A. Boals, *J. Exp Psychol. Gen*. **130**, 3 (2001).

Letters to the Editor

Letters (~300 words) discuss material published in *Science* in the past 3 months or matters of general interest. Letters are not acknowledged upon receipt. Whether published in full or in part, Letters are subject to editing for clarity and space. Letters submitted, published, or posted elsewhere, in print or online, will be disqualified. To submit a Letter, go to www.submit2science.org.

CORRECTIONS AND CLARIFICATIONS

Reports: "pH-Dependent gating in a FocA formate channel" by W. Lü *et al*. (15 April, p. 352). In addition to his affiliation with the Lehrstuhl für Biochemie, Oliver Einsle is affiliated with the Center for Biological Signaling Studies (BIOSS), Albert-Ludwigs-Universität Freiburg, Hebelstrasse 25, 79104 Freiburg, Germany. The affiliation has been added in the HTML version online.

Cover Caption: (8 April, p. 139). The caption stated that a magnet was levitating above a superconducting ceramic yttrium barium copper oxide disc, when in fact the disc was levitating above the magnet.

Books *et al*.: "The immortalist" by M. Shermer (1 April, p. 40). The title of the review is "The immortalist," not "The immoralist." Also, in the last sentence of the fourth paragraph, "absolutely" should be "absolute." The HTML version online has been corrected.

News & Analysis: "Japan's research facilities down but not out" by D. Normile (25 March, p. 1509). The name of physicist Youhei Morita, KEK's press officer, was misspelled.

Published by AAAS

NEUROPHILOSOPHY

Our Caring Neurons

Richard S. Mathis

Morality has long presented difficult questions to philosophers and others. How can we know with any certainty what actions are right or wrong or which are just or unjust? Can we arrive at principles or rules that satisfy all or even most of us or that apply across societies? A more recent concern is how to apply scientific research to thinking about morality. Patricia S. Churchland takes on this last concern in *Braintrust*. A philosopher (at the University of California, San Diego), she is interested in drawing on advances in neuroscience and psychology to understand the origins of morality. She begins with the basic question of why humans are even concerned with one another. Understanding the answer to that question can help us to understand why social values exist and why we seem so concerned with moral behavior.

Braintrust
What Neuroscience Tells Us About Morality
by Patricia S. Churchland
Princeton University Press, Princeton, NJ, 2011. 285 pp. $24.95, £16.95. ISBN 9780691137032.

Churchland argues that we are concerned about one another because of common neurological processes that cause us to form social bonds. The neuropeptide oxytocin enables mothers to bond with their children and, beyond that, is part of our seeking to bond with others. She argues that oxytocin plays a role in mammals providing care to their offspring and is also involved in such behaviors as grooming and touching those outside of their families. Although not entirely understood, it appears that the peptide is associated with the release of endogenous opiates so that, as she puts it, "Doing good feels good." Experiments with humans link oxytocin specifically with trusting behavior, which is obviously important to forming social bonds. Administered through nasal spray, oxytocin seems to make people more willing to trust. Interestingly, mothers who abuse cocaine have lower levels of oxytocin and display less maternal bonding. Thus, oxytocin is a proximal reason why humans are interested in cooperating with and supporting one another.

This raises the question of whether there is a specific gene linked to trusting and bonding and, therefore, to moral action itself. As is true of much recent work in genetics, the relation between a gene and a particular psychological trait is not as direct as one might think. A genetic predisposition to higher or lower levels of oxytocin must be balanced with several other factors, such as other genes and the individual's environment. Churchland argues that the genetic predisposition to produce higher levels of oxytocin is likely a factor in what we would consider trusting or bonding behavior, but it is not entirely predictive as it is only one factor among many.

Churchland rounds out her discussion of our impetus to morality with a look at the social and environmental factors encouraging bonding and trust. Such behaviors are reinforced in society because cooperative behavior is essential to survival. Humans, as rational beings, understand the importance of trust and reciprocity in building mutually beneficial relationships. Recently studied processes such as mimicry are also important. Studies show that people have an unconscious tendency to mimic one another in personal interactions. This strengthens our social glue, because identifying with others makes trusting them easier.

Importantly, Churchland does not go on to promulgate moral principles that are based on such neurological and psychological processes. Rather than advancing a naturalistically or scientifically based moral code, she sees science as deepening our understanding of the "nature of our sociality" and shedding light on our practices and institutions so that we "think more wisely about them." She is less interested in specifying moral rules or principles. Indeed, she makes rather short work of the late John Rawls, the influential philosopher who formulated principles of justice using ideas of rationality and his own reading of psychological studies.

The lack of concern with identifying overarching moral principles carries over into the final chapter, where Churchland discusses religion and morality. She notes that "[p]erhaps life would be a whole lot simpler if there were a divine being who could reliably be appealed to for a straight answer on moral issues, an answer made clear to all." Unfortunately, lacking such answers, "we have no option but to wrestle with difficult social issues, to hear the other side and to heed the differences, to negotiate as wisely as we can, to understand the history, and to try to foresee future consequences."

Perhaps the book's weakest aspect is its tendency to dismiss rather too quickly less scientific viewpoints of morality (as, for example, in the above quote on religion and morality). This accords with Churchland's argument that morality does not have a supernatural basis. Yet many religious or supernatural views of morality are much more subtle and allow room for discussion and debate. Indeed, some might argue that the neurological processes that Churchland discusses complement rather than refute some metaphysical explanations. This dismissive tendency also colors her discussions of other moral viewpoints. For example, Rawls's work, so important to the field of social justice, is discounted with only a few observations from his opponents.

Such criticisms aside, Churchland provides an important service in *Braintrust* by applying recent scientific research to moral concerns. No doubt debates involving science, religion, and philosophy will continue without ever reaching conclusions about morality that are satisfactory to even the wisest in such areas. It helps, though, to understand the scientific underpinnings of why we are concerned with one another and, beyond that, with morality itself.

10.1126/science.1205721

The reviewer is at the Ochs Center for Metropolitan Studies, Post Office Box 4029, Chattanooga, TN 37405, USA. E-mail: rmathis@ochscenter.org

CREDIT: © SEBASTIAN KAULITZKI/SHUTTERSTOCK; © CLEARVIEWSTOCK/SHUTTERSTOCK; DESIGN, MARCELLA ENGEL ROBERTS; COURTESY PRINCETON UNIVERSITY PRESS

NEUROSCIENCE

Arts and the Dreaming Mind

Tim Requarth[1] and Meehan Crist[2]

In a small but elegant museum on Manhattan's West Side, one finds watchful Buddhas, many-limbed goddesses, and tapestries depicting religious visions. The Rubin Museum is a place where people come to learn about Himalayan art, and for three months of the year it is also a place where people come to learn about the science of the human brain.

The museum's fourth annual Brainwave Festival brought heavy hitters from the worlds of art and science to explore the theme of dreaming. How do we dream? Why? What can dreams teach us about who we are? The festival investigated these questions through a wide-ranging variety of events, from a series of workshops linked to the U.S. premiere of Amy Hardie's award-winning documentary *The Edge of Dreaming* to the museum's first "dream-over," an adult sleepover at the museum that included art meditation workshops and personal dream analysis. At the heart of the festival was a series of 15 onstage conversations between prominent artists and neuroscientists, including evenings that paired actress Debra Winger with Robert Stickgold, puppeteer Roman Paska with Rodolfo Llinás, musician Henry Rollins with David Eagleman, and painter David Salle with Ian McGilchrist.

The Edge of Dreaming.

[1]Department of Neuroscience, Columbia University, New York, NY 10032, USA. [2]*The Believer*, www.believermag.com. E-mail: trequarth@gmail.com; meehancrist@gmail.com

These carefully considered pairings offered the opportunity for insight through unexpected juxtaposition. In their conversation, cognitive neuroscientist Amir Raz and writer Nathan Englander compared the hyperfocused state of consciousness the author experiences while writing to the state of consciousness achieved during dreaming. Englander likened writing to the sensation of watching oneself that is so common in dreams, and Raz speculated that writers are experts at achieving this unusually dissociated state, in which the brain can explore avenues of thought not possible during normal attentional states.

Brainwave 2011
Dreams
Tim McHenry, Producer
Rubin Museum of Art, New York, 7 February to 29 April 2011. www.rmanyc.org/brainwave

Whereas dreaming and creativity offered an obvious focus for these conversations, many stepped beyond such comfortable ground and even eschewed the topic of dreaming altogether. Best-selling author and attorney Scott Turow and cognitive neuroscientist Michael Gazzaniga engaged in an illuminating discussion of neuroscience and the law. How does the court define a defendant's mental state in a given context, thereby ascribing responsibility? If a neurological disorder is found to underlie psychopathy, does that somehow absolve a murderer of guilt? When, if ever, can the death penalty be said to have a place in a just judicial system? Profound considerations about the notion of brain states and the self emerged from these questions.

Some events, however, seem to offer only a tenuous association with science. For the dream-over, participants signed up to sleep under a piece of art and have their potentially art-inspired dreams interpreted by a team of analysts led by psychiatrist Edward Nersessian. Although it was great fun to spend the night in the museum, the evening's preparation for dreaming and the morning's "personal dream analysis" felt less like a scientific endeavor than a creative and amusing parlor game.

Nonetheless, most events offered satisfyingly robust connections between science and art. In her lyrical, autobiographical *The Edge of Dreaming*, Hardie recreates a nightmare in which her late first husband foretells her death in the upcoming year, a "prophecy" that seems even more ominous after she develops an ailment that threatens to collapse her lungs. Her quest to understand the dream eventually leads her to undergo a shamanic journey in which she revisits the memory of her late husband to "undo" the prophecy. Although such a film could easily fall into the familiar trope of spiritual awakening, Hardie takes a more measured approach, using the neuroscience of memory and dreaming to investigate her experience. The film implies that experience is real for the brain, whether it is lived, imagined, or dreamt. Only by returning the awake brain to the state of the dreaming brain, during which her fateful memory was formed, could she alter the pathways that had locked it into place. While Hardie's experience clearly remains beyond the explanatory grasp of modern neuroscience, there is accumulating evidence that brain state affects the properties of memory formation. Highly emotionally charged memories are thought to be consolidated by a pathway that involves the amygdala (central to fear circuits) instead of the hippocampus (which seems to help consolidate many other memories). By recreating her experience emotionally, Hardie may have gained access to such alternative memory formation circuits—a strategy commonly employed by psychologists treating patients with such disorders as posttraumatic stress disorder.

The Brainwave Festival's greatest strength may lie in its potential to bring together the scientific and artistic communities. Yet the audiences were composed mostly of artistically minded folks curious about science. There was a conspicuous lack of scientifically minded folks curious about art; at most events, the neuroscientist seemed like an exotic animal in the room. The question-and-answer periods were generally thoughtful and intelligent, but the questions, not surprisingly, often reflected curious but uninformed minds grappling with complex scientific concepts. If the ever-increasing roster of public events that purport to build bridges between science and the arts are to be more than just glittery bones tossed to a hungry crowd, a greater engagement from the scientific community is in order. If more scientists engaged with public events such as the Brainwave Festival, that could help add depth to a widening public conversation—and help put a face on the abstract and often misunderstood endeavor of science.

10.1126/science.1204104

CLIMATE CHANGE

Toward the Second Commitment Period of the Kyoto Protocol

Black carbon should be included in the Kyoto framework, and treatment of short-lived gases like methane should change.

Andrew J. Weaver

Expectations are high that the Kyoto Protocol, intended to reduce emissions of certain greenhouse gases (GHGs), will be extended after its first reporting period ends in 2012. The mechanisms available to meet Kyoto targets will likely also be extended. But our scientific understanding of the carbon and methane cycles and the radiative effects of black carbon were less developed in 1997, when the Kyoto Protocol was established, and in 2001, when the Marrakesh Accords solidified mechanism details. Before entering the second commitment period, international policy instruments should be both modified to correct internal inconsistencies and updated to reflect recent scientific advances. Such advances support changes to the protocol's treatment of short-lived gases, such as methane, and the inclusion of black carbon within the Kyoto framework.

Developed nations (Annex B nations under the Kyoto Protocol) that are able to reduce emissions beyond their Kyoto targets can sell excess reduction credit to other Annex B nations through the Emissions Trading mechanism. Under the Joint Implementation (JI) mechanism, an Annex B country can gain credit by developing an emissions reduction project in another Annex B country. The Clean Development Mechanism (CDM) allows countries to gain credit toward Kyoto targets by enabling emission-reducing projects in developing nations. A major outcome of the Cancun 2010 United Nations climate conference was the empowering of the Executive Board of the CDM to accelerate investment in emission reduction projects in developing nations. Parties were also encouraged to continue efforts aimed at Reducing Emissions from Deforestation and forest Degradation (REDD+ Partnership). It is expected that REDD+ negotiations will lead to an additional Kyoto mechanism.

Black Carbon

Black carbon is soot released into the atmosphere during burning of fossil fuels and biomass. It has a relatively short atmospheric lifetime, only a few days to weeks, as it is effectively scavenged by precipitation. However, black carbon is very effective at absorbing incoming solar radiation. In terms of radiative forcing (which describes an imbalance between incoming and outgoing radiation), black carbon is the next biggest player in global warming behind CO_2 (*1*). Black carbon is primarily released in developing nations during deforestation and the inefficient combustion of fossil fuels (see the figure).

Amending the Kyoto Protocol to include black carbon as a regulated substance would be beneficial for several reasons. First, it would allow developing nations a relatively straightforward means of participating in second-reporting-period emissions reduction through more efficient burning of fossil fuels and reduction or elimination of deforestation. Second, air quality would be improved. Third, an additional area of potential projects would exist under the CDM. Finally, the benefits of reducing black carbon emissions are realized almost immediately owing to its short atmospheric lifetime. Measurement, reporting, and verification of black carbon would fall under current national GHG inventory reporting and REDD+.

Methane

Methane is the next biggest contributor to global warming after black carbon. It is a short-lived GHG with an atmospheric lifetime of about 12 years. In 1995 the global warming potential (GWP) of methane was estimated to be 21 (that is, 21 times greater than CO_2) over a 100-year time horizon and 56 over 20 years (*2*). The GWP of 21 was used in the Kyoto Protocol, where it has become entrenched within first reporting period methodologies. However, up-to-date estimates are that the methane GWP is 25 over 100 years and 72 over 20 years (*3*). Recent research has demonstrated that these new numbers are conservative (*4*).

With the first reporting period ending, it is time to update the treatment of methane and other short-lived GHGs within the Kyoto mechanisms. The United Nations Environment Programme (UNEP) recently released an assessment report pointing out that steps taken now to reduce black carbon, tropospheric ozone, and methane would have immediate and multiple benefits for human well-being (*5*). Also, in October 2010, the 38 countries that account for 70% of the global anthropogenic methane production launched the Global Methane Initiative to work together to accelerate methane mitigation by implementing national and international abatement and emissions avoidance projects.

Unfortunately, barriers have inadvertently been put in place for the implementation of such abatement projects under the JI and CDM. For example, the CDM defines an arbitrary crediting period over which avoided methane emissions are calculated and credited to a project. Projects can use one of two options: a single 10-year period or a 7-year period that is renewable twice. Although projects can only earn emission reduction credits over these relatively brief periods, a methane GWP of 21, reflecting the 100-year horizon, is used. This makes little sense, as the CDM's focus is on short-term emissions avoidance and diminishes the viability of projects that could afford immediate realization of the benefits of methane abatement. To be fair and accurate, a GWP of ~72 should be used if it is to reflect the true reduction in warming over the 10- to 21-year crediting period. As a specific example, we consider methane emissions from landfills.

Methane from landfills contributes an estimated 3 to 4% of total anthropogenic GHG emissions (*6*), although this is based on only 1 year of the anaerobic decomposition process that releases methane and can last 100 to 150 years. This methane contribution would be much larger if life-cycle impacts were considered. Preventing landfill methane from reaching the atmosphere is well within the capabilities of existing technologies. Unfortunately, under the CDM, cost barriers have been inadvertently introduced through issuing too few carbon credits for the resulting methane emission avoidance.

Projects that keep waste from entering a landfill, such as recycling, composting, and energy from waste projects, avoid future methane emissions over the lifetime of the waste (not just the crediting period). Yet these are doubly penalized through the application of a short crediting period and an outdated GWP. If a crediting period of 100 years and,

School of Earth and Ocean Sciences, University of Victoria, Victoria, BC, V8W 3V6 Canada. E-mail: weaver@uvic.ca

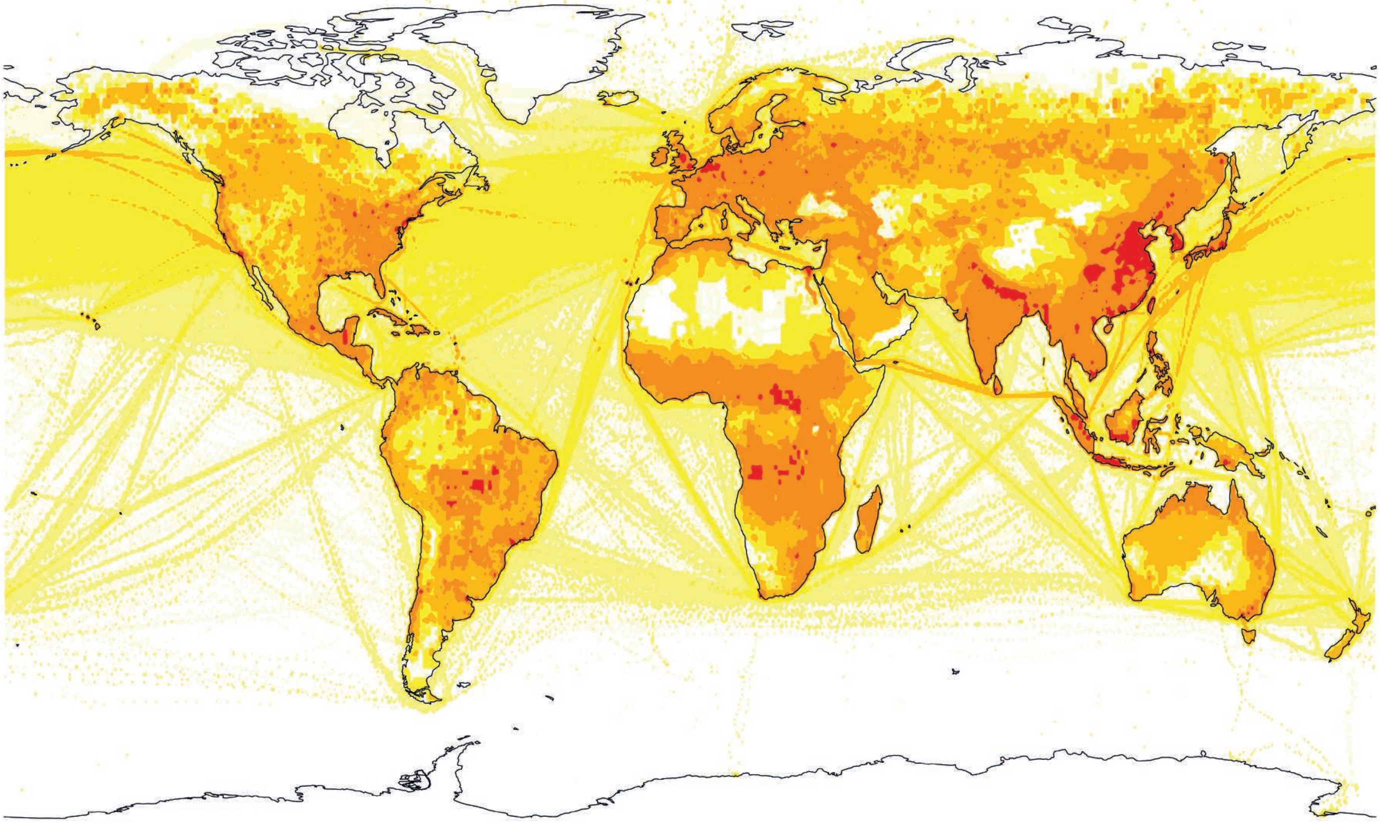

Black carbon emissions in 2000. Includes emissions from forest and grassland burning; waste treatment; residential, commercial, and agricultural activities; transportation (air, land, and sea); industry; and electricity generation. Data from (*14*).

therefore, appropriate GWP of 25 is applied, avoided methane emissions would be properly accounted for, with the projects receiving carbon credits that could make them viable. Alternatively, if crediting periods remain unchanged, a GWP of ~72 should be used to reflect the shorter time horizon.

Carbon Dioxide

Scientific advances since the adoption of the Kyoto Protocol have led to the recognition that stabilization of atmospheric CO_2 at any level requires anthropogenic CO_2 emissions to go eventually to zero. The actual level of stabilization is determined by cumulative anthropogenic emissions (*7*, *8*) and is independent of the actual pathway of global annual emissions. From a policy perspective, this has certain advantages. Rather than negotiating CO_2 emission reduction targets on a nation-by-nation basis, as currently embedded in the Kyoto framework, a future level of maximum allowable global temperature increase can be chosen. Under the Copenhagen Accord, it appears that 2°C above preindustrial levels has already been agreed upon. The allowable future cumulative emissions required to keep global warming below this temperature threshold can then be calculated. Determining how such future CO_2 emissions are partitioned, perhaps under a contraction and convergence framework (*9*), could then be the subject of international negotiations.

The case for developing parallel policy initiatives for near- and short-term climate mitigation (*10*) is compelling. Reducing anthropogenic CO_2 emissions to zero in order to stabilize atmospheric temperatures is an onerous task. Socioeconomic, cultural, and behavioral inertia preclude rapid transformation of global energy systems away from dependence on fossil fuel combustion. However, gradual reduction of anthropogenic CO_2 emissions within a cumulative emissions framework could allow for a smooth transition to renewable and zero-emission energy systems. Shorter-lived GHGs, such as methane, or aerosols, such as black carbon, both of which have much greater GWPs than CO_2 (*3*, *11*) can then be dealt with separately. Steps taken to reduce their emissions would have immediate effects on global warming (*12*) and would allow time for the turnover of existing energy infrastructure (*13*).

References

1. V. Ramanathan, G. Carmichael, *Nat. Geosci.* **1**, 221 (2008).
2. D. Schimel *et al.*, in *Climate Change 1995: The Science of Climate Change. Contribution of Working Group I to the Second Assessment Report of the Intergovernmental Panel on Climate Change (IPCC)*, J. T. Houghton *et al.*, Eds. (Cambridge Univ. Press, Cambridge, UK, 1996), pp. 407–444.
3. P. Forster *et al.*, in *Climate Change 2007: The Physical Science Basis. Contribution of Working Group I to the Fourth Assessment Report of the IPCC*, S. Solomon *et al.*, Eds. (Cambridge Univ. Press, Cambridge, 2007), pp. 129–234.
4. D. T. Shindell *et al.*, *Science* **326**, 716 (2009).
5. UNEP, *Integrated Assessment of Black Carbon and Tropospheric Ozone: Summary for Policy Makers* (UNEP, Nairobi, 2011); www.unep.org/dewa/.
6. S. Monni, R. Pipatti, A. Lehtilä, I. Savolainen, S. Syri, *Global Climate Change Mitigation Scenarios for Solid Waste Management* (VTT Publications 603, Tech. Res. Centre of Finland, Espoo, 2006), 51 pp.
7. K. Zickfeld, M. Eby, H. D. Matthews, A. J. Weaver, *Proc. Natl. Acad. Sci. U.S.A.* **106**, 16129 (2009).
8. M. Meinshausen *et al.*, *Nature* **458**, 1158 (2009).
9. A. Weaver, *Keeping Our Cool: Canada in a Warming World* (Viking Canada, Toronto, Ontario, 2008).
10. S. C. Jackson, *Science* **326**, 526 (2009).
11. M. S. Reddy, O. Boucher, *Geophys. Res. Lett.* **34**, L11802 (2007).
12. J. Hansen, M. Sato, *Proc. Natl. Acad. Sci. U.S.A.* **101**, 16109 (2004).
13. S. J. Davis, K. Caldeira, H. D. Matthews, *Science* **329**, 1330 (2010).
14. Representative Concentration Pathways (RCP) emissions database, www.iiasa.ac.at/web-apps/tnt/RcpDb.

10.1126/science.1202087

Published by AAAS

PLANETARY SCIENCE

Cold-Trapping Mars' Atmosphere

Peter C. Thomas

The Mars Reconnaissance Orbiter has observed large deposits of frozen CO_2 at Mars' southern polar region.

Earth's climate is buffered by massive oceans of liquid water and by gases, such as carbon dioxide (CO_2), which cycle through the atmosphere and through biologic and geologic reservoirs. Mars has no oceans to buffer its temperatures, and the thin atmosphere (95% CO_2) provides little thermal buffering. The surface pressure is close to that in equilibrium with solid CO_2 at Mars' polar temperatures, and early space probes explored whether large CO_2-ice deposits might buffer the atmospheric pressure of Mars (*1*). Subsequent investigations found reservoirs of frozen water in thick polar layered deposits, but revealed only thin perennial deposits of CO_2 at the south pole (termed "residual cap") in addition to the ~30% of atmospheric CO_2 that is cycled through the seasonal caps. On page 838 of this issue, Phillips *et al*. (*2*) report the discovery of thick deposits in the south polar region that are most likely composed of solid CO_2 and comparable in mass to the present Mars atmosphere.

Interest in the mechanisms of Mars' climate comes from its position as the only other terrestrial planet with a surface and atmosphere comparable to Earth's and from evidence that its climate has changed over time scales of billions of years, as well as over much shorter cycles (*3*). Changes in Mars' orbital and spin characteristics likely force many climate cycles (*4*). Obliquity, the angle between the spin axis and the normal to the orbital plane, is one such climate forcing factor. Its predicted variations are particularly great for Mars (Earth's obliquity range is restricted by the presence of the Moon). On Mars, CO_2 buffering is analogous to a laboratory cold finger—excess atmospheric gas accumulates at the coldest spot on the planet. For high values of obliquity solar heating at the poles can exceed that on the equator, with a possible shift of any buffering deposits, including both water and CO_2. At the current obliquity (25.2°), the poles should act as cold fingers and promote deposition of more volatile components.

Over time scales of billions of years, Mars shows evidence of periods when liquid water was available at the surface: morphology such as channels and probable standing-water deposits, as well as chemical species found in sedimentary rocks by the Mars Exploration Rovers (*5*). For time scales of only a few million years or less, distinctive stacks of layered materials at both poles (*6*) have been the focus of inquiry into cold-trapped volatiles.

A picture of the materials above this stack has emerged, with thin water-ice caps at both poles (*7*, *8*), covered in the south only by a thin residual cap (<15 m) of CO_2 ice. Some of the CO_2 residual cap is being eroded year to year (*9*). The ongoing erosion of the CO_2 residual materials raises the question of whether the residual cap is likely to last for more than a few years, and if it is part of a hierarchy of climate cycles. The amount of material on this residual cap is only a few percent of the mass of atmospheric CO_2 (*10*); thus, it is unlikely to be a record of changes in the mass of Mars' atmosphere.

Prior results from SHARAD (Shallow Radar, on the Mars Reconnaissance Orbiter) and the deeper-penetrating MARSIS (Mars Advanced Radar for Subsurface and Ionosphere Sounding, from Mars Express) (*11*, *12*) had revealed the subsurface complexity of the polar layered deposits. However, these studies gave no indication that the thick polar layered deposits were other than water-ice rich. In the south polar region, SHARAD (*2*) has revealed regions that scatter back extremely small signals. Termed reflection-free zones, and unlike any other areas on Mars, these regions have been interpreted as CO_2 ice based on modeling the variation of the calculated depths of underlying layers; the results are more consistent with radar velocities in CO_2 ice than in water ice. The geographically varying calculated thicknesses reach as much as ~700 m, but generally are less than 250 m. The 700-m value is close to a predicted maximum of ~1 km based on the expected depth of liquefaction (*13*, *14*). The geographical extent of one such reflection-free zone closely matches that of an outcropping layer mapped from orbital images that has distinctive collapse forms just below the thin water-ice–rich material below the CO_2 residual cap (see the figure).

If released into the atmosphere, the mass of material in the main reflection-free zone would nearly double the present surface pressure; this tabulation does not include all the reflection-free zones near the south pole (*2*). This reservoir implies a previous state of Mars' climate that had a higher atmospheric pressure and which then changed to conditions in which a substantial part of that atmosphere collapsed onto the pole. This possibly happened after the last maximal obliquity-driven south polar summer heating, about 600,000 years ago (*4*), although there are predicted younger obliquity excursions nearly as great.

Mars' atmosphere at present appears to be largely vapor-pressure controlled. Although the newly found

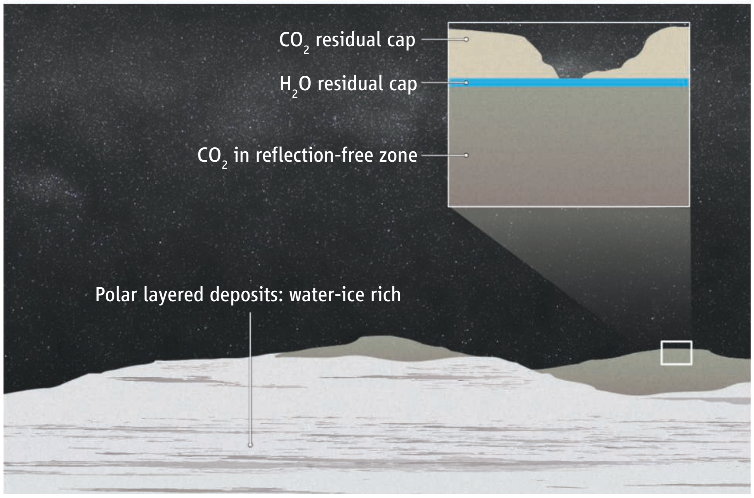

A complicated cold finger. A schematic of the south polar deposits of Mars. The oldest and most voluminous materials are the "polar layered deposits" (PLD), probably water-ice rich with some admixed dust, up to 3 km in thickness. The CO_2 deposits in the newly found reflection-free zones (*2*) occupy several regions within the area of the PLD. Above the CO_2 deposits is the residual cap, with an upper part of CO_2 with varying thicknesses of up to ~15 m, and an underlying water–ice rich layer of unknown thickness. The CO_2 in the reflection-free zones is apparently dust covered where it is exposed without the residual CO_2 and water ice residual cap cover.

CREDIT: P. HUEY/SCIENCE

Center for Radiophysics and Space Research, Cornell University, Ithaca, NY 14853, USA. E-mail: pthomas@astro.cornell.edu

CO_2 reservoir could nearly double Mars' atmospheric mass, the resulting climate alterations would be modest, and as pointed out by Phillips *et al.*, would involve effects of dust raising and extent and longevity of seasonal frosts, as well as the enhanced CO_2 pressure. These ice reservoirs are not the path to a "warm, wet" Mars. Indeed, the limitations of the depth of CO_2-ice reservoirs (*13*, *14*) probably require that high former CO_2 pressures needed for much warmer conditions must involve carbonate or other rock reservoirs, in addition to ice deposits. The new findings of large, and possibly multiple, buried CO_2 reservoirs show how complex a seemingly simple cold finger system can be. Mars' cold trapping is clearly affected by seasonal kinetics, changing dust loading of the atmosphere, obliquity and other orbital cycles, and longer-term evolution of Mars geology. There is much yet to learn about this simple system. The north-south polar asymmetry is but one example of continuing puzzles.

References and Notes

1. R. B. Leighton, B. C. Murray, *Science* **153**, 136 (1966).
2. R. J. Phillips *et al.*, *Science* **332**, 838 (2011); 10.1126/science.1203091
3. F. P. Fanale, S. E. Postawko, J. B. Pollack, M. H. Carr, R. O. Pepin, in *Mars*, H. H. Kieffer, B. M. Jakosky, C. Snyder, M. S. Mathews, Eds. (Univ. of Arizona Press, Tucson, 1992), pp. 1135–1179.
4. J. Laskar *et al.*, *Icarus* **170**, 343 (2004).
5. S. W. Squyres *et al.*, *Science* **306**, 1698 (2004).
6. B. C. Murray *et al.*, *Icarus* **17**, 328 (1972).
7. T. N. Titus, H. H. Kieffer, P. R. Christensen, *Science* **299**, 1048 (2003).
8. J.-P. Bibring *et al.*, *Nature* **428**, 627 (2004).
9. M. C. Malin et al., *Science* **294**, 2146 (2001).
10. P. C. Thomas, P. B. James, W. M. Calvin, R. Haberle, M. C. Malin, *Icarus* **203**, 352 (2009).
11. J. J. Plaut *et al.*, *AGU Fall Meet. Abstr.* P13D-06 (2006).
12. D. C. Nunes *et al.*, *Lunar Planet. Sci. Conf.* **37**, 1450 (2006).
13. C. Sagan, *J. Geophys. Res.* **78**, 4250 (1973).
14. M. T. Mellon, *Icarus* **124**, 268 (1996).

15. I thank P. Gierasch for discussions.

Published online 21 April 2011;
10.1126/science.1205169

EVOLUTION

The Cost of Being Male

Mitochondrial mutations influence nuclear gene expression more in male *Drosophila* than in females.

John Parsch

Although we often hear of "the human genome," human cells, like all other eukaryotic cells, actually contain two genomes. The nuclear genome, which garners most of the attention, is composed of the chromosomal DNA within the nucleus and encodes tens of thousands of proteins. The mitochondrial genome, which is present in the organelles that serve as the major site of energy production in the cell's cytoplasm, consists of a circular piece of DNA that encodes fewer than 20 proteins. The two genomes must function together for the cell to survive. However, because the two genomes differ in their mode of inheritance, their interaction may not be completely harmonious. On page 845 of this issue, Innocenti *et al.* (*1*) report experimental findings from the fruit fly demonstrating a sex-specific breakdown of the cooperation between the nuclear and mitochondrial genomes. In this case, it is the males who get the short end of the stick.

Upon reproduction, both mother and father pass half of their nuclear genomes to their offspring. An exception is the Y chromosome, which is passed only from father to son. In contrast, the mitochondrial genome is inherited maternally. That is, it is passed only from the mother to the offspring of both sexes (see the figure). Viewed from the mitochondrial genome's perspective, males are an evolutionary dead end: Regardless of the mitochondria's effect on a male's survival or reproductive success, they have no chance to contribute their genetic information to the next generation. This implies that natural selection will be inefficient at removing mitochondrial mutations that have a negative impact on male, but not female, fitness (*2*). Thus, mitochondrial genomes are expected to harbor more mutations that are deleterious to males than to females. This phenomenon is referred to as the "male mutational load" or, more colorfully, "mother's curse" (*3*).

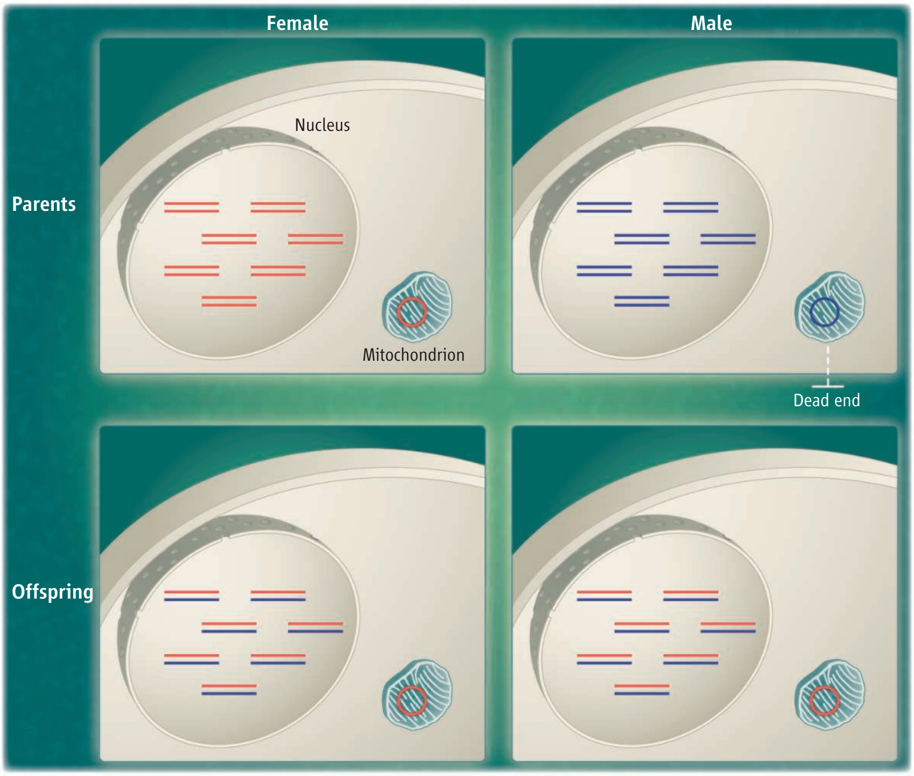

Dead-end males. Males are an evolutionary "dead end" for the mitochondrial genome. Although offspring (**bottom**) inherit the nuclear genome from both parents (**top**), they inherit the mitochondrial genome only from the mother. This can lead to the accumulation of mitochondrial mutations that have a deleterious effect in males, but not in females.

CREDIT: P. HUEY/SCIENCE

Department of Biology II, Ludwig-Maximilians-Universität, 82152 Planegg-Martinsried, Germany. E-mail: parsch@zi.biologie.uni-muenchen.de

In their study, Innocenti *et al*. provide direct experimental evidence for an increased mitochondrial mutational load affecting gene expression levels in male *Drosophila*. They performed careful genetic manipulations to create strains of *Drosophila* that differed only in their mitochondrial genomes. They then used DNA microarrays to measure differences in nuclear gene expression associated with the different mitochondrial genomes. They performed their experiments separately on males and females. The results were striking: In females, exchanging mitochondrial genomes altered the expression of only a handful of nuclear genes; in contrast, in males, more than a thousand genes showed a significant change in expression. Assuming that most changes in gene expression are deleterious (*4*), this indicates a much greater mutational load in males than females. Additional support for this interpretation comes from the expression profiles of the genes that were affected in males. There was a significant over-representation of male-biased genes (those that are expressed at a higher level in males than females) (*5*) and genes expressed specifically in male reproductive tissues. Furthermore, previous studies have shown that the expression level of many of the variable genes is associated with male reproductive output (*6*).

In addition to providing experimental validation of theoretical predictions, Innocenti *et al*. provide at least a partial explanation for the observed difference in gene expression polymorphism between males and females in natural populations of *Drosophila*. Previous studies have shown that, in general, male-biased genes are more variable in expression among individuals than female-biased genes, and that there is greater gene expression polymorphism among males than among females (*7–9*). Because individuals in natural populations harbor genetic polymorphism within their mitochondrial genomes, it is reasonable to assume that this polymorphism contributes to the observed variation in nuclear gene expression.

Recent studies have shown that another genetic element with sex-specific inheritance, the Y chromosome, also makes a large contribution to gene expression polymorphism among males (*10*). Like the mitochondrial genome, the Y chromosome encodes very few proteins. However, the Y chromosome contains a large amount of noncoding DNA (known as heterochromatin), and it is this heterochromatin that appears to modulate the expression of many nuclear genes (*10*, *11*). Y-chromosomal polymorphism has a disproportionate effect on genes whose products localize to the mitochondria (*11*). This raises the possibility that the male nuclear genome coevolves with the mitochondrial genome to alleviate some of the deleterious effects caused by mitochondrial mutations.

There are at least two open questions regarding the influence of the mitochondrial genome on nuclear gene expression. The first is mechanistic. How does a tiny genome that encodes only 13 proteins affect the expression of hundreds of nuclear genes in a sex-specific manner? Thousands of nuclear gene products are required for proper mitochondrial function, but further research is needed to elucidate the complex interactions that underlie this ancient symbiosis. The second question pertains to the effect of male-deleterious mitochondrial mutations in females. Are these mutations slightly deleterious, neutral, or even beneficial to females? The effect in females is a critical parameter that determines the rate at which these mutations will spread in a population. It is also important for extrapolating the *Drosophila* results to other species that have much smaller effective population sizes, such as mammals. For example, if most of the mutations have slightly deleterious effects on female fitness, one would predict a greater male mutational load in humans than in *Drosophila*, because natural selection is expected to be less efficient in humans (*12*).

References

1. P. Innocenti *et al.*, *Science* **332**, 845 (2011).
2. S. A. Frank, L. D. Hurst, *Nature* **383**, 224 (1996).
3. N. J. Gemmell, V. J. Metcalf, F. W. Allendorf, *Trends Ecol. Evol.* **19**, 238 (2004).
4. Y. Gilad, A. Oshlack, S. A. Rifkin, *Trends Genet.* **22**, 456 (2006).
5. H. Ellegren, J. Parsch, *Nat. Rev. Genet.* **8**, 689 (2007).
6. P. Innocenti, E. H. Morrow, *PLoS Biol.* **8**, e1000335 (2010).
7. C. D. Meiklejohn, J. Parsch, J. M. Ranz, D. L. Hartl, *Proc. Natl. Acad. Sci. U.S.A.* **100**, 9894 (2003).
8. S. Hutter, S. S. Saminadin-Peter, W. Stephan, J. Parsch, *Genome Biol.* **9**, R12 (2008).
9. L. Müller *et al.*, *BMC Genomics* **12**, 81 (2011).
10. B. Lemos, L. O. Araripe, D. L. Hartl, *Science* **319**, 91 (2008).
11. B. Lemos, A. T. Branco, D. L. Hartl, *Proc. Natl. Acad. Sci. U.S.A.* **107**, 15826 (2010).
12. A. Eyre-Walker, P. D. Keightley, *Nat. Rev. Genet.* **8**, 610 (2007).

10.1126/science.1206352

DEVELOPMENT

Planarian Pluripotency

Jonathan M. W. Slack

Cellular and molecular details underlying tissue regeneration are revealed in the flatworm.

Many animals can regenerate tails, but few can regenerate heads, and how they do so is a fascinating problem. Tiny flatworms called planaria have long been famous for the ability to regenerate body parts (*1–3*) and as such, they are a valuable model system for elucidating mechanisms that control cell and tissue replacement, a process that is important for the survival of most organisms. On page 811 of this issue, Wagner *et al*. (*4*) examine the nature of the cells (called neoblasts) responsible for regeneration in planaria, and on page 852, Petersen and Reddien (*5*) reveal more about how the worm decides whether to regenerate a head or a tail.

Neoblasts are small undifferentiated cells that have long been thought responsible for normal growth and regeneration in planarians (*6*). Labeling of DNA synthesis shows that they are the only cells in the worm that undergo division (*7*). Neoblasts are often described as "stem cells," but unlike mammalian stem cell systems, little is known about them. In mammals, a tissue with continuous cell renewal contains a small number of stem cells that survive for the lifetime of the animal and generate all cell types of the relevant tissue. For example, the hematopoietic stem cells of the bone marrow generate all the cell types of the blood and immune system (*8*, *9*). The stem cells are found in special niches where the microenvironment maintains their self-renewal capability (*10*, *11*). But most dividing cells of renewal tissues are not stem cells, but progenitor cells, which have a finite potential to divide and are committed to form one subset of cell types. For example, the hematopoietic stem cell gives rise to a common lymphocyte progenitor cell, and this gives rise to progenitor cells for particular types of lymphocyte.

Given the lack of knowledge about the organization of the neoblast population, the question asked by Wagner *et al*. was simple: Are there any cells among the neoblasts that are fully pluripotent, or are all neoblasts committed to form particular subsets of differentiated cell types? The term "pluripotent" generally denotes the ability to develop into any cell type in the body, whereas "multipotent"

Stem Cell Institute, The University of Minnesota, 2001 6th Street SE, Minneapolis, MN 55455, USA. E-mail: slack017@umn.edu

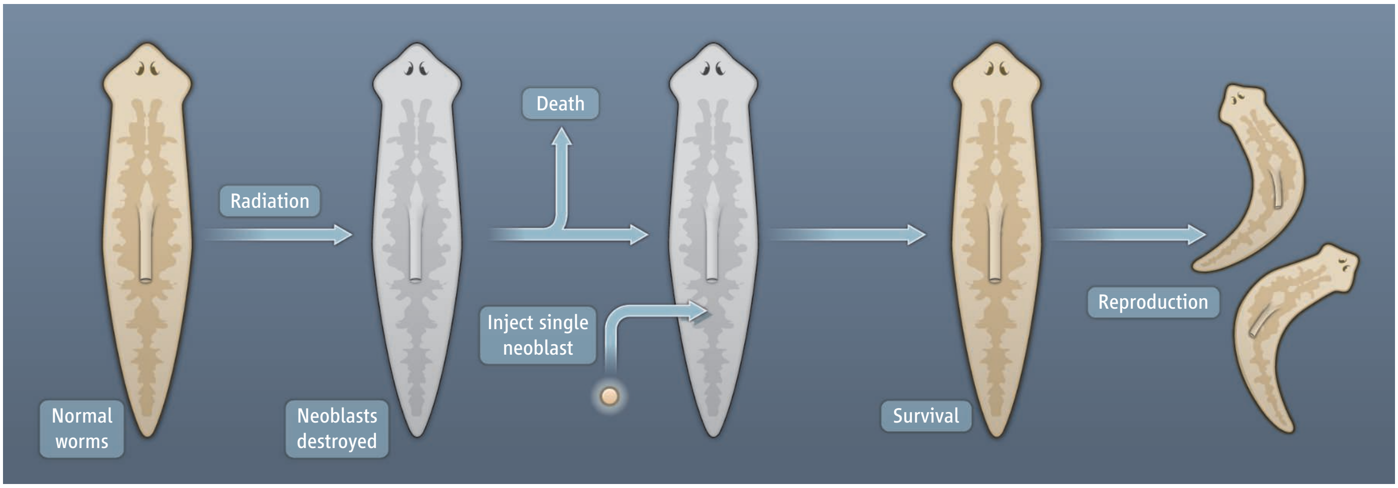

Regeneration. An experimental approach of Wagner *et al*. is shown, demonstrating that pluripotent cells reside among the neoblast population and can regenerate an entire worm.

indicates the ability to form more than one cell type, usually the few types present in a single tissue.

Wagner *et al*. used two experimental approaches. One involved exposing worms to lethal doses of radiation that destroy almost all the neoblasts. Under such conditions, simple Poisson statistics enables one to calculate the proportion of worms retaining a particular number of viable neoblasts. This corresponds well with the number of observable neoblast cell colonies that grow back in the irradiated hosts, which can be identified by a specific active gene of neoblasts called *smedwi-1* (*12*). By labeling newly synthesized DNA in actively dividing neoblasts with bromodeoxyuridine (a DNA precursor) prior to irradiation, the authors show that neoblast colonies that arise after irradiation derive from formerly dividing cells—that is, from surviving neoblasts, rather than from differentiated cells. Furthermore, each neoblast clone generates differentiated cells of several types. This demonstrates that the neoblast pool is not composed entirely of committed progenitors for individual cell types, but must contain multipotent or pluripotent cells. A similar approach in mice has shown that single stem cells can generate the various cell types of the intestinal epithelium (*13*, *14*).

Another method used by Wagner *et al.* involved isolating neoblasts by flow cytometry from planaria. A single neoblast was then injected into a host worm lacking all neoblasts (as a consequence of irradiation; see the figure). Again, the neoblast-derived clones gave rise to several cell types. Seven of 130 single-cell grafts rescued the lethally irradiated hosts to restore complete and viable worms. Three of these seven worms displayed repeated binary fission to generate new asexual strains having the genotype of the donor cell. If one neoblast can generate a whole worm, it must by definition be pluripotent.

The study of Wagner *et al*. provides the first clear evidence that the neoblast population contains pluripotent cells. However, they raise a whole set of new questions. What proportion of the neoblasts are pluripotent in situ? It is also not clear whether the pluripotent cells lie within a special niche made up of other cell types. What is the structure of the hierarchy leading from the pluripotent cells to the 30 or so cell types believed to be present in a planarian? Consideration of other stem cell systems suggests that future progress will require more molecular markers to identify and fractionate subsets of neoblasts.

If you cut a planarian in half, the two pieces will each regrow into a complete worm in 4 to 14 days, depending on the species. After transection, the local neoblasts must decide whether to become a head or a tail. It is well established that signaling by the secreted factor Wnt, important in many other developmental systems, including mammals, promotes tail regeneration in planaria, whereas inhibitors of Wnt signaling promote head regeneration (*15*, *16*). Petersen and Reddien identified another component of this regeneration system. The gene *notum*, first discovered in the model fruit fly *Drosophila melanogaster*, encodes a hydrolase enzyme that modifies a class of cell surface molecule and thereby inhibits Wnt signaling. The authors show that expression of *notum* is increased in cells near anterior-facing cuts, which will form heads, and not in those near posterior-facing cuts, which will form tails. Inhibition of *notum* activity reduces the frequency of head regeneration and shifts the character of the anterior regenerate toward "tailness." In addition, it seems that if two neighboring cuts are made, *notum*-positive cells only appear next to the posterior cut, suggesting that somehow both facets of the anterior cut have been inhibited by the proximity of the posterior cut. The study of Petersen and Reddien confirms the importance of the Wnt system in controlling head-tail polarity. However, understanding regeneration in planaria will ultimately require identification of the long-range polarity system that must exist to initiate head or tail character after transection.

Although the human body does not face the demands of regenerating new body parts, it is constantly replacing lost cells, such as during wound healing, renewal of the intestinal lining, and replenishment of blood constituents. Stem cells make these processes possible, but we are still deciphering the underlying cellular, genetic, and molecular mechanisms. Now that planarian neoblasts appear generally similar in function to mammalian pluripotent stem cells, knowledge of their basic biological properties may extend to their human counterparts and provide insights into whether and how stem cells may be used as effective therapeutic agents.

References

1. E. Saló, J. Baguñà, *J. Exp. Zool.* **292**, 528 (2002).
2. K. Agata, *Curr. Opin. Genet. Dev.* **13**, 492 (2003).
3. P. W. Reddien, A. Sánchez Alvarado, *Annu. Rev. Cell Dev. Biol.* **20**, 725 (2004).
4. D. E. Wagner *et al*., *Science* **332**, 811 (2011).
5. C. P. Petersen, P. W. Reddien, *Science* **332**, 852 (2011).
6. G. T. Eisenhoffer *et al*., *Cell Stem Cell* **3**, 327 (2008).
7. P. A. Newmark, A. Sánchez Alvarado, *Dev. Biol.* **220**, 142 (2000).
8. M. Kondo *et al*., *Annu. Rev. Immunol.* **21**, 759 (2003).
9. D. Metcalf, *Stem Cells* **25**, 2390 (2007).
10. K. A. Moon, I. R. Lemischka, *Science* **311**, 1880 (2006).
11. D. L. Jones, A. J. Wagers, *Nat. Rev. Mol. Cell Biol.* **9**, 11 (2008).
12. P. W. Reddien *et al*., *Science* **310**, 1327 (2005).
13. H. R. Withers, M. M. Elkind, *Radiat. Res.* **38**, 598 (1969).
14. M. Inoue *et al*., *Am. J. Pathol.* **132**, 49 (1988).
15. K. A. Gurley *et al*., *Science* **319**, 323 (2008).
16. C. P. Petersen, P. W. Reddien, *Cell* **139**, 1056 (2009).

10.1126/science.1206913

CREDIT: Y. HAMMOND/SCIENCE

BIOCHEMISTRY

From Computational Design to a Protein That Binds

Researchers use computational approaches to design two proteins from scratch that bind to the flu virus.

Bryan S. Der and Brian Kuhlman

Protein-protein interactions are critical for many biological processes, and over the past several decades, this importance has prompted researchers to investigate the physical and chemical bases of protein binding. How much do we now understand about how proteins interact? Perhaps the most rigorous way to answer this question is to endeavor to design, at an atomic level of detail, such an interaction from scratch. On page 816 of this issue, Fleishman *et al*. (*1*) take on this challenge. They used a computational method that enabled them to design two proteins that bind to a preselected surface on an influenza virus. This work demonstrates how far we have come in understanding and being able to predict protein-protein interactions, and the technique could prove useful for developing biosensors, reagents, and more effective drugs.

The basic task in computational protein interface design is finding low-energy amino acid sequences with configurations that enable them to "dock" with targeted protein surfaces (*2*, *3*). Candidate sequences must have side chain and backbone atoms that fit together like a jigsaw puzzle, featuring no overlaps, little empty space, and precise chemical complementarity. By designing a protein that binds the stem region of influenza hemagglutinin—a protein that enables the virus to infect a target cell—Fleishman *et al*. solved an enormously complicated jigsaw puzzle. Instead of a large table and hours of free time, however, solving their puzzle required cutting-edge software developed by ~20 groups worldwide (*4*) and 100,000 hours of highly parallel computing time. It also involved using a technique known as yeast display to screen candidate proteins and select those with high binding affinities, as well as x-ray crystallography to validate designs.

The primary novelty of this work is the use of computational methods to generate the high-affinity binders. Common existing approaches involve using animal immune systems to generate antibodies, or screening large "libraries" of candidate proteins (*5*). These two approaches are very powerful for many purposes but do not offer precise control over the binding location or orientation. This specificity is of utmost importance in efforts to develop drugs that target flu's hemagglutinin protein; previous efforts featured antibodies that ended up binding to the protein's rapidly varying head region (*6*), making it harder to prevent acquired resistance. By targeting hemagglutinin's more conserved stem region (*7*, *8*), researchers may be able to develop therapies that are effective against many virus subtypes and prevent acquired resistance. Fleishman *et al*. selected a surface patch in the conserved stem region for this reason and were successful in designing a protein that bound to the patch with the desired orientation.

Previous efforts in computational de novo protein interface design yielded binders with lower affinity (*9*, *10*) or that did not bind in the designed orientation (*11*). What did Fleishman *et al*. do differently to achieve high affinity? One answer is a rapid experimental approach for testing designs. By using yeast display (*12*), the authors were able to test 73 designs while limiting time and resources at the lab bench. Yeast can perform recombina-

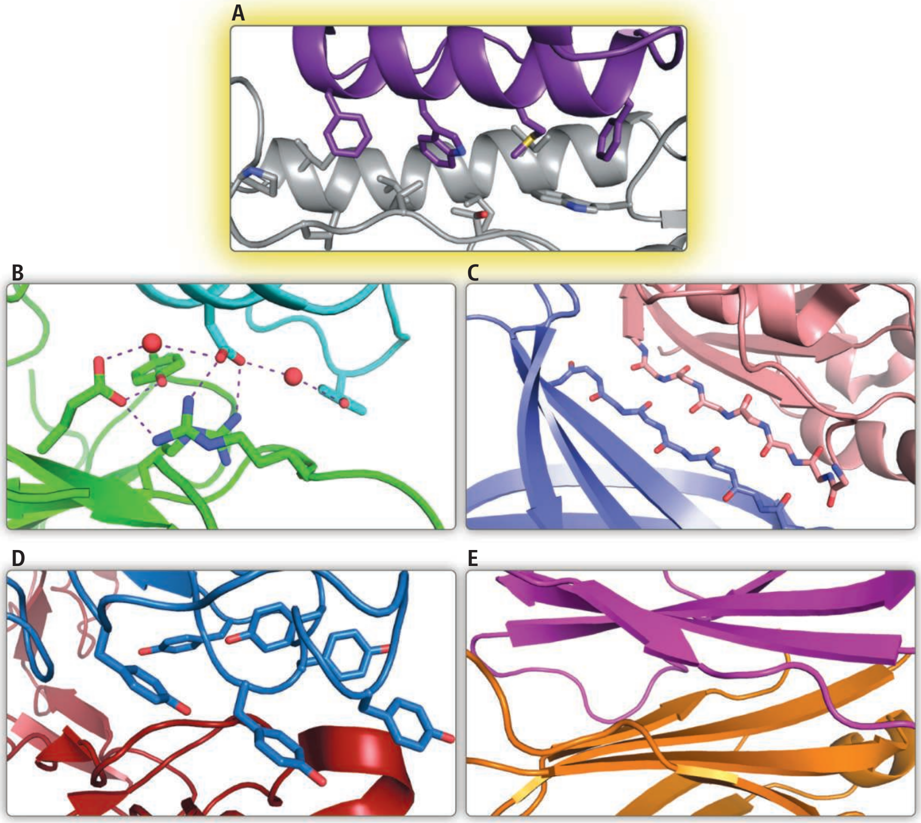

Computational challenges ahead. The diversity of protein interface characteristics observed in nature suggests future challenges for computational design. (**A**) Fleishman *et al*. designed a hydrophobic helix (purple) to bind a hydrophobic groove (gray) with unprecedented accuracy in binding location and orientation. (**B**) The high-affinity interaction between the bacterial proteins barnase and barstar features a sophisticated hydrogen bond network that also includes water molecules. (**C**) Strand-strand pairings at an interface feature regular repeats of polar atoms. (**D**) Imitating an antibody interface that features long loops will require precise backbone conformational sampling and scoring methods. Loops provide a rich diversity of backbone conformations, such that binding can occur using only tyrosine and serine side chains (*5*). (**E**) The quaternary structure of an antibody is stabilized by a sheet-sheet interface.

CREDIT: BRYAN S. DER AND BRIAN KUHLMAN

Department of Biochemistry and Biophysics, University of North Carolina, Chapel Hill, NC 27599, USA. E-mail: bder@email.unc.edu; bkuhlman@email.unc.edu

Published by AAAS

tion, avoiding gene-cloning steps, and investigators can obtain initial measures of binding affinity while the protein is displayed on the yeast surface. This obviates the need to individually purify 73 different proteins. And after biophysical characterization of the two binders, the yeast are then used for a selection process called affinity maturation. The effectiveness of this experimental workflow may pave the way for future efforts to test computationally designed protein interactions.

Another possible reason for their achievement involves the computational design protocol. Previous modest-affinity binders were developed by focusing first on the placement of the two proteins, and then on high-resolution all-atom side chain design (*9*, *10*). Fleishman *et al*. took a different approach. They first focused on all-atom placement of disembodied side chains to establish critical "hot spot" interactions, and then on docking the designed protein to its target. This strategy is reminiscent of a previous approach that involved grafting key residues from a known interaction onto a new protein scaffold to generate a new binding pair (*13*). If there are no known hot spot binding motifs, however, these hot spot interactions must be designed de novo (*1*).

To create tight binders (dissociation constant < 50 nM) from their initial hits (apparent affinities of >2000 nM and >5000 nM), Fleishman *et al*. performed affinity maturation with yeast display. An examination of the stabilizing mutations suggested ways of improving their computational methods; for instance, the authors concluded that future modeling efforts should try to take into account subtle movements of sequence backbones, attractive forces known as long-range electrostatics, and the energy costs associated with protein interactions (such as the desolvation cost for "burying" polar atoms). Optimizing a protein energy function, however, presents a challenge, and the insights gained from this single study will need to be combined with results from other design and modeling studies in order to identify robust improvements.

Although Fleishman *et al*. have produced a landmark result, it is evident that computational protein interface design is not a solved problem. Researchers should not be satisfied with one or a few successes in solving these astronomically complex molecular puzzles. Each new puzzle is different from the last; for example, the region of hemagglutinin targeted in this work was hydrophobic and α-helical. Will the computational protocol developed by Fleishman *et al*. also be effective for designing binders for polar surface patches, or targeting alternative secondary structures (see the figure) such as β sheets, strands, or loops? Creating many of these interfaces will require accurate modeling of protein conformations and accurate evaluation of desolvation, electrostatics, and hydrogen bonding.

The endeavor to understand protein interactions will undoubtedly continue for decades to come. And the pursuit should remain persistent, as the impacts of rational design and manipulation of protein-protein interactions can hardly be overstated.

References

1. S. J. Fleishman *et al*., *Science* **332**, 816 (2011).
2. D. J. Mandell, T. Kortemme, *Nat. Chem. Biol.* **5**, 797 (2009).
3. J. Karanicolas, B. Kuhlman, *Curr. Opin. Struct. Biol.* **19**, 458 (2009).
4. A. Leaver-Fay *et al*., *Methods Enzymol.* **487**, 545 (2011).
5. S. S. Sidhu, S. Koide, *Curr. Opin. Struct. Biol.* **17**, 481 (2007).
6. I. A. Wilson, N. J. Cox, *Annu. Rev. Immunol.* **8**, 737 (1990).
7. D. C. Ekiert *et al*., *Science* **324**, 246 (2009).
8. J. Sui *et al*., *Nat. Struct. Mol. Biol.* **16**, 265 (2009).
9. P.-S. Huang *et al*., *Protein Sci.* **16**, 2770 (2007).
10. R. K. Jha *et al*., *J. Mol. Biol.* **400**, 257 (2010).
11. J. Karanicolas *et al*., *Mol. Cell* **42**, 250 (2011).
12. S. A. Gai, K. D. Wittrup, *Curr. Opin. Struct. Biol.* **17**, 467 (2007).
13. S. Liu *et al*., *Proc. Natl. Acad. Sci. U.S.A.* **104**, 5330 (2007).

10.1126/science.1207082

PHYSICS

Brownian Motion Goes Ballistic

Peter N. Pusey

Measurements of the Brownian motion of particles in air and in water reveal a smooth "ballistic" motion at very short times.

When Einstein explained the origin of Brownian motion in 1905, he described the erratic movement of a microscopic particle driven by the thermal motion of liquid molecules as a random walk with sharp changes of direction between each step (*1*). He realized that this picture—the one we seem to see if we watch a particle under the microscope—must break down if we were to look more closely. A moving object would require an infinite force to change its speed or direction discontinuously. The particle actually moves "ballistically" along a smooth trajectory (*2*–*4*), as if it were a microscopic ocean liner on an erratic course (see the first figure, panels A and B). It has taken more than a century to observe this ballistic motion. The studies of Li *et al*. (*5*) were conducted on particles in air; its low viscosity allowed ballistic motion to be followed accurately for extended periods and showed that a particle's instantaneous velocities along its path obey a statistical distribution consistent with thermal motion. Huang *et al*. (*6*) used liquid water; in this higher-density medium, the transition from ballistic motion at short times to diffusive motion at longer ones could be studied in detail.

Einstein estimated (*2*–*4*) that a particle of diameter 1 μm in water would move for only about 0.1 μs over a distance of only about 2 Å before completely changing its speed and direction. The minute magnitudes of these estimates led Einstein to conclude that only the larger-scale diffusive random walk would be observed in practice. The present experiments used technologies undreamed of in Einstein's time. Single particles were held in optical traps—radiation pressure prevents them from settling under gravity. A fast position-sensitive detector (*7*) split the interference pattern formed between light scattered by the particle and the trapping laser beam itself and fed the two parts to two photodiode detectors. Lateral motion of a particle in the trap increases the intensity at one detector but decreases it at the other. The difference between the two signals measures one component of the particle's position. Coupled to fast electronics, this system can measure displacements as small as 0.3 Å in time intervals as short as 0.01 μs.

In a vacuum, a particle in an optical trap would oscillate indefinitely. Gas molecules both dampen the oscillations and introduce random impulses that induce Brownian motion. Li *et al*. determined the time evolution of the position and velocity of a 3-μm-diameter silica sphere trapped in air at about 1/36 of atmospheric pressure (see the second figure, panel A). The underlying oscillatory motion, with a period of about 300 μs, is evident, as is a degree of randomness induced by the gas molecules. Einstein (*2*–*4*) estimated the duration of ballistic Brownian motion to be the time $\tau_p = m/\gamma$

SUPA, School of Physics, University of Edinburgh, Edinburgh EH9 3JZ, UK. E-mail: p.n.pusey@ed.ac.uk

over which the particle's velocity would decay through friction with the gas (or liquid), if the random impulses from its molecules were neglected; here m is the particle's mass and γ is its Stokes friction coefficient that describes drag (*8*, *9*). For the experiment of Li *et al.*, $\tau_p \approx 150$ µs, so that random changes in the velocity occurred on a time scale similar to that of the coherent oscillations (the motion is underdamped).

Li *et al.* constructed histograms of the instantaneous velocities at air pressures of both 1/36 and 1 atm, where the particle's velocity changed more rapidly ($\tau_p \approx 50$ µs). These were accurately described by the Maxwell-Boltzmann distribution with a root-mean-square (rms) velocity of about 0.42 mm/s, in good agreement with the theoretical value from equipartition of energy for conditions of thermal equilibrium [$v_{rms} = (k_B T/m)^{1/2}$, where k_B is the Boltzmann constant and T the temperature]. Li *et al.* also showed that the particle's mean-square displacement (MSD, a measure of average distance traveled) agreed well with old calculations of underdamped Brownian motion in a harmonic potential (*10*).

In a liquid, the duration of a Brownian step, $\tau_p \approx 0.1$ µs, is much smaller than the natural oscillation period of the trap, making the motion strongly overdamped. Although it is more difficult to access the ballistic regime itself, experimental studies in liquids enable a detailed examination of the transition from ballistic to diffusive motion. Huang *et al.* measured the MSD of a 1-µm-diameter silica sphere in water (*11*) (see the second figure, panel B). At the shortest times ($t \approx 0.01$ to 0.03 µs), the MSD increases as t^2 (a line of slope 2 in the double logarithmic plot), which corresponds to ballistic motion. Between roughly 2 µs $< t <$ 20 µs, the particle makes many random steps, and the MSD increases as t, which is characteristic of diffusion (*11*). The particle's free diffusion is finally limited by the trapping potential, causing the MSD to saturate at $t > 100$ µs.

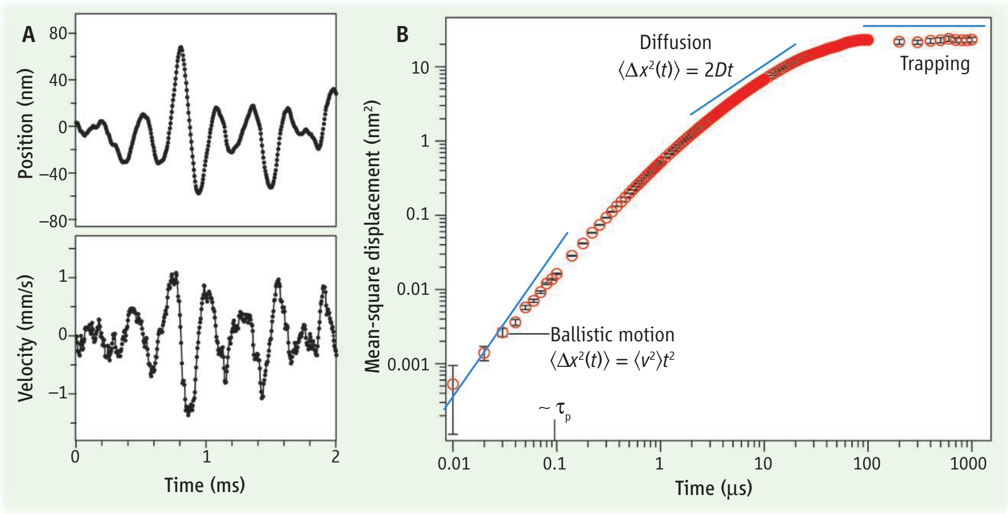

Resolving ballistic motion. (**A**) Li *et al.* measured the position and velocity of a 3-µm-diameter silica sphere optically trapped in air at about 1/36 of atmospheric pressure. Oscillations in the underdamped motion were randomly perturbed by collisions with the gas molecules. (**B**) Huang *et al.* measured the mean-square displacement of a 1-µm-diameter silica sphere trapped in water, which displayed the slow transition from ballistic to diffusive Brownian motion. Note the remarkable resolution of the measurement: 0.001 nm^2 corresponds to a displacement of 0.3 Å, measured in about 0.02 µs. [Panel B adapted from (*6*)]

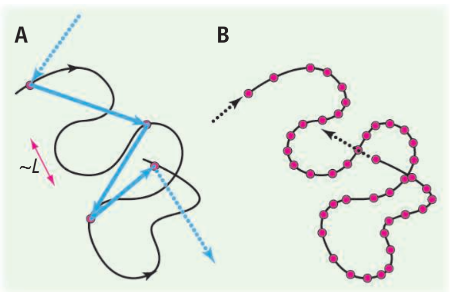

Timing is everything. (**A** and **B**) A particle undergoing Brownian motion is buffeted at random by thermally agitated fluid molecules, and it follows a tortuous but locally smooth path (black line). It loses memory of its speed and direction over the very small distance ~L. What an observer actually sees depends on the resolution of the position measurement. In the case considered by Einstein (A), the particle's speed and direction have changed many times between measurements (the red dots), and the observer sees a diffusive random walk with uncorrelated steps (the blue arrows). Measurements made at shorter time intervals (B) resolve the smooth ballistic motion.

For many years after Einstein's contributions, it was expected that the transition from ballistic to diffusive motion would be quite sharp, corresponding to an exponential decay of the particle's memory of its earlier velocity. However, about 50 years ago, hints from computer simulations and theory started to suggest a more complex scenario. In particular, hydrodynamic vortices in the liquid created by the particle's motion lead to memory effects, and the particle's velocity decays much more slowly than exponentially, exhibiting a $t^{-3/2}$ "long-time-tail" (*12*). Detailed analysis by Huang *et al.* of data like that shown in the second figure, panel B, where the ballistic-to-diffusive transition spans more than three decades in time, has now provided a thorough verification of the full, complicated hydrodynamic theory (*13*, *14*). Although several previous experiments had observed the breakdown of the simple diffusion picture [e.g., (*15*)], the present studies extend into the ballistic regime.

What next? Li *et al.* mention the fascinating prospect of laser cooling a trapped particle to a temperature at which quantization of the energy of this mesoscopic object could be observed (*16*). Huang *et al.* suggest extending their measurements to Brownian motion in confined regions and heterogeneous media. Here, understanding the details of prediffusive motion over subnanometer distances could well be relevant to some biological processes, such as the lock-and-key mechanism of enzyme action.

References and Notes

1. A. Einstein, *Ann. Phys.* **322**, 549 (1905).
2. A. Einstein, *Zeit. Elektrochem.* **13**, 41 (1907).
3. Both (*1*) and (*2*) are translated and reprinted in (*4*).
4. A. Einstein, in *Investigations on the Theory of Brownian Movement*, R. Fürth, Ed. (Dover, New York, 1956).
5. T. Li *et al.*, *Science* **328**, 1673 (2010).
6. R. Huang *et al.*, *Nat. Phys.* (2011); 10.1038/nphys1953:arxiv:1003.1980.
7. I. Chavez *et al.*, *Rev. Sci. Instrum.* **79**, 105104 (2008).
8. The Stokes friction coefficient is given by $\gamma = 6\pi\eta R$, with R the particle's radius and η the shear viscosity of the liquid. At low pressure, where the mean-free path of a gas molecule is comparable to R, the friction is reduced by a substantial "Cunningham slip correction" (*9*).
9. E. Cunningham, *Proc. R. Soc. A* **83**, 357 (1910).
10. G. E. Uhlenbeck, L. S. Ornstein, *Phys. Rev.* **36**, 823 (1930).
11. In an isotropic random process like Brownian motion, the average velocity and average displacement are zero. The simplest descriptor of average motion is the MSD, the square of $\Delta x(t)$, the distance moved in time t, averaged over many measurements. For ballistic motion (straight line and constant speed) $\langle \Delta x^2(t) \rangle = \langle v^2 \rangle t^2$; for diffusion, Einstein's result is $\langle \Delta x^2(t) \rangle = 2Dt$, with the diffusion constant given by $D = k_B T/\gamma$ (*1*).
12. B. J. Alder, T. E. Wainwright, *Phys. Rev. A* **1**, 18 (1970).
13. E. J. Hinch, *J. Fluid Mech.* **72**, 499 (1975).
14. H. J. H. Clercx, P. P. J. M. Schram, *Phys. Rev. A* **46**, 1942 (1992).
15. B. Lukic *et al.*, *Phys. Rev. Lett.* **95**, 160601 (2005).
16. T. Li *et al.*, *Nat. Phys.* (2011); 10.1038/nphys1952.

10.1126/science.1192222

RETROSPECTIVE

Walter M. Fitch (1929–2011)

A meticulous biologist developed fundamental tools for the field of molecular evolution.

William R. Atchley

Walter Monroe Fitch, founder of the field of molecular phylogenetics, passed away in Irvine, California, on 10 March at the age of 81. He was active until the time of his death, just finishing a book on the creationism-evolution controversy. He strongly promoted the widespread teaching of evolution.

Throughout his career, Walter made substantial contributions to the theory underlying molecular evolutionary change. In the 1960s and 1970s, he developed computer algorithms to infer evolutionary relationships among organisms based on molecular data (protein and DNA sequences), as demonstrated in his classic studies on evolutionary divergence in cytochrome c. His seminal work on molecular homology and estimation of ancestral protein sequences greatly facilitated analytical procedures for describing evolutionary change. He pioneered methods to generate branching diagrams or "phylogenetic trees" to reflect the relationships among species based upon similarities and differences in their physical and/or genetic characteristics. Fitch's work had a major impact on not only biologists but also mathematicians and computer scientists. More recently, he published important contributions to understanding the molecular evolution of influenza virus and HIV.

Walter was the cofounder of the Society for Molecular Biology and Evolution and its journal *Molecular Biology and Evolution*. He was the society's first president and editor-in-chief of the journal for 10 years. The "Walter M. Fitch Award" given by the society to the most deserving young scientists is a continuing reminder of his legacy.

Walter was born in San Diego, California, on 21 May 1929. He received his A.B. in chemistry (1953) and his Ph.D. in biochemistry (1958) from the University of California, Berkeley. He was a member of the faculty of Physiological Chemistry at the University of Wisconsin, Madison, from 1962 until 1986. He was professor of Biological Sciences at the University of Southern California from 1986 to 1989, after which he was professor of Ecology and Evolutionary Biology at the University of Calfornia, Irvine until his death.

Department of Genetics, North Carolina State University, Raleigh, NC 27695, USA. E-mail: bill@atchleylab.org

His many scientific accomplishments led to multiple academy memberships including the United States National Academy of Sciences, the American Academy of Arts and Sciences, the Linnean Society of London, and the American Philosophical Society. He was awarded a number of additional international honors and honorary degrees.

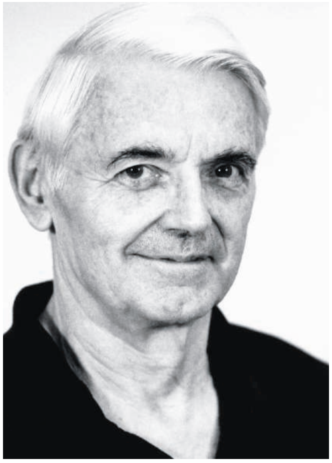

Walter had a marvelous and very quick mind. He has been described as a "towering intellect." He delighted in discussing intellectually challenging scientific issues, particularly in the area of evolution. Given more to geometric rather than algebraic approaches, Walter often resorted to pencil-and-paper solutions to understand complex issues, particularly for phylogenetic problems. I assume that his development of parsimony and least-squares algorithms for phylogenetic analyses was worked out largely by hand.

In projects that Walter and I worked on, he was rigorous in his approach to science and meticulous in his analyses. His sequence evolution studies always involved time-consuming hand correction of alignments produced by computer algorithms. This was done laboriously and painstakingly before any subsequent analyses. Walter didn't trust global sequence-alignment algorithms and demonstrated to me and others many instances in which alignment algorithms gave erroneous results. In ways such as this, he was a wonderful mentor to younger scientists, demonstrating that they must be extremely precise with even the most fundamental aspects of a project.

Those who knew him were quick to realize that Walter was highly competitive and reveled in intellectual jousting with his colleagues. He had a sharp mind and was very quick on his feet, which made him a formidable intellectual adversary. However, he was also very kind and held himself to the highest standards. Even in the vitriolic confrontations during the infamous "phenetics versus cladistics" wars in the 60s and 70s, Walter was never verbally or intellectually abusive, even when dealing with the most obnoxious individuals. At the time, both methods were proposed to resolve evolutionary relationships, the former based on overall similarity, and the latter, based on shared derived characteristics.

Walter loved jazz, humor, fine wine, and good food. While a student at Berkeley, he became interested in the iconoclastic pianist Thelonious Monk and tried to play some of Monk's tunes on the piano. He always played in the key of C, which corresponds to the white piano keys, because he wasn't sure what to do with the black keys. I have always suspected that had he not become a scientist, he might have studied jazz piano.

Walter also loved to share jokes and funny stories, and his involvement in practical jokes was well known. One of the best-known of the practical jokes was actually played on Walter. While he was away on sabbatical leave, a colleague and I fabricated an announcement for a seminar by a well-known biochemist disproving Fitch's classic evolutionary work on cytochrome c. There were weeks of anxiety for Walter before he learned that he was the victim of a hoax.

Walter was an informal person despite his international fame as a scientist. One could easily see this in his manner of dress. His standard uniform was shorts, a T-shirt, and flip-flops. He wore this attire to meetings with the university higher administration, to scientific conferences, and just about everywhere he went. Indeed, in January one year, he appeared in his "California" attire for the 2-week-long Manfred Eigen Winter Seminar in Klosters, Switzerland. We had to stop on the way from the train station to get him properly clothed so he wouldn't freeze!

Walter's methodological and theoretical achievements about estimating evolutionary relationships among species drove the maturation of the field. He was a great source of intellectual stimulation to his colleagues, a wonderful mentor to younger scientists, and a great friend to many. He will be sorely missed.

10.1126/science.1207426

Comparing Photosynthetic and Photovoltaic Efficiencies and Recognizing the Potential for Improvement

Robert E. Blankenship,[1]* David M. Tiede,[2]* James Barber,[3] Gary W. Brudvig,[4] Graham Fleming,[5] Maria Ghirardi,[6] M. R. Gunner,[7] Wolfgang Junge,[8] David M. Kramer,[9] Anastasios Melis,[10] Thomas A. Moore,[11] Christopher C. Moser,[12] Daniel G. Nocera,[13] Arthur J. Nozik,[14] Donald R. Ort,[15] William W. Parson,[16] Roger C. Prince,[17] Richard T. Sayre[18]

Comparing photosynthetic and photovoltaic efficiencies is not a simple issue. Although both processes harvest the energy in sunlight, they operate in distinctly different ways and produce different types of products: biomass or chemical fuels in the case of natural photosynthesis and nonstored electrical current in the case of photovoltaics. In order to find common ground for evaluating energy-conversion efficiency, we compare natural photosynthesis with present technologies for photovoltaic-driven electrolysis of water to produce hydrogen. Photovoltaic-driven electrolysis is the more efficient process when measured on an annual basis, yet short-term yields for photosynthetic conversion under optimal conditions come within a factor of 2 or 3 of the photovoltaic benchmark. We consider opportunities in which the frontiers of synthetic biology might be used to enhance natural photosynthesis for improved solar energy conversion efficiency.

Sunlight is the most abundant and sustainable source of energy available to humanity. Earth receives solar energy at the rate of approximately 120,000 TW (1 TW = 10^{12} W) in a highly reliable and distributed fashion. This vastly exceeds the current annual worldwide energy consumption rate of ~15 TW and any conceivable future needs in this century (*1*–*3*). However, sunlight is dilute; the yearly averaged solar power striking the Earth's surface is about 170 W per square meter, which varies depending on geographical location (*4*). Devising methods by which to efficiently capture and store this energy for societal use is one of the great challenges of our age. There is general agreement that no one approach is capable of solving our energy needs for the future and that a mix of sustainable technologies will be required (*5*).

There is considerable confusion, especially in the popular press, about how to compare the efficiency of solar energy capture in photovoltaic devices with a corresponding characteristic of photosynthetic organisms. The problem hinges on the different assumptions and conditions underlying the definition of efficiency in each case (*6*, *7*). To facilitate direct comparisons between photosynthetic and photovoltaic (PV) systems, we provide consistent definitions and examine the major factors that define the efficiencies of both processes—first considering current technology, then looking forward to possible strategies for improvements. In all cases, we consider the efficiency of harvesting the entire solar spectrum as a basis for comparison.

We focus exclusively here on conversion efficiency. However, the total integrated cost of the systems, including land, water, capital, operations and maintenance, waste disposal, transmission, transportation and storage, as well as risks from manufacturing and possible interactions with the food supply and climate change, must also be considered. Therefore, the technology with the highest efficiency may not necessarily be the best choice to implement in a given situation. Ultimately, a comparison of solar energy options must come from the perspective of a complete life-cycle assessment in order to evaluate the full suite of energy inputs, infrastructure and renewal requirements, and environmental factors, including greenhouse gas balance. This is a critical and active area of research for both photosynthetic and PV systems (*8*, *9*), but currently there is little consistency in the methods used. Differences in assumptions about efficiency terms, life-cycle inventory components, and systems boundaries create large variations in the metadata generated from the many concomitant efforts.

Comparing Photosynthetic and Photovoltaic Efficiencies

Efficiency is a concept that is deceptively simple yet can be elusive for comparisons between such different systems as living organisms and photovoltaic cells. The solar conversion efficiency of a PV device can be directly measured with high accuracy and is usually quoted by researchers and manufacturers in terms of power: electrical power out (W/cm^2) divided by incident solar irradiance (W/cm^2) measured over the entire solar spectrum. This instantaneous metric, measured at peak solar intensity, does not include energy storage and transmission. In contrast, natural photosynthesis stores energy in the chemical bonds of its molecular products and uses much of this energy to sustain and replicate the organism, typically over a defined growing season.

A more direct comparison of PV and photosynthetic solar energy conversion efficiencies would consider a process in which PV also stores energy in chemical bonds. Application of PV-derived energy to electrolysis of water is a good choice for this purpose: Existing commercial electrolyzers afford accurate efficiency benchmarks, and the free energy needed in order to split H_2O into H_2 and O_2 ($\Delta G° = 1.23$ eV) is essentially equal to the free energy change associated with photosynthesis [$\Delta G° = 1.24$ eV for $CO_2 + H_2O$ to $(CH_2O) + O_2$, where (CH_2O) is shorthand for carbohydrate].

The power conversion efficiency of present commercial single-junction (single photosystem) silicon solar cell modules is typically 18 ± 2% (*10*). This value pertains to peak solar intensity (1 kW/m^2), with an AM1.5 spectral distribution or solar zenith angle of 48.2° (sunlight passing through 1.5 atmospheres). The efficiency of a PV module changes during the day and throughout the year because of the changing solar zenith angle, and the PV efficiency averaged over a 1-year cycle is about 95% of the maximum AM1.5 value. Modern commercial electrolyzers have efficiencies as high as 80% [based

[1]Departments of Biology and Chemistry, Washington University in St. Louis, St. Louis, MO 63130, USA. [2]Chemical Sciences and Engineering Division, Argonne National Laboratory, Argonne, IL 60439, USA. [3]Division of Molecular Biosciences, Imperial College London, London SW7 2AZ, UK; Department of Material Sciences and Engineering, Polytechnic of Turin, 10129 Turin, Italy. [4]Department of Chemistry, Yale University, New Haven, CT 06520–8107, USA. [5]Department of Chemistry, University of California, Berkeley, and Physical Biosciences Division, Lawrence Berkeley National Laboratory, Berkeley, CA 94720, USA. [6]Biosciences Center, National Renewable Energy Laboratory, Golden, CO 80401, USA. [7]Department of Physics, City College of New York, New York, NY 10031, USA. [8]Division of Biophysics, University of Osnabrück, D-49069 Osnabrück, Germany. [9]Biochemistry and Molecular Biology and DOE-Plant Research Laboratory, Michigan State University, East Lansing, MI 48824, USA. [10]Department of Plant and Microbial Biology, University of California, Berkeley, Berkeley, CA 94720–3102, USA. [11]Department of Chemistry and Biochemistry, Arizona State University, Tempe, AZ 85287–1604, USA. [12]Department of Biochemistry and Biophysics, University of Pennsylvania, Philadelphia, PA 19104, USA. [13]Department of Chemistry, Massachusetts Institute of Technology, Cambridge, MA 02139–4307, USA. [14]National Renewable Energy Laboratory, Golden, CO 80401, USA; Department of Chemistry and Biochemistry, University of Colorado, Boulder, CO 80309, USA. [15]U.S. Department of Agriculture/Agricultural Research Service, Photosynthesis Research Unit, University of Illinois, Urbana, IL 61801, USA. [16]Department of Biochemistry, University of Washington, Seattle, WA 98195, USA. [17]ExxonMobil Biomedical Sciences, Annandale, NJ 08801, USA. [18]Donald Danforth Plant Science Center, St. Louis, MO 63132, USA.

*To whom correspondence should be addressed. E-mail: blankenship@wustl.edu (R.E.B.); tiede@anl.gov (D.M.T.)

on heat of combustion of H_2 to H_2O in liquid form at atmospheric pressure and 25°C, standard temperature and pressure (STP) conditions]. Thus, an annual averaged efficiency for solar water splitting by PV-driven electrolysis would be about (0.18) × (0.95) × (0.8) ~ 14% (*11*). This assumes that there is no mismatch between the photovoltage generated by the PV array and the voltage required for electrolysis. Present Si PV modules arranged in electrical series would suffer mismatch losses as high as 20 to 30%, bringing the overall H_2O splitting efficiency down to ~10 to 11%. This constitutes the first benchmark to compare with the efficiency of photosynthetic fuel production. As discussed below, ongoing research is providing opportunities to construct PV devices with considerably higher efficiencies.

Several different measures of efficiency have been used in describing natural photosynthesis. The quantum efficiency is the percentage of absorbed photons that give rise to stable photoproducts. Photosynthetic organisms typically can operate at nearly 100% quantum efficiency under optimum conditions (*12*). For comparison with PV electrolysis over an annual cycle, the energy efficiency of photosynthesis is a more useful parameter and is defined as the energy content (heat of combustion of glucose to CO_2 and liquid H_2O at STP) of the biomass that can be harvested annually divided by the annual solar irradiance over the same area. Using this definition, solar energy conversion efficiencies for crop plants in both temperate and tropical zones typically do not exceed 1% (*7*, *13*), a value that falls far below the benchmark for PV-driven electrolysis. Higher 3% annual yields are reported for microalgae grown in bioreactors (*14*).

Short-term (rapid growth phase) efficiencies measured during the growing season are higher, reaching 3.5% for C3 and 4.3% for C4 plants (*7*), and perhaps 5 to 7% for microalgae in bubbled bioreactors (*15*). These efficiencies are measured in the absence of restrictions imposed by plant life-cycle regulation or by light and gas exchange limitations in the case of algae. Even so, these values fall below theoretical limits and ultimately limit the net annual productivity. Most natural photosynthetic systems store solar energy only during a growing season; efficiencies measured during that period must therefore be reduced accordingly to make valid comparisons on an annual basis, although the extent of reduction depends on the type of crop and the environmental conditions.

Theoretical Limits to Solar Energy Conversion

Both PV and natural photosynthetic systems obey the same fundamental laws of thermodynamics, which impose firm upper bounds on efficiency. There is an extensive literature on each process dating back over 50 years, and although the formulations differ substantially, the overall conclusions are similar. Following pioneering studies by Duysens (*16*), many authors have examined the thermodynamics of photosynthesis, most recently Knox and Parson (*17*). Shockley and Queisser pioneered studies on the maximal efficiency of PV cells (*18*); a recent analysis by Hanna and Nozik considers multiple-junction cells and other modern developments (*19*).

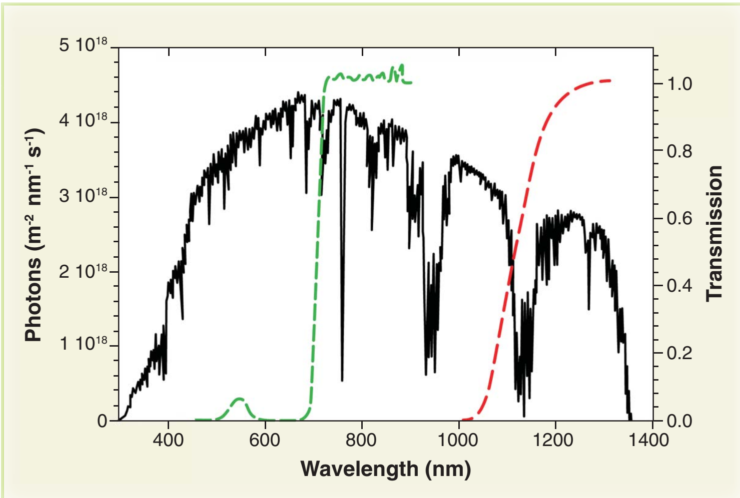

Fig. 1. The photon flux spectrum of solar radiation reaching Earth's surface (plotted in black) (*66*) and the transmission spectra of a natural photosynthetic organism, the cyanobacterium *Synechocystis* PCC 6803 (green dot-dashed line) and of crystalline silicon [red dashed line, redrawn with permission from (*67*)]. The transmission spectra show that both the cyanobacteria and silicon absorb almost all photons at shorter wavelengths above the threshold energy but transmit photons at longer wavelengths below the threshold energy. The cyanobacterial sample has a window of transmission in the green region of the spectrum that causes the culture to appear green. The cyanobacterial sample had an absorbance of 3.4 at 678 nm and was digitally corrected for scattering.

The first step in each system's energy conversion process is light absorption, which is governed by quantum mechanics. Figure 1 shows a reference solar spectrum at the surface of the Earth, with transmission spectra of a cyanobacterium and a silicon cell superimposed. The radiant energy intercepted by the chlorophyll, carotenoids, and other accessory pigments in oxygenic photosynthetic organisms is usually limited to the visible region of the spectrum (400 to 700 nm). Photosynthetic organisms thus access only ~50% of the incident solar energy (*7*, *20*, *21*). The silicon cell has a broader absorption range, extending from the ultraviolet (UV) to nearly 1200 nm in the near-infrared (near-IR).

Thermodynamics furthermore dictates that not all the energy in each absorbed photon can be captured for productive use. Figure 2 shows the relevant energy diagrams. In photosynthetic organisms, absorption initially creates an excited state of chlorophyll or an accessory pigment. Although photons with blue wavelengths may be efficiently absorbed, ultrafast internal conversion processes relax higher excited states through release of heat to the energy of the lowest (redmost) absorption band. Similarly, conventional semiconductor-based PV cells can absorb photons with energy equal to or greater than the bandgap separating the valence-band from the conduction-band, but any photon energy in excess of the bandgap is lost as heat. Thus, both systems have a threshold energy that defines attainable light absorption, conversion efficiency, and energy storage capabilities.

When these considerations are included in a more detailed thermodynamic analysis using the entire solar spectrum, a single-junction PV system has a maximal instantaneous power conversion efficiency of ~32% at one-sun intensity and an AM1.5 spectral distribution, the so-called Shockley-Queisser limit (*18*). The Shockley-Queisser treatment is the isothermal equivalent of the Carnot cycle and assumes that all processes are reversible (no overpotentials, no dissipative losses), with the consequence that extracting chemical or electrical work from the system would be infinitely slow. In a realistic photoelectrolysis cell based on a single-threshold semiconductor photoelectrode (in direct contact with water) that generates hydrogen and oxygen at finite rates, the overvoltage would be finite. At unconcentrated solar intensities, the current density is relatively low (<35 mA cm^{-2}), so that an overvoltage of ~0.15 V is a reasonable assumption; this would decrease the maximum Shockley-Queisser efficiency for a photoelectrolysis cell to ~24% (*19*).

A theoretical limit of ~ 12% for the efficiency of photosynthetic glucose production from CO_2 and water (based on free energy) can be calculated by considering the chlorophyll band-edge absorption and the two-photosystem structure of oxygenic photosynthesis (*6*, *13*). Taking into account the known losses in light harvesting, overpotentials, and respiration, the maximum limit to photosynthetic efficiency is reduced to 4.6 and 6.0% for C3 and C4 plants, respectively (*7*). Short-term (rapid-growth phase) conversion

efficiencies come within 70 to 75% of meeting these limits. The passive diffusion of CO_2 at atmospheric concentration will set a conversion limit for fixation in both photosynthesis and artificial devices. Indeed, dense stands of rapidly photosynthesizing crops such as corn or soybean can lower CO_2 levels within the canopy 50 parts per million (ppm) or more below ambient (*22*), suggesting that CO_2 delivery affects the rate of carbon fixation. Given these constraints, opportunities to enhance photosynthetic productivity lie in the development of plant and microalgal systems that achieve sustained CO_2 fixation at yields close to the theoretical limits. Further productivity gains in both photosynthetic and PV systems could potentially be realized by designing systems that reset the limits to energy conversion as described below.

Improved System Design Raising Theoretical Limits

A key opportunity for raising the efficiency ceiling in PV systems lies in replacing single-junction devices with tandem cells optimized for water oxidation and hydrogen production. This approach could give efficiencies approaching 40% (free energy basis) as overvoltages approach zero (*19*, *23*). Further increases in PV efficiencies might be obtained by devices that use the blue and near-UV region of the solar spectrum more effectively or capture the energy of the sub-bandgap IR photons. Prospects under study include hot-carrier solar cells, intermediate-band solar cells, multijunction tandem architectures, and absorbing media that generate multiple charge carriers per absorbed photon. In these cases, the theoretical thermodynamic limit set by the second law reaches 66% at one-sun intensity (*24*, *25*), with corresponding increases in the yield of electrochemical products.

Turning to photosynthesis, one straightforward strategy for improving the efficiency limit would involve tuning the light-absorbing pigments to extend the range of solar light absorption (*26*). A related, substantial source of inefficiency arises from nature's use of two photochemical systems connected in series to generate the electric potential difference required to split water and reduce nicotinamide adenine dinucleotide phosphate ($NADP^+$). The effective bandgaps (absorption thresholds) of the two photosystems are similar. In practical terms, this means that the two photosystems compete for the same regions of the solar spectrum, cutting the energy efficiency nearly in half compared with what might be achieved if the bandgaps were different and optimized to use different regions of the spectrum (*19*, *27*).

Photosynthesis is unique in its capacity to produce a diverse array of complex organic compounds (leading to replication of the organism) through light-driven CO_2 reduction. There is no PV device that can deliver comparably selective carbon-fixation photochemistry, nor of course can PV devices replicate themselves. Although it can be argued that self-replication represents a real advantage for natural photosynthesis, it is also clear that the structure and function of the photosynthetic apparatus are limited by the need to operate within a living organism, for which they were tailored by evolution. The comparatively low efficiency of natural photosynthesis may result partly from the "legacy biochemistry" photosynthetic organisms inherited from earlier non-photosynthetic organisms that used biochemical pathways with redox cofactors not optimally matched for photochemical processes (*28*). Some factors that limit the efficiency of natural photosynthetic systems are intrinsic to the basic structure and organization of the photosynthetic apparatus and would require a major re-engineering to improve, whereas other improvements may be attained by more straightforward adjustments in the structure of the organisms or the growth conditions. Although this approach may seem daunting, agricultural breeding has been steadily achieving these goals for millennia, albeit primarily for food production, and typically not necessarily for high-efficiency energy storage. Because we have only just started breeding or engineering plants and algae for fuels production, it is likely that substantial improvements are feasible.

Photosynthetic organisms in the wild are selected through evolution for reproductive success, not for high biomass production in plant monocultures in which competition for resources (including light) is, in many cases, a disadvantage (*29*). Likewise, crop plants have been bred for various properties of the harvestable product but not for overall photosynthetic efficiency, while being nurtured by intensive agricultural practices that use substantial inputs of fossil fuels. Consequently, photosynthetic rates are often limited or down-regulated even below the theoretical limits imposed by the slowest reactions of CO_2 fixation and electron transport, leading to strategic down-regulation of productivity. This problem could be alleviated with breeding or engineering, even without radical changes to the photosynthetic apparatus (*7*, *30*). An interesting example of the importance of regulatory strategy is the acclimation of plants to higher CO_2 levels. In principle, the recent increase in atmospheric CO_2 levels should alleviate limitations of photosynthesis at the enzyme ribulose-bisphosphate carboxylase-oxygenase (RuBisCO); however, these gains may not be realized in plants that evolved to use the lower CO_2 levels that prevailed before the industrial revolution (*31*). This lack of acclimation to current and future CO_2 levels, which results in kinetic mismatches among the component processes of photosynthesis, is an obvious target for plant breeding and engineering. Further, cellular growth and maintenance of the organism can also be viewed as a loss of at least 30% of the stored energy (*7*). Part of this energy is used to synthesize large quantities of RuBisCO to compensate for the enzyme's relatively low catalytic rate constant.

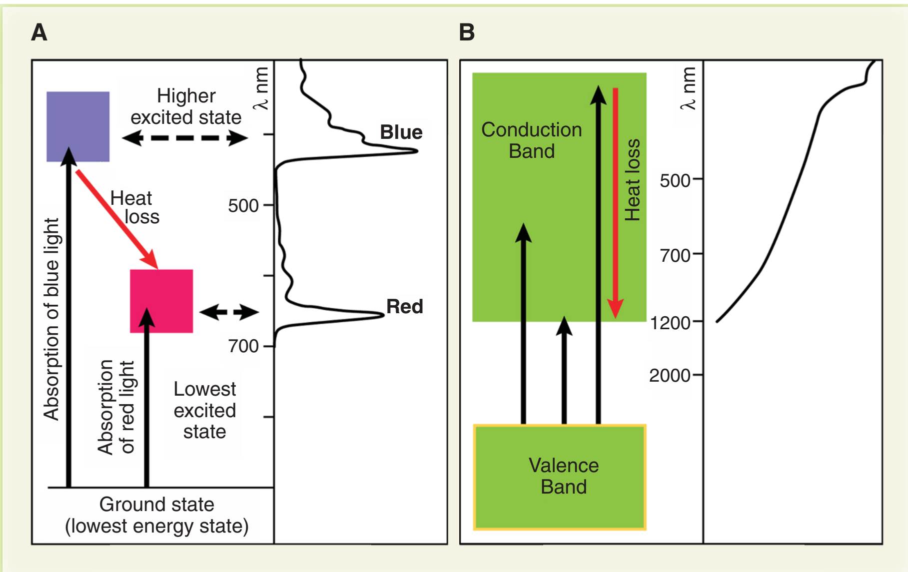

Fig. 2. Comparison of the threshold properties of photosynthetic and silicon-based PV systems. (**A**) Energy-level diagram for chlorophyll *a*, the major pigment found in most oxygenic photosynthetic organisms. The excited state is populated by blue light absorption and rapidly relaxes through heat loss to the energy level accessed by red light absorption, which is the effective threshold for energy storage. An absorption spectrum for chlorophyll *a* is shown for comparison. (**B**) Energy-level diagram for crystalline silicon, which is characteristic of the band structure of a semiconductor. The threshold absorption energy just bridges the bandgap (middle black arrow). Photons with a range of higher energies can still be absorbed, but their energy in excess of the bandgap is lost as heat before it can be stored. An absorption spectrum of silicon is shown for comparison (*67*).

Another instance of inefficiency in natural photosynthesis occurs when RuBisCO fixes the competitive substrate O_2 instead of CO_2, initiating the energy-intensive recovery process of photorespiration (*32*). Photorespiration can consume up to 25% of the initially stored energy (*7*). Some cyanobacteria, algae, and plants have evolved CO_2-concentration processes that largely circumvent photorespiration (*33*, *34*). However, these processes also entail an energetic cost that prevents realization of the entire advantage. In C4 photosynthesis, CO_2 is initially fixed into compounds with four carbon atoms (hence, the term "C4") and subsequently released at high concentrations near RuBisCO, where it competes more effectively with O_2 and reduces the oxygenation reaction substantially (*35*, *36*). Efforts are currently underway to introduce C4 photosynthesis or other carbon-concentrating systems into higher plants where they are currently lacking (*35*). If successful, these efforts may not only increase maximal photosynthetic rates and efficiencies directly but could reduce the large investment of energy and nutrients that C3 plants make in the synthesis of RuBisCO.

The amount of photorespiration can also potentially be reduced by engineering improved versions of RuBisCO with higher specificity for CO_2 over O_2, although this has proven difficult (*36*). A promising approach is the insertion of the *Escherichia coli* pathway for glycolate catabolism into *Arabidopsis* chloroplasts, introducing a bypass of the normal photorespiratory pathway by converting glycolate to glycerate directly in the chloroplast (*7*, *37*). Additionally, natural variants of RuBisCO that are better suited to current and anticipated CO_2 levels may be useful (*38*). Photorespiration also might be virtually eliminated by using flue gases from fossil fuel– or biomass-burning installations (such as power plants) as input gases for microalgal-based photobioreactor systems (*39*). These flue gases typically comprise ~10% CO_2, a concentration sufficient to suppress photorespiration almost completely.

All natural photosynthetic organisms contain light-gathering antenna systems, in which specialized pigments (typically several hundred) collect energy and transfer it to a reaction center where photochemistry takes place (*6*, *40*). With so many pigments absorbing light, full sunlight rapidly exceeds the capacity of the photosynthetic apparatus to process the influx of energy. In leaves in full sun, up to 80% of the absorbed energy must be dissipated or risk causing serious damage to the system (*41*). Plants have evolved a variety of mechanisms for dealing with this excess energy, including non-photochemical quenching pathways to prevent damage (*42*) and repair mechanisms if damage to reaction center proteins has occurred (*43*). However, the consequence is that surface cells exposed to the most light dissipate much of the available energy, whereas cells in lower layers remain starved for light. This overly aggressive capture of light may have an evolutionary advantage (for example, by shading competitors), but it decreases the overall efficiency of energy storage.

To address this issue, research efforts are underway in microorganisms to reduce the size of the antenna system (*44*, *45*). Truncated light-harvesting antennas can simultaneously reduce the problem of saturation at the surface and reduce shading deep in the water column, permitting more uniform illumination of the culture. In crop plants, modifying plant architecture can allow more light to pass to lower levels of the canopy, although lowering the chlorophyll content may be a more robust way to promote light energy distribution and canopy photosynthetic efficiency (*46*).

As noted earlier, plants and algae are generally restricted to absorbing visible light. Some species of cyanobacteria possess variants of chlorophyll that absorb further into the near-IR (740- to 750-nm wavelength range), increasing the amount of solar energy that can potentially be stored (*26*, *47*, *48*). Reducing the size of the antenna as discussed above might make it possible to expand the absorption spectrum without increasing saturation effects.

Synthetic Biology

The techniques of synthetic biology (*49*) may allow a more radical redesign of the photosynthetic apparatus for both bioenergy and food production applications. As mentioned above, the two photosystems required for oxygenic photosynthesis compete for the same wavelengths of light, reducing overall photochemical efficiency. An ambitious modification would be to maintain the two photosystems but engineer one of them to use the bacteriochlorophylls found in many anoxygenic photosynthetic organisms, which have absorption maxima that extend out to ~1100 nm. Figure 3 presents a schematic il-

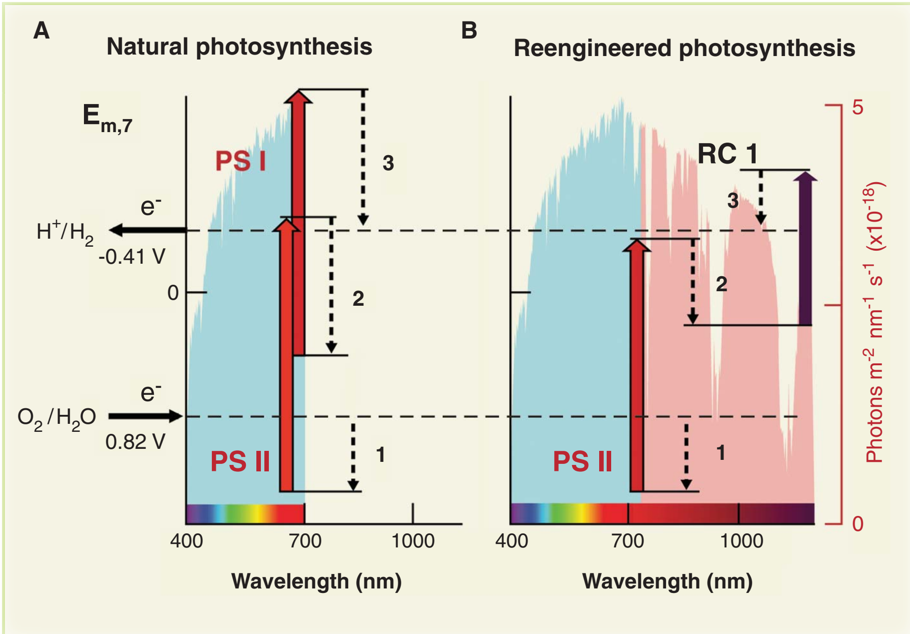

Fig. 3. (**A**) Photoelectrochemical energy capture diagram for photosynthesis and (**B**) photosynthesis reengineered following the thermodynamic principles in (*19*) for improved efficiency. The lengths of the upward arrows mark the initial photoinduced ground-to-excited-state electrochemical energy change of the reaction center primary donor chlorophylls. The position of the arrows along the wavelength axis is fixed by their length and is approximately at the red-most absorption edge of these chlorophylls. In (A), the vertical positions of the bases of the upward arrows reflect the approximate reduction potentials for the radical cation of the primary donor chlorophylls of photosystem I and photosystem II. In (B), the vertical and horizontal positions of the upward arrows are optimized for photosystems operating in tandem and providing 800 mV of overpotential to drive a chemical reaction having ΔG^0 of 1.23 eV that converts solar energy to electrochemical potential. The lengths of the downward dashed arrows indicate intrinsic free-energy losses associated with charge separation and electron transfer between photosystem II and reaction center I (arrow 2) and the overpotential necessary to drive the chemical oxidation-reduction reactions (arrows 1 and 3). In (A), electron transfer between the photosystems (dashed arrow 2) is associated with an energy-conserving ATP-coupling site. The background shows the portion of incident solar photons captured in each case. In (B) reengineered photosynthesis, photosystem I is replaced by a new reaction center, RC1, with farther-red-absorbing pigments. This increases the efficiency of photosynthesis by approximately doubling the solar photon capture and, using this biological version of a tandem cell, better matching the solar spectrum to the electrochemical work. For this illustration, reaction centers using chlorophyll *d* and bacteriochlorophyll *b* would be optimal for driving the redox catalysts.

lustration of a radically redesigned system in which the two photosystems have complementary optical spectra, conferring pseudotandem photocell function. The extent to which true tandem-cell efficiency were achieved would depend on the success of directing energy transfer from antennas absorbing 400- to 730-nm and 730- to ~1100-nm photons to different reaction centers. Wiring each antenna to the appropriate reaction center could potentially take advantage of structures in which exciton coupling or quantum coherence effects direct energy flow more efficiently (*50*). An optimum configuration could mimic a two-junction tandem photovoltaic cell (*19*).

Substantial improvements can be envisaged even within the context of the two-photosystem architecture of current oxygenic photosynthesis. As discussed earlier, for example, the carbon fixation process is currently limited by photorespiration associated with the low substrate selectivity of RuBisCO. Although RuBisCO is found in all oxygenic photosynthetic organisms, it might nonetheless be possible to introduce a different carbon-fixation cycle in place of the Calvin-Benson cycle (*51*, *52*). Most of the known alternative cycles are highly O_2 sensitive and are probably unsuitable for organisms that live in the presence of oxygen. However, the hydroxypropionate cycle found in filamentous anoxygenic phototrophs is not O_2-sensitive (*53*). An alternative is to forego production of reduced carbon storage products and produce H_2 by reduction of H^+. This process can be accomplished by using hydrogenase enzymes (*54*) or platinum nanoparticles (*55*) that are tethered to photosystem I. Because most hydrogenase enzymes are destroyed by O_2, re-engineering this system to be less O_2-sensitive is an important objective (*56*, *57*). In addition, a range of promising, O_2-tolerant transition metal catalysts are being developed (*58*). An intermediate enzymatic approach that is under investigation would treat CO_2 as an electron acceptor but reduce it only to the level of formate by using the enzyme formate dehydrogenase (*59*). The production of either hydrogen or formate may at the same time reduce the problem of light saturation because these systems have intrinsically very high capacity and could be capable of processing the electrons delivered by the reaction centers at a much higher rate than that of the RuBisCO-based C3 carbon-fixation cycle.

Outlook

We have sought here to make the most consistent comparison possible between the fundamental solar energy storage efficiencies of photovoltaic and photosynthetic systems. In this context, the efficiency advantage clearly goes to photovoltaic systems. However, there is clearly need to apply both in the service of sustainable energy conversion for the future. Approaches in which photovoltaics are coupled to redox chemistry in photoelectrochemical cells and even living organisms (*60*, *61*) also hold promise for solar fuels production. Numerous points of inefficiency in the natural system are amenable to improvement by using genetic engineering and more aggressive techniques of synthetic biology.

References and Notes

1. M. I. Hoffert *et al.*, *Science* **298**, 981 (2002).
2. N. S. Lewis, D. G. Nocera, *Proc. Natl. Acad. Sci. U.S.A.* **103**, 15729 (2006).
3. J. Barber, *Chem. Soc. Rev.* **38**, 185 (2009).
4. World Energy Council, www.worldenergy.org/publications/survey_of_energy_resources_2007/solar/720.asp (2007).
5. Committee on America's Future, *America's Energy Future: Technology and Transformation: Summary Edition* (National Academy Press, Washington, DC, 2009).
6. R. E. Blankenship, *Molecular Mechanisms of Photosynthesis*, Blackwell Science, Oxford, UK (2002).
7. X.-G. Zhu, S. P. Long, D. R. Ort, *Annu. Rev. Plant Biol.* **61**, 235 (2010).
8. S. C. Davis, K. J. Anderson-Teixeira, E. H. Delucia, *Trends Plant Sci.* **14**, 140 (2009).
9. A. F. Sherwani, J. A. Usmani, *Renew. Sustain. Energy Rev.* **14**, 540 (2010).
10. M. A. Green, K. Emery, Y. Hishikawa, W. Warta, *Prog. Photovolt. Res. Appl.* **18**, 144 (2010).
11. M. Topic, K. Brecl, J. Sites, Performance assessment of PV modules relationship between STC rating and field performance, in *Conference Record of the 2006 IEEE 4th World Conference on Photovoltaic Energy Conversion, vol. 1 and 2* (IEEE, New York 2006), pp. 2141–2144.
12. C. A. Wraight, R. K. Clayton, *Biochim. Biophys. Acta* **333**, 246 (1974).
13. D. A. Walker, *J. Appl. Phycol.* **21**, 509 (2009).
14. R. H. Wijffels, M. J. Barbosa, *Science* **329**, 796 (2010).
15. M. Janssen, J. Tramper, L. R. Mur, R. H. Wijffels, *Biotechnol. Bioeng.* **81**, 193 (2003).
16. L. N. M. Duysens, *Brookhaven Symp. Biol.* **11**, 10 (1959).
17. R. S. Knox, W. W. Parson, *Biochim. Biophys. Acta* **1767**, 1189 (2007).
18. W. Shockley, H. J. Queisser, *J. Appl. Phys.* **32**, 510 (1961).
19. M. C. Hanna, A. J. Nozik, *J. Appl. Phys.* **100**, 74510 (2006).
20. The 400-to 700-nm spectral range is commonly referred to as photosynthetically active radiation (PAR). This spectral range applies to organisms that carry out oxygenic photosynthesis, in which H_2O is oxidized to O_2 and CO_2 is reduced to sugars. There are also numerous anoxygenic (non-O_2–evolving) phototrophs that use bacteriochlorophyll *b* absorbing out to ~1100 nm (*62*). These organisms primarily drive cyclic electron transfer reactions and only secondarily oxidize reduced substrates such as H_2S.
21. J. R. Bolton, D. O. Hall, *Annu. Rev. Energy* **4**, 353 (1979).
22. N. Buchmann, J. R. Ehleringer, *Agric. For. Meteorol.* **89**, 45 (1998).
23. J. Genovese, K. Harg, M. Paster, J. Turner, Current (2009) state of the art hydrogen production cost estimate using water electrolysis. NREL/BK-6A1-46676, www.hydrogen.energy.gov/pdfs/46676.pdf (2009).
24. N. S. Lewis, G. Crabtree, A. J. Nozik, M. R. Wasielewski, P. Alivisatos, *Basic research needs for solar energy utilization* (U.S. Department of Energy, Office of Basic Energy Sciences, Washington, DC, 2005).
25. M. Green, *Third Generation Photovoltaics* (Springer-Verlag, Berlin, 2003).
26. M. Chen, R. E. Blankenship, *Trends Plant Sci.*, published online 12 April 2011.
27. Two coupled photosystems (large integral membrane pigment-protein complexes) connected in series are needed to carry out the complete oxygenic photosynthetic process. Photosystem II oxidizes H_2O and produces O_2 and a weak reductant, whereas photosystem I oxidizes a weak reductant and reduces $NADP^+$ to NADPH, which along with adenosine 5′-triphosphate (ATP) provides the free energy for the Calvin-Benson carbon fixation cycle. The theoretical minimum quantum requirement (the inverse of the quantum yield) for the complete photosynthetic process leading to production of one molecule of O_2 is 8 because each photosystem transfers one electron per photon absorbed, and the oxidation of H_2O to O_2 is a four-electron process. Experimental values for quantum requirements for O_2 evolution under optimal laboratory conditions are 9 to 10 (*63–65*).
28. D. Gust, D. Kramer, A. Moore, T. A. Moore, W. Vermaas, *MRS Bull.* **33**, 383 (2008).
29. N. P. R. Anten, *Ann. Bot. (Lond.)* **95**, 495 (2005).
30. C. A. Raines, *Photosynth. Res.* **75**, 1 (2003).
31. S. P. Long, X.-G. Zhu, S. L. Naidu, D. R. Ort, *Plant Cell Environ.* **29**, 315 (2006).
32. C. H. Foyer, A. J. Bloom, G. Queval, G. Noctor, *Annu. Rev. Plant Biol.* **60**, 455 (2009).
33. M. Giordano, J. Beardall, J. A. Raven, *Annu. Rev. Plant Biol.* **56**, 99 (2005).
34. M. R. Badger, G. D. Price, *J. Exp. Bot.* **54**, 609 (2003).
35. J. M. Hibberd, S. Covshoff, *Annu. Rev. Plant Biol.* **61**, 181 (2010).
36. R. J. Spreitzer, M. E. Salvucci, *Annu. Rev. Plant Biol.* **53**, 449 (2002).
37. R. Kebeish *et al.*, *Nat. Biotechnol.* **25**, 593 (2007).
38. X.-G. Zhu, A. R. Portis Jr., S. P. Long, *Plant Cell Environ.* **27**, 155 (2004).
39. R. T. Sayre, *Bioscience* **60**, 722 (2010).
40. B. R. Green, W. W. Parson, Eds., *Light-Harvesting Antennas in Photosynthesis, vol. 13* (Kluwer, Dordrecht, Netherlands, 2003).
41. A. Melis, *Plant Sci.* **177**, 272 (2009).
42. N. R. Baker, *Annu. Rev. Plant Biol.* **59**, 89 (2008).
43. W. Sakamoto, *Annu. Rev. Plant Biol.* **57**, 599 (2006).
44. J. H. Mussgnug *et al.*, *Plant Biotechnol. J.* **5**, 802 (2007).
45. M. Mitra, A. Melis, *Opt. Express* **16**, 21807 (2008).
46. D. R. Ort, Xo Zhu, A. Melis, *Plant Physiol.* **155**, 79 (2011).
47. H. Miyashita *et al.*, *Nature* **383**, 402 (1996).
48. M. Chen *et al.*, *Science* **329**, 1318 (2010).
49. D. F. Savage, J. Way, P. A. Silver, *ACS Chem. Biol.* **3**, 13 (2008).
50. G. S. Engel *et al.*, *Nature* **446**, 782 (2007).
51. R. K. Thauer, *Science* **318**, 1732 (2007).
52. A. Bar-Even, E. Noor, N. E. Lewis, R. Milo, *Proc. Natl. Acad. Sci. U.S.A.* **107**, 8889 (2010).
53. J. Zarzycki, V. Brecht, M. Müller, G. Fuchs, *Proc. Natl. Acad. Sci. U.S.A.* **106**, 21317 (2009).
54. M. Ihara, H. Nakamoto, T. Kamachi, I. Okura, M. Maeda, *Photochem. Photobiol.* **82**, 1677 (2006).
55. L. M. Utschig *et al.*, *J. Phys. Chem. Lett.* **2**, 236 (2011).
56. P. M. Vignais, B. Billoud, *Chem. Rev.* **107**, 4206 (2007).
57. M. L. Ghirardi *et al.*, *Annu. Rev. Plant Biol.* **58**, 71 (2007).
58. J. L. Dempsey, B. S. Brunschwig, J. R. Winkler, H. B. Gray, *Acc. Chem. Res.* **42**, 1995 (2009).
59. T. Reda, C. M. Plugge, N. J. Abram, J. Hirst, *Proc. Natl. Acad. Sci. U.S.A.* **105**, 10654 (2008).
60. K. P. Nevin, A. E. Woodard, A. E. Franks, Z. M. Summers, D. R Lovley, *mBio* **1(2)**, e00103 (2010).
61. J. J. Kan, L. Hsu, A. C. M. Cheung, M. Pirbazari, K. H. Nealson, *Environ. Sci. Technol.* **45**, 1139 (2011).
62. R. E. Blankenship, M. T. Madigan, C. E. Bauer, Eds., *Anoxygenic Photosynthetic Bacteria* (Kluwer Academic Publishing, Dordrecht, Netherlands, 1995).
63. R. Emerson, *Annu. Rev. Plant Physiol.* **9**, 1 (1958).
64. A. C. Ley, D. C. Mauzerall, *Biochim. Biophys. Acta* **680**, 95 (1982).
65. J. B. Skillman, *J. Exp. Bot.* **59**, 1647 (2008).
66. A. S. T. M. Standard, G173-03 (2008), Standard tables for reference solar spectral irradiances: Direct normal and hemispherical on 37° tilted surface (10.1520/G0173-03R08), available online: www.astm.org/Standards/G173.htm, http://rredc.nrel.gov/solar/spectra/am1.5.
67. G. E. Jellison, F. A. Modine, *J. Appl. Phys.* **53**, 3745 (1982).

68. This article evolved from presentations and discussions at the workshop "What is the Efficiency of Photosynthesis?" held in May 2009 in Albuquerque, New Mexico, sponsored by the Council on Chemical and Biochemical Sciences of the U.S. Department of Energy, Office of Science, Office of Basic Energy Sciences. The authors thank the members of the Council for their encouragement and assistance in developing this workshop. In addition, the authors are indebted to the agencies responsible for funding their individual research efforts, without which this work would not have been possible.

10.1126/science.1200165

Clonogenic Neoblasts Are Pluripotent Adult Stem Cells That Underlie Planarian Regeneration

Daniel E. Wagner,[1]* Irving E. Wang,[1]* Peter W. Reddien[1]†

Pluripotent cells in the embryo can generate all cell types, but lineage-restricted cells are generally thought to replenish adult tissues. Planarians are flatworms and regenerate from tiny body fragments, a process requiring a population of proliferating cells (neoblasts). Whether regeneration is accomplished by pluripotent cells or by the collective activity of multiple lineage-restricted cell types is unknown. We used ionizing radiation and single-cell transplantation to identify neoblasts that can form large descendant-cell colonies in vivo. These clonogenic neoblasts (cNeoblasts) produce cells that differentiate into neuronal, intestinal, and other known postmitotic cell types and are distributed throughout the body. Single transplanted cNeoblasts restored regeneration in lethally irradiated hosts. We conclude that broadly distributed, adult pluripotent stem cells underlie the remarkable regenerative abilities of planarians.

Pluripotent cells, such as embryonic blastomeres, differentiate into mature cell types spanning three germ layers (*1*–*3*). Although essential for development, pluripotent cells are generally not known to be present in adult animals (*4*, *5*). Adult tissues, in contrast, are typically maintained by specialized, tissue-specific adult stem cells (*5*–*11*). Planarians are flatworms well known for the ability to regenerate whole animals from small pieces of tissue (*12*). Planarian regeneration requires a population of proliferative cells, historically known as neoblasts, that exist throughout the body and collectively produce all known differentiated cell types (*13*, *14*). Neoblasts have great potential for molecular genetic studies in *Schmidtea mediterranea*, in which a sequenced genome and molecular tools (including RNA interference technology) enable the identification and study of genes controlling regeneration (*14*, *15*). To date, however, neoblast properties have only been studied at the level of a population (*14*, *16*–*21*). The cell population known as neoblasts, therefore, could either contain only lineage-restricted cells that together allow regeneration or could contain, within the population, stem cells that are pluripotent at the single-cell level. A fundamental issue to address for understanding planarian regeneration, therefore, is the in vivo potential of individual proliferating planarian cells.

Colonies are generated from single *smedwi-1*$^+$ cells after irradiation. With the use of ionizing radiation, we developed an in vivo method that permits the study of rare, individual proliferating cells and their descendants (*22*). Irradiation eliminates dividing cells and is a classic strategy for studying stem cells (*23*, *24*). All dividing cells in adult planarians express the *smedwi-1* gene (Fig. 1A) (*25*); these cells are specifically, rapidly, and completely depleted after exposure to high irradiation doses (for example, 6000 rad) (*17*, *25*, *26*). Low irradiation doses (such as 500 rad) eliminate some proliferating cells, leaving a large number spread ventrally throughout the animal (*19*). We identified an irradiation dose (1750 rad) that eliminated all *smedwi-1*$^+$ cells from most (78%) animals (Fig. 1B). However, 7 days after 1750-rad exposure, rare *smedwi-1*$^+$ cells were present in the minority of animals (22%) as sparse "clusters" (Fig. 1, B and C). Clusters consistently displayed compact, isolated, colonylike morphology and originated ventrally throughout the body (Fig. 1D and fig. S1, A to C) but were not associated with specific known tissues (fig. S1, D and E). If resulting from clonal growth of single *smedwi-1*$^+$ cells, these clusters provide the opportunity to study the developmental potential of individual planarian cells.

Numerous *smedwi-1*$^+$ cluster attributes indicate they result from clonal growth. *smedwi-1*$^+$ clusters were preceded by isolated *smedwi-1*$^+$ cells present 3 to 4 days after irradiation and typically displayed 3 to 10 cells after one week (Fig. 1, E and F). Based on the low proportion of animals with *smedwi-1*$^+$ cells in close proximity 3 days post-irradiation with 1750 rad (fig. S2), it is improbable that clusters arose from multiple adjacent *smedwi-1*$^+$ cells ($P = 0.0138$, two-tailed Fisher's exact test). Cluster size increased dramatically over time, suggesting exponential growth and ultimately yielding hundreds of *smedwi-1*$^+$ cells 14 to 18 days post-irradiation (Fig. 1, E and F). Consistent with clusters originating from preexisting *smedwi-1*$^+$ cells that survived irradiation, a cluster-location scatter plot resembled the normal *smedwi-1*$^+$ expression pattern (Fig. 1D), and cluster frequency decreased with increasing irradiation doses (see below). Bromodeoxyuridine (BrdU) delivery labels *smedwi-1*–expressing cells (fig. S3A) (*25*), followed by a rapid decline in incorporation within 24 to 48 hours (fig. S3, B to D) (*17*), demonstrating that unincorporated BrdU does not persist over the long term. A BrdU pulse followed by irradiation resulted in clusters consisting entirely of BrdU$^+$; *smedwi-1*$^+$ cells (fig. S3E), indicating that *smedwi-1*$^+$ cluster expansion results from division of existing *smedwi-1*$^+$ cells (i.e., by clonal growth). If some other process, such as dedifferentiation, had produced *smedwi-1*$^+$ cluster cells, these cells should have been BrdU$^-$.

After irradiation, every proliferative cell detected by an 8-hour BrdU pulse (Fig. 1G)—or by using probes for the conserved proliferation marker genes *histone h2b* (*Smed-h2b*) (*27*), *pcna* (*Smed-pcna*) (*28*), or *ribonucleotide reductase* (*Smed-RRM2-1*) (fig. S3, F to H) (*17*, *29*)—existed in clusters and expressed *smedwi-1* (n = 815/815 cells). Therefore, no other source (non-*smedwi-1*$^+$) for proliferating cells exists outside of *smedwi-1*$^+$ clusters in irradiated animals. Furthermore, if additional sources for *smedwi-1*$^+$ cells (other than clonal growth) existed, the cluster number would be expected to increase with time and small, newly formed clusters might be present at late time points after irradiation. Neither of these possibilities was observed (Fig. 1F). New cluster production was also not observed after amputation or feeding (fig. S4), which elicit proliferative responses (*30*, *31*). These data indicate that clonal expansion (producing colonies) represents the source of new *smedwi-1*$^+$ dividing cells during cluster formation and growth.

Not all proliferating cells (neoblasts) necessarily have the capacity to form colonies. We term cells displaying this capacity "clonogenic neoblasts" (cNeoblasts); these cells express *smedwi-1*, have a body-wide (head-to-tail) distribution (Fig. 1D), and generate large, expanding colonies of *smedwi-1*$^+$ cells. The ability of small numbers of colonies to ultimately restore both *smedwi-1*$^+$ cells and mitotic activity to normal levels (fig. S5) suggests a stem cell–like capacity for self-renewal.

To investigate the potential of individual cNeoblasts, we used three well-established differentiation assays involving a SMEDWI-1 antibody (*25*, *30*, *32*), BrdU pulse-chase (*17*, *18*, *32*), and postmitotic cell type markers (*17*, *30*, *32*, *33*) to analyze *smedwi-1*$^+$ colonies. SMEDWI-1 protein is present in *smedwi-1* mRNA$^+$ dividing cells and temporarily remains detectable in postmitotic descendant cells (*25*). Therefore, differentiating cells transit through a SMEDWI-1(protein)$^+$; *smedwi-1*(mRNA)$^-$ state (*30*, *32*). All colonies examined (n = 12/12 colonies) contained SMEDWI-1$^+$; *smedwi-1*$^-$ cells (Fig. 1H). Independently, BrdU can label cells that divide and exit the *smedwi-1*$^+$ state. All colonies analyzed by 4-day BrdU pulse-chase (n = 31/31 colonies) contained BrdU$^+$;

[1]Howard Hughes Medical Institute, Department of Biology, Massachusetts Institute of Technology (MIT), Whitehead Institute for Biomedical Research, 9 Cambridge Center, Cambridge, MA 02142, USA.

*These authors contributed equally to this work.
†To whom correspondence should be addressed. E-mail: reddien@wi.mit.edu

$smedwi\text{-}1^{-}$ cells (Fig. 2), and no $BrdU^{+}$ cells existed in worms lacking $smedwi\text{-}1^{+}$ colonies (n = 25/25 animals), indicating that colonies produce and are the only source for cells exiting the $smedwi\text{-}1^{+}$ undifferentiated state. $SMEDWI\text{-}1^{+}$ or $BrdU^{+}$ colony cells can thus be assessed for lineage-specific marker expression to determine the developmental potential of individual cNeoblasts.

cNeoblasts display broad differentiation capacity. Described adult stem cells typically produce only differentiated cells corresponding to their germ layer and tissue of origin (*5*). To address whether cNeoblasts, in contrast, could produce cell types derived from multiple germ layers, we identified and characterized markers for neuronal (ectoderm-derived) and intestinal (endoderm-derived) lineages. In untreated animals, some $SMEDWI\text{-}1^{+}$ descendant cells expressed a choline acetyl-transferase ortholog, *Smed-chat* (fig. S6); *chat* expression is widely conserved in cholinergic neurons (*34*). $SMEDWI\text{-}1^{+}$; $chat^{+}$ cells were enriched in brain regions and had neuronal morphology, and $chat^{+}$ cells coexpressed additional neuronal markers (fig. S6), indicating that $SMEDWI\text{-}1^{+}$; $chat^{+}$ cells are differentiating neurons. *Smed-gata4/5/6* and *Smed-hnf4*, orthologs of endoderm-promoting GATA4/5/6 and HNF4 transcription factors, respectively (*35*), were expressed in intestinal cells and also in interspersed cells surrounding the intestine (figs. S7 to S10). Many of these interspersed cells were irradiation-sensitive and $SMEDWI\text{-}1^{+}$, indicating that they represent differentiating endodermal cells (figs. S8 and S10). A third endoderm marker gene, *Smed-mat*, was expressed in intestinal branches (figs. S8 and S10). Finally, additional differentiation marker genes (*Smed-AGAT-1*, NB.21.11E, *Smed-MCP-1*, *Smed-ODC-1*, *Smed-CYP1A1-1*, and NB.52.12F) are expressed in partially overlapping mesenchymal populations of postmitotic cells (fig. S11, A to F) (*17*). These populations have unknown lineage relationships but turn over rapidly and are consequently depleted after irradiation (fig. S11, G to L) (*17*).

Using the SMEDWI-1 antibody to label colony cell descendants, we examined individual colonies for the presence of both $gata4/5/6^{+}$ and $chat^{+}$, both $gata4/5/6^{+}$ and $AGAT\text{-}1^{+}$, or both $AGAT\text{-}1^{+}$ and $chat^{+}$ differentiating cells. In nearly all cases (n = 20/22 colonies), individual colonies contained newly produced cells of both lineages that we tested (Fig. 2, A to C and fig. S12). The 1750-rad dose yields rare, well-separated colonies (Fig. 1C); animals fixed 7 days after irradiation contained single colonies (n = 12/28 animals), no colonies (n = 12/28 animals), and, only rarely, more than one colony (n = 4/28 animals). Given the high frequency of colonies producing multiple lineages (n = 20/22 colonies), it is improbable that all such cases were the result of multiple colonies merging ($P < 0.0001$, Fisher's exact test). In addition, we used a 4-day BrdU pulse chase as an independent method to identify several colonies containing both $BrdU^{+}$; $chat^{+}$ (neuronal) and $BrdU^{+}$; mat^{+} (intestinal) cells (Fig. 2D). Nearly all colonies examined, using the SMEDWI-1 antibody or BrdU, produced differentiated cells for any single lineage analyzed (n = 61/64 colonies) (fig. S13). These colonies were distributed throughout the body and not restricted to specific anatomical regions (Fig. 2E). Finally, nearly every $smedwi\text{-}1^{+}$ colony examined had associated cells expressing every additional differentiation marker that we tested (NB.21.11E, *MCP-1*, *ODC-1*, *CYP1A1-1*, NB.52.12F, *AGAT-1*) (n = 110/115 colonies) (fig. S14, A to F). Furthermore, descendant cell clusters were never observed in regions lacking $smedwi\text{-}1^{+}$ colonies (fig. S11, G to L). In addition, even early colonies (7 days post-irradiation) had associated differentiated cells (fig. S14G). Together, these data indicate that broad multipotency and a body-wide distribution are fundamental attributes of individual cNeoblasts.

Small numbers of cNeoblasts restore regenerative ability. Irradiated planarians cannot regenerate (*36*) and suffer massive tissue loss because of failed replacement of aged differentiated cells (*36*, *37*). However, transplantation of large numbers of cells (*16*) or tissue fragments can restore regenerative ability to irradiated hosts and change sexual behavior to that of the donor (*16*, *20*, *21*, *38*). We sought to determine whether small numbers of cNeoblasts would restore regenerative ability to irradiated animals. After irradiation, some animals were fixed and colony

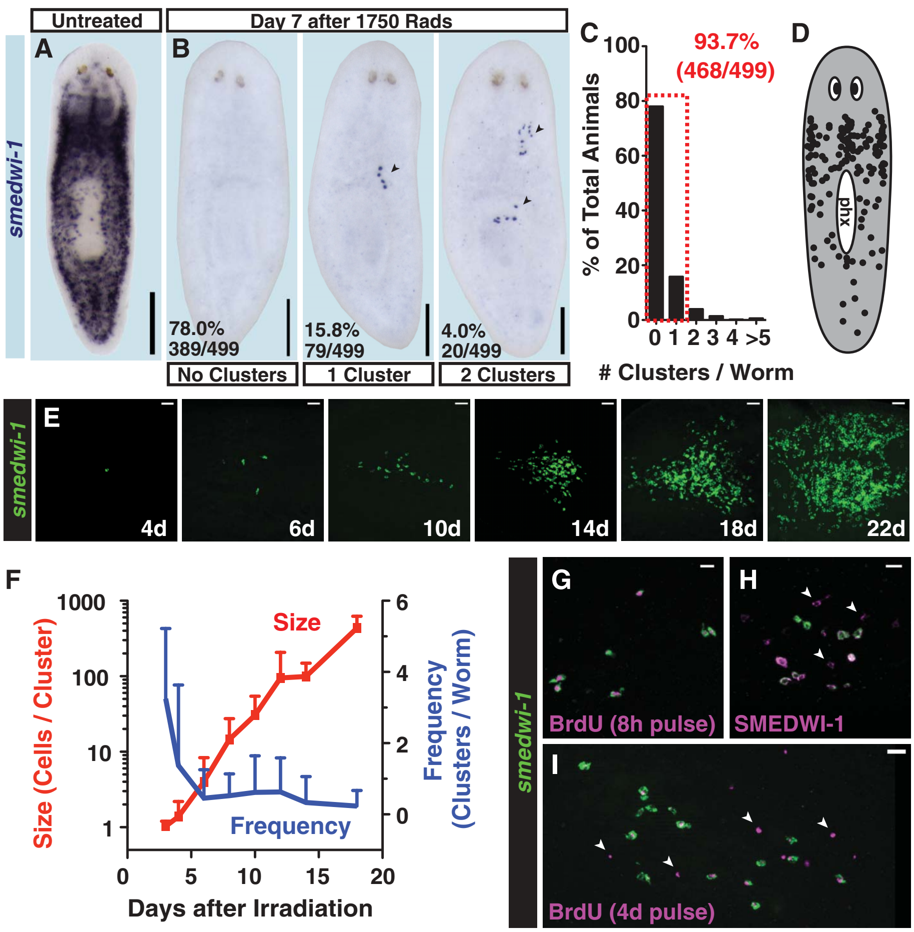

Fig. 1. Expanding colonies are generated from isolated $smedwi\text{-}1^{+}$ cells after irradiation. (**A** and **B**) Proliferating cells were detected by *smedwi-1* expression using whole-mount in situ hybridization (ISH). Anterior, up; ventral surface shown. (B) Representative images 7 days after 1750-rad treatment show clusters (arrowheads) of $smedwi\text{-}1^{+}$ cells (individual purple dots). (**C**) Histogram of cluster frequencies after 1750-rad treatment. The dashed red box indicates that the majority of animals contained either zero or one cluster. (**D**) Clusters observed by *smedwi-1* ISH 7 days post–1750-rad treatment displayed in a scatter plot. phx, pharynx. (**E** and **F**) Animals fixed in a time course after 1750-rad treatment analyzed by *smedwi-1* fluorescence in situ hybridization (FISH). d, days. (F) Mean cluster frequency (number of clusters per worm) and size (number of $smedwi\text{-}1^{+}$ cells per cluster) are plotted. Error bars indicate SD (n = 17 to 22 animals per time point). (**G**) Immunofluorescence (IF) (BrdU) and FISH (*smedwi-1*). 234/234 $BrdU^{+}$ cells (8-hour BrdU pulse in 7-day–irradiated worms) were *smedwi-1* positive. (**H**) IF (SMEDWI-1) and FISH (*smedwi-1*); 12/12 colonies contained $SMEDWI\text{-}1^{+}$; $smedwi\text{-}1^{-}$ cells (arrowheads) 7 days post–1750-rad treatment. (**I**) IF (BrdU) and FISH (*smedwi-1*). 31/31 colonies (with BrdU pulse days 7 to 11 post-1750 rad) contained $BrdU^{+}$; $smedwi\text{-}1^{-}$ cells. Scale bars, 200 μm [(A) and (B)]; 20 μm [(E) and (G) to (I)].

numbers determined; the remaining animals were followed to assess survival and regeneration frequencies. Increasing irradiation doses resulted in decreasing colony numbers (Fig. 3, A and B) and survival rates (fig. S15A). Regeneration, which involves the production of diverse cell types (fig. S16), was initially impeded in animals cut 4 days post-irradiation (fig. S15, B and C); however, many animals both survived and ultimately regenerated at doses that produced sparse, measurable colony numbers (Fig. 3, A to D and table S1). These animals regenerated heads containing neurons (ectoderm), muscle (mesoderm), and intestine (endoderm) (Fig. 3, D and E). The minimum number of cNeoblasts initially present in irradiation survivors can be estimated by comparing the number of colonies present (in fixed animals) to observed regeneration frequencies (see table S1). Our data indicate as few as three ($P = 0.0478$), four ($P = 0.0017$), or five colonies ($P < 0.0001$, Fisher's exact test) can be sufficient to restore regenerative ability to entire animals.

Transplantation of individual cNeoblasts. To determine whether a single cNeoblast can generate all essential adult cells, we developed a method for isolating and transplanting individual cNeoblasts into lethally irradiated hosts. Previous flow cytometry studies identified an irradiation-sensitive cell population (the X1 fraction) with a high percentage of *smedwi-1*$^+$ cells (*26*, *39*). However, the Hoechst 33342 DNA dye used in this method is cytotoxic. Therefore, size and complexity properties of cells within the X1 fraction were used to define a gate for sorting unlabeled cells, which we refer to as the X1(FS) fraction (Fig. 4, A and B).

X1(FS) cells are heterogeneous; however, cells with a similar morphology to X1 cells can be identified microscopically (Fig. 4C). Single selected cells were loaded into needles and transplanted postpharyngeally into lethally irradiated hosts (Fig. 4D). To confirm that only single cells were transplanted, needles were loaded and the contents expelled into media. In all cases, only a single cell was observed exiting the needle (n = 136/136 test ejections). Furthermore, some animals were fixed immediately after transplant and labeled with a *smedwi-1* RNA probe. All injected animals had either one (n = 20/60 animals) or zero (n = 40/60 animals) *smedwi-1*$^+$ cells (Fig. 4, E and F).

If a transplanted cell was a cNeoblast capable of engraftment, then clonal growth of progeny cells would be expected. Indeed, animals examined 6 days after single-cell transplantation displayed clusters with 1 to 13 *smedwi-1*$^+$ cells (n = 23/100 animals) (Fig. 4G). Furthermore, selecting for X1(FS) cells that were approximately 10 μm in diameter and had blebs and/or cytoplasmic processes increased engraftment rates, which ranged from 12% (n = 2/17 animals) to 75% (n = 15/20 animals) (fig. S17). Cells with properties of cNeoblasts, therefore, are present in the X1(FS) fraction and can be successfully transplanted.

If cNeoblasts are pluripotent stem cells capable of self-renewal, then a single cNeoblast should, in principle, be capable of restoring tissue turnover and regenerative capacity to lethally irradiated hosts. However, for this to occur the irradiated host must survive long enough for the cNeoblast to repopulate the *smedwi-1*$^+$ population and replenish dying tissue. Therefore, we used a sexual *S. mediterranea* strain (S2F1L3F2) that can survive longer than the asexual strain (CIW4) after a 6000-rad irradiation dose (fig. S18). Sexual hosts transplanted with single asexual cells had colonies consisting of large numbers of SMEDWI-1$^+$ cells 30 days after transplantation (n = 4/17 animals) (Fig. 4H). Every colony examined contained SMEDWI-1$^+$; *Smed-gata4/5/6*$^+$ double-positive cells (n = 4/4 colonies), and most of these colonies also contained SMEDWI-1$^+$; *Smed-chat*$^+$ double-positive cells (n = 3/4 colonies) (Fig. 4H). Transplant data thus independently confirm attributes of colonies described post–1750 rad, further indicating that clonal growth and multipotency are important features of individual cNeoblasts.

Entire animals and strains regenerated from a single transplanted cNeoblast. Two weeks after irradiation, lesions appeared at sexual animal head tips, followed by progressive anterior-to-posterior tissue regression with 100% penetrant animal death after approximately 6 weeks (n = 78/78 animals) (Fig. 5A). Remarkably, several transplant recipients lived past 7 weeks and eventually developed blastemas at the site of tissue regression (n = 7/130 animals) (Fig. 5A). Animals that developed blastemas regenerated anterior and mid-body structures, such as photoreceptors and pharynges (Fig. 5A), and regained feeding behavior by 8 weeks after irradiation. Of the seven rescued animals, three were expanded into strains (R1, R2, and R3) by serial amputation

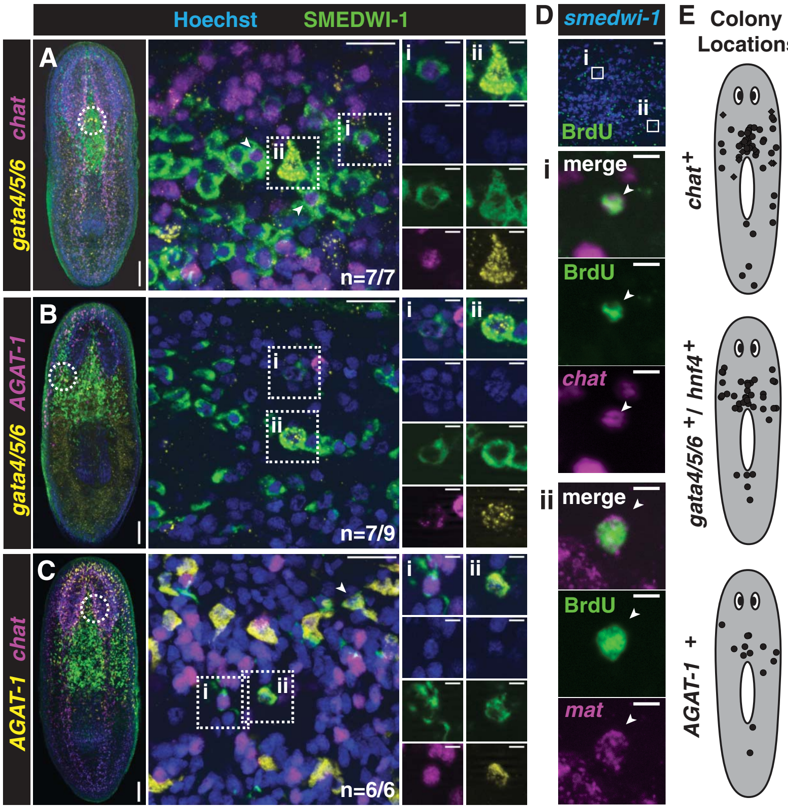

Fig. 2. Clonogenic neoblasts display broad differentiation capacity. (**A** to **C**) Triple-labeling of individual colonies 22 days after irradiation. Projections through optical sections from irradiated animals are shown here. (Left) Tiled images (images from overlapping regions assembled) of representative animals with individual colonies (anterior, up). Dotted circles indicate the approximate location of regions imaged at high magnification (middle panels); the middle images are optical sections with anterior to the right. Example differentiating cells from individual colonies labeled by IF (SMEDWI-1) and double FISH for *gata4/5/6* and *chat* (A), *gata4/5/6* and *AGAT-1* (B), or *AGAT-1* and *chat* (C) are shown. Proportions of colonies displaying multiple differentiating cell types are indicated. Roman numerals indicate double-positive cells, with individual channels shown in columns to the right. Additional double-positive cells are indicated by arrowheads (see also fig. S12). (**D**) IF (BrdU) and double FISH (*Smed-chat; Smed-mat*) worms with BrdU-pulse days 14 to 18 after irradiation. Single colonies (n = 7/7 colonies) contained both BrdU$^+$; *chat*$^+$ (neuronal) and BrdU$^+$; *mat*$^+$ (intestinal) descendants. Boxes indicate zoomed-in regions. (**E**) Scatter plots showing locations of individual colonies producing differentiated cell types (see also fig. S13). Colony cell differentiation was assessed by labeling with SMEDWI-1 (circles) or BrdU (diamonds). Scale bars, (A to C) left, 100 μm; middle 20 μm; right 5 μm; (D) top image, 20 μm; others, 5 μm.

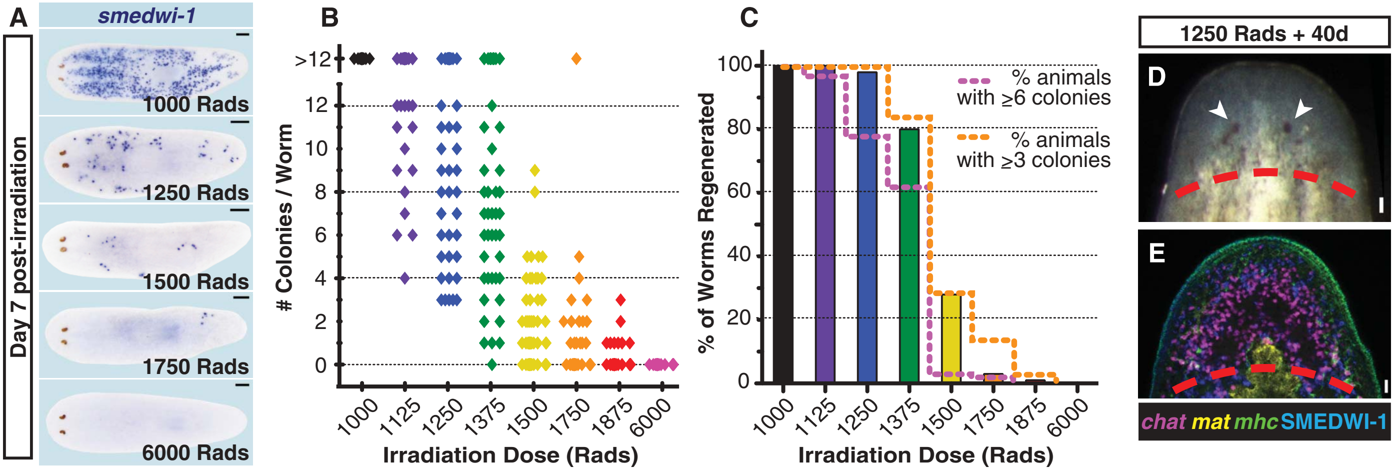

Fig. 3. Small numbers of cNeoblasts can restore tissue turnover and regenerative ability. (**A** and **B**) Animals were irradiated at different doses. Some of these animals were fixed 7 days post-irradiation (1000 rad, 25 animals; between 1125 and 1875 rad, >38 animals per dose; for 6000 rad, 26 animals) and labeled by *smedwi-1*$^{+}$ ISH. (A) Representative *smedwi-1*$^{+}$ ISH images. Anterior, left. (B) Colony numbers per worm are plotted (each dot represents one animal). (**C**) Percentage of animals with restored regeneration after irradiation is shown [≥98 worms per dose were examined; animals were from the same irradiated cohort as in (A) and (B)]. Data indicate that three or more cNeoblasts were sufficient to restore regeneration (see also table S1). (**D**) Normal head regeneration in 97/99 worms amputated 39 or 40 days after 1250-rad treatment. Arrowheads denote photoreceptors. (**E**) Heads regenerated after irradiation contained differentiated neuronal (*chat*$^{+}$), intestinal (*mat-1*$^{+}$), and muscle (*mhc-1*$^{+}$) cells (41/41 worms, 1250 rad; 15/15 worms, 1500 rad). SMEDWI-1^{+} cells were also restored (n = 9/9 worms, 1250 rad). Dotted lines denote the approximate amputation plane. Scale bars, 200 μm (A); 20 μm [(D) to (E)].

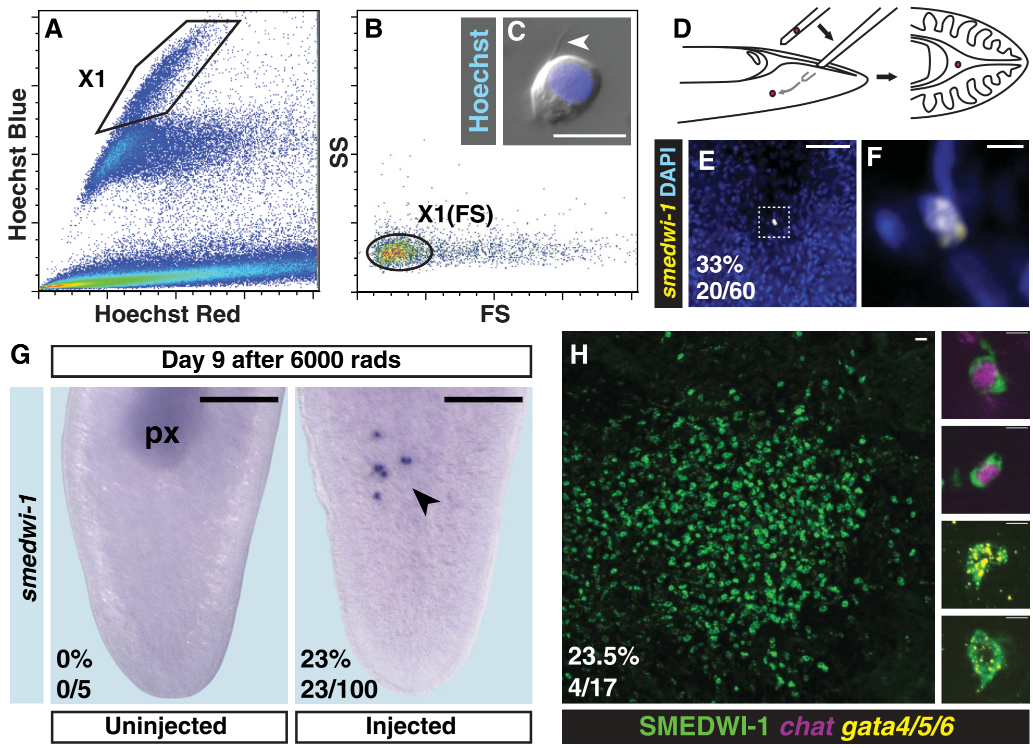

Fig. 4. Single transplanted cNeoblasts display properties of clonal growth and multipotency. Irradiation-sensitive cells (polygonal gate) were identified by Hoechst 33342 labeling (**A**) and back-gated to set the X1(FS) gate (oval) based on size (FS) and complexity (SS) parameters (**B**). The X1(FS) fraction is heterogeneous and contains some cells approximately 10 μm in diameter with processes (arrowhead) (**C**). (**D**) Individual cells were loaded into needles (one needle used per injection) and transplanted into the medial, postpharyngeal, parenchymal space of hosts. (**E** and **F**) FISH (*smedwi-1*) of a host immediately after transplantation. Anterior, up. The ventral surface is shown. Zero (n = 40/60 animals) or one (n = 20/60 animals) *smedwi-1*$^{+}$ cells were observed in all cases, with expected size and morphology. (F) is a zoomed-in image of (E). (**G**) Colony formation 9 days after irradiation, 6 days after transplant. Anterior, up. The ventral surface is shown. Colonies of *smedwi-1*$^{+}$ cells (arrowhead) appeared in transplant recipients (n = 23/100 animals) but not in untreated animals (n = 0/5 animals). px, pharynx. (**H**) IF (SMEDWI-1) and double FISH (*Smed-gata4/5/6*; *Smed-chat*) 33 days after irradiation, 30 days after transplant. Single colonies were observed (n = 4/17 animals); example differentiating cells from displayed colony are shown. Scale bars, 10 μm (C); 50 μm (E); 5 μm (F) and zoomed images in (H); 20 μm (H); 200 μm (G).

and regeneration (fig. S19). These animals exhibited normal blastema formation and the capacity to regenerate photoreceptors and intestine after amputation (Fig. 5B). The ability to produce multiple regenerating animals from a single transplanted cell indicates a self-renewing capability of cNeoblasts. Rescued strains did not display sexual features, such as large size and a gonopore; in contrast, animals in all three strains reproduced by binary fission, an asexual behavior seen very rarely in sexual animals (fig. S19).

To confirm that all new tissue in rescued strains resulted from clonal division from the donor cNeoblast, we genotyped the animals using single-nucleotide polymorphisms (SNPs) identified between the asexual strain and the sexual strain (*22*). Genomic DNA was isolated from strain R1, R2, and R3 animals after two rounds of regeneration; growth and regeneration should replace host tissues with donor-derived cells (Fig. 6A). If, on the other hand, host cells continue to replenish tissues

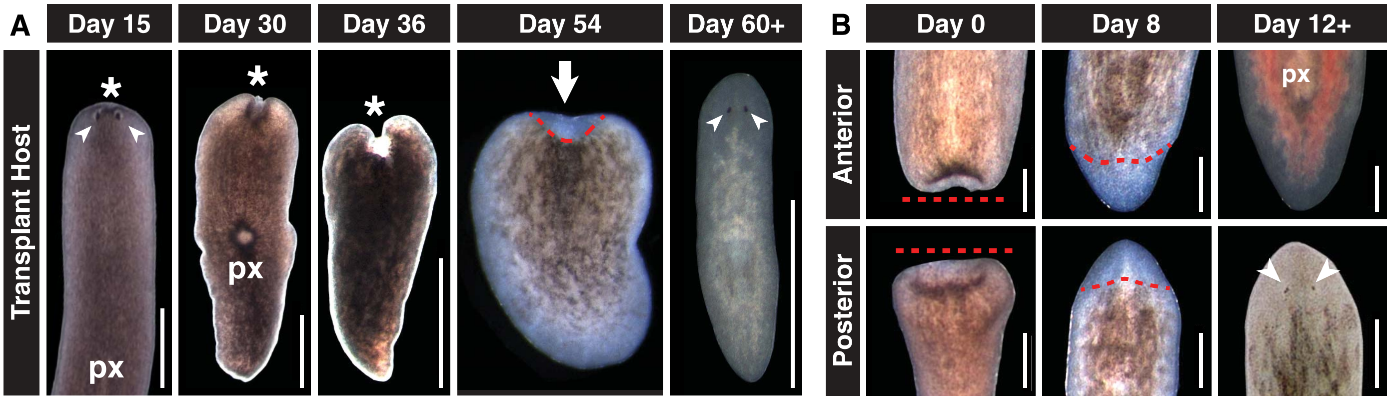

Fig. 5. Restoration of regeneration in lethally irradiated hosts by single transplanted cNeoblasts. (**A**) Representative images of transplant hosts. Tissue regression (asterisks) began anterior to photoreceptors (arrowheads) and progressed from anterior to posterior (px, pharynges). Rescued animals developed blastemas (arrow) at the regression site (red dotted line) after 7 weeks and fully regenerated after 8 weeks. Anterior, up. The dorsal surface is shown. (**B**) Representative images of rescue strains undergoing regeneration after amputation. Blastemas formed at approximate amputation plane (red dotted line). Intestine (labeled with red food coloring) and photoreceptors (arrowheads) were observed in blastemas after 12 days of regeneration. Anterior, up. The dorsal surface is shown. Scale bars, 1 mm (A); 500 μm (B).

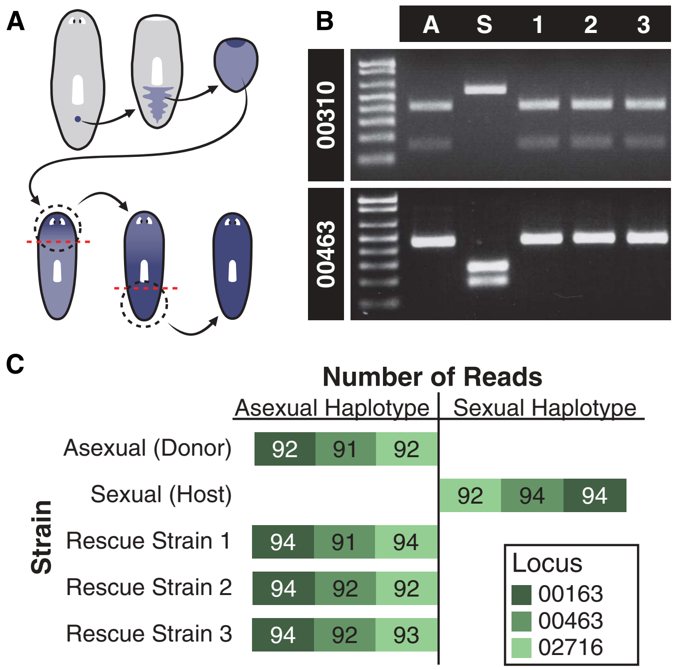

Fig. 6. Genotype conversion by single transplanted cNeoblasts. (**A**) Schematic showing replacement of host tissue by transplanted donor cells (blue); animals for genotyping were amputated (dotted lines) and allowed to regenerate twice. (**B**) PCR-RFLP analysis of rescued strains. Locus 00310 was cut by HpaI in asexual animals (A) and the rescued strains (1, 2, 3), but not in sexual animals (S). Locus 00463 was cut by ScaI in sexual animals, but not in asexual animals or the rescued strains. (**C**) Haplotype sequencing (*22*). Stacked histogram representing the number of sequencing reads from each locus for each strain. Bars extend left for number of reads corresponding to the asexual haplotype and right for number of reads corresponding to the sexual haplotype. Bar absence indicates no reads.

after irradiation, host SNPs in the collected genomic DNA would be expected. Polymerase chain reaction-restriction fragment length polymorphism (PCR-RFLP) analysis of two loci (RFLP 00310 and RFLP 00463) revealed that the rescued strains have the asexual strain RFLPs, indicating that the majority of cells in these animals were donor-derived (Fig. 6B). Sequencing of three independent homozygous haplotypes (00163, 00463, and 02716), each containing six SNPs that distinguish asexual CIW4 and sexual S2F1L3F2 strains, confirmed that the rescue strains possessed the donor rather than host genotype (Fig. 6C). These data indicate that descendants of a single cNeoblast ultimately transformed the recipient into a genetic clone of the donor by replacing all cells present in the original host. We conclude that cNeoblasts are pluripotent stem cells with a broad, body-wide distribution and that persistence into adulthood of pluripotent stem cells enables the extraordinary regenerative feats of planarians.

References and Notes

1. M. J. Evans, *J. Embryol. Exp. Morphol.* **28**, 163 (1972).
2. M. J. Evans, M. H. Kaufman, *Nature* **292**, 154 (1981).
3. G. R. Martin, *Proc. Natl. Acad. Sci. U.S.A.* **78**, 7634 (1981).
4. A. J. Wagers, R. I. Sherwood, J. L. Christensen, I. L. Weissman, *Science* **297**, 2256 (2002); 10.1126/science.1074807.
5. A. J. Wagers, I. L. Weissman, *Cell* **116**, 639 (2004).
6. I. L. Weissman, *Cell* **100**, 157 (2000).
7. G. J. Spangrude, S. Heimfeld, I. L. Weissman, *Science* **241**, 58 (1988).
8. N. Uchida *et al.*, *Proc. Natl. Acad. Sci. U.S.A.* **97**, 14720 (2000).
9. C. Blanpain, W. E. Lowry, A. Geoghegan, L. Polak, E. Fuchs, *Cell* **118**, 635 (2004).
10. B. Ohlstein, A. Spradling, *Nature* **439**, 470 (2006).
11. N. Barker *et al.*, *Nature* **449**, 1003 (2007).
12. T. H. Morgan, *Arch. Entw. Mech. Org.* **7**, 364 (1898).
13. J. Keller, *Jen Zeit Naturw* **28**, 370 (1894).
14. P. W. Reddien, A. Sánchez Alvarado, *Annu. Rev. Cell Dev. Biol.* **20**, 725 (2004).
15. P. W. Reddien, A. L. Bermange, K. J. Murfitt, J. R. Jennings, A. Sánchez Alvarado, *Dev. Cell* **8**, 635 (2005).
16. J. Baguñà, E. Saló, C. Auladell, *Development* **107**, 77 (1989).
17. G. T. Eisenhoffer, H. Kang, A. Sánchez Alvarado, *Cell Stem Cell* **3**, 327 (2008).
18. P. A. Newmark, A. Sánchez Alvarado, *Dev. Biol.* **220**, 142 (2000).
19. A. Salvetti *et al.*, *Dev. Biol.* **328**, 305 (2009).
20. C. S. Lange, C. W. Gilbert, *Int. J. Radiat. Biol.* **14**, 373 (1968).
21. E. Wolff, F. Dubois, *Rev. Suisse Zool.* **55**, 218 (1948).
22. Materials and methods are available as supporting material on *Science* Online.
23. A. J. Becker, E. A. McCulloch, J. E. Till, *Nature* **197**, 452 (1963).
24. J. E. Till, E. A. McCulloch, *Radiat. Res.* **14**, 213 (1961).
25. T. Guo, A. H. Peters, P. A. Newmark, *Dev. Cell* **11**, 159 (2006).
26. P. W. Reddien, N. J. Oviedo, J. R. Jennings, J. C. Jenkin, A. Sánchez Alvarado, *Science* **310**, 1327 (2005).
27. T. D. Hewitson, K. J. Kelynack, I. A. Darby, *Methods Mol. Biol.* **326**, 219 (2006).
28. R. Bravo, R. Frank, P. A. Blundell, H. Macdonald-Bravo, *Nature* **326**, 515 (1987).
29. S. Eriksson, A. Gräslund, S. Skog, L. Thelander, B. Tribukait, *J. Biol. Chem.* **259**, 11695 (1984).

30. D. Wenemoser, P. W. Reddien, *Dev. Biol.* **344**, 979 (2010).
31. J. Baguñà, *J. Exp. Zool.* **195**, 53 (1976).
32. M. L. Scimone, J. Meisel, P. W. Reddien, *Development* **137**, 1231 (2010).
33. B. J. Pearson, A. Sánchez Alvarado, *Development* **137**, 213 (2010).
34. K. Nishimura, Y. Kitamura, T. Taniguchi, K. Agata, *Neuroscience* **168**, 18 (2010).
35. E. E. Morrisey *et al.*, *Genes Dev.* **12**, 3579 (1998).
36. C. R. Bardeen, F. H. Baetjer, *J. Exp. Zool.* **1**, 191 (1904).
37. F. Dubois, *Bull. Biol. Fr. Belg.* **83**, 213 (1949).
38. T. Lender, A. Gabriel, *C. R. Acad. Sc. Paris* **260**, 4095 (1965).
39. T. Hayashi, M. Asami, S. Higuchi, N. Shibata, K. Agata, *Dev. Growth Differ.* **48**, 371 (2006).

Acknowledgments: We thank D. Kim for manuscript comments; S. Lapan for neuronal and intestinal markers; M. Srivastava for phylogenetics advice; D. Wenemoser for SMEDWI-1 antibody purification; J. Owen for Illumina data; M. Griffin for flow cytometry assistance; and P. Hsu, G. Bell, R. Young, and all members of the Reddien Lab for extensive comments and discussion. P.W.R. is an early career scientist of the Howard Hughes Medical Institute and an associate member of the Broad Institute of Harvard and MIT. We acknowledge support from the NIH (grant R01GM080639) and the Keck Foundation.

Supporting Online Material
www.sciencemag.org/cgi/content/full/332/6031/811/DC1
Materials and Methods
Figs. S1 to S19
Table S1
References

8 February 2011; accepted 11 April 2011
10.1126/science.1203983

Computational Design of Proteins Targeting the Conserved Stem Region of Influenza Hemagglutinin

Sarel J. Fleishman,[1*] Timothy A. Whitehead,[1*] Damian C. Ekiert,[2*] Cyrille Dreyfus,[2] Jacob E. Corn,[1†] Eva-Maria Strauch,[1] Ian A. Wilson,[2] David Baker[1,3‡]

We describe a general computational method for designing proteins that bind a surface patch of interest on a target macromolecule. Favorable interactions between disembodied amino acid residues and the target surface are identified and used to anchor de novo designed interfaces. The method was used to design proteins that bind a conserved surface patch on the stem of the influenza hemagglutinin (HA) from the 1918 H1N1 pandemic virus. After affinity maturation, two of the designed proteins, HB36 and HB80, bind H1 and H5 HAs with low nanomolar affinity. Further, HB80 inhibits the HA fusogenic conformational changes induced at low pH. The crystal structure of HB36 in complex with 1918/H1 HA revealed that the actual binding interface is nearly identical to that in the computational design model. Such designed binding proteins may be useful for both diagnostics and therapeutics.

Molecular recognition is central to biology, and high-affinity binding proteins, such as antibodies, are invaluable for both diagnostics and therapeutics (*1*). Current methods for producing antibodies and other proteins that bind a protein of interest involve screening large numbers of variants generated by the immune system or by library construction (*2*). The computer-based design of high-affinity binding proteins is a fundamental test of current understanding of the physical-chemical basis of molecular recognition and, if successful, would be a powerful complement to current library-based screening methods, because it would allow targeting of specific patches on a protein surface. Recent advances in computational design of protein interactions have yielded switches in interaction specificity (*3*), methods to generate modest-affinity complexes (*4*, *5*), two-sided design of a novel protein interface (*6*), and design of a high-affinity interaction by grafting known key residues onto an unrelated protein scaffold (*7*). However, the capability to target an arbitrarily selected protein surface has remained elusive.

Influenza presents a serious public health challenge, and new therapies are needed to combat viruses that are resistant to existing antiviral medicines (*8*) or that escape neutralization by the immune system. Hemagglutinin (HA) is a prime candidate for drug development as it is the major player in viral invasion of cells lining the respiratory tract. Although most antibodies bind to the rapidly varying head region of HA, recently two antibodies, CR6261 and F10, were structurally characterized (*9*, *10*) and found to bind to a region on the HA stem, which is conserved among all group 1 influenza strains (fig. S1) (*11*). Here, we describe a computational method for designing protein-protein interactions de novo and use the method to design high-affinity binders to the conserved stem region on influenza HA.

Computational Design Method

In devising the computational design strategy, we considered features common to dissociable protein complexes. During protein complex formation, proteins bury on average ~1600 Å^2 of solvent-exposed surface area (*12*). Interfaces typically contain several residues that make highly optimized van der Waals, hydrogen bonding, and electrostatic interactions with the partner protein; these interaction hot spots contribute a large fraction of the binding energy (*13*).

Our strategy thus centers on the design of interfaces that have both high shape complementarity and a core region of highly optimized, hot spot–like residue interactions (*14*). We engineered high-affinity interactions and high shape complementarity into scaffold proteins in two steps (see Fig. 1): (i) disembodied amino acid residues were computationally docked or positioned against the target surface to identify energetically favorable configurations with the target surface; and (ii) shape-complementary configurations of scaffold proteins were computed that anchor these energetically favorable interactions.

Design of HA-Binding Proteins

The surface on the stem of HA recognized by neutralizing antibodies consists of a hydrophobic groove that is flanked by two loops that place severe steric constraints on binding to the epitope (Fig. 2, A and B) (*15*). In the first step of our design protocol (Fig. 1), the disembodied hot spot residues found through computational docking cluster into three regions contacting HA (HS1, HS2, and HS3) (Fig. 1). In HS1, a Phe side chain forms an energetically favorable aromatic stacking interaction with Trp^{21} on chain 2 of the HA (HA2) (HA residue numbering corresponds to the H3 subtype sequence-numbering convention) (*16*). In HS2, the nonpolar residues Ile, Leu, Met, Phe, and Val, make favorable van der Waals interactions with both the hydrophobic groove and HS1 (Fig. 1 and fig. S2). In HS3, a Tyr side chain forms a hydrogen bond to Asp^{19} on HA2 and van der Waals interactions with the A helix on HA2. The Tyr in HS3 resembles the conformation of a Tyr residue observed on the antibody in the structure of the HA and CR6261 Fab complex (figs. S1 and S2); the HS1 and HS2 interactions are not found in the antibody structures (*9*, *10*, *17*) (fig. S1).

In the second step, we searched a set of 865 protein structures selected for ease of experimental manipulation (*18*) (table S1) for scaffolds capable of supporting the disembodied hot spot residues and that are shape complementary to the stem region. Each scaffold protein was docked against the stem region using the feature-matching algorithm PatchDock (*19*), which identified hun-

[1]Department of Biochemistry, University of Washington, Seattle, WA 98195, USA. [2]Department of Molecular Biology and the Skaggs Institute for Chemical Biology, The Scripps Research Institute, 10550 North Torrey Pines Road, La Jolla, CA 92037, USA. [3]Howard Hughes Medical Institute, University of Washington, Seattle, WA 98195, USA.

*These authors contributed equally to this manuscript.
†Present address: Genentech, 1 DNA Way, South San Francisco, CA 94080, USA.
‡To whom correspondence should be addressed. E-mail: dabaker@uw.edu

dreds of compatible binding modes for each scaffold (260,000 in total). These coarse-grained binding modes were then refined using RosettaDock (*20*) with a potential scoring function that favored configurations that maximized the compatibility of the scaffold protein backbone with as many hot spot residues as possible (*14*). Next, residues from the hot spot residue libraries were incorporated onto the scaffold. First, for each Phe conformation in HS1, scaffold residues with backbone atoms within 4 Å of the hot spot residue were identified. For each of these candidate positions, the scaffold protein was placed to coincide with the backbone of the hot spot, the residue was modeled explicitly, and the rigid-body orientation was optimized. If no steric clashes were observed and the Phe was in contact with Trp^{21} and Thr^{41} of HA2 (Fig. 2B), the placement of the first hot spot residue was deemed successful; otherwise, another HS1 Phe conformation was selected and the process was repeated. For each success with HS1, an attempt was made to realize the HS2 interactions by incorporating nonpolar residues at appropriate positions in the scaffold protein, and the remainder of the scaffold protein surface was then redesigned using RosettaDesign (*21*).

Designing proteins also containing HS3 interactions was more challenging because of the large number of combinations of residue placements to be considered. To generate designs containing all three hot spot regions, we started by superimposing the scaffold protein on the backbone of the Tyr residue in HS3 (as for the Phe HS1 residue above). We then searched for two positions on the scaffold protein that were nearest to residues in HS1 and HS2 and were best aligned to them (*14*). These positions were then simultaneously designed to Phe in the case of HS1 and to nonpolar residues in the case of HS2. RosettaDesign (*21*) was then used to redesign the remainder of the interface on the scaffold protein, with sequence changes allowed within a distance of 10 Å of the HA.

Experimental and Structural Characterization

A total of 51 designs with the two–hot spot–residue concept and 37 with the three-residue concept were selected for testing (table S2 in SOM text and supplemental coordinate files of all models). The designs are derived from 79 different protein scaffolds and differ from the scaffold by on average 11 mutations. Genes encoding the designs were synthesized, cloned into a yeast-display vector, and transformed into yeast strain EBY100 (*22*). Upon induction, the designed protein is displayed on the cell surface as a fusion between the yeast Aga2p protein and a C-terminal c-Myc tag. Cells expressing designs were incubated with 1 μM of biotinylated SC1918/H1 [A/South Carolina/1/1918 (H1N1)] HA ectodomain, washed, and dual-labeled with phycoerythrin-conjugated streptavidin and fluorescein-conjugated antibody against c-Myc. Display of the designed protein on the yeast surface and binding to HA were simultaneously measured by flow cytometry.

Of the 73 designs that displayed on the yeast surface, 2 showed reproducible binding activity toward the HA stem region (*23*) (table S2) (for models, see Fig. 2, C to F). One design, HA binder 36 (HB36) used the two-residue hot spot and bound to the HA with an apparent dissociation constant (K_d) of 200 nM (*24*) (Fig. 2G and fig. S4). The starting scaffold, structural genomics target APC36109, a protein of unknown function from *Bacillus stearothermophilus* [Protein Data Bank (PDB) entry 1U84], did not bind HA (fig. S4), which indicated that binding is mediated by

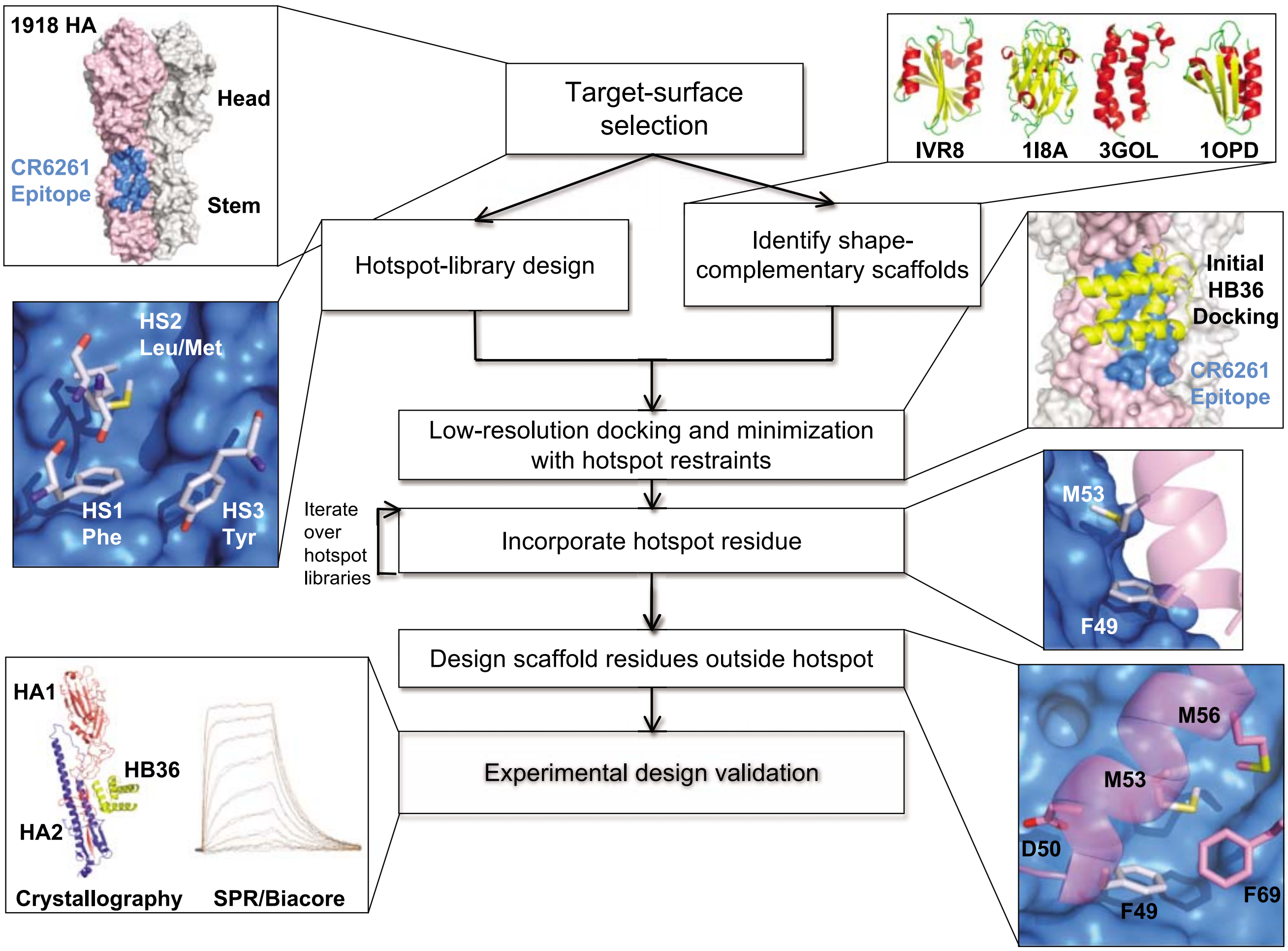

Fig. 1. Flow chart illustrating the key steps in the design of novel binding proteins. The thumbnails illustrate each step in the creation of binders that target the stem of the 1918 HA. Abbreviations (*29*).

the designed surface on HB36. A second design, HB80, used the three-residue hot spot and bound HA only weakly (Fig. 2H). The scaffold from which this design was derived, the MYB domain of the RAD transcription factor from *Antirrhinum majus* (PDB code: 2CJJ) (*25*), again did not bind the HA (fig. S5).

In the computational models of the two designs (Fig. 2, C to F), the hot spot residues are buttressed by a concentric arrangement of hydrophobic residues with an outer ring of polar and charged residues as is often observed in native protein-protein interfaces. Both designs present a row of hydrophobic residues on a helix that fits into the HA hydrophobic groove. The complexes each bury ~1550 Å^2 surface area (total), close to the mean value for dissociable protein interactions (*12*) and slightly larger than the total surface area buried by each of the two neutralizing antibodies (*9*, *10*) (fig. S1). The helical binding modes in these designs are very different from the loop-based binding observed in the antibody-bound structures.

Affinity Maturation

The computational design protocol is far from perfect; the energy function that guides design contains numerous approximations (*26*), and conformational sampling is incomplete. We used affinity maturation to identify shortcomings in the design protocol. Libraries of HB36 and HB80 variants were generated by single site–saturation mutagenesis at the interface, or by error-prone polymerase chain reaction (epPCR), and subjected to two rounds of selection for binding to HA using yeast surface display (*22*).

For both designed binders, the selections converged on a small number of substitutions that increase affinity and provide insight into how to improve the underlying energy function. Among the key contributions to the energetics of macromolecular interactions are short-range repulsive interactions due to atomic overlaps, electrostatic interactions between charged and polar atoms, and the elimination of favorable interactions with solvent (desolvation). The affinity-increasing substitutions point to how each of these contributions can be better modeled in the initial design calculations.

Repulsive interactions. For HB36, replacement of Ala^{60} with the isosteres Thr and Val increased the apparent binding affinity 25-fold (apparent K_d values for all design variants are listed in Table 1). These substitutions fill a void between the designed protein and the HA surface, but were not included in the original design because they were disfavored by steric clashes within HB36 (Fig. 3A). Backbone minimization, however, readily relieved these clashes and resulted in higher predicted affinity for the substitutions. More direct incorporation of backbone minimization in the design algorithm should allow identification of such favorable interactions from the start. For HB80, a M26T mutation significantly increased binding compared with the starting design; modeling suggested that Met^{26} disfavored the conformation of the Tyr hot spot residue (Fig. 3B). The design process should ensure that residues, which make favorable interactions across the interface, also make favorable interactions in the unbound state of the designed protein.

Electrostatics. In HB36, the substitution with Lys at position 64 places a complementary charge adjacent to an acidic pocket on HA near the conserved stem region (Fig. 3C); in HB80, an N36K substitution positions a positive charge 6.5 Å from the negative Asp^{19} on HA2 (Fig. 3D). These substitutions enhance electrostatic complementarity in the complex. The lysines were not selected in the design calculations because the magnitude of surface electrostatic interactions between atoms outside of hydrogen-bonding range are largely reduced; improvement of the electrostatic model would evidently allow design of higher-affinity binders from the start.

Desolvation. In HB36, eight different substitutions at Asp^{47} increased apparent affinity by more than an order of magnitude compared with the original design (table S3); the highest-affinity substitution was D47S, which increased binding

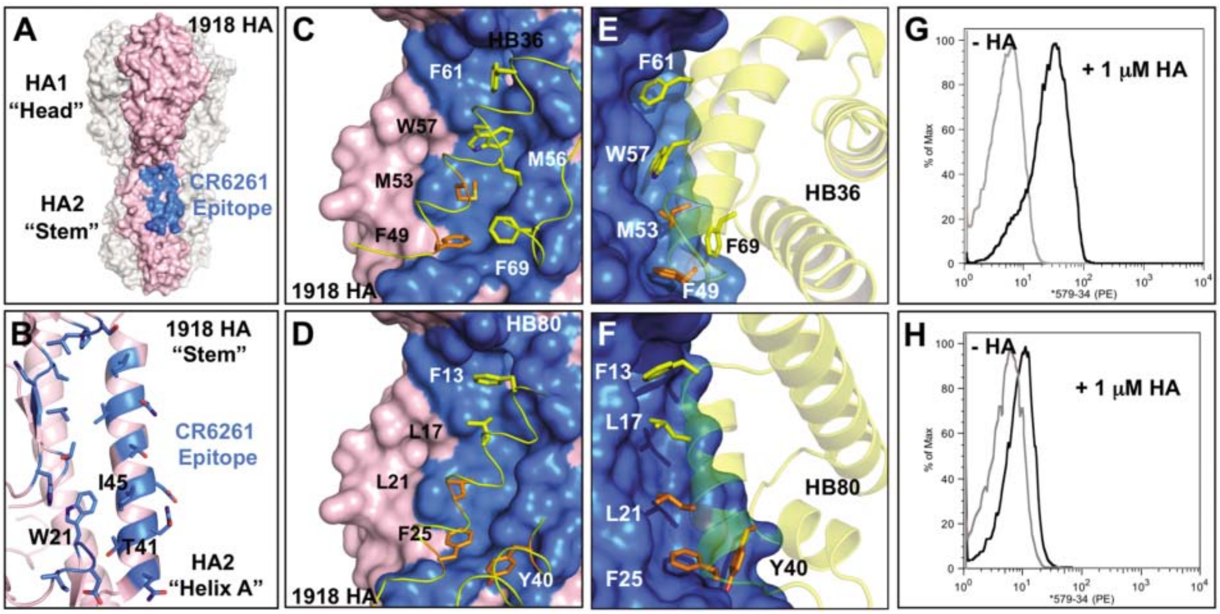

Fig. 2. The HB36 and HB80 designs target the stem of the 1918 HA. (**A**) Surface representation of the trimeric HA structure (PDB 3R2X) from the 1918 pandemic virus, with one of the three protomers highlighted in pink. Broadly neutralizing antibody CR6261 binds a highly conserved epitope in the stem region (blue patch on surface), close to the viral membrane (bottom). (**B**) Enlarged view of the CR6261 epitope [blue region from (A)], with CR6261 contact residues depicted as sticks. This target site on HA contains a groove lined by multiple hydrophobic residues. Loops on either side of this hydrophobic groove (above and below) constrain access to this region. Key residues on HA2 are noted. (**C** and **D**) Front view of the designed interaction between HB36 (C) and HB80 (D) and the target site on HA. HA is rotated ~45° relative to (A). Contact segments of HB36 and HB80 are colored yellow, and residues are depicted as sticks, with hot spot residues highlighted in orange (F49 and M53 for HB36 and L21, F25, and Y40 for HB80). Polar atoms of side chains are shown in red (oxygen) and blue (nitrogen). For clarity, the noncontacting regions from the designs have been omitted. (**E** and **F**) Side view of the designed interactions of HB36 (E) and HB80 (F) with 1918/H1 HA. (**G** and **H**) Initial binding data for HB36 (G) and HB80 (H) designs (before affinity maturation). When incubated with 1 μM 1918 HA, yeast displaying the two designed proteins show an increase in fluorescent phycoerythrin signal (*x* axis) compared with the absence of 1918 HA. Coordinate files of models of 1918 HA in complex with HB36 and HB80 are available as SOM.

affinity about 40-fold. The design calculations underestimated the energetic cost of desolvating Asp^{47} by the aliphatic Ile^{18} on HA2 (Fig. 3E); the substitutions remedy this error by replacing the Asp with residues that are less costly to desolvate upon binding. In HB80, a D12G substitution relieves the desolvation by the neighboring Ile^{56} on HA2 (Fig. 3F). With improvements in the solvation model, the deleterious Asp residues would not be present in starting designs.

The favorable substitutions were combined, and the proteins were expressed with a His tag in *Escherichia coli* and purified by nickel-affinity and size-exclusion chromatography. The variant HB36.3, incorporating the D47S and A60V substitutions, bound to SC1918/H1 HA as confirmed by surface plasmon resonance (SPR) (fig. S6), enzyme-linked immunosorbent assay (ELISA), and coelution on a size-exclusion column (fig. S7). The HB36.4 variant, which incorporates D47S, A60V, and N64K, bound to SC1918/H1 HA with a dissociation constant measured by SPR of 22 nM and an off-rate of $7 \times 10^{-3}\ s^{-1}$ (table S4). Coincubation with an excess of CR6261 Fab abolished binding to the HA (Fig. 3G), consistent with HB36.4 binding in close proximity to the same stem epitope on the HA. For the HB80 design, the combination of the affinity-increasing mutations reduced surface expression on yeast, indicative of poor stability. Therefore, we excised a C-terminal stretch (Δ54–95) greatly boosting surface expression of the design with no significant loss of binding affinity (fig. S9). HB80.3, which incorporates the truncation as well as the D12G, A24S, M26T, and N36K substitutions, has a K_d = 38 nM with off-rate of $4 \times 10^{-2}\ s^{-1}$ by SPR. As with HB36.4, coincubating HA with the CR6261 Fab completely abolished binding to HB80.3 (Fig. 3H), consistent with the designed binding mode.

Alanine substitutions at core positions on each affinity-matured design partially or completely knocked out HA binding (table S5 and fig. S10), which supported the computational models of the designed interfaces (*27*). No mutations were uncovered during selection for higher affinity that were inconsistent with the designed binding modes.

Table 1. Summary of dissociation constants between SC1918/H1 HA and selected design variants. Apparent K_d was determined using yeast surface display titrations. Numbers in parentheses indicate K_d determined by SPR. NB, no binding.

Design	K_d (nM)
1U84 (HB36 scaffold)	NB (NB)
HB36	200 (>2000)
HB36 D47S	5
HA36 A60V	8
HB36.3 (HB36 D47S, A60V)	4 (29)
HB36.4 (HB36 D47S, A60V, N64K)	4 (22)
2CJJ (HB80 scaffold)	NB
HB80	>5000
HB80 M26T	100
HB80 N36K	300
HB80 M26T N36K	7.5
HB80 Δ54-95, M26T, N36K	5
HB80.3 (HB80 Δ54-95, D12Gly, A24S, M26T, N36K)	3 (38)

Crystal Structure of the HB36.3-SC1918 HA Complex

The crystal structure of HB36.3 in complex with the SC1918 HA ectodomain was determined to 3.1 Å resolution. After molecular replacement using only the 1918/H1 HA structure as the search model (~86% of the protein mass in the crystal asymmetric unit), clear electron density was observed for HB36.3 near the target surface in the HA stem region into which HB36.3 could be unambiguously placed. The orientation was essentially identical to the designed binding mode, with the modified surface of the main recognition helix packed in the hydrophobic groove on HA (Fig. 4, A and B). To obtain unbiased density for the designed side chains, the native structure from which HB36.3 was

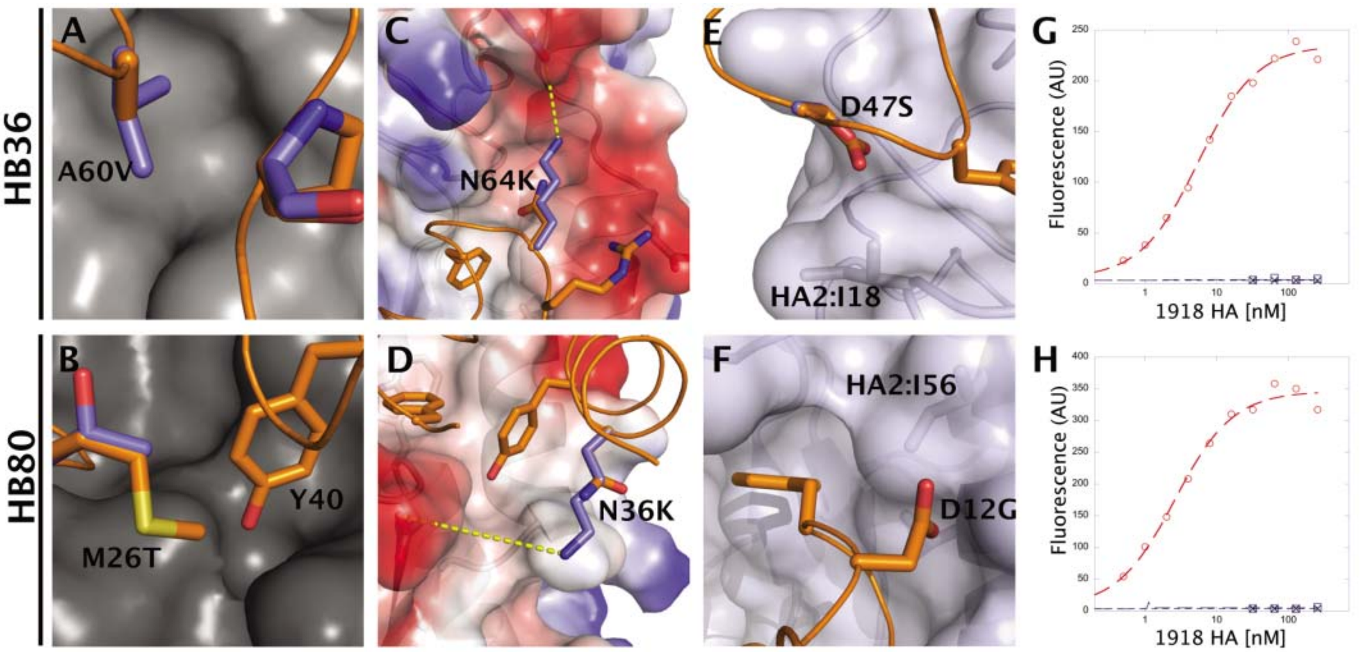

Fig. 3. Affinity maturation. Substitutions that increase the affinity of the original designs reflect deficiencies in modeling the (**A** and **B**) repulsive interactions HB36 A60V (A), HB80 M26T (B); (**C** and **D**) electrostatics HB36 N64K (C), HB80 N36K (D); and (**E** and **F**) solvation HB36 D47S (E), HB80 D12G (F). Binding titrations of HB36.4 (**G**) and HB80.3 (**H**) to SC1918/H1 HA as measured by yeast surface display. Red circles represent the affinity-matured design; blue squares, the scaffold protein from which the design is derived; and black crosses, the design in the presence of 750 nM inhibitory CR6261 Fab.

derived (PDB entry: 1U86) was manually fit into the electron-density maps, and designed side chains were pruned back to their β carbon. After crystallographic refinement, electron density became apparent for the side chains of most of the contact residues on HB36.3, which allowed the predominant rotamers to be assigned for Phe^{49}, Trp^{57}, Phe^{61}, and Phe^{69}. This unbiased density clearly shows that these four hydrophobic side chains are all positioned as in the designed model (Fig. 4C). The Met^{53} side chain is consistent with the design model, although other rotamers could also be fit to the map. For Met^{56}, only very weak side-chain density was observed. Overall, the crystal structure is in excellent agreement with the designed interface, with no significant deviations at any of the contact positions.

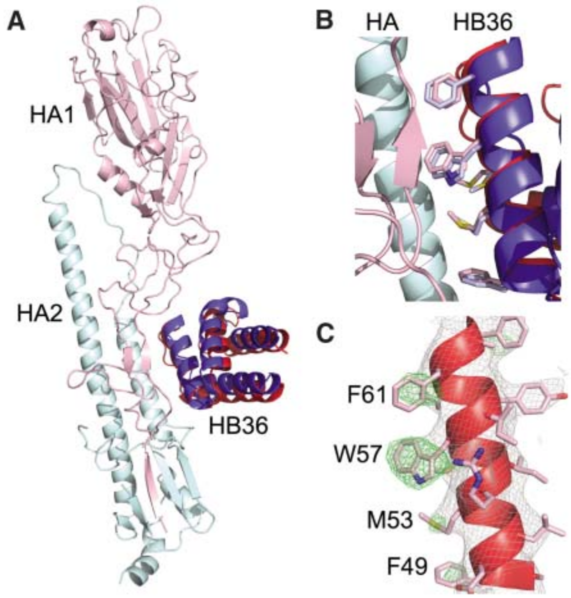

Fig. 4. Crystal structure of HB36.3-SC1918/H1 complex shows the precision of the computational design. (**A**) Superposition of the crystal structure of HB36.3-SC1918/H1 complex (HB36.3 in red with SC1918 HA1 subunit in pink and HA2 subunit in cyan) and the computational design (blue) reveals good agreement in the position of the main recognition helix, with a slight rotation of the rest of the protein domain. Superposition was performed using the HA2 subunits. For clarity, only the HA from the crystal structure is depicted here (the HA used for superposition of the design, which is essentially identical to the crystal structure, was omitted). (**B**) Close up of the SC1918 HA-HB36.3 interface, highlighting the close agreement between the design and the crystal structure. The main recognition helix is oriented as in (A), with the HB36.3 crystal structure in red (pink side chains), the design in blue (light blue side chains), and HA in cyan and pink at left. (**C**) Unbiased $2F_{obs} - F_{calc}$ (gray mesh, contoured at 1σ) and $F_{obs} - F_{calc}$ (green mesh, contoured at 3σ) electron-density maps for the main recognition helix of HB36.3. The helix is oriented as in (B), with key HA-contacting residues labeled (residues on the right of the helix interact with the core of HB36). Additional density was observed for most of the large side chains at the interface with HA, including F49, M53, W57, F61, and F69 (not visible in this view). Although side chains are shown here to illustrate their agreement with the experimental electron density, maps were calculated after initial refinement of an HA-HB36.3 model with the interface side chains F49, M53, M56, W57, F61, and F69 truncated to alanine.

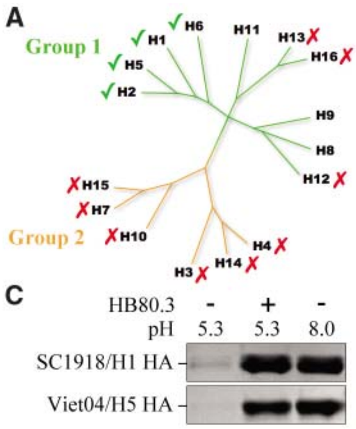

B

Strains	Binding HB80.3	Binding CR6261
A/South Carolina/1/1918 (H1N1)	++	+++
A/AA/Marton/1943 (H1N1)	++	+++
A/USSR/90/1977 (H1N1)	++	+++
A/Beijing/262/1995 (H1N1)	++	+++
A/Solomon Islands/3/2006 (H1N1)	+	+++
A/Japan/305/1957 (H2N2)	+	++
A/goose/Guangdong/1/1996 (H5N1)	+	+++
A/turkey/Massachusetts/3740/1965 (H6N2)	++	+++
A/duck/Alberta/60/1976 (H12N5)	-	-
A/gull/Maryland/704/1977 (H13N6)	-	+++
A/black-headed gull/Sweden/4/1999 (H16N3)	-	++
A/Hong Kong/1/1968 (H3N2)	-	-
A/duck/Czechoslovakia/1956 (H4N6)	-	-
A/Netherlands/219/2003 (H7N7)	-	-
A/chicken/Germany/N/1949 (H10N7)	-	-
A/mallard duck/Astrakhan/263/1982 (H14N5)	-	-
A/shearwater/West Australia/2576/1979 (H15N8)	-	-

Fig. 5. HB80.3 binds and inhibits multiple HA subtypes. (**A**) Phylogenetic tree depicting the relation between the 16 influenza A HA subtypes. These subtypes can be divided into two main lineages, groups 1 and 2. CR6261 has broad activity against group 1 viruses. HB80.3 has a similar cross-reactivity profile and binds multiple group 1 subtypes, including H1 and H5. (**B**) Binding data for HB80.3 and CR6261 Fab against a panel of HAs. +, ++, and +++ indicate relative degree of binding (dissociation constant approximately 10^{-7}, 10^{-8}, and 10^{-9} M, respectively), whereas a minus sign (–) indicates no detectable binding at the highest concentration tested (100 nM). (**C**) HB80.3 inhibits the pH-induced conformational changes that drive membrane fusion. Exposure to low pH converts 1918 H1 HA (top) and the Viet04 H5 HA to a protease-susceptible state (lane 1), whereas HAs maintained at neutral pH are highly resistant to trypsin (lane 3). Preincubation of HB80.3 with H1 and H5 prevents pH-induced conformational changes and retains the HAs in the protease-resistant, prefusion state (lane 2).

Given the quite low (2 out of the 73 surface-displayed proteins) design success rate and starting affinities, the atomic-level agreement between the designed and experimentally determined HB36.3–SC1918 HA complex is very encouraging and suggests that, despite their shortcomings, the current energy function and design methodology capture essential features of protein-protein interactions.

Cross-Reactivity and Inhibitory Activity

The surface contacted by HB36.3 is accessible and highly conserved in the HAs of most group 1 influenza viruses, which suggests that it may be capable of binding not only other H1 HAs, but also other HA subtypes. Indeed, binding of HB36.3 to A/South Carolina/1/1918 (H1N1) and A/WSN/1933 (H1N1) is readily detectable in solution by gel filtration (fig. S7), as is high-affinity binding of HB36.4 to A/Vietnam/1203/2004 H5 subtype by yeast display (fig. S11).

Although a crystal structure of HB80 in complex with HA has not been obtained, the mutational data and the antibody-competition results suggest that HB80 also binds to the designed target surface and overlaps with HB36 and CR6261. Consequently, HB80.3 is also expected to be highly cross-reactive and, indeed, binds with high affinity to A/Vietnam/1203/2004 H5 HA (fig. S11) and to H1, H2, H5, and H6 subtypes in biolayer interferometry experiments (Fig. 5, A and B). Overall, HB80 binds most of the group 1 HAs tested but does not have detectable binding to group 2 HAs, mirroring the binding profile of CR6261.

Antibody CR6261 inhibits influenza virus replication by blocking the pH-induced refolding of HA, which drives fusion of the viral envelope with the endosomal membrane of the host cell. Given extensive overlap between the HB80.3 and CR6261 binding sites and its high affinity for SC1918 HA, it seemed plausible that HB80.3 would also block this conformational change. Indeed, HB80.3 inhibits the pH-induced conformational changes in both H1 and H5 HAs (Fig. 5C and fig. S12) (*10*), which suggests that this design may have virus-neutralizing activity against multiple influenza subtypes (*28*). Further work will be needed to explore the potential utility of HB80.3 in a therapeutic or diagnostic setting, but these results suggest that de novo computational design of antiviral proteins is feasible.

References and Notes

1. H. Ledford, *Nature* **455**, 437 (2008).
2. R. A. Lerner, *Angew. Chem. Int. Ed. Engl.* **45**, 8106 (2006).

3. T. Kortemme et al., Nat. Struct. Mol. Biol. **11**, 371 (2004).
4. R. K. Jha et al., J. Mol. Biol. **400**, 257 (2010).
5. P. S. Huang, J. J. Love, S. L. Mayo, Protein Sci. **16**, 2770 (2007).
6. J. Karanicolas et al., Mol. Cell **42**, 250 (2011).
7. S. Liu et al., Proc. Natl. Acad. Sci. U.S.A. **104**, 5330 (2007).
8. Writing Committee of the WHO Consultation on Clinical Aspects of Pandemic (H1N1) 2009 Influenza, N. Engl. J. Med. **362**, 1708 (2010).
9. J. Sui et al., Nat. Struct. Mol. Biol. **16**, 265 (2009).
10. D. C. Ekiert et al., Science **324**, 246 (2009).
11. Group 1 includes 10 of the 16 HA subtypes: H1, H2, H5, H6, H8, H9, H11, H12, H13, and H16. Group 2 includes the remaining six subtypes: H3, H4, H7, H10, H14, and H15.
12. L. Lo Conte, C. Chothia, J. Janin, J. Mol. Biol. **285**, 2177 (1999).
13. T. Clackson, J. A. Wells, Science **267**, 383 (1995).
14. Materials and methods are available as supporting material on Science Online.
15. M. G. Rossmann, J. Biol. Chem. **264**, 14587 (1989).
16. J. Chen, J. J. Skehel, D. C. Wiley, Proc. Natl. Acad. Sci. U.S.A. **96**, 8967 (1999).
17. The other hot spot residues (HS1 and HS2) differed from the side chains observed in the crystal structures in their conformation or identity. Each hot spot residue was further diversified by constructing all conformations, the terminal atoms of which coincided with those modeled above. For instance, for HS3, these consisted of all Tyr conformations that matched the position of the aromatic ring and hydrogen bond. This diversification step produced a "fan" of backbone positions for each residue in the hot spot libraries.
18. Proteins in the scaffold set contained no disulfides, were expressed in E. coli, and were predicted to form monomers (14).
19. D. Schneidman-Duhovny, Y. Inbar, R. Nussinov, H. J. Wolfson, Nucleic Acids Res. **33** (Web Server issue), W363 (2005).
20. J. J. Gray et al., J. Mol. Biol. **331**, 281 (2003).
21. B. Kuhlman et al., Science **302**, 1364 (2003).
22. G. Chao et al., Nat. Protoc. **1**, 755 (2006).
23. A third design HB35 bound HA at apparent low-micromolar affinity; however, binding was only partially abolished upon coincubation of HA with the CR6261 Fab, which indicated, at most, partial contact with the target surface on the stem region of HA, and so this design was eliminated from further consideration (fig. S7). A handful of other designs bound HA, albeit weakly and with incomplete reproducibility (14).
24. We recorded dissociation constants using two main methods: by titration of HA against yeast surface-displayed designs and by fitting both kinetic and equilibrium measurements using surface plasmon resonance. As there is a discrepancy in determining K_d values between the methods, measurements derived from yeast surface-display titrations are listed as apparent K_d and should be viewed qualitatively (14).
25. C. E. Stevenson et al., Proteins **65**, 1041 (2006).
26. R. Das, D. Baker, Annu. Rev. Biochem. **77**, 363 (2008).
27. The alanine-scan mutations were as follows: for HB36.3, Phe[49], Met[53], and Trp[57]; for HB80.1 Phe[13], Phe[25], and Tyr[40] (table S4 and SOM text).
28. HB36.3 was not able to block the pH-induced conformational changes in the H1 and H5 HAs under identical assay conditions, even though HB36.3 and HB80.3 have very similar dissociation constants and kinetic off-rates at pH 7.5 (fig. S12 and SOM text).
29. Single-letter abbreviations for the amino acid residues are as follows: A, Ala; C, Cys; D, Asp; E, Glu; F, Phe; G, Gly; H, His; I, Ile; K, Lys; L, Leu; M, Met; N, Asn; P, Pro; Q, Gln; R, Arg; S, Ser; T, Thr; V, Val; W, Trp; and Y, Tyr.

Acknowledgments. Computational designs were generated on resources generously provided by participants of Rosetta @ Home and the Argonne National Leadership Computing Facility. We thank J. L. Gallaher for protein preparation. S.J.F. was supported by a long-term fellowship from the Human Frontier Science Program, J.E.C. was supported by the Jane Coffin Childs Memorial Fund, and E.M.S. by a career development award from the National Institute of Allergy and Infectious Diseases, NIH, AI057141. Research in the Baker laboratory was supported by grants from the Defense Advanced Research Projects Agency, the NIH yeast resource center, the Defense Threat Reduction Agency, and the Howard Hughes Medical Institute and in the Wilson laboratory by NIH AI058113, predoctoral fellowships from the Achievement Rewards for College Scientists Foundation and the NIH Molecular Evolution Training Program GM080209 (D.C.E.), and the Skaggs Institute for Chemical Biology. X-ray diffraction data sets were collected at the Stanford Synchrotron Radiation Lightsource beamline 9-2 and at the Advanced Photon Source (APS) beamline 23ID-B (GM/CA-CAT). The GM/CA CAT 23-ID-B beamline has been funded in whole or in part with federal funds from National Cancer Institute (Y1-CO-1020) and the National Institute of General Medical Science, NIH (Y1-GM-1104). Use of the APS was supported by the U.S. Department of Energy, Basic Energy Sciences, Office of Science, under contract no. DE-AC02-06CH11357. Coordinates and structure factors were deposited in the Protein Data Bank as entry 3R2X.

Supporting Online Material
www.sciencemag.org/cgi/content/full/332/6031/816/DC1
Materials and Methods
SOM Text
Figs. S1 to S12
Tables S1 to S7
References

7 January 2011; accepted 8 April 2011
10.1126/science.1202617

REPORTS

Interplay of Rotational, Relaxational, and Shear Dynamics in Solid ^{4}He

E. J. Pratt,[1,2]* B. Hunt,[1,3]* V. Gadagkar,[1] M. Yamashita,[4] M. J. Graf,[5] A. V. Balatsky,[5] J. C. Davis[1,6,7]†

Using a high-sensitivity torsional oscillator (TO) technique, we mapped the rotational and relaxational dynamics of solid helium-4 (^{4}He) throughout the parameter range of the proposed supersolidity. We found evidence that the same microscopic excitations controlling the torsional oscillator motions are generated independently by thermal and mechanical stimulation. Moreover, a measure for the relaxation times of these excitations diverges smoothly without any indication for a critical temperature or critical velocity of a supersolid transition. Finally, we demonstrated that the combined temperature-velocity dependence of the TO response is indistinguishable from the combined temperature-strain dependence of the solid's shear modulus. This implies that the rotational responses of solid ^{4}He attributed to supersolidity are associated with generation of the same microscopic excitations as those produced by direct shear strain.

Solid ^{4}He may become a supersolid (1) when its temperature T and mass-flow velocity V fall below their critical (2) values T_c and V_c. Indeed, torsional oscillator (TO) studies (3, 4) reveal that the resonant angular frequency of rotation ω increases rapidly below both $T \sim 250$ mK and rim velocity $V \sim 10^{-4}$ ms^{-1}, as if superfluid inertia decouples at a critical temperature and velocity. These ω increases (3–10) are greatly diminished by blocking the TO annulus (4, 11), as if superfluid inertia is thereby reconnected. Signatures in the heat capacity ascribed to supersolidity also occur in this same temperature range (12). However, direct mass-flow studies detect maximum currents that are far smaller than those implied by the TO experiments (13–15). Moreover, the temperature dependence of the resonance frequency $f(T) = \omega(T)/2\pi$ of TOs containing solid ^{4}He (3–11) resembles closely that of its shear modulus $\mu(T)$ (16). Coincident with the maximum rates of increase of $f(T)$ and $\mu(T)$ are maxima in TO dissipation (4–6, 8, 9) and shear dissipation (16, 17), respectively. Such effects should not exist during a bulk Bose-Einstein condensation transition, although they do occur in the Berezinskii-Kosterlitz-Thouless (BKT) transition of a superfluid film (18) [see Supporting Online Material (SOM) section I (19)]. Finally, the increases in both f and μ are quickly extinguished by increasing TO maximum rim velocity V (3–8, 10) or shear strain ε (16, 20), respectively.

Several theoretical models have been proposed to explain the unexpectedly complex rotational dynamics of solid ^{4}He. The first is a simple supersolid (1) in which Bose-Einstein condensation of vacancies produces an inter-

[1]Laboratory for Atomic and Solid State Physics, Department of Physics, Cornell University, Ithaca, NY 14853, USA. [2]Kavli Institute for Theoretical Physics, University of California, Santa Barbara, CA 93016, USA. [3]Department of Physics, Massachusetts Institute of Technology, Cambridge, MA 02139, USA. [4]Department of Physics, Kyoto University, Kyoto 606-8502, Japan. [5]Theoretical Division and Center for Integrated Nanotechnologies, Los Alamos National Laboratory, Los Alamos, NM 87545, USA. [6]Condensed Matter Physics and Materials Science Department, Brookhaven National Laboratory, Upton, NY 11973, USA. [7]School of Physics and Astronomy, University of St. Andrews, St. Andrews, Fife KY16 9SS, UK.

*These authors contributed equally to this work.
†To whom correspondence should be addressed. E-mail: jcdavis@ccmr.cornell.edu

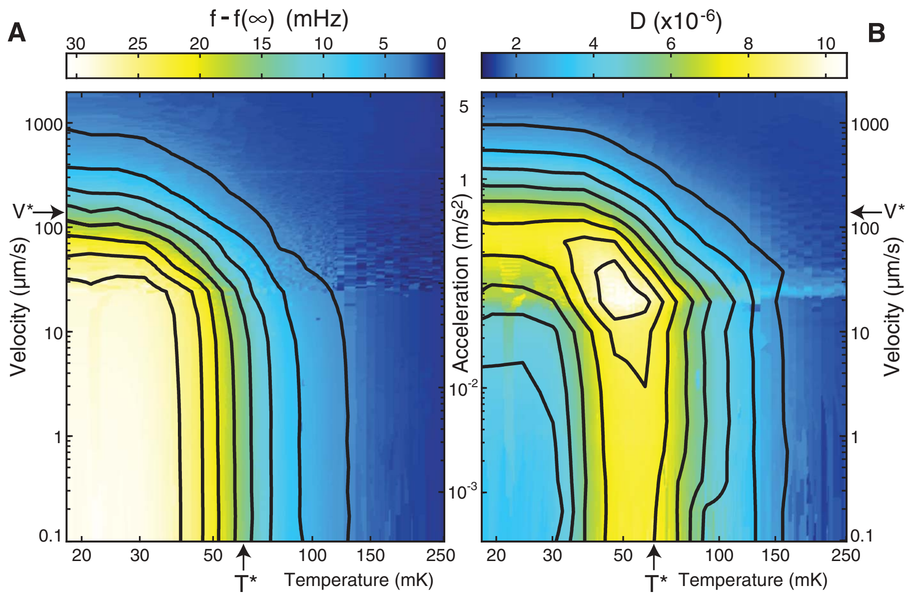

Fig. 1. TO resonant frequency shift $f(T)$ (**A**) and dissipation data (**B**) mapped throughout the V-T plane. Ninety-eight free inertial decay curves (each at a different temperature) were smoothly interpolated into the two color-coded surfaces displayed here on identical log-log axes. The low-velocity maximum frequency shift (~30 mHz) would correspond to a superfluid fraction of 5.6%.

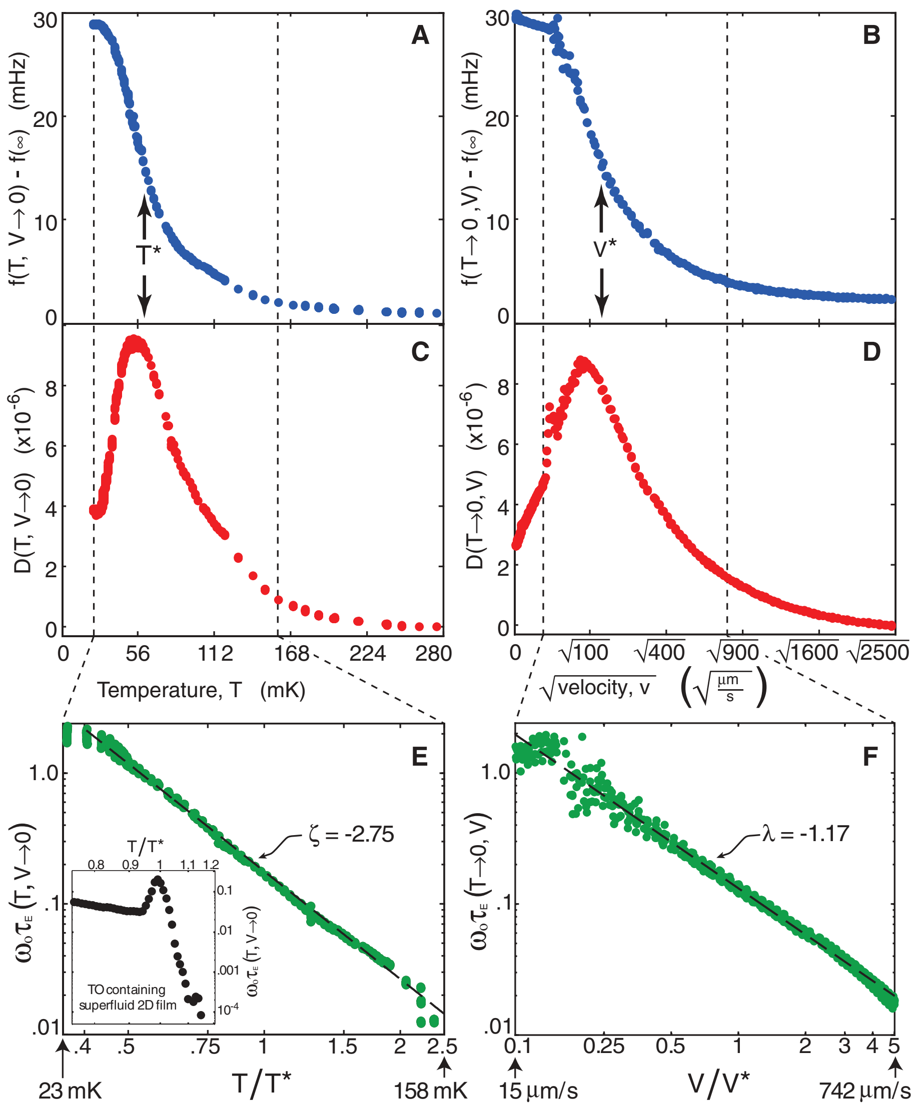

Fig. 2. (**A**) TO resonant frequency shift $f(T)$ measured at lowest rim velocity. T^* is defined as the temperature at which 50% of the frequency change has occurred (Fig. 1). (**B**) TO resonant frequency shift $f(\sqrt{V})$ measured at lowest temperature. V^* is defined as the rim velocity at which 50% of the frequency change has occurred (Fig. 1). (**C**) TO dissipation $D(T)$ measured at lowest rim velocity. (**D**) TO dissipation $D(\sqrt{V})$ measured at lowest temperature. (**E**) The empirical measure of microscopic relaxation times $\omega_0\tau_E(T)|_{V\to 0}$ from data in Fig. 2, A and C. The inset shows the equivalent analysis using Eq. 3 for the BKT transition of a superfluid ^{4}He film (see SOM section I). (**F**) The empirical measure of microscopic relaxation times $\omega_0\tau_E(V)|_{T\to 0}$ from data in Fig. 2, B and D. It diverges smoothly as V^λ with $\lambda = -1.17 \pm 0.05$.

penetrating superfluid with well-defined T_c and V_c. The second is an incipient supersolid lacking long-range phase coherence (*21*, *22*). A third class of model posits disorder-induced superfluidity (*9*, *23–29*). The final proposal is that solid ^{4}He contains a population of inertially active crystal excitations (*30–35*), whose relaxation time τ lengthens smoothly with falling T and V. These excitations are variously proposed to be a dynamical network of pinned dislocations (*17*, *30*, *35*), atomic-scale tunneling two-level systems (*34*), or the glassy response of defects distributed throughout the solid (*31–33*). All models positing inertially active crystal excitations have the property that, as $\tau(T)$ passes through the condition $\omega\tau = 1$, a strong maximum in $|df/dT|$ and TO dissipation D should occur (*9*, *31–35*), even though there is no supersolid T_c and V_c. By contrast, a bulk superfluid phase transition should exhibit clear signatures of both T_c and V_c (*2*). One way to distinguish between such models is to determine the evolution of microscopic relaxational time constants τ, in search of either the smoothly diverging τ of a system governed by $\omega\tau = 1$ phenomenology or the sudden changes expected in τ at a thermodynamic T_c and/or V_c.

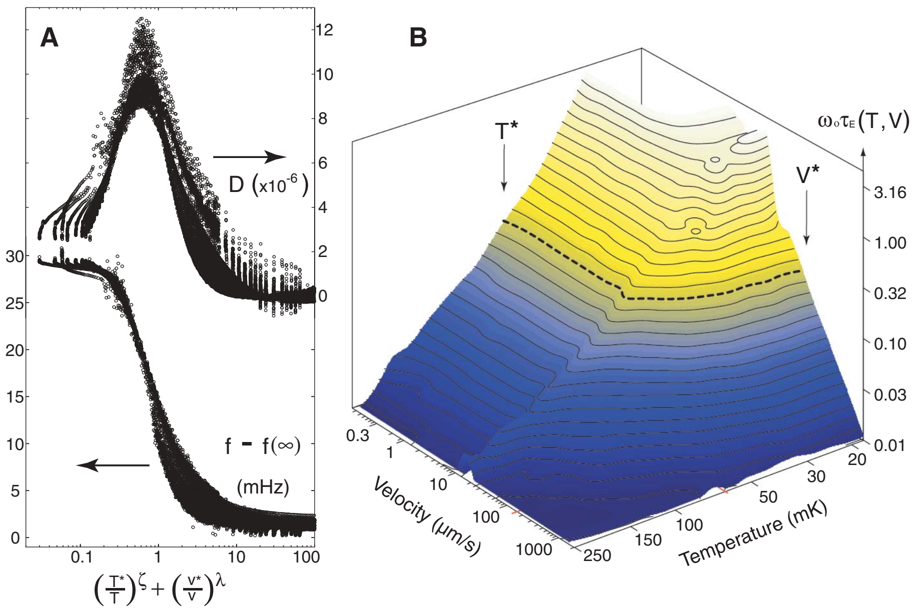

Fig. 3. (**A**) All of the TO dynamical responses throughout the V-T plane [$f(T,V)$ from Fig. 1A and $D(T,V)$ from Fig. 1B] are collapsed onto just two curves (very similar in structure to the $\mathrm{Re}(\chi^{-1})$ and $\mathrm{Im}(\chi^{-1})$ components of the Debye susceptibility) by plotting $f[(T^*/T)^\zeta + (V^*/V)^\lambda]$ and $D[(T^*/T)^\zeta + (V^*/V)^\lambda]$ (SOM section IV). Here, we find that $\mathrm{Re}(\chi^{-1}) \propto f[(T^*/T)^\zeta + (V^*/V)^\lambda]$ is always too large, in comparison with $\mathrm{Im}(\chi^{-1}) \propto D[(T^*/T)^\zeta + (V^*/V)^\lambda]$, to be explained quantitatively by a Debye susceptibility model; this point has been used to motivate a "superglass" hypothesis (*9*). (**B**) A comprehensive map of empirical relaxation times $\omega_0\tau_E(T,V)$ deduced using Eq. 3 represented as a surface in the log$T$-log$V$ plane. The equally spaced contour lines in log $\omega_0 t_E(T,V)$ reveal the underlying divergence of $\omega_0\tau_E(T,V)$ as combined power laws $[(T^*/T)^\zeta + (V^*/V)^\lambda]$.

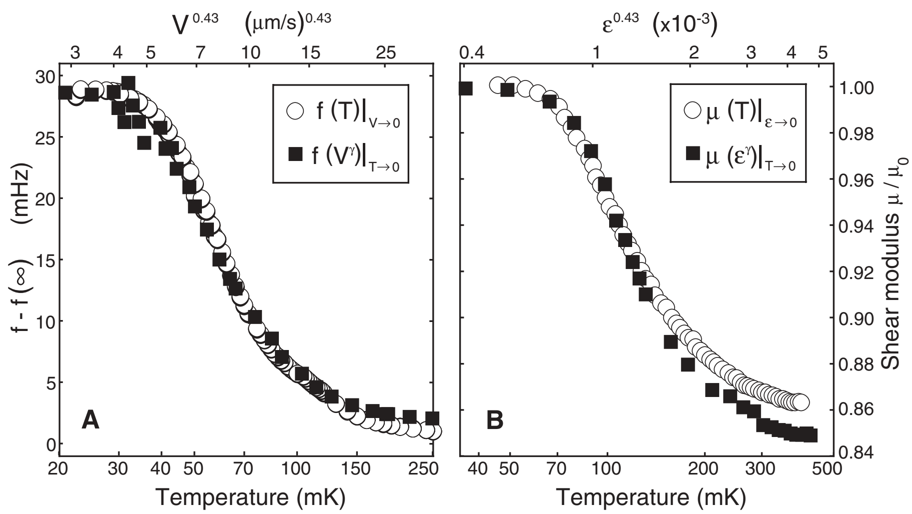

Fig. 4. (**A**) Plots of our simultaneously measured $f(T)|_{V\to0}$ (open circles) and $f(V^\gamma)|_{T\to0}$ (filled squares) from Figs. 1 and 2. (**B**) Simultaneous plots of measured $\mu(T)|_{\varepsilon\to0}$ (open circles) and $\mu(\varepsilon^\gamma)|_{T\to0}$ (filled squares) from (*20*) acquired at 2000 Hz.

An unbiased approach to TO studies of solid ^{4}He can be achieved by using the TO rotational susceptibility $\chi(\omega,T) = \theta(\omega,T)/\Gamma(\omega)$ (*9*). Here, $\theta(\omega,T)$ represents the amplitude of angular displacement as a function of ω and T in response to a harmonic torque $\Gamma(\omega)$ of constant magnitude. Then (*31–33*)

$$\chi^{-1}(\omega,T) = K - I\omega^2 - i\gamma\omega - \chi^{-1}_{4He}(\omega,T) \quad (1)$$

represents the properties of the bare TO plus the "back action" of the solid ^{4}He upon it through the solid's rotational susceptibility $\chi^{-1}_{4He}(\omega,T)$. Here, I is the combined moment of inertia of the TO plus ^{4}He at zero temperature, K is the torsional spring constant, and γ is the TO damping constant. To clarify these concepts, we consider a Debye rotational susceptibility $\chi^{-1}_{4He}(T) = g/[1 - i\omega_0\tau(T)]$ (*9*, *31–33*) with relaxational time constants $\tau(T)$ increasing with decreasing T. For this susceptibility

$$\frac{\mathrm{Im}(\chi^{-1}_{4He})}{\mathrm{Re}(\chi^{-1}_{4He})} = \frac{D(T)f(0)}{2[f(0) - f(T)]} = \omega_0\tau(T) \quad (2)$$

where $\mathrm{Re}(\chi^{-1}_{4He})$ and $\mathrm{Im}(\chi^{-1}_{4He})$ are its real and imaginary parts, respectively (*32*), and $D(T) = Q^{-1}(T) - Q^{-1}(T\to\infty)$ is the inverse contribution to the TO quality factor Q from the solid ^{4}He. Access to $\tau(T)$ for the microscopic excitations is therefore possible in principle from measurements of $\mathrm{Re}(\chi^{-1}_{4He})$ and $\mathrm{Im}(\chi^{-1}_{4He})$.

Following this approach, we mapped the rotational susceptibility of a TO containing solid ^{4}He throughout the V-T plane (SOM section II). The results in Fig. 1, A and B, reveal immediately that the frequency increase and dissipation peak are bounded by closely corresponding V-T contours. Thus, the same unexplained dissipation seen with falling temperature near the proposed supersolid T_c is found also with diminishing V in the range of the proposed (*3*, *4*) supersolid V_c. The highly similar contours of both $f(T,V)$ and $D(T,V)$ also reveal that the maxima in $|df/dT|$ and D are always linked, as if controlled by some combined function of T and V. Similar results were observed in all three distinct solid ^{4}He samples studied.

Next, we compared the solid ^{4}He rotational dynamics versus T as $V\to0$ to those versus $V^{0.5}$ as $T\to0$ (the rationale for $V^{0.5}$ will become clear below). Figure 2, A and C, shows $f(T)|_{V\to0}$ and $D(T)|_{V\to0}$, whereas Fig. 2, B and D, shows $f(V)|_{T\to0}$ and $D(V)|_{T\to0}$ (Fig. 1 data used are identified in fig. S5). Figure 2 reveals a striking and unexpected similarity between the results of what, for a simple superfluid, would be two com-

pletely different experiments (one stimulating the sample thermally and the other mechanically). To examine this, we define an empirical measure τ_E of relaxation times for any combination of T and V.

$$\tau_E(T,V) = \frac{D(T,V)\, f(0)}{2\omega_0[\, f(0) - f(T,V)]} \qquad (3)$$

In Fig. 2E, we show $\log\tau_E(T)$ plotted versus $\log(T/T^*)$ for the lowest rim velocity data (Fig. 2, A and C). In Fig. 2F, $\log\tau_E(V)$ is likewise plotted versus $\log(V/V^*)$ for the lowest temperature data (Figs. 2, B and D). Here, we define T^* and V^* as the temperature and rim velocity, respectively, at which half the total frequency shift has occurred (Fig. 1 and Fig. 2, A and B). This analysis reveals that the τ_E diverges smoothly as T^ζ with $\zeta = -2.75 \pm 0.1$ when $V \to 0$ and as V^λ with $\lambda = -1.17 \pm 0.05$ when $T \to 0$. Thus, the effects of temperature on $f(T)|_{V\to 0}$ and $D(T)|_{V\to 0}$ appear identical to those of rim velocity on $f(V^\gamma)|_{T\to 0}$ and $D(V^\gamma)|_{T\to 0}$, respectively, where $\gamma = \lambda/\zeta = 0.43$ is the ratio of power-law exponents. Figure 2, E and F, also shows that no matter how complex the actual rotational dynamics (Fig. 2, A to D), the peak in D is always canceled by the peak in $|df/dT|$ to produce smoothly diverging functions $\tau_E(T)|_{V\to 0}$ and $\tau_E(V)|_{T\to 0}$ (fig. S7). Microscopic relaxational processes represented by τ_E should change dramatically at a superfluid phase transition; an excellent example of this is seen in $\tau_E(T)$ at the BKT superfluid phase transition of liquid ^{4}He, shown in the inset to Fig. 2E (fig. S1). However, no indications of the sudden change that would signify the supersolid T_c or V_c exist in Fig. 2, E and F. Instead, τ_E exhibits everywhere the smooth divergence expected in $\omega\tau = 1$ models.

Figures 1 and 2 provide direct empirical evidence that the effects of T and V on the TO are intimately related to each other. One may therefore ask whether a single Debye-like rotational susceptibility could describe the whole V-T plane dynamics in Fig. 1 when the effects of V on the relaxation time τ are correctly incorporated. Hypothesizing a total relaxation rate $1/\tau(T,V)$ due to a combination of two effects

$$\frac{1}{\tau(T,V)} = \frac{1}{\tau(T)} + \frac{1}{\tau(V)} \qquad (4)$$

along with the knowledge that the overall phenomenology appears identical as a function of $T^\zeta|_{V\to 0}$ and $V^\lambda|_{T\to 0}$ (Fig. 2) and interpolates smoothly between these limits (Fig. 1), yields an ansatz.

$$\frac{1}{\tau(T,V)} = \frac{\Sigma}{T^\zeta} + \frac{\Lambda}{V^\lambda} \qquad (5)$$

Here, Σ and Λ quantify the relative contributions to the relaxation rate from thermally and mechanically stimulated excitations (SOM section IV). Figure 3A shows that by using this ansatz, virtually all the complex solid ^{4}He rotational dynamics in $f(T,V)$ and $D(T,V)$ of Fig. 1 can be collapsed onto just two functions, $\mathrm{Re}(\chi^{-1})$ and $\mathrm{Im}(\chi^{-1})$, merely by plotting $f[(T^*/T)^\zeta + (V^*/V)^\lambda]$ and $D[(T^*/T)^\zeta + (V^*/V)^\lambda]$. Moreover, this apparent unification of rotational dynamics implies that Eq. 3 could yield a comprehensive image of $\tau_E(T,V)$ throughout the V-T plane by dividing all the data in Fig. 1B by that in Fig. 1A, as shown in Fig. 3B. Although the proposed V-T ranges for a supersolid phase transition (*3*, *4*, *12*) are at or below the dashed T^*-V^* contour, the τ_E surface exhibits everywhere the smoothly diverging relaxation processes expected in $\omega\tau = 1$ models. We emphasize here that all the above results (Figs. 1 to 3) are independent of any choice of $\chi^{-1}_{4He}(T,V)$ and therefore strongly constrain eventual microscopic models for the dynamics of solid ^{4}He.

Figures 1 and 2 provide evidence that the identical microscopic excitations are being generated by thermal and mechanical stimulation and that the overall rotational dynamics in $f(V,T)$ and $D(V,T)$ are consistent with a single $\omega\tau = 1$ mechanism that is controlled by a relaxation rate $(T^*/T)^\zeta + (V^*/V)^\lambda$ due to the combined influences from these two sources (Fig. 3). Because these unified dynamics also appear inconsistent with expectations for T_c or V_c of a superfluid transition (*2*), one must ask which model could account for them. Because the solid ^{4}He shear modulus $\mu(T)$ exhibits a very similar temperature dependence to $f(T)$ (*16*), and because this shear stiffening effect is extinguished by a characteristic strain as opposed to a critical velocity (*20*), a key question has been whether excitations generated by direct shearing are the same as those controlling the TO dynamics.

Our approach provides an opportunity to address this issue. If crystal excitations induced by inertial strain ε in the TO (where $\varepsilon \propto V$) are the cause of the anomalous rotational dynamics, then the indistinguishable structure of $f(T)|_{V\to 0}$ and $f(V^\gamma)|_{T\to 0}$ (Fig. 4A) should be mirrored by an equivalently indistinguishable relationship in shear modulus between $\mu(T)|_{\varepsilon\to 0}$ and $\mu(\varepsilon^\gamma)|_{T\to 0}$. When the measured μ from (*20*) is plotted simultaneously versus T and ε^γ in Fig. 4B (using the power-law ratio γ derived from our TO studies), this is precisely what we find. That the combined temperature-velocity dependence of the TO response mirrors quantitatively the combined temperature-strain dependence of the shear modulus, along with the original observation that $\mu(T)$ tracks $f(T)$ (*16*), implies that the rotational dynamics of solid ^{4}He are associated with the generation (presumably by inertial shearing) of the same type of microscopic excitations that are generated by direct shear strain ε. These conclusions appear to be in good accord with the observed smoothly diverging microscopic relaxation times as expected of $\omega\tau = 1$ models (Fig. 3) and with the absence of a signature in $\tau_E(T,V)$ for the T_c or V_c of a supersolid phase transition (Figs. 2 and 3). These results will motivate efforts to (i) identify directly whether the microscopic excitations are crystal dislocations as implied and (ii) determine whether they admit any associated zero-frequency contribution to the rotational susceptibility that would represent a superfluid component (*9*).

References and Notes

1. S. Balibar, *Nature* **464**, 176 (2010).
2. D. R. Tilley, J. Tilley, *Superfluidity and Superconductivity* (IOP, Bristol, UK, ed. 3, 1990).
3. E. Kim, M. H. W. Chan, *Nature* **427**, 225 (2004).
4. E. Kim, M. H. W. Chan, *Science* **305**, 1941 (2004).
5. A. S. C. Rittner, J. D. Reppy, *Phys. Rev. Lett.* **97**, 165301 (2006).
6. Y. Aoki, J. C. Graves, H. Kojima, *Phys. Rev. Lett.* **99**, 015301 (2007).
7. A. Penzev, Y. Yasuta, M. Kubota, *J. Low Temp. Phys.* **148**, 677 (2007).
8. M. Kondo, S. Takada, Y. Shibayama, K. Shirahama, *J. Low Temp. Phys.* **148**, 695 (2007).
9. B. Hunt *et al.*, *Science* **324**, 632 (2009).
10. H. Choi, S. Kwon, D. Y. Kim, E. Kim, *Nat. Phys.* **6**, 424 (2010).
11. A. S. C. Rittner, J. D. Reppy, *Phys. Rev. Lett.* **101**, 155301 (2008).
12. X. Lin, A. C. Clark, M. H. W. Chan, *Nature* **449**, 1025 (2007).
13. J. Day, J. Beamish, *Phys. Rev. Lett.* **96**, 105304 (2006).
14. S. Sasaki, R. Ishiguro, F. Caupin, H. J. Maris, S. Balibar, *Science* **313**, 1098 (2006).
15. M. W. Ray, R. B. Hallock, *Phys. Rev. Lett.* **100**, 235301 (2008).
16. J. Day, J. Beamish, *Nature* **450**, 853 (2007).
17. O. Syshchenko, J. Day, J. Beamish, *Phys. Rev. Lett.* **104**, 195301 (2010).
18. D. J. Bishop, J. D. Reppy, *Phys. Rev. Lett.* **40**, 1727 (1978).
19. Materials and methods are available as supporting material on *Science* Online.
20. J. Day, O. Syshchenko, J. Beamish, *Phys. Rev. Lett.* **104**, 075302 (2010).
21. P. W. Anderson, *Nat. Phys.* **3**, 160 (2007).
22. A. Penzev, Y. Yasuta, M. Kubota, *Phys. Rev. Lett.* **101**, 065301 (2008).
23. S. I. Shevchenko, *Sov. J. Low Temp. Phys.* **13**, 61 (1987).
24. M. Boninsegni *et al.*, *Phys. Rev. Lett.* **99**, 035301 (2007).
25. J. Wu, P. Phillips, *Phys. Rev. B* **78**, 014515 (2008).
26. J. Bossy, J. V. Pearce, H. Schober, H. R. Glyde, *Phys. Rev. B* **78**, 224507 (2008).
27. G. Biroli, C. Chamon, F. Zamponi, *Phys. Rev. B* **78**, 224306 (2008).
28. B. Svistunov, *Physica B* **404**, 521 (2009).
29. K.-M. Tam, S. Geraedts, S. Inglis, M. J. P. Gingras, R. G. Melko, *Phys. Rev. Lett.* **104**, 215301 (2010).
30. X. Rojas, A. Haziot, V. Bapst, S. Balibar, H. J. Maris, *Phys. Rev. Lett.* **105**, 145302 (2010).
31. A. V. Balatsky, M. J. Graf, Z. Nussinov, S. A. Trugman, *Phys. Rev. B* **75**, 094201 (2007).
32. Z. Nussinov, A. V. Balatsky, M. J. Graf, S. A. Trugman, *Phys. Rev. B* **76**, 014530 (2007).
33. M. J. Graf, Z. Nussinov, A. V. Balatsky, *J. Low Temp. Phys.* **158**, 550 (2010).
34. A. F. Andreev, *JETP Lett.* **85**, 585 (2007).
35. I. Iwasa, *Phys. Rev. B* **81**, 104527 (2010).

Acknowledgments: We are grateful for discussions and communications with J. Beamish, D. M. Ceperley, M. H. W. Chan, J. Day, A. T. Dorsey, R. B. Hallock, H. Kojima, D. M. Lee, A. J. Leggett, E. Mueller, D. R. Nelson, J. M. Parpia, N. V. Prokof'ev, J. D. Reppy, P. C. E. Stamp, B. Svistunov, and M. Troyer. These studies were supported by the National Science Foundation under grants DMR-0806629 and NSF PHY05-51164 to the Kavli Institute for Theoretical Physics. Work at Los Alamos was supported by U.S. Department of Energy grant DE-AC52-06NA25396 to the Center for Integrated Nanotechnologies and through the Laboratory Directed Research and Development program.

Supporting Online Material

www.sciencemag.org/cgi/content/full/332/6031/821/DC1
Materials and Methods
SOM Text
Figs. S1 to S7
References

19 January 2011; accepted 4 April 2011
10.1126/science.1203080

Very Large Capacitance Enhancement in a Two-Dimensional Electron System

Lu Li,[1] C. Richter,[2] S. Paetel,[2] T. Kopp,[2] J. Mannhart,[2] R. C. Ashoori[1]*

Increases in the gate capacitance of field-effect transistor structures allow the production of lower-power devices that are compatible with higher clock rates, driving the race for developing high-κ dielectrics. However, many-body effects in an electronic system can also enhance capacitance. Onto the electron system that forms at the $LaAlO_3/SrTiO_3$ interface, we fabricated top-gate electrodes that can fully deplete the interface of all mobile electrons. Near depletion, we found a greater than 40% enhancement of the gate capacitance. Using an electric-field penetration measurement method, we show that this capacitance originates from a negative compressibility of the interface electron system. Capacitance enhancement exists at room temperature and arises at low electron densities, in which disorder is strong and the in-plane conductance is much smaller than the quantum conductance.

The concept of negative compressibility describes an effect of electron-electron interactions, in which the exchange and correlation energies among electrons lower the chemical potential of an electron system as the electron density increases (*1–9*). This effect has been observed to enhance the capacitance of semiconductor two-dimensional (2D) electronic systems by a few percent (*7*) beyond the expected geometric capacitance. Here, we report very large capacitance enhancements (>40%) in capacitor devices that are made with the electron system generated at the TiO_2-terminated $LaAlO_3/SrTiO_3$ (LAO/STO) interface (*10*, *11*). Simple modifications to the structures described could yield a capacitance enhancement greater than 100%. Strong electronic correlations (*12–14*) may be used to engineer yet larger capacitances (*15*).

We fabricated capacitor devices on LAO/STO heterostructures through in situ growth of $YBa_2Cu_3O_{7-\delta}$ (YBCO) or Au films on the surface of the LAO. As shown in Fig. 1A, we then patterned the films on top of the LAO surface. Nb films were deposited into ion-milled holes to make ohmic contacts to the conductive layer at the LAO/STO interface (*16*). Each top gate provides a two-terminal capacitor. The thickness of the LAO layer was either 10 or 12 unit cells. A photograph of a sample is displayed in Fig. 1B, with electrical leads wire-bonded to the ohmic contacts near the edge of the wafer and a lead connected to a circular top gate.

The two-terminal capacitance of the capacitor device was measured with a home-built capacitance bridge, which enabled us to measure the capacitance in the frequency range between 1 Hz to 2 MHz with ~20-μrad resolution in the phase measurement of the impedance. We were able to vary the DC voltage on the top gate and track the capacitance change with gate voltage (*16*).

We measured the capacitance between a top gate and the interface at frequencies f ranging from 8 to 2000 Hz while varying a top gate voltage V_g. Device 1 was fabricated on a sample with 12 unit cells of LAO. On the top surface of the LAO film, a circular YBCO top gate with a diameter of 200 μm was patterned. Figure 2A displays the capacitance C versus V_g curves of device 1 at 4.2 K. Similar curves are shown in Fig. 2B for device 2 with an LAO thickness of 10 unit cells and a 350-μm-diameter YBCO top gate. Substantial leakage (resistances less than 5 megohms) through the LAO barrier occurred at voltages to the left of the red line in Fig. 2A and to the right of the red line in Fig. 2B. Data in these regions were not used in the analysis because the leakage resistance dropped to the magnitude of the in-plane resistance. We expect that such leakage current alters the voltage across the device and changes the charge distribution within the sample. By examining the capacitance at high electron densities at which interaction effects on the capacitance are usually small, we determined the dielectric constant of the insulating LAO layer. Given the capacitance values at V_g = 0 and at large positive V_g for device 1, the size of the gate, and the thickness of the LAO film, we found the LAO dielectric constant $D \sim 18D_0$, where D_0 is the dielectric constant of vacuum. This value is lower than the dielectric constant of single crystals of LAO but agrees with one of the molecular beam epitaxy–grown films (*17*).

Both of the capacitor devices showed a sharp depletion signal at well-defined gate fields. For device 1, at $V_g < 0.2$ V the capacitance is strongly diminished, which suggests that the electron density underneath the circular gate was substantially suppressed by the electric field. For device 2, a positive $V_g \geq 0.28$ V is needed to create a conducting channel underneath the top gate. In this case, we observed a clear and sharp depletion in the capacitance curves, which suggests that the mobile carrier density at the interface is tuned to zero by V_g.

For device 2, the interface underneath the gate was not conductive at V_g = 0, even though the regions away from the YBCO circular pads were conductive (the two-terminal resistance between the Nb ohmic contacts is of order 500 ohms at 4.2 K). In testing these samples during at least four different coolings from room temperature to 4.2 K for each sample, we noticed that the depletion voltage varied slightly with thermal cycling. However, the depletion voltage of devices with 12–unit cell LAO was always negative, whereas that for devices with 10–unit cell LAO layers was positive. This difference suggests that the YBCO top gate tends to deplete the interface underneath the gate: The larger the

[1]Department of Physics, Massachusetts Institute of Technology (MIT), Cambridge, MA 02139, USA. [2]Center for Electronic Correlations and Magnetism, University of Augsburg, Augsburg 86135, Germany.

*To whom correspondence should be addressed. E-mail: ashoori@mit.edu

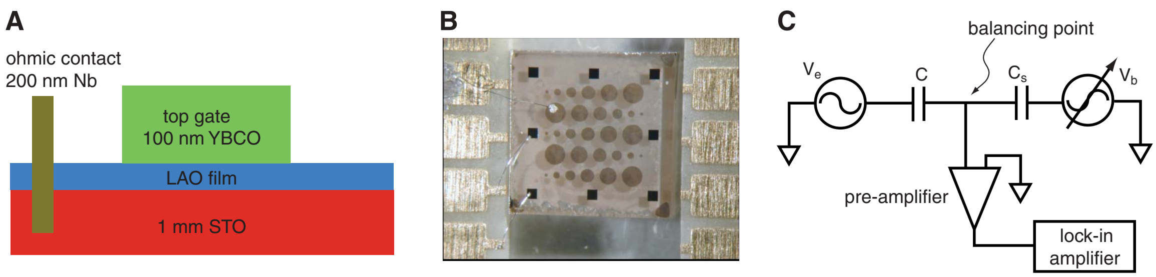

Fig. 1. Sample layout and capacitance bridge setup. (**A**) Sketch of the oxide interface layout. A thin layer of LAO (10 or 12 unit cells thick) is deposited onto the top of a TiO_2-terminated STO substrate. YBCO top gates are deposited and patterned above the LAO layer, and Nb ohmic contacts are deposited close to the corners of the wafer. (**B**) Picture of a YBCO/LAO/STO sample with leads attached. The wafer is square with a side length of 5 mm. The diameter of the YBCO circular top gates varies between 50 and 500 μm. (**C**) Setup sketch of the capacitance bridge. In one arm of the bridge, C stands for the sample capacitor, excited by an ac excitation voltage V_e. In the other arm, another ac voltage V_s with the same frequency is applied to a standard capacitor C_s. The signal at the balancing point is measured with a pre-amplifier and a lock-in amplifier. During the measurement, with the phase and the amplitude of V_e held stable, V_s is varied both in phase and in amplitude to null the signals at the balancing point.

distance is between the interface and the gate, the smaller is the depletion effect. This response might be attributable to the difference between the work function of YBCO and the vacuum, to the polar nature of the YBCO ionic layers, or to strain by lattice mismatch.

Near depletion, we observed a large enhancement of the capacitance, shown in detail in the inset of Fig. 2A. At its peak, the capacitance considerably exceeds C_{hd}, the capacitance at high densities $C_{hd} \sim C_{geom} = DA/d$, where A and d are the cross sections and the dielectric thicknesses of the capacitors, respectively. The difference between C_{hd} and C_{geom} is usually small. (Below, all the C_{geom} values are treated to be the same as C_{hd}.) The capacitance upturn at small n, where n is the carrier density, was observed at low frequency ($f < 15$ Hz). As shown by Fig. 2A, as the frequency f decreases from 20 kHz to 20 Hz, C is independent of frequency over a large range of V_g. However, at low densities the peak in C continues to grow and moves to lower V_g as f is reduced. This frequency dependence is reproduced in other devices. Figure 2B shows the $C - V_g$ curves of device 2 with 10–unit cell LAO film, displaying a considerably larger low-density capacitance enhancement than that of device 1. For measurements at two different frequencies, the upturns coincide between $0.33\ \mathrm{V} \le V_g \le 0.4$ V. Below $V_g = 0.33$ V, the curve taken at $f = 14.231$ Hz diminishes, whereas that at $f = 5$ Hz keeps increasing and drops at lower V_g. The overlapping part of these two capacitance curves is the dc limit of the capacitance curve. In this regime, the out-of-phase charging signal stays small, displaying a different trend (*16*).

Measuring at frequencies as low as 5 Hz, we have not found a limit to the divergence. For these low frequencies, we observed a >40% enhancement in the sample capacitance, which is far larger than ever previously observed, even in high-mobility GaAs-based devices (*7*). Presumably, at sufficiently low frequencies disorder and the proximity of the metal-insulator phase transition limits the sharpness of the upturn. The greater capacitance upturn in device 2 (10 unit cells thick) than that in device 1 (12 unit cells thick) may reflect less disorder. The capacitance enhancement observed at low frequencies does not arise from the frequency dependence of the LAO dielectric constant. Instead, the low-frequency upturn arises from the large *RC*-time constants of the devices. Because the mobile carrier density is strongly suppressed near the depletion (*16*), the resistance R of the long-distance lateral current path through the interface is high.

As a quantum paraelectric (*18*), STO is ferroelectric-like at low temperature, at which its dielectric constant is enhanced greatly. The enhancement of STO dielectric constant vanishes above 30 to 50 K. However, we still observed a capacitance enhancement similar to the one found at 4 K at room temperature. Figure 2C shows the $C - V_g$ curves (*16*) close to the depletion in device 3. In this device, a circular Au pad with 350 μm was deposited to serve as top gate because it was found that at 300 K, gold caused less leakage than did YBCO (*16*). Although a leakage current to the gate appeared below –0.6 V [the gate-to-channel resistance drops to the megohm range near depletion (fig. S3) (*16*)], the room-temperature $C - V_g$ curves are similar to those of the YBCO-gated devices shown in Fig. 2, A and B. As V_g decreased from 0 V, C decreased slowly. However, near depletion C increased rapidly at low f. Measured at $f = 5$ Hz, the peak of C was 10% greater than that of C_{hd}. This room-temperature behavior provides additional evidence ruling out anomalies of the dielectric function of STO as the origin of the capacitance enhancement.

Charging a capacitor C with charge e does not simply require a change in voltage $\delta V = e/C_{geom}$. Because of the finite $dn/d\mu$, an extra voltage $(d\mu/dn)/eA$ is required, where μ is the chemical

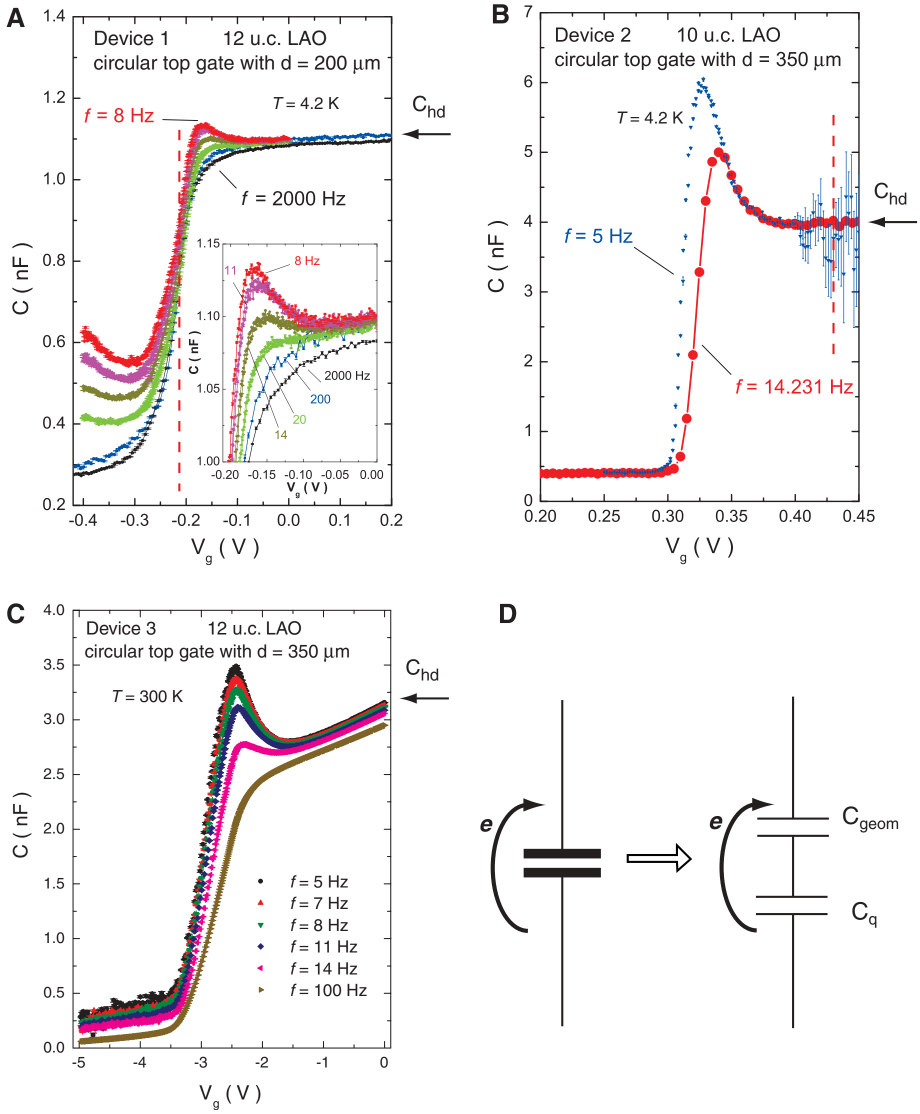

Fig. 2. The gate voltage dependence of the capacitance. (**A**) The C versus V_g curve of device 1 with a diameter of 200 μm and LAO 12 unit cells thick. The curves are taken at $T = 4.2$ K at various frequencies between 8 and 2000 Hz. The capacitance at high carrier density C_{hd} is marked with an arrow. As shown in the inset for the region near depletion, the capacitance values increase and exceed C_{hd}. At V_g smaller than −0.22 V, marked by the red dashed line, the capacitance curves are frequency dependent, which is probably a result of dc leakage through the LAO barrier. (**B**) The $C - V_g$ curve of device 2 with diameter 350 μm and LAO 10 unit cells thick. The enhancement of the capacitance is even more pronounced because the peak of C is about 40% larger than C_{hd} at $f = 5$ Hz. For this device, a leakage current develops at higher V_g, and the 5 Hz capacitance measurement becomes noisier. The red dashed line indicates a leakage resistance of 5 megohms. (**C**) The $C - V_g$ curve of device 3 with 350 μm gold top gate and LAO 12 unit cells thick, measured at room temperature. (**D**) Equivalent circuit of geometric capacitance C_{geom} and the quantum capacitance C_q. The charging of the electrodes is represented by arrows. The geometric capacitance C_{geom} is determined by the device dimensions, marked as C_{hd} in (A) to (C).

potential. As shown in Fig. 2D, the measured capacitance C is the in-series combination of the geometric capacitance C_{geom} and the quantum capacitance $C_q = Ae^2 dn/d\mu$:

$$\begin{aligned} 1/C &= 1/C_{geom} + 1/C_q \\ &= 1/C_{geom} + 1/[Ae^2(dn/d\mu)] \end{aligned} \quad (1)$$

The observed enhancement of C reveals that $dn/d\mu$ is negative, providing evidence for a negative electronic compressibility (*3*). In measurements that display negative compressibility in semiconductor samples, the effect arises from the electron-electron interactions beyond the Hartree approximation (*1*, *2*). These interactions increase the chemical potential with decreasing electron density.

One consequence of the negative quantum capacitance is that the interface overscreens the external electric fields (*4*–*8*). To explore the possible existence of this overscreening effect, we carried out a field penetration measurement using a technique developed by Eisenstein (*4*, *5*). As shown in Fig. 3A, the interface was grounded, and we measured the current to the top gate as we applied a small ac excitation voltage V_{ac} on the back gate. The current I_y is proportional to the electric field penetrating from the back gate through the grounded interface (*16*). The results are shown in Fig. 3, B and C, in which I_y/f is proportional to $d\mu/dn$, the inverse of the compressibility. A negative divergence of the penetration field occurs close to depletion, at which the carrier density is below 2×10^{12} cm^{-2}. Here, the carrier density is estimated by integrating the

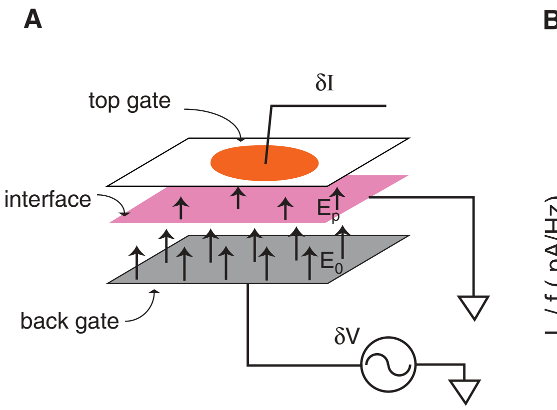

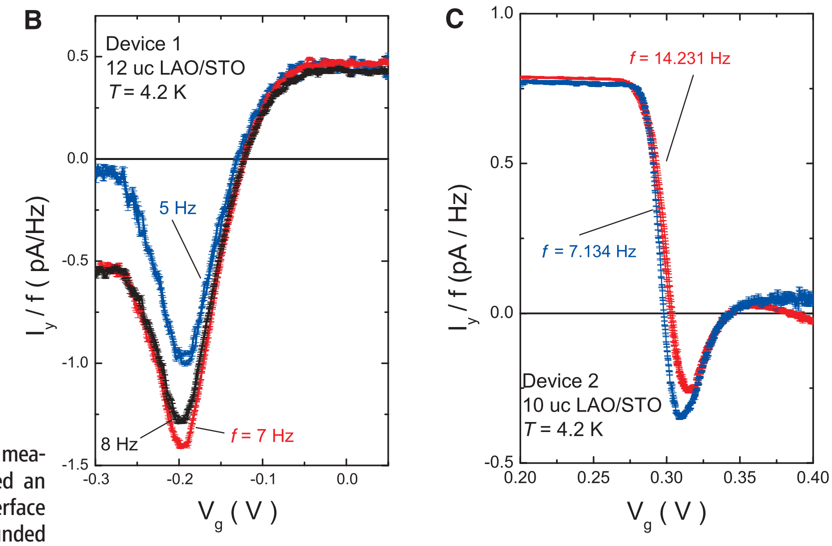

Fig. 3. Penetration field measurement. (**A**) Sketch of the measurement setup. With the interface grounded, we applied an external electric field E_0 from the back gate to the interface and detected the electric field that penetrates the grounded interface layer. The penetration field E_p is determined by measuring the current from the device top gate. (**B**) The penetration current I_y divided by the measurement frequency for device 1 at $T = 4.2$ K measured at three excitation frequencies. At V_g near zero, the penetration current is proportional to f and is constant over a broad range of -0.05 V $\leq V_g \leq 0.05$ V. For $V_g < -0.18$ V, I_y/f displays a frequency dependence, which is probably caused by effects of current leakage through the LAO layer. (**C**) The penetration signal for device 2 at $T = 4.2$ K measured at two selected frequencies. At 0.31 V $< V_g <$ 0.34 V, the negative values of the penetration current demonstrate that E_p is opposite to E_0; the conductive interface overscreens the external fields at low carrier densities. At larger $V_g >$ 0.37 V, again a f-dependent signal is present, together with a measurable current leakage through the LAO barrier.

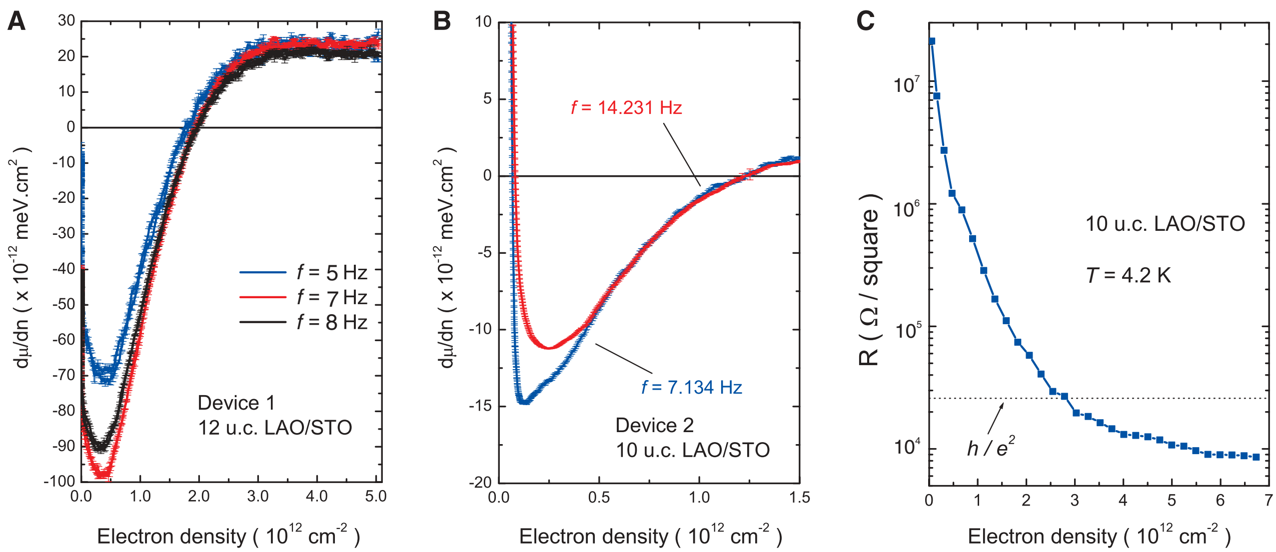

Fig. 4. The inverse of compressibility $d\mu/dn$ determined from penetration field measurements on (**A**) device 1 and (**B**) device 2. The electron density at the interface is determined by integrating the C versus V_g curve at the lowest frequency achieved. (**C**) The density n dependence of the lateral resistivity of a different device fabricated in the same 10–unit cell LAO/STO wafer. The device diameter is 500 μm. The resistivity is determined by tracking the frequency dependence of the out-of-phase charging signals (figs. S1 and S2) (*16*).

capacitance between the top gate and the interface at the lowest measurement frequency. The negative current observed at low carrier densities reveals that the electric field penetrating through the metallic interface is negative, which arises from overscreening of the external field by the mobile electrons at the LAO/STO interface. Such a negative signal cannot be reconciled with any change of the dielectric properties of the LAO layer or the STO substrate. To further explore the electronic properties of the interface, we follow the analysis of (*6*), which has shown that for low frequencies f the penetration current I_y goes as

$$I_y = 2\pi f C_1 C_2 V_{ac}/C_q \quad (2)$$

where C_2 is the geometric capacitance between the top gate and the interface and C_1 is that between the back gate and the interface normalized by the area of the top gate. We measured C_1 and C_2 directly. For device 1, C_1 = 4.67 pF, C_2 = 1.1 nF, and V_{ac} = 20 mV. For device 2, C_1 = 14.3 pF, C_2 = 4.01 nF, and V_{ac} =10 mV. [For device 3, the penetration signal was small and difficult to resolve at 300 K because the STO dielectric constant decreases by three orders of magnitude (figs. S4 and S5)].

For device 1, at $V_g < -0.18$ V, the penetration current I_y was no longer proportional to f, which might be attributed to the dc leakage in this region, although we do not know the precise mechanism by which a dc leakage would affect the measurement. The same deviation occurred with device 2 at positive $V_g > 0.37$ V. Thus, we excluded these regions in the analysis.

Using the penetration current data, we determined the quantum capacitance C_q and used Eq. 2 to compute $d\mu/dn$. Figure 4, A and B, shows the $d\mu/dn(n)$ dependence of devices 1 and 2, respectively. The zero of density was not well defined because the measurement frequency at very small densities was not sufficiently low to charge the device fully. In a wide-density range, $d\mu/dn$ stayed negative, which provides direct evidence of the negative compressibility of the interface electron system.

The observed enhancement of capacitance and negative compressibility exist in a disordered electron system. As shown in Fig. 4C, near depletion the sheet resistivity of the interfacial layer becomes much larger than the resistance quantum h/e^2. Thus, the electrons are localized at low densities, and the system is well outside the range of the free electron approximation (figs. S1 and S2).

The large capacitance enhancement that results from the negative compressibility offers a possible gating mechanism to switch transistors by using small gate voltages. This could diminish heating in future devices (*15*, *19*, *20*). We emphasize that the observed large enhancement of C is affected by the large geometric capacitance C_{geom}. Taking derivatives on both sides of Eq. 1, we get $\delta C/C = C\delta C_q/C_q^2$; a device with larger C_{geom} per unit area will have a larger relative enhancement of the total capacitance. An interface capacitor device with a thinner $LaAlO_3$ layer may thus reveal an even larger capacitance enhancement at low carrier densities. As material quality improves, it is plausible that at low densities the effective gate-layer capacitance could increase to several times the geometric value. Transistors fashioned from the oxide interface or other systems with small carrier densities could then have an effectively very "high-κ" electrode, allowing the creation of small transistors that switch at low voltages and minimal gate-to-channel leakage (*20*).

References and Notes

1. B. I. Bello *et al.*, *Zh. Eksp. Teor. Fiz.* **80**, 1596 (1981) [Sov. Phys. JETP 53, 822 (1981)].
2. B. Tanatar, D. M. Ceperley, *Phys. Rev. B* **39**, 5005 (1989).
3. S. V. Kravchenko, D. A. Rinberg, S. G. Semenchinsky, V. M. Pudalov, *Phys. Rev. B* **42**, 3741 (1990).
4. J. P. Eisenstein, L. N. Pfeiffer, K. W. West, *Phys. Rev. Lett.* **68**, 674 (1992).
5. J. P. Eisenstein, L. N. Pfeiffer, K. W. West, *Phys. Rev. B* **50**, 1760 (1994).
6. S. C. Dultz, H. W. Jiang, *Phys. Rev. Lett.* **84**, 4689 (2000).
7. G. Allison *et al.*, *Phys. Rev. Lett.* **96**, 216407 (2006).
8. S. Shapira *et al.*, *Phys. Rev. Lett.* **77**, 3181 (1996).
9. R. C. Ashoori, R. H. Silsbee, *Solid State Commun.* **81**, 821 (1992).
10. A. Ohtomo, H. Y. Hwang, *Nature* **427**, 423 (2004).
11. S. Thiel, G. Hammerl, A. Schmehl, C. W. Schneider, J. Mannhart, *Science* **313**, 1942 (2006).
12. S. Okamoto, A. J. Millis, N. A. Spaldin, *Phys. Rev. Lett.* **97**, 056802 (2006).
13. J. Mannhart, D. G. Schlom, *Science* **327**, 1607 (2010).
14. J. Mannhart, D. H. A. Blank, H. Y. Hwang, A. J. Millis, J.-M. Triscone, *MRS Bull.* **33**, 1027 (2008).
15. T. Kopp, J. Mannhart, *J. Appl. Phys.* **106**, 064504 (2009).
16. Materials and methods are available as supporting material on *Science* Online.
17. A. F. Edge *et al.*, *Appl. Phys. Lett.* **88**, 112907 (2006).
18. K. A. Müller, H. Burkard, *Phys. Rev. B* **19**, 3593 (1979).
19. M. S. Loth, B. Skinner, B. I. Shklovskii, *Phys. Rev. E Stat. Nonlin. Soft Matter Phys.* **82**, 056102 (2010).
20. P. M. Solomon, in *Future Trends In Microelectronics: From Nanoparticles to Sensors and Energy*, S. Luryi, J. M. Xu, A. Zaslavsky, Eds. (Wiley IEEE Press, Hoboken, NJ, 2010), pp. 127–140.

21. The authors gratefully acknowledge helpful discussions and interactions with O. E. Dial, M. M. Fogler, R. Jany, P. A. Lee, L. S. Levitov, A. J. Millis, B. Shklovskii, P. Solomon, and J.-M. Triscone. This work was supported by ARO-54173PH, by the National Science Foundation through the Nanoscale Science and Engineering Center program, by the Deutsche Forschungsgemeinschaft (TRR 80), the European Commission (OxIDes), and by the Nanoscale Research Initiative. L. Li thanks the MIT Pappalardo Fellowships in Physics for support.

Supporting Online Material

www.sciencemag.org/cgi/content/full/332/6031/825/DC1
Materials and Methods
SOM Text
Figs. S1 to S5
References

11 February 2011; accepted 28 March 2011
10.1126/science.1204168

Beating Crystallization in Glass-Forming Metals by Millisecond Heating and Processing

William L. Johnson,* Georg Kaltenboeck, Marios D. Demetriou, Joseph P. Schramm, Xiao Liu, Konrad Samwer, C. Paul Kim, Douglas C. Hofmann

The development of metal alloys that form glasses at modest cooling rates has stimulated broad scientific and technological interest. However, intervening crystallization of the liquid in even the most robust bulk metallic glass-formers is orders of magnitude faster than in many common polymers and silicate glass-forming liquids. Crystallization limits experimental studies of the undercooled liquid and hampers efforts to plastically process metallic glasses. We have developed a method to rapidly and uniformly heat a metallic glass at rates of 10^6 kelvin per second to temperatures spanning the undercooled liquid region. Liquid properties are subsequently measured on millisecond time scales at previously inaccessible temperatures under near-adiabatic conditions. Rapid thermoplastic forming of the undercooled liquid into complex net shapes is implemented under rheological conditions typically used in molding of plastics. By operating in the millisecond regime, we are able to "beat" the intervening crystallization and successfully process even marginal glass-forming alloys with very limited stability against crystallization that are not processable by conventional heating.

A glass is formed when a liquid is undercooled below the melting point, T_M, of the competing crystalline solid(s) and then freezes at a glass transition temperature, T_g, without crystallizing. Undercooled liquids and glasses are metastable phases, implying that given sufficient time, both will transform to more stable crystalline solids. The glass-forming ability of a liquid is a measure of its metastability; that is, its resistance to crystallization in the undercooled temperature region between T_g and T_M. Robust glass-forming silicate, polymer, and molecular melts exhibit superior metastability, with

Keck Laboratory of Engineering, California Institute of Technology, Pasadena, CA 91125, USA.

*To whom correspondence should be addressed. E-mail: wlj@caltech.edu

crystallization time scales that range from minutes to hours, or longer, over the entire undercooled liquid region. Metallic glass formation was first reported by Klement *et al*. (*1*) in a eutectic Au-Si alloy that was rapidly quenched through the undercooled liquid region at a cooling rate of 10^6 K/s. At the time, this result was considered surprising because crystallization in undercooled metals and atomic liquids was presumed to be so rapid as to preclude glass formation altogether. Metal alloys with enhanced liquid metastabiity that form glass at substantially lower cooling rates (1 to 10^3 K/s), so-called bulk metallic glasses, were first developed in the early 1980s (*2*). Their development (*2*, *3*) and the use of techniques to suppress the nucleation of crystals such as containerless processing (*4*, *5*), fluxing (*2*), and preparation of high-purity alloys (*6*) led to improved metastability of metallic glass-forming melts. Nevertheless, the crystallization rates of these glass-forming metallic liquids remain orders of magnitude higher than those of common glass-forming polymers, silicates, or molecular liquids. Consequently, experimental studies in undercooled metallic liquids are broadly limited by the intervening crystallization of the melt (*7*, *8*). Measurements of thermodynamic functions, viscosity, atomic diffusion, and crystallization kinetics are generally restricted to temperatures just below T_M or just above T_g and are precluded at intermediate undercooling. For instance, viscosity data on metallic glass-forming melts are generally nonexistent for viscosities in the range from 10^1 to 10^6 Pa·s, because time scales for traditional rheometry exceed crystallization time scales. On the technology side, the application of net-shape thermoplastic forming processes such as injection molding (*9*, *10*), blow molding (*11*), and microreplication (*12*–*14*) to fabricate high-performance, net-shape metal-glass hardware was met with limited success (*15*). For polymer plastics, these technologies have been transformative due in large part to using relatively low process viscosities of 1 to 10^4 Pa·s (*16*). Implementation of these methods for metallic glasses has been restricted, however, because of high melt viscosities (>10^6 Pa·s) in the accessible temperature range near the glass transition.

To appreciate the difficulty of avoiding crystallization while processing a liquid at intermediate undercooling, consider the time scale required to relax spatial temperature variations within a sample by heat conduction. For a metallic glass of typical thermal diffusivity of ~10^{-2} cm^2/s and sample dimensions of several millimeters, this time scale is typically 1 to 10 s. Several multiples of this time are required to establish a uniform temperature. Heating methods that supply heat through the sample boundary do not permit uniform heating in shorter times. To heat more rapidly requires that power be dissipated homogeneously and volumetrically throughout the sample so that temperature variations are never created. Ohmic dissipation by a uniform current density is one way to achieve this. In this work, we exploited the large and nearly temperature-independent electrical resistivity of metallic glasses (*17*, *18*) and used an intense millisecond current pulse to achieve uniform ohmic heating from the glass to the undercooled liquid at rates of ~10^6 K/s. We used high-frame-rate video, thermal imaging, and high-speed infrared pyrometry to conduct millisecond time-scale viscosity and dynamic enthalpy measurements in the undercooled liquid at temperatures where intervening crystallization precludes conventional rheometry and calorimetry, which are limited to much lower heating and cooling rates. We further demonstrated rapid millisecond injection molding of metallic glass rods into net-shape metallic glass parts under liquid viscosity, pressure, and strain rate conditions widely established as optimum in plastic-forming technology.

When a metallic glass is continuously heated, the glass transition at T_g and onset of crystallization at T_x are heating rate–dependent, and the rate-dependent temperature interval, $\Delta T = T_x - T_g$, defines an available process window for the undercooled liquid. Larger values of ΔT indicate higher metastability of the liquid with respect to crystallization. Figure 1 illustrates the dependence of T_x and T_g on heating rate for the highly processable bulk metallic glass Vitreloy 1 ($Zr_{41.2}Ti_{13.8}Cu_{12.5}Ni_{10}Be_{22.3}$). This alloy is a superior metallic glass-former, with a critical casting thickness of 3 to 4 cm. At a conventional heating rate of 20 K/min, one has $T_g \approx 620$ K, $T_x \approx 705$ K, and $\Delta T \approx 85$ K (*19*). Above a critical heating rate of ~200 K/s, crystallization is avoided entirely during heating (*20*). This heating rate is roughly two orders of magnitude greater than the critical cooling rate of ~2 K/s (*21*) that is required to avoid crystallization during quenching of the liquid from high temperature to form the glass. Such heating and cooling rate asymmetry is observed for other systems [such as $Pd_{43}Ni_{10}Cu_{27}P_{20}$ (*22*)] and is believed to be a general feature of the crystallization kinetics of a metallic glass. For comparison, a marginal glass-forming alloy (a metallic glass with critical casting thickness limited to few millimeters) will exhibit a crystallization curve as in Fig. 1 that is shifted to the left by about two orders of magnitude and thereby have a critical heating rate of ~10^4 K/s. As illustrated in Fig. 1, our novel approach permits heating at rates of ~10^6 K/s to a preselected liquid temperature and thereby enables access to temperatures shown in the upper left quadrant of Fig. 1 on time scales many orders of magnitude shorter than previously possible.

The use of electrical current or current pulses and associated Joule heating to locally cut and shear metallic-glass ribbons was reported 20 years ago by Ballard *et al*. (*23*). In what could be viewed as a precursor to the present work, Gibbs *et al*. (*24*) and Zaluska, Kulik, and Matyja (*25*, *26*) used ohmic heating to carry out rapid transient annealing of ferromagnetic metallic-glass ribbons. Yavari and co-workers (*27*, *28*) used a current-carrying tungsten electrode tip to locally heat and engrave surfaces, and performed joining-welding of rods by passing a large current density through the junction between the rods. In contrast, we focused on uniform volumetric heating of bulk samples to temperatures spanning the entire undercooled liquid region and on subsequent rapid characterization and processing of the undercooled melt.

The electrical resistivity ρ_e of metallic glasses and corresponding liquids is relatively large (~100 to 250 μΩ·cm), exhibits a small and frequently negative temperature coefficient [$|S| = |(1/\rho_e)d\rho_e/dT| \leq 1 \times 10^{-4}$ K^{-1}] (*17*, *18*), and varies smoothly and continuously as the glass transition at T_g is traversed. Crystalline metals and alloys have much smaller resistivity (typically 1 to 50 μΩ·cm), a larger and positive temperature coefficient ($S \sim 10^{-2}$ to 10^{-4} K^{-1}), and

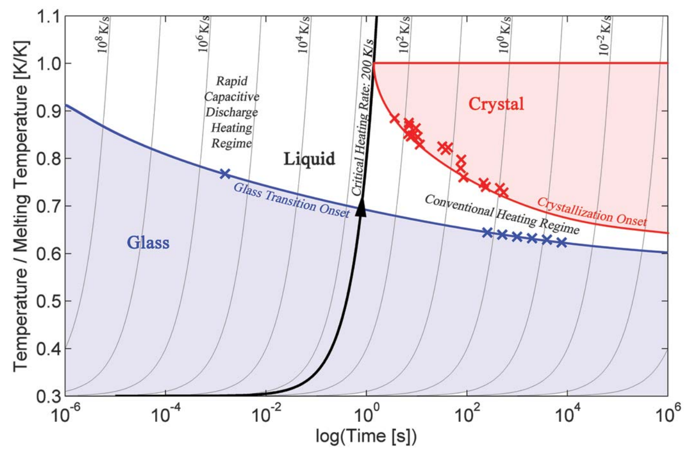

Fig. 1. Glass-transition onset temperature and crystallization onset temperature versus time for the metallic glass Vitreloy 1 at varying heating rates. Glass transition data are taken from Wang *et al*. (*19*) and crystallization data from Schroers *et al*. (*20*). The critical heating rate to completely bypass crystallization on heating from the glass through the liquid is about 200 K/s (*20*). Conventional heating rates on the order of 1 K/s provide access to the undercooled liquid over a rather narrow temperature range, above which crystallization becomes kinetically favorable. Using the present approach, which enables heating rates on the order of 10^6 K/s, the undercooled liquid is accessible at any temperature above the glass transition, through the melting point and beyond, where the liquid enters the equilibrium state (upper left quadrant in the diagram). The glass transition data point plotted in this regime was obtained in the present study under a heating rate of ~3×10^5 K/s (Fig. 3B).

large discontinuous jump in resistivity on melting. Under high imposed current densities and ohmic dissipation, the heating of crystalline metals tends to spatially localize. Local resistivity and temperature variations (at contacts, interfaces, or inhomogeneities) along the direction of current flow are amplified by increased dissipation in hotter regions. This results in a runaway melting instability as observed, for example, in capacitive discharge welding of metals, in which melting spatially localizes at interfaces, contacts, and areas of high initial resistance. Heating localization in metallic glasses is mitigated by their small $|S|$ and by the absence of a melting discontinuity. A discussion of the requirements for rapid uniform ohmic heating and their application to metallic glasses is provided in the supporting online material (SOM).

In the present work, a capacitor bank with capacitance C = 0.264 F and charging voltage up to V_0 = 200 V was used to store energies up to $E = CV_0^2/2$ = 5280 J. The discharge circuit used was a series RLC circuit tuned to near the critical damping condition that permits a maximum rate of energy dissipation with no circuit ringing or overshoot. For the critically damped circuit, the characteristic time constant for the discharge and dissipation of electrical energy is $\tau_h \approx$ 0.4 ms. See the SOM for details of the RLC circuit and its time response.

Vitreloy 1 rods 4 mm in diameter and 2 cm in length were uniformly heated by capacitive discharge coupled through copper electrodes. The rod was heated from ambient temperature to processing temperatures between T_g and T_M in about 1 ms. After heating, the rod was deformed under a compressive force of ~400 N applied via the electrodes. Figure 2 shows infrared images (20,480 pixels) of the central portion of a rod at 0.75-ms intervals during heating to a final average temperature of 799 K. This final temperature, T_F, is ~180 K above the reported T_g measured by conventional calorimetry (Fig. 1) at a heating rate of 20 K/min. The sample geometry used is shown in Fig. 3A. The center column of Fig. 2 shows the temperature profile measured by the row of pixels located along the rod's vertical centerline. The distribution of temperatures measured by all pixels is shown in the right column of Fig. 2. The half width at half maximum of final temperature distribution (right column of Fig. 2) was ~3.5 K. The low-temperature tail observed in the overall distribution is caused by edge effects visible in the thermal images. Although thermal imaging measures surface temperature, an analysis of dynamic electric field penetration effects by Lohöfer and Pottlacher (29) (see the SOM for more details) shows that temperature inhomogeneity along the radial direction in the rod interior should be less than 1% of the total heating interval, or less than 5 K, with the rod centerline expected to be slightly cooler than the surface. The overall temperature distribution of the heated metallic glass rod is remarkably uniform.

After heating, deformation under the applied load began at an elapsed time of about 3 ms and continued to about 8 ms (Figs. 2 and 3B). The average temperature rose by about 10 to 15 K during compressive deformation of the rod. This delayed rise is attributed to dissipation of the mechanical work performed by the piston during deformation. Beyond 10 ms, the deformed sample began to cool by radiative and conductive heat loss to the surroundings. Cooling, however, becomes significant only on time scales of several tenths of a second—considerably longer than the time scales for which the present data are analyzed.

To observe detailed transient features of the heating history, an ultrafast infrared pyrometer

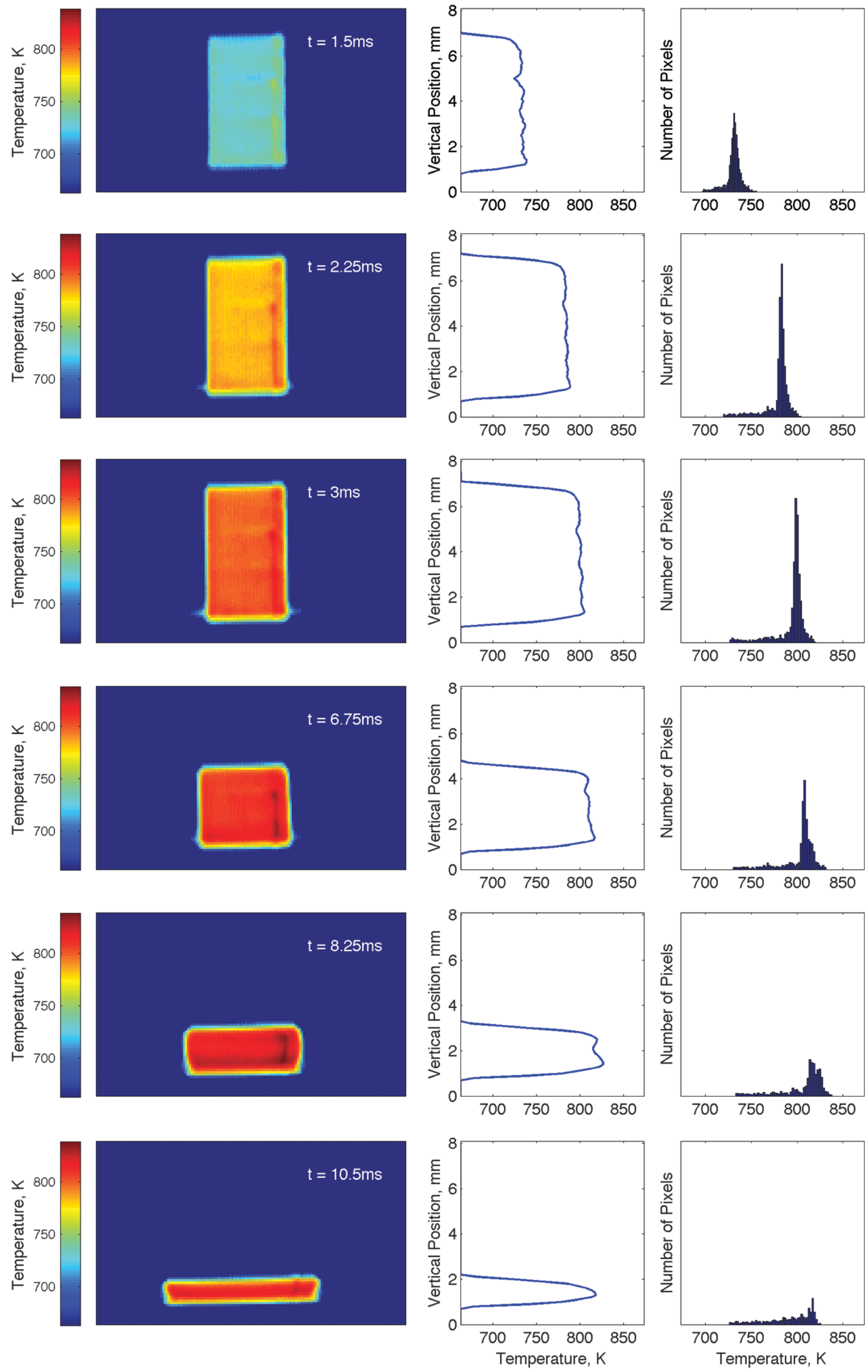

Fig. 2. Thermal imaging during capacitive discharge heating. (**Left column**) Selected frames taken from an infrared imaging camera movie; (**middle column**) temperature measured by pixels along the vertical centerline of the rod; (**right column**) histogram of temperature measured by all pixels in the image. The half width at half maximum of final temperature distribution (right column) is ~3.5 K. The low-temperature tail observed in the overall distribution is caused by edge effects that are visible in the thermal images.

with time resolution of 5 μs (SOM) was used to track temperature with much higher time resolution. The high-resolution heating curve of a separate Vitreloy 1 sample is shown in red in the inset of Fig. 3B. The dimensions and heating parameters of this sample were identical to the one discussed above, but it was heated in the absence of an applied force so that no viscous deformation occurs. A dynamic glass transition at ~775 K was observed, as revealed by a large horizontal step in the time-temperature trace. The step corresponds to an endothermic heat absorption. At the applied heating rate of ~3 × 10^5 K/s, the T_g was shifted by ~155 K above that observed by conventional calorimetry (620 K at a much lower heating rate of 0.67 K/s; Fig. 1). After the glass transition, temperature stabilized at a steady plateau value for several milliseconds, indicating that the final heated liquid lost negligible heat to the surroundings for the duration of the plateau. Measurements performed in this plateau regime will therefore be essentially adiabatic. We fitted the high-resolution heating curve below T_g to the analytic solution for dissipation of power by the RLC circuit, given by $T(t) - T_0 \sim \int_0^t t^2 \exp(-t/\tau_h)dt$, to estimate the heating time constant $\tau_h \approx 0.33$ ms (SOM). The discrepancy between the final steady-state temperature predicted by the fit and that measured by the pyrometer is attributed to the enthalpy absorption associated with the dynamic transition from an overheated glass to the equilibrium liquid, commonly referred to as enthalpy recovery. The rapid pyrometry with microsecond time resolution, together with the known transient power dissipation, permits enthalpy versus temperature measurements at very high heating rates. The system is effectively a scanning calorimeter operating at scanning rates of 10^5 to 10^6 K/s. As discussed earlier, this is enabled by the uniform ohmic dissipation of heat, whereby temperature gradients are never created. In conventional calorimetry, heat is supplied from the sample boundaries, and scanning rates are limited by thermal relaxation times on the order of 1 to 10 s.

Figure 3C summarizes relevant data on the total specific energy dissipated in the rod, h, and average final sample temperature T_F, for numerous experiments. The specific enthalpy per mole, $h = (\varepsilon M/2m)CV^2$ (m is sample mass, and M is the average atomic weight), dissipated in the rod is the total energy stored in the capacitor corrected by an efficiency factor, $\varepsilon = R_s/(R_s + R_0)$, where R_s is the sample resistance, and R_0 is the resistance of the circuit with no sample (SOM). The $h(T_F)$ data collected from a number of experiments are plotted in Fig. 3C to obtain a complete $h(T)$ relation for liquid Vitreloy 1 over the undercooled liquid region between 700 and 900 K, previously inaccessible. This $h(T)$ relation is for a configurationally relaxed liquid (as opposed to an overheated glass). Using conventional calorimetry, Busch *et al.* (*30*) reported the experimental heat capacity (c_P) of Vitreloy 1 for both the glassy and liquid states up to about 700 K and for the high-temperature liquid near T_M down to about 900 K. For the liquid, they fitted their data to interpolate $c_P(T)$ over the undercooled liquid region using a standard functional form $c_P = 3R + 7.50 \times 10^{-3}\ T + 8.17 \times 10^6\ T^2$ (J/mol K), where first two terms in this equation describe the glass below T_g (R is the gas constant). Integrating this expression gives a predicted specific enthalpy $h(T)$ curve that is compared with the present $h(T)$ data plotted in Fig. 3C. The comparison shows excellent agreement.

During dynamic deformation, the time-dependent height of the deforming rod, $y(t)$, was measured using frame-by-frame video images. The digitized data were fitted to an analytic functional form that can be differentiated to determine the velocity, dy/dt, and acceleration, d^2y/dt^2, of the pneumatic drive assembly during defor-

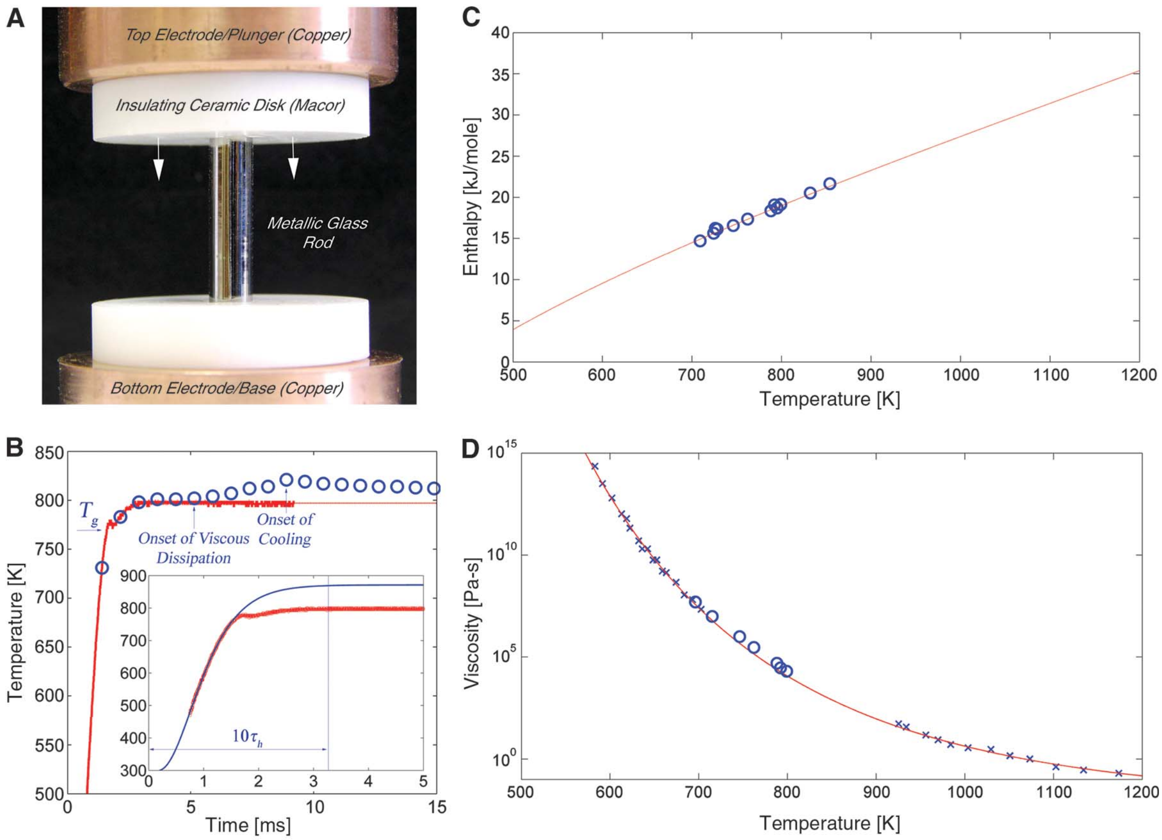

Fig. 3. Thermodynamic and rheological measurements using capacitive discharge heating. (**A**) Experimental setup used to measure enthalpy and viscosity. The metallic glass rod is inset into ceramic disks making contact with copper electrodes. (**B**) (Solid red curve) Thermal trace of an undeformed Vitreloy 1 rod as recorded by a single-pixel high-frame-rate infrared pyrometer. The onset of T_g at 770 K is indicated. (Blue circles) Temperature response of a deforming Vitreloy 1 rod versus time (same dimensions and conditions as above), averaged over multiple pixels as recorded by an infrared thermal imaging camera. The onset of viscous dissipation caused by deformation and the onset of cooling caused by heat loss to the surroundings are indicated. The inset shows a fit (thin blue line) to the thermal trace (thick red line) of the form $T(t) - T_0 \sim \int_0^t t^2 \exp(-t/\tau_h)dt$, predicted for a critically damped RLC circuit (SOM). The fitting formula does not account for the enthalpy absorbed at T_g and consequently overshoots the measured thermal response. (**C**) Experimental enthalpy $h = (\varepsilon/2)CV^2$ versus temperature T_F (blue circles) and enthalpy computed from liquid heat capacity data of Busch *et al.* (*30*) (solid red curve) for Vitreloy 1. (**D**) Viscosity versus temperature for Vitreloy 1 measured using capacitive discharge heating (blue circles) compared with viscosity data reported in the literature (blue crosses) using beam bending, parallel plate rheometry, and Couette viscometry (*34*).

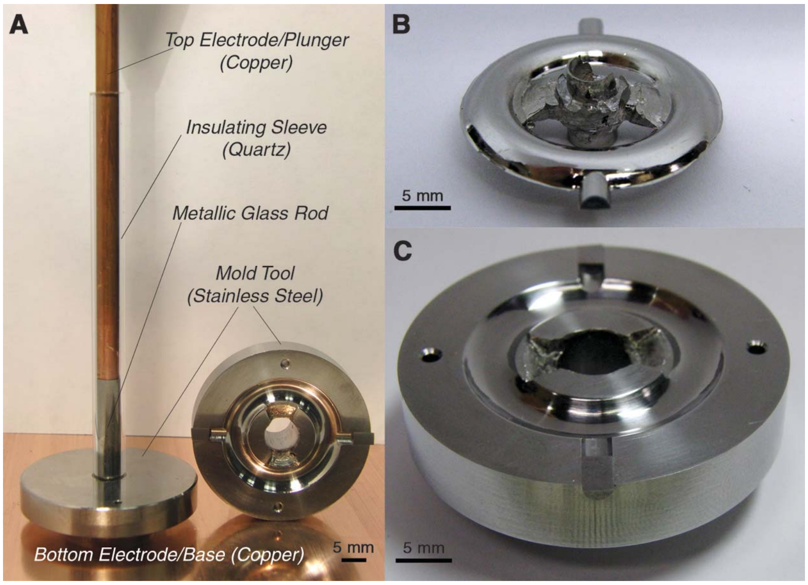

Fig. 4. Experimental setup based on the capacitive discharge heating approach used to demonstrate injection molding of a metallic glass component. (**A**) Basic setup comprising an upper copper electrode used as a plunger, a lower copper electrode used as a base (not shown), and a quartz sleeve used as an insulating barrel to electrically insulate and confine the sample charge. A groove is introduced in the quartz sleeve at the point of contact with the mold runner to enable entry of the softened glass into the mold (not shown). (**B**) A simple "as-molded" $Pd_{43}Cu_{27}Ni_{10}P_{20}$ toroidal metallic glass part formed at a processing temperature of ~720 K using a plunger pressure of ~20 MPa. The sample is free of visible flow defects, and no oxidation can be detected despite being processed in open air. (**C**) Lower half of the mold tool used to mold the metallic glass component.

mation. These data were used to compute strain rate versus time, and with knowledge of the applied force, the viscosity η at T_F. Because the sample temperature increases slightly during deformation (Fig. 3B), the viscosity is measured over a slightly increasing temperature interval. As explained in the SOM, the limited force available (400 N) and response time of the drive system (inertial effects) make the present setup most suitable for measuring viscosities in the range from 10^4 to 10^7 Pa·s. Radiative heat loss from the rod surface to the surroundings, and heat loss by conduction to the ceramic plates and cold electrodes (located several millimeters behind the ceramic surface), can be neglected in the deforming region on the time scale of the experiment (typically 5 to 15 ms). In other words, the viscosity measurements are carried out under essentially adiabatic conditions. Using the relation $\eta = Fy^2/[3\upsilon_0(dy/dt)]$ (*31*), appropriate to the early stage of deformation (SOM), where F is the applied force and υ_0 the sample volume, the viscosity was determined from a number of experiments at various T_F's. In Fig. 3D, the results are compared with previously reported viscosity data on Vitreloy 1 obtained with conventional rheology. Conventional beam-bending and parallel plate rheometry (*32*, *33*) require time scales of at least tens of seconds, which limits data to about 80 K above T_g. Couette viscometry (*34*) at higher temperature (and lower viscosities) similarly requires time scales of at least tens of seconds and is precluded by the intervention of crystallization at temperatures below ~900 K.

The ability to dynamically process metallic glasses at any undercooled liquid temperature on millisecond time scales creates the opportunity to carry out rapid thermoplastic forming at far lower process viscosities and pressures than was previously possible. Commercial injection molding of plastics is carried out at typical temperatures of 450 to 700 K, process viscosities of 1 to 10^4 Pa·s, and injection pressures of 1 to 30 MPa (*16*). To demonstrate injection molding of bulk metallic glasses using typical plastic molding conditions, we designed and constructed a simple injection-molding apparatus. The basic elements of the setup are shown in Fig. 4A. Several variants of this apparatus were used to injection-mold net-shape components from Vitreloy 1 and $Pd_{43}Ni_{10}Cu_{27}P_{20}$. Figure 4B shows a net-shape metallic glass component with semicircular toroidal geometry molded from a glassy rod of $Pd_{43}Cu_{10}Ni_{27}P_{20}$. Figure 4C shows the upper mold tool used to produce the component. The part was produced by rapid heating at 10^6 K/s to $T_F \approx 720$ K, followed by injection into the mold cavity with an applied pressure of ~20 MPa. The processing viscosity of the $Pd_{43}Ni_{10}Cu_{27}P_{20}$ melt at 720 K is estimated to be ~10^3 Pa·s (*35*). The total time required to form this component was about 40 ms, as determined by monitoring the displacement of the electrode/plunger using high-speed video. This implies strain rates on the order of 10^3 to 10^4 s^{-1} during the molding process. The rheological conditions (viscosity, pressure, and strain rate) are typical of those used in commercial injection molding of plastic hardware (*16*). X-ray diffraction and differential scanning calorimetry show that the product parts are fully glassy for both the Vitreloy 1 and the $Pd_{43}Cu_{10}Ni_{27}P_{20}$ alloy. This is expected because the processing times are much shorter than the time for intervening crystallization (as seen in Fig. 1). Moreover, no visible oxidation was detected in either of the parts, despite being processed in open air.

Concerning intervening crystallization, it is of obvious interest to explore the applicability of our rapid heating and forming methods to less robust, or marginal, metallic glass-formers, such as those with critical casting thicknesses of several millimeters (as opposed to several centimeters). As discussed earlier, marginal glass-formers have crystallization curves shifted to time scales about two orders of magnitude shorter than the robust glass-formers Vitreloy 1 and $Pd_{43}Cu_{10}Ni_{27}P_{20}$ (Fig. 1). The marginal metallic glass-forming alloy $Zr_{11}Ti_{33}Cu_{47}Ni_8Si_1$ (*36*) has a critical casting rod diameter of 5 to 6 mm and exhibits a very restricted processing window $\Delta T \approx 50$ K at conventional heating rates. Thus, its crystallization curve is shifted not only to shorter times but also to lower temperatures closer to T_g (Fig. 1). Fully glassy sample rods 3 mm in diameter and 2 cm long were prepared and heated by rapid discharge at ~10^6 K/s to temperatures midway between T_g and T_M. The rods were deformed under a compressive load of ~400 N between copper electrode plates (as in Fig. 3A) but without ceramic spacers. The rods were heated and deformed to flat uniform disks of final thicknesses ranging from 0.5 to 1 mm in total elapsed times of less than 30 ms. The deforming samples were effectively quenched between the copper electrode plates. X-ray diffraction and differential scanning calorimetry verified that the deformed disks were fully glassy, thereby demonstrating that crystallization was avoided in this marginal glass-former.

The rapid uniform heating approach introduced here allows access to metastable undercooled liquid states of intermediate mobility at temperatures and time scales far outside those probed by traditional methods. This platform enhances the experimental study of thermophysical properties, flow behavior, relaxation phenomena, and crystallization kinetics of undercooled metallic liquids. For example, it enables scanning calorimetry at heating rates of ~10^6 K/s. On the technology side, the method circumvents intervening crystallization and enables thermoplastic processing and forming of robust as well as marginal glass-forming alloys over the entire range of viscosity observed in undercooled metallic glass-forming melts.

References and Notes

1. W. Klement, R. H. Willens, P. Duwez, *Nature* **187**, 869 (1960).
2. H. W. Kui, A. L. Greer, D. Turnbull, *Appl. Phys. Lett.* **45**, 615 (1984).
3. A. Peker, W. L. Johnson, *Appl. Phys. Lett.* **63**, 2342 (1993).
4. D. M. Herlach, R. F. Cochrane, I. Egry, H. J. Fecht, A. L. Greer, *Int. Mater. Rev.* **38**, 273 (1993).

5. Y. J. Kim, R. Busch, W. L. Johnson, A. J. Rulison, W. K. Rhim, *Appl. Phys. Lett.* **65**, 2136 (1994).
6. X. H. Lin, W. L. Johnson, W. K. Rhim, *Mater. Trans. Jpn. Inst. Metals* **38**, 473 (1997).
7. W. L. Johnson, *MRS Bull.* **24**, 42 (1999).
8. A. Inoue, *Acta Mater.* **48**, 279 (2000).
9. G. Duan *et al.*, *Adv. Mater. (Deerfield Beach Fla.)* **19**, 4272 (2007).
10. A. Wiest, J. S. Harmon, M. D. Demetriou, R. D. Conner, W. L. Johnson, *Scr. Mater.* **60**, 160 (2009).
11. J. Schroers, Q. Pham, A. Peker, N. Paton, R. V. Curtis, *Scr. Mater.* **57**, 341 (2007).
12. Y. Saotome, Y. Noguchi, T. Zhang, A. Inoue, *Mater. Sci. Eng. A* **375-377**, 389 (2004).
13. G. Kumar, H. X. Tang, J. Schroers, *Nature* **457**, 868 (2009).
14. G. Kumar, A. Desai, J. Schroers, *Adv. Mater. (Deerfield Beach Fla.)* **23**, 461 (2010).
15. J. Schroers, *Adv. Mater. (Deerfield Beach Fla.)* **22**, 1566 (2010).
16. C. D. Han, *Rheology and Processing of Polymeric Materials: Polymer Processing* (Oxford Univ. Press, Oxford, 2007).
17. H. J. Güntherodt, *Adv. Solid State Phys.* **17**, 25 (1977).
18. S. R. Nagel, *Phys. Rev. B* **16**, 1694 (1977).
19. W. H. Wang, L. L. Li, M. X. Pan, R. J. Wang, *Phys. Rev. B* **63**, 052204 (2001).
20. J. Schroers, A. Masuhr, W. L. Johnson, R. Busch, *Phys. Rev. B* **60**, 11855 (1999).
21. Y. J. Kim, R. Busch, W. L. Johnson, A. J. Rulison, W. K. Rhim, *Appl. Phys. Lett.* **68**, 1057 (1996).
22. J. Schroers, W. L. Johnson, R. Busch, *Appl. Phys. Lett.* **77**, 1158 (2000).
23. D. E. Ballard, P. G. Frischmann, A. I. Taub, U.S. Patent 5,005,456 (1991).
24. M. R. J. Gibbs, D. H. Lee, J. E. Evetts, *IEEE Trans. Magn.* **20**, 1373 (1984).
25. A. Zaluska, H. Matyja, *Int. J. Rapid Solidif.* **2**, 205 (1986).
26. T. Kulik, H. Matyja, *Mater. Sci. Eng. A* **133**, 232 (1991).
27. M. F. de Oliveira, W. J. Botta, C. S. Kiminami, A. Inoue, A. R. Yavari, *Appl. Phys. Lett.* **81**, 1606 (2002).
28. A. R. Yavari, M. F. de Oliveira, C. S. Kiminami, A. Inoue, W. J. F. Botta, *Mater. Sci. Eng. A* **375-377**, 227 (2004).
29. G. Lohöfer, G. Pottlacher, *Int. J. Thermophys.* **26**, 1239 (2005).
30. R. Busch, Y. J. Kim, W. L. Johnson, *J. Appl. Phys.* **77**, 4039 (1995).
31. J. Lu, G. Ravichandran, W. L. Johnson, *Acta Mater.* **51**, 3429 (2003).
32. G. J. Dienes, H. F. Klemm, *J. Appl. Phys.* **17**, 458 (1946).
33. T. A. Waniuk, R. Busch, A. Masuhr, W. L. Johnson, *Acta Mater.* **46**, 5229 (1998).
34. A. Masuhr, T. A. Waniuk, R. Busch, W. L. Johnson, *Phys. Rev. Lett.* **82**, 2290 (1999).
35. G. J. Fan, H.-J. Fecht, E. J. Lavernia, *Appl. Phys. Lett.* **84**, 487 (2004).
36. H. Choi-Yim, R. Busch, W. L. Johnson, *J. Appl. Phys.* **83**, 7993 (1998).

Acknowledgments: The authors acknowledge partial support by the II-VI Foundation, the assistance of R. Overstreet with the thermal imaging unit, and useful discussions with M. A. Nicolet. A patent filed by the California Institute of Technology is currently pending. The U.S. patent application number is US2009/0236017 A1.

Supporting Online Material
www.sciencemag.org/cgi/content/full/332/6031/828/DC1
Materials and Methods
Figs. S1 and S2
References

7 December 2010; accepted 1 April 2011
10.1126/science.1201362

Three-Dimensional Orientation Mapping in the Transmission Electron Microscope

H. H. Liu,[1] S. Schmidt,[1] H. F. Poulsen,[1] A. Godfrey,[2] Z. Q. Liu,[3] J. A. Sharon,[4] X. Huang[1,5]*

Over the past decade, efforts have been made to develop nondestructive techniques for three-dimensional (3D) grain-orientation mapping in crystalline materials. 3D x-ray diffraction microscopy and differential-aperture x-ray microscopy can now be used to generate 3D orientation maps with a spatial resolution of 200 nanometers (nm). We describe here a nondestructive technique that enables 3D orientation mapping in the transmission electron microscope of mono- and multiphase nanocrystalline materials with a spatial resolution reaching 1 nm. We demonstrate the technique by an experimental study of a nanocrystalline aluminum sample and use simulations to validate the principles involved.

Many materials are polycrystalline, meaning that they are composed of a large number of grains (crystallites) of different crystallographic orientations. A full three-dimensional (3D) orientation mapping of such polycrystalline grain structures (with information about the position, size, morphology, and orientation of each grain, as well as the topological connectivity between the grains) is needed to relate the structure to properties. Such information can be obtained with the 3D electron backscatter diffraction technique (3D-EBSD) (*1*). This technique has a spatial resolution of ~20 nm, but it requires serial sectioning of the sample as part of the data collection process and, thus, is destructive. Recently, two nondestructive 3D x-ray techniques that have a spatial resolution of, at best, 200 nm (*2*, *3*) have been demonstrated. Electron tomography has been used to determine the shape of isolated crystals with a resolution down to 1 nm, but this method cannot be used to obtain orientation maps (*4*). Furthermore, several approaches (*5–10*) have been developed for 2D orientation mapping in the transmission electron microscope (TEM). In these approaches, the crystal orientation is determined from diffraction patterns that are either recorded directly using the diffraction mode (*5–7*) or reconstructed indirectly from conical-scanning dark-field images (*8–10*). These 2D methods are relevant when the specimen thickness is smaller than the size of the grains.

We describe here a technique for 3D orientation mapping in the TEM (3D-OMiTEM) with a spatial resolution on the order of 1 nm for specimens that may be substantially thicker than the average grain size. Similar to some of the 2D techniques (*8–10*), the data collection is based on conical-scanning dark-field imaging. However, to enable the simultaneous reconstruction of a complete 3D orientation map of all grains in a sample volume, images are recorded at many sample tilt angles. Furthermore, we have developed a new approach for the orientation determination and 3D reconstruction, based on the GrainSweeper (*11*) and GrainSpotter (*12*) algorithms originally developed for 3D reconstruction of synchrotron diffraction data. In this approach, the orientation of each voxel in the sample is determined by a simultaneous analysis of all contributing diffraction vectors derived from the dark-field images over all beam and sample tilt positions, thereby reducing the effects caused by dynamical diffraction and multiple scattering. A volume formed by adjacent voxels of the same orientation is identified as a grain. The shape and location of each grain are determined with the use of a ray-tracing method based on the sample tilt angles where the grain is visible in the dark-field images. The angular resolution for the orientation mapping is primarily determined by the step sizes used for the conical scanning and the sample tilting, whereas the spatial resolution is also determined by the magnification used to record the images. In general, however, more than 100,000 images are required to obtain nanoscale orientation maps.

To validate the principles of all procedures involved in the data analysis, we used a software package that incorporates dynamical diffraction and multiple scattering effects (*13*) to simulate electron diffraction from overlapping grains of different orientations. This package was used in combination with a 3D grain-orientation map

[1]Center for Fundamental Research: Metal Structures in Four Dimensions, Materials Research Division, Risø National Laboratory for Sustainable Energy, Technical University of Denmark, DK-4000 Roskilde, Denmark. [2]Laboratory of Advanced Materials, Department of Materials Science and Engineering, Tsinghua University, 100084 Beijing, P.R. China. [3]Shenyang National Laboratory for Materials Science, Institute of Metal Research, Chinese Academy of Sciences, 110016 Shenyang, P.R. China. [4]Department of Mechanical Engineering, Johns Hopkins University, Baltimore, MD 21218, USA. [5]Danish-Chinese Center for Nanometals, Materials Research Division, Risø National Laboratory for Sustainable Energy, Technical University of Denmark, DK-4000 Roskilde, Denmark

*To whom correspondence should be addressed. E-mail: xihu@risoe.dtu.dk

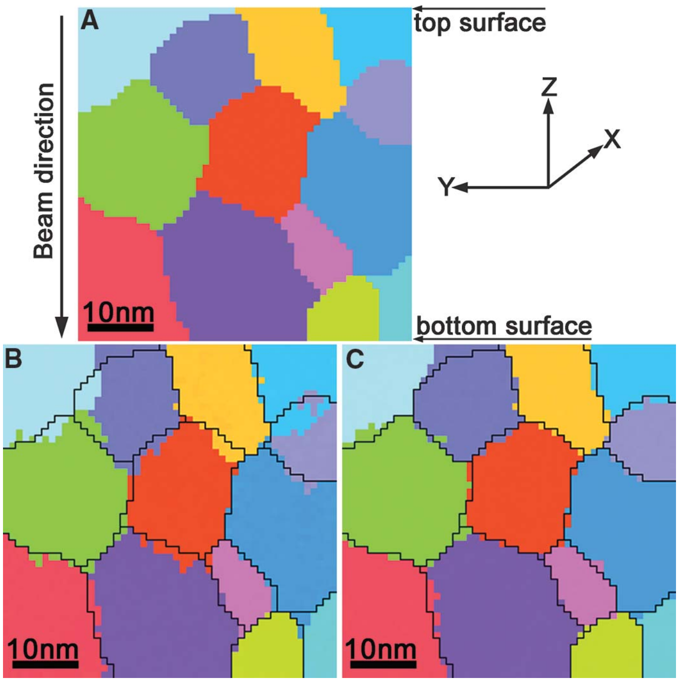

Fig. 1. (**A**) Section of a rescaled experimentally obtained 3D-EBSD grain-orientation map of aluminum. The tilt axis is parallel to the *x* axis. (**B**) Reconstructed grain-orientation map for the same section based on a sample tilt range of ±60°. (**C**) Reconstructed grain-orientation map for the same section based on a sample tilting range of ±90°. The same color coding, representing crystallographic orientation, is used throughout. The black lines in (B) and (C) indicate the grain boundary positions in the original map (A).

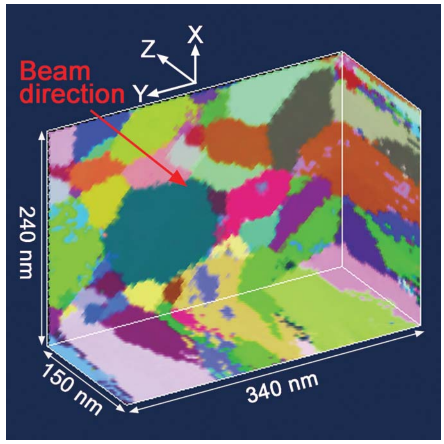

Fig. 2. 3D grain-orientation map from part of a 150-nm-thick aluminum film specimen. The colors represent different crystal orientations with a tolerance of 2°.

of an aluminum polycrystal experimentally generated using 3D-EBSD to simulate a set of dark-field images over a wide range of specimen and beam tilt angles. The original grain size of the aluminum sample is 2 μm, which is scaled down by a factor of 100 to simulate a nanocrystalline sample with grains of an average size of 20 nm at a voxel resolution of 1 nm^3. Figure 1A shows a section through this "original" grain-orientation map used as the input for the simulations. The vertical direction is parallel to the sample thickness direction, giving up to five overlapping grains in the through-thickness direction. We performed two simulations that generated conical-scanning dark-field images over sample tilt angle ranges of ±60° and ±90°, in each case with a step size of 1°. These dark-field images were then used as input data for the 3D-OMiTEM software. Figure 1, B and C, shows the reconstructed grain-orientation maps for the same section, for the two cases. The black lines superposed on Fig. 1, B and C, indicate the grain boundary positions in the original map (Fig. 1A). The mean mismatch error is 0.9 pixels (0.9 nm) and 0.5 pixels (0.5 nm) in the two cases, respectively. The orientation difference for each grain between the reconstructed maps (Fig. 1, B and C) and the original map (Fig. 1A) is less than 0.2°. The good match in both the grain orientations and the grain boundary locations suggests that the algorithms used for the data collection and analysis in the 3D-OMiTEM method are valid.

We demonstrate the 3D-OMiTEM technique by generating a 3D grain-orientation map of a sample of nanocrystalline aluminum. An aluminum film of 150-nm thickness was produced by pulsed electron beam evaporation (*14*). 2D observations from the surface plane and cross section revealed the film to be composed of a mixture of elongated grains and smaller equiaxed grains. Using a tilt range from –30° to +30°, about 110,000 dark-field images were generated from a selected area of 850 by 850 nm^2 (*14*). Part of a 3D grain-orientation map reconstructed using the new technique is shown in Fig. 2. More than 100 grains with a wide spectrum of crystallographic orientations are identified. The 3D shapes of many grains are revealed as elongated, but equiaxed grains of smaller sizes embedded in the analyzed volume are also found, in good agreement with the 2D observations. Based on a comparison of the reconstructed grain structure with the dark-field images of individual grains, the resolution of the technique is estimated to be ~two to three pixels (for the magnification range typically used for analysis of nanocrystalline materials, one pixel corresponds to 0.2 to 2 nm).

The volume that can be mapped using 3D-OMiTEM is determined by the TEM sample thickness, which is typically 100 to 300 nm in foils examined at standard operating voltages (200 to 300 kV) and up to 1 μm in 1-MeV instruments, and by the electron illuminated area, which can be as large as several tens of square micrometers, depending on the magnification used in the microscope. For a nanocrystalline material with a grain size of 30 nm in a sample of thickness 200 nm and at a magnification giving a resolution of 1 nm, there will be on the order of 10,000 grains in the analyzed volume, providing good statistics of 3D structural parameters. The ability to observe changes in grain structure in the interior of nanocrystalline samples under conditions such as variable stress and temperature will yield information on materials behavior with minimized surface effects and will allow, for the first time, direct testing of physically based models of 3D structural evolution in nanocrystalline materials.

References and Notes

1. A. D. Rollett, S. B. Lee, R. Campman, G. S. Rohrer, *Annu. Rev. Mater. Res.* **37**, 627 (2007).
2. H. F. Poulsen, *Three Dimensional X-Ray Diffraction Microscopy* (Springer, Berlin, 2004).
3. B. C. Larson, W. Yang, G. E. Ice, J. D. Budai, J. Z. Tischler, *Nature* **415**, 887 (2002).
4. P. A. Midgley, R. E. Dunin-Borkowski, *Nat. Mater.* **8**, 271 (2009).
5. J.-J. Fundenberger, A. Morawiec, E. Bouzy, J. S. Lecomte, *Ultramicroscopy* **96**, 127 (2003).
6. E. R. Rauch, A. Duft, *Mater. Sci. Forum* **495-497**, 197 (2005).
7. K. J. Ganesh, M. Kawasaki, J. P. Zhou, P. J. Ferreira, *Microsc. Microanal.* **15**, 752 (2009).
8. D. J. Dingley, *Microchim. Acta* **155**, 19 (2006).
9. G. L. Wu, S. Zaefferer, *Ultramicroscopy* **109**, 1317 (2009).
10. www.cmu.edu/news/archive/2009/June/june4_barmak.shtml
11. S. Schmidt *et al.*, *Scr. Mater.* **59**, 491 (2008).
12. S. Schmidt, http://sourceforge.net/apps/trac/fable/wiki/grainspotter.
13. K. Sugio, H. H. Liu, H. F. Poulsen, X. Huang, *Nanostructured Metals – Fundamentals to Applications*, J.-C. Grivel *et al.*, Eds. (Risø DTU, Roskilde, 2009), pp. 337–342.
14. Materials and methods are available as supporting material on *Science* Online.

Acknowledgments: We thank K. Sugio for the development of software simulating electron diffraction; E. Johnson, B. Ralph, R. Gardner, H. O. Sørensen, R. Dunin-Borkowski, D. Juul Jensen, N. Hansen, and K. J. Hemker for helpful discussions; and J. R. Bowen and N. Saowadee for providing the 3D-EBSD data. Financial support was provided by the Danish National Research Foundation. A.G. acknowledges support from the National Natural Science Foundation of China under contract numbers 50571049 and 50911130230, Z.Q.L. acknowledges support from the National Basic Research Program of China (grant no. 2010CB631006), and J.A.S. acknowledges support for the thin-film deposition from the U.S. Department of Energy under grant number DE-FG02-07ER46437.

Supporting Online Material
www.sciencemag.org/cgi/content/full/332/6031/833/DC1
Materials and Methods
Reference 15

27 December 2010; accepted 1 April 2011
10.1126/science.1202202

Silver-Catalyzed C-C Bond Formation Between Methane and Ethyl Diazoacetate in Supercritical CO_2

Ana Caballero,[1] Emmanuelle Despagnet-Ayoub,[2,3] M. Mar Díaz-Requejo,[1] Alba Díaz-Rodríguez,[1,4] María Elena González-Núñez,[4] Rossella Mello,[4] Bianca K. Muñoz,[2,3] Wilfried-Solo Ojo,[2,3] Gregorio Asensio,[4]* Michel Etienne,[2,3]* Pedro J. Pérez[1]*

Even in the context of hydrocarbons' general resistance to selective functionalization, methane's volatility and strong bonds pose a particular challenge. We report here that silver complexes bearing perfluorinated indazolylborate ligands catalyze the reaction of methane (CH_4) with ethyl diazoacetate (N_2CHCO_2Et) to yield ethyl propionate ($CH_3CH_2CO_2Et$). The use of supercritical carbon dioxide ($scCO_2$) as the solvent is key to the reaction's success. Although the catalyst is only sparingly soluble in CH_4/CO_2 mixtures, optimized conditions presently result in a 19% yield of ethyl propionate (based on starting quantity of the diazoester) at 40°C over 14 hours.

The use of methane, the lightest hydrocarbon and the primary component of natural gas, as a source for the production of fine chemicals remains an appealing goal on scientific, economic, and environmental grounds (*1–4*). Transition metal–catalyzed C-H bond activation is a promising approach by which to achieve functionalization of the strong and relatively inert C-H bonds of alkanes, more generally. In one possible scenario, these reactions proceed by metal-promoted C-H bond oxidative cleavage followed by insertion of a suitable X group into the M-C bond and release of the functionalized product by means of reductive elimination of the C-X-H unit (*5*). Individual reaction steps for this and related catalytic cycles have been widely reported (*6*), but a major challenge has been that removal of the functionalized fragments from the metal coordination sphere is often unfavorable, due to the robustness of the M-C bonds. Only a few examples of catalytic C-H bond functionalizations of alkanes with transition metal complexes have been described (*4*, *6*), including C-H/C-D exchange (*7*), dehydrogenation (*8*), tandem dehydrogenation-metathesis (*9*), dehydrogenative silylation (*10*), and borylation (*11*) processes.

None of the scarce examples mentioned above have led to the catalytic functionalization of methane. On the other hand, an early example of distinct, electrophilic activation was Shilov and Shul'pin's landmark discovery of the conversion of alkanes, including methane, into alcohols under acidic conditions (*12*). Using Shilov-type chemistry, Periana and co-workers have developed catalytic systems based on mercury (*13*), platinum (*14*), or gold (*15*) that convert methane into methyl bisulfate, usually in sulphuric acid media and at high temperature. Subsequently, Periana (*16*) and Kirillova (*17*) independently reported conversion of methane into acetic acid, with the use of palladium- and vanadium-based catalysts, respectively.

A different approach to the catalytic functionalization of alkanes involves electrophilic X atom insertion into C-H bonds, described for the heteroatom insertion into methane C-H bonds catalyzed by superacids, with hydrogen peroxide, ozone, or chlorine as X sources (*18*, *19*). In transition metal–catalyzed versions of this approach, a polarized M-X bond is formed before the X atom insertion into the C-H bond. This process implies no direct metal-alkane interaction; consequently, release of the reaction products does not require cleavage of strong M-C or M-H bonds. An example is the metal catalyzed carbene insertion into a hydrocarbon C-H bond by reaction with a diazocompound (*20*, *21*), which has been successfully applied to simple alkanes using rhodium (*22*, *23*) and group 11 (copper, silver, gold) metal-based catalysts (*24*). However, it is as yet unknown for methane.

We have previously designed highly electrophilic silver catalysts based on perbrominated tris(pyrazolyl)- or perfluorinated tris(indazolyl)borate ligands. We first reported the functionalization of alkanes (*25*) with the use of ethyl diazoacetate as the carbene source, catalyzed by $[Tp^{Br3}Ag]_2$ (**1**) [Tp, tris(pyrazolyl)borate]. Later, $[F_{21}\text{-}Tp^{4Bo,3CF3}Ag(OCMe_2)]$ (**2**) (Bo, benzo; Me, methyl) was found to be more active and selective toward primary sites (Fig. 1) (*26*). With pentane as a representative example, both catalysts, as well as the new complex—$[F_{27}\text{-}Tp^{4Bo,3CF2CF3}Ag(thf)]$ (**3**) (thf, tetrahydrofuran)—reported herein, led to mixtures of the three products resulting from the insertion of the carbene: $CHCO_2Et$ (Et, ethyl) into the primary and the secondary C-H bonds.

Challenges arose in applying this methodology to methane, due to its gaseous nature (critical pressure and temperature p_c = 45.96 atm and T_c = –82.7°C), low solubility in organic solvents, and poor solvating ability. Moreover, carbene insertion into any C-H bond present in the reaction medium would be faster than reaction of the stronger bonds in methane, and chlorinated solvents do not represent a viable alternative, as these silver catalysts preferentially induce the insertion of $CHCO_2Et$ units into C-X (X = halogen) bonds (*27*).

In the present contribution, these difficulties have been circumvented by the use of supercritical carbon dioxide ($scCO_2$) as the reaction solvent, given its inertness toward reactive intermediates, complete miscibility with methane, strong solvating ability toward ethyl diazoacetate (EDA), and excellent transport properties (*28*). We per-

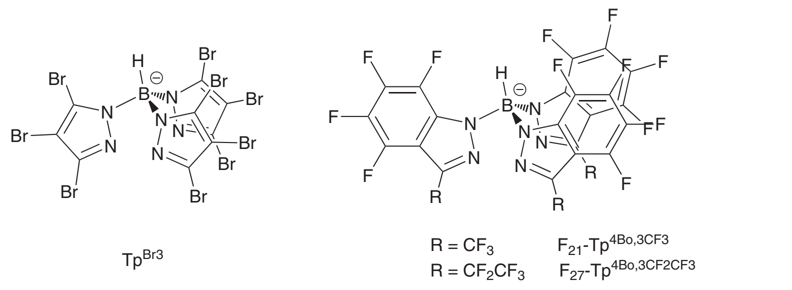

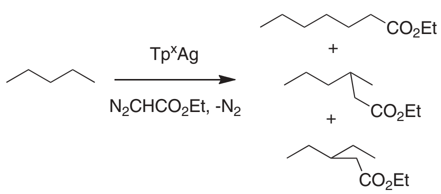

$Tp^{Br3}Ag$ (**1**)	$F_{21}\text{-}Tp^{4Bo,3CF3}Ag$ (**2**)	$F_{27}\text{-}Tp^{4Bo,3CF2CF3}Ag$ (**3**)
27%	37%	47%
53%	49%	44%
13%	14%	9%

Fig. 1. Functionalization of C-H bonds by carbene insertion from ethyl diazoacetate using Tp^xAg complexes as catalysts. Percentages correspond to yields after complete consumption of the initial EDA (the remaining portion up to 100% of initial EDA forms diethyl fumarate and maleate by catalytic EDA dimerization).

[1]Laboratorio de Catálisis Homogénea, Departamento de Química y Ciencia de los Materiales, Unidad Asociada al Consejo Superior de Investigaciones Científicas, Centro de Investigación en Química Sostenible, Universidad de Huelva, Campus de El Carmen, 21007-Huelva, Spain. [2]CNRS, Laboratoire de Chimie de Coordination (LCC), 205 Route de Narbonne, F-31077 Toulouse, France. [3]Université de Toulouse, Université Paul Sabatier, Institut National Polytechnique de Toulouse, LCC, F-31077 Toulouse, France. [4]Departamento de Química Orgánica, Facultad de Farmacia, Universidad de Valencia, Burjassot 46100-Valencia, Spain.

*To whom correspondence should be addressed. E-mail: gregorio.asensio@uv.es (G.A.); michel.etienne@lcc-toulouse.fr (M.E.); perez@dqcm.uhu.es (P.J.P.)

formed an initial set of experiments by placing ethyl diazoacetate and one of the silver complexes **1** to **3** (0.03 mmol of silver, initial molar ratio Tp^xAg:EDA 1:100) into separate polypropylene containers fitted into a high-pressure reactor thermostated at 40°C (*29*). The system was charged with 160 atm of methane and then pressurized up to 250 atm with carbon dioxide. A 0.96 n_{CH4}:n_{CO2} ratio of gases was determined by weighing the reactor immediately after charging with each of them. Observation through the reactor sapphire windows revealed that the solid catalyst did not dissolve substantially in the supercritical medium, whereas EDA dissolved completely within 1 hour. Control experiments showed that EDA is not soluble in the reaction medium in the absence of $scCO_2$, and complex **3** (0.03 mmol) completely dissolves in neat $scCO_2$ (250 atm). The reaction was maintained at 40°C, with stirring, for 14 hours and then directly analyzed by a gas chromatograph connected in-line to the high-pressure reactor (fig. S3). Products were quantified using calibration curves previously derived with pure commercial samples. Mass balances were assessed in a set of separate experiments in which the reactor was completely depressurized through a micrometric high-pressure valve and the products were collected in a trap cooled to –78°C. The residues were dissolved in deuterated chloroform. Integration of the nuclear magnetic resonance signals (using styrene as internal standard) gave product ratios identical to those obtained in the gas chromatography (GC) analysis.

Ethyl propionate (EP), the product of: $CHCO_2Et$ insertion into a C-H bond of methane, was detected in the experiments with all three catalysts, along with diethyl fumarate and maleate, which are common by-products of metal-catalyzed dimerization of EDA (*30*). The use of **1** led to substoichiometric amounts of EP (0.03 mmol of the catalyst was employed), whereas complexes **2** and **3** as catalyst precursors gave 0.198 and 0.204 mmol of EP, respectively (Fig. 2). These results demonstrate the ability of complexes **2** and **3** to catalyze the formal insertion of the carbene: $CHCO_2Et$ into a C-H bond of methane, with the formation of a new C-C bond.

As indicated above, the catalyst seems to remain undissolved in the reaction vessel. In fact, the weight of the catalyst-containing vessel appeared unchanged before and after the experiment. However, a homogeneous process catalyzed by small amounts (<10^{-3} mmol) of the silver complex cannot be ruled out. To gain further insight, we ran a catalytic experiment in which the volatile products of the reaction were collected in a cold trap. The catalyst vessel was then removed and the reactor washed with CH_2Cl_2. No measurable variation in the initial catalyst weight could be recorded, and inductively coupled plasma mass spectroscopy (ICP-MS) analysis of the combined extracts from the cold trap and the reactor revealed the presence of ~4.2×10^{-4} mmol of silver (corresponding to dissolution of <0.1 mg of the starting complex). We then performed a series of experiments identical to that above but with varied relative pressures of methane and carbon dioxide, with the amount of dissolved silver complex **3** again determined by ICP-MS (Table 1). The exact ratio of methane and carbon dioxide was determined by weight.

These studies revealed that the solubility of the silver catalyst is enhanced by increasing the proportion of carbon dioxide in the fluid, in good agreement with the well-known capacity of $scCO_2$ to dissolve fluorinated compounds (*28*). Specifically, a linear correlation pertained between the catalyst concentration in the fluid and the relative n_{CH4}:n_{CO2} ratio (Fig. 3). Unfortunately, the corresponding conversion to the desired product (EP) decreased with rising CO_2:methane ratios. We attribute this result to higher catalyst concentrations promoting not only the formation of ethyl propionate but also the competing formation of undesired diethyl fumarate and maleate products via carbene dimerization. The latter transformation is enhanced at lower hydrocarbon concentration and at high catalyst loadings (*31*).

A well-known related feature in this type of reaction is that very low concentrations of the diazo compound disfavor the formation of the undesired fumarate and maleate derivatives. Hence, we performed an experiment using 0.7 mmol of EDA (instead of 3 mmol) and 0.007 mmol of **3**, the latter still well in excess (15×) of the determined solution catalyst concentration in Table 1, entry 1. After 14 hours under 160 atm of methane and a CO_2 balance up to a total pressure of 250 atm, 0.134 mmol of EP was detected by GC. In a second run, with a longer reaction time of 70 hours, 0.162 mmol of EP was obtained. These values represent 19 and 23% yields, respectively, into EP

Table 1. Methane functionalization with ethyl diazoacetate using complex **3** as catalyst. Reaction conditions described in Fig. 2.

Entry	P_{CH4}:P_{CO2}	n_{CH4}:n_{CO2}*	mmol EP	mmol Ag dissolved	TON†
1	160:90	0.96	0.204	0.00042	478
2	125:125	0.88	0.130	0.0043	30
3	80:170	0.34	0.140	0.023	6
4	0:250	0	0	0.031	0

*Determined by weight (see SOM). †Defined as millimole of EP per millimole of Ag dissolved.

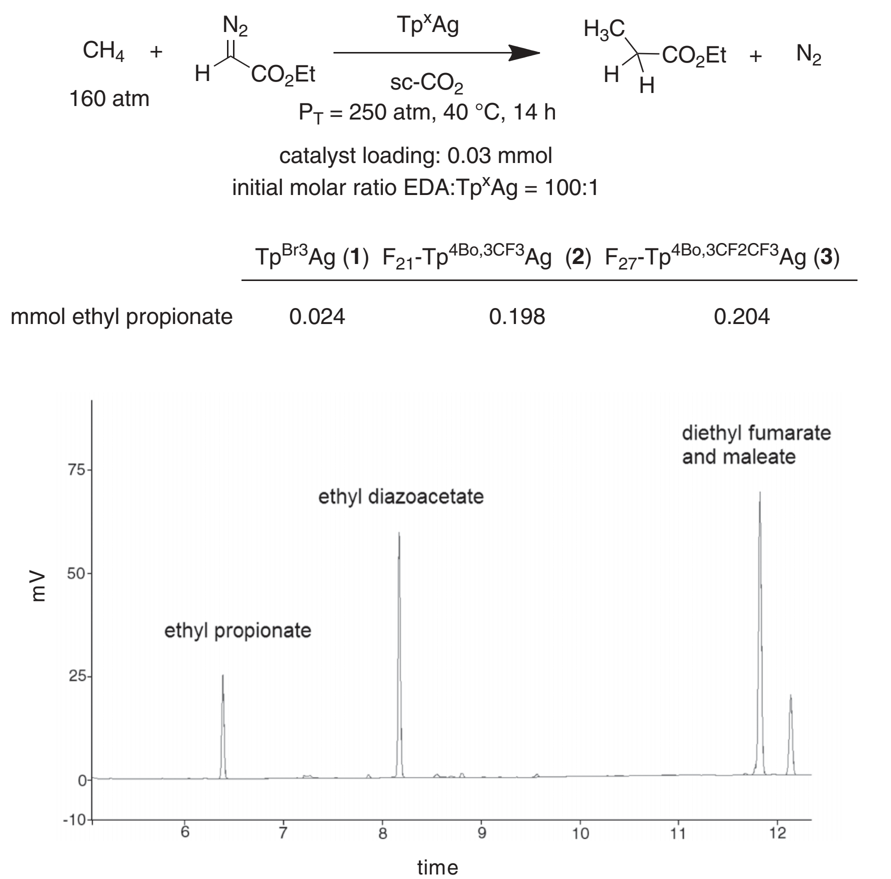

Fig. 2. Gas chromatogram of the reaction of methane with EDA catalyzed by the F_{27}-$Tp^{4Bo,3CF2CF3}Ag$ complex after 14 hours (entry 1, Table 1).

based on the initial amount of EDA, demonstrating the benefit of the aforementioned dilution effect.

We found that complex **3** also catalyzed reaction of EDA with ethane (Fig. 4), affording ethyl butyrate over 14 hours with a turnover number (TON) value of 30, under a total pressure of 250 atm (35 atm of ethane; n_{CO2}:n_{C2H6} = 7.35). The lower hydrocarbon pressure needed in this case is in agreement with the lower bond dissociation energy of the ethane C-H bond (~101 versus 104.5 kcal/mol in methane) (*32*). Complex **3** completely dissolved under these reaction conditions. The low TON value results from the low ethane concentration in the mixture. To establish the relative reactivities of methane and ethane, we performed a competition experiment at 40°C using 0.03 mmol of **3** in a mixture of 135 atm of CH_4, 35 atm of C_2H_6, and a balance of CO_2 to reach a total pressure of 250 atm (Fig. 4). The distribution of products favored the ethane derivative by a factor of ~7.5. Taking into account the experimentally determined mass ratio of the gases and the statistical correction for the number of C-H bonds, we estimated the selectivity C-$H_{methane}$:C-H_{ethane} to be ~1:14 [see supporting online material (SOM) for details].

We also investigated pentane C-H functionalization in $scCO_2$. In 2 mL of pentane under 200 atm of CO_2 at 40°C, catalyst **3** (0.03 mmol) partially dissolved (~60% according to ICP-MS studies) to yield a mixture of insertion products (Fig. 4), with a regioselectivity virtually identical to that obtained under homogeneous conditions using pentane as both solvent and reactant (Fig. 1). These results suggest that the insertion mechanism operative in homogeneous solution is conserved in the supercritical medium.

A plausible mechanism for C-H functionalization of methane (and other hydrocarbons) involves metal-catalyzed N_2 elimination from the diazo substrate followed by carbene transfer (*33*, *34*) mediated by a highly electrophilic metal carbene intermediate (Fig. 5) (*35*). The reactivity of **A** toward C-H bonds gives a product distribution that is governed, at least in part, by the bond dissociation energy of the C-H bonds, justifying the observation that ethane functionalization is favored over methane by a factor of ~ 14.

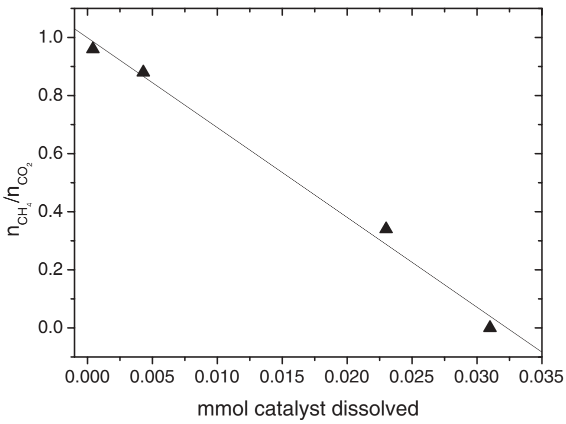

Fig. 3. Dependence of the solubility of F_{27}-$Tp^{4Bo,3CF2CF3}$Ag (**3**) on the fluid composition.

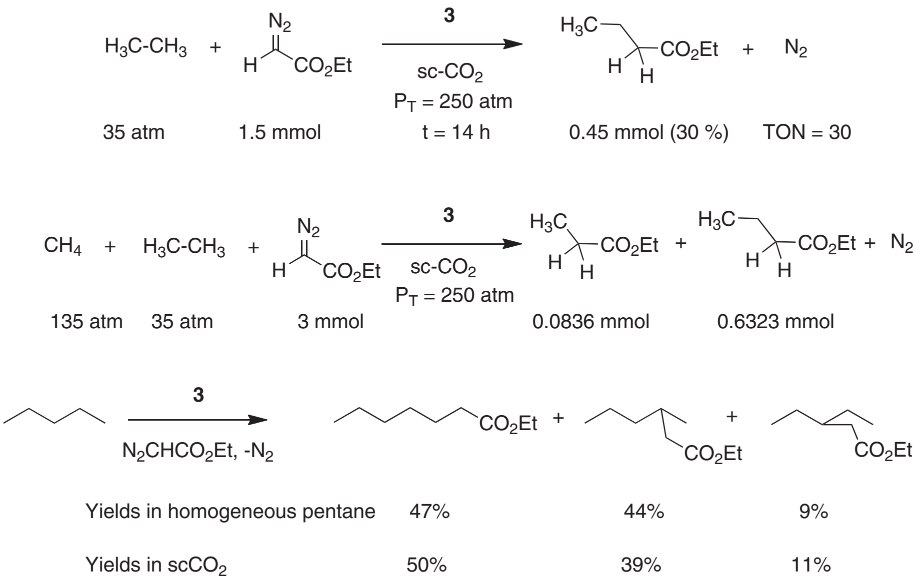

Fig. 4. Methane, ethane, and pentane functionalization. P_T, total pressure; t, time

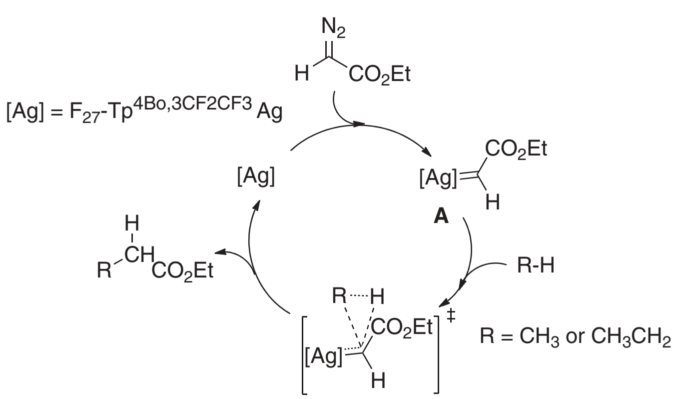

Fig. 5. Mechanistic hypothesis for silver-catalyzed alkane functionalization by ethyl diazoacetate.

References and Notes

1. R. H. Crabtree, *Chem. Rev.* **110**, 575 (2010).
2. R. G. Bergman, *Nature* **446**, 391 (2007).
3. J. A. Labinger, J. E. Bercaw, *Nature* **417**, 507 (2002).
4. K. I. Goldberg, A. S. Goldman, Eds., *Activation and Functionalization of C-H Bonds* [American Chemical Society (ACS) Symposium Series 885, ACS, Washington, DC, 2004].
5. B. A. Arndtsen, R. G. Bergman, T. A. Mobley, T. H. Petersen, *Acc. Chem. Res.* **28**, 154 (1995).
6. J. F. Hartwig, *Organotransition Metal Chemistry: From Bonding to Catalysis*, (University Science Books, Sausalito, CA, 2009).
7. J. T. Golden, R. A. Andersen, R. G. Bergman, *J. Am. Chem. Soc.* **123**, 5837 (2001).
8. C. M. Jensen, *Chem. Commun.* **1999**, 2443 (1999).
9. A. S. Goldman *et al.*, *Science* **312**, 257 (2006).
10. A. D. Sadow, T. D. Tilley, *J. Am. Chem. Soc.* **127**, 643 (2005).
11. I. A. I. Mkhalid, J. H. Barnard, T. B. Marder, J. M. Murphy, J. F. Hartwig, *Chem. Rev.* **110**, 890 (2010).
12. A. E. Shilov, G. B. Shul'pin, *Chem. Rev.* **97**, 2879 (1997).
13. R. A. Periana *et al.*, *Science* **259**, 340 (1993).
14. R. A. Periana *et al.*, *Science* **280**, 560 (1998).
15. C. J. Jones *et al.*, *Angew. Chem. Int. Ed.* **43**, 4626 (2004).
16. R. A. Periana, O. Mironov, D. J. Taube, G. Bhalla, C. J. Jones, *Science* **301**, 814 (2003).
17. M. V. Kirillova *et al.*, *J. Am. Chem. Soc.* **129**, 10531 (2007).
18. G. A. Olah, *Acc. Chem. Res.* **20**, 422 (1987).
19. G. A. Olah, A. Molnar, in *Hydrocarbon Chemistry* (Wiley-Interscience, Hoboken, NJ, ed. 2, 2003), chap. 9, pp. 427–575.
20. M. P. Doyle, R. Duffy, M. Ratnikov, L. Zhou, *Chem. Rev.* **110**, 704 (2010).
21. M. M. Díaz-Requejo, T. R. Belderraín, M. C. Nicasio, P. J. Pérez, *Dalton Trans.* **2006**, 5559 (2006).
22. H. M. L. Davies, T. Hansen, M. R. J. Churchill, *J. Am. Chem. Soc.* **122**, 3063 (2000).
23. H.-Y. Thu *et al.*, *Angew. Chem. Int. Ed.* **47**, 9747 (2008).
24. M. M. Díaz-Requejo, P. J. Pérez, *Chem. Rev.* **108**, 3379 (2008).

25. J. Urbano *et al.*, *Organometallics* **24**, 1528 (2005).
26. E. Despagnet-Ayoub *et al.*, *Organometallics* **27**, 4779 (2008).
27. J. Urbano *et al.*, *Organometallics* **28**, 5968 (2009).
28. J. M. DeSimone, E. Tumas, Eds., *Green Chemistry Using Liquid and Supercritical Carbon Dioxide* (Oxford Univ. Press, Oxford, 2003).
29. Materials and methods are available as supporting material on *Science* Online.
30. M. P. Doyle, M. A. McKervey, T. Ye, *Modern Catalytic Methods for Organic Synthesis with Diazo Compounds* (Wiley, New York, 1998).
31. A. Caballero, A. Prieto, M. M. Diaz-Requejo, P. J. Pérez, *Eur. J. Inorg. Chem.* **2009**, 1137 (2009).
32. S. J. Blanksby, G. B. Ellison, *Acc. Chem. Res.* **36**, 255 (2003).
33. E. Nakamura, N. Yoshikai, M. Yamanaka, *J. Am. Chem. Soc.* **124**, 7181 (2002).
34. A. A. C. Braga *et al.*, *Organometallics* **25**, 5292 (2006).
35. A reviewer mentioned the possibility of the involvement of radical species. Extensive previous work favors the metallocarbene route [see (*19*) and references therein]. Moreover, these experiments were carried out in a vessel that was neither purged nor vented; therefore, 100 mL of air was present in the reaction mixture. The oxygen contained in that volume would preclude the conversion of any radical into the desired product. See (*36*).
36. G. Asensio, R. Mello, M. E. González-Núñez, C. Boix, J. Royo, *Tetrahedron Lett.* **38**, 2373 (1997).

Acknowledgments: We dedicate this work to Professor Ernesto Carmona. Support for this work was provided by the Ministerio de Ciencia e Innovación (grants CTQ2008-00042-BQU, CTQ2007-65251-BQU, and CTQ2007-30762-E), the European Research Area Chemistry Programme (2nd call "Chemical activation of carbon dioxide and methane" contract no. 1736154), the Consolider Ingenio 2010 (grants CSD2006-003 and CSD2007-00006), the Institut de Chimie of the CNRS, the Junta de Andalucía (P07-FQM-2870), and the Generalitat Velenciana (ACOMP/2010/155). We thank the Servicio Central de Soporte a la Investigación Experimental (Universidad de Valencia) for access to the instrumental facilities and J. de la Rosa and A. Sánchez de la Campa (Universidad de Huelva) for ICP-MS analyses.

Supporting Online Material

www.sciencemag.org/cgi/content/full/332/6031/835/DC1
Materials and Methods
SOM Text
Figs. S1 to S7
Tables S1 and S2
References *25*, *26*, and *37*

10 February 2011; accepted 19 March 2011
10.1126/science.1204131

Massive CO_2 Ice Deposits Sequestered in the South Polar Layered Deposits of Mars

Roger J. Phillips,[1]* Brian J. Davis,[2]† Kenneth L. Tanaka,[3] Shane Byrne,[4] Michael T. Mellon,[5] Nathaniel E. Putzig,[2] Robert M. Haberle,[6] Melinda A. Kahre,[7] Bruce A. Campbell,[8] Lynn M. Carter,[9] Isaac B. Smith,[10] John W. Holt,[10] Suzanne E. Smrekar,[11] Daniel C. Nunes,[11] Jeffrey J. Plaut,[11] Anthony F. Egan,[12] Timothy N. Titus,[3] Roberto Seu[13]

Shallow Radar soundings from the Mars Reconnaissance Orbiter reveal a buried deposit of carbon dioxide (CO_2) ice within the south polar layered deposits of Mars with a volume of 9500 to 12,500 cubic kilometers, about 30 times that previously estimated for the south pole residual cap. The deposit occurs within a stratigraphic unit that is uniquely marked by collapse features and other evidence of interior CO_2 volatile release. If released into the atmosphere at times of high obliquity, the CO_2 reservoir would increase the atmospheric mass by up to 80%, leading to more frequent and intense dust storms and to more regions where liquid water could persist without boiling.

The martian atmosphere is dominated by CO_2 with an annual mean pressure currently about 6 mbar (6 hPa) (*1*), although early in the planet's history CO_2 likely existed at the ~1 bar level. Some of this ancient atmospheric CO_2 may be stored in the polar layered deposits (PLD) (*2*), although, it is now thought, only in modest quantities. The water-ice–dominated southern PLD (SPLD) presently host a small [<5-m thick, ~90,000 km^2 (*3*)] perennial CO_2-ice deposit (*4*) overlying a thin water-ice layer (*5*), which together compose the south pole residual cap (SPRC). If the SPRC CO_2 material were to be released completely into the atmosphere, the increase in pressure would be only a few tenths of a mbar and insufficient to buffer the atmospheric CO_2 during changing climatic conditions (*5*). Here, we use radar-sounder data to show that the volume of sequestered CO_2 in the SPLD is substantially larger than previously believed, competing in magnitude with the present atmospheric abundance.

SHARAD (Shallow Radar) is a sounding radar on the Mars Reconnaissance Orbiter (MRO) mission (*6*), and its results are displayed in radargrams with axes of time delay and orbital position (Fig. 1). Previous mapping of subsurface reflectors by SHARAD in the north PLD (NPLD) revealed a crisp radar stratigraphy to the base of the deposits (*7*, *8*). For the SPLD, the radar signal does not penetrate the deposits as deeply as in the NPLD, and in only a limited number of places is there a well-defined stratigraphy (*9*). There are some regions with nearly reflection-

[1]Planetary Science Directorate, Southwest Research Institute, Boulder, CO 80302, USA and Department of Earth and Planetary Sciences, Washington University, St. Louis, MO 63130, USA. [2]Department of Space Studies, Southwest Research Institute, Boulder, CO 80302, USA. [3]Astrogeology Science Center, U.S. Geological Survey, Flagstaff, AZ 86001, USA. [4]Lunar and Planetary Laboratory, University of Arizona, Tucson, AZ 85721, USA. [5]Laboratory for Atmospheric and Space Physics, University of Colorado, Boulder, CO 80303, USA. [6]Space Science and Astrobiology Division, National Aeronautics and Space Administration (NASA) Ames Research Center, Moffett Field, CA 94035, USA. [7]Bay Area Environmental Research Institute/NASA Ames Research Center, Moffett Field, CA 94035, USA. [8]Center for Earth and Planetary Studies, Smithsonian Institution, Washington, DC 20013, USA. [9]Science and Exploration Directorate, NASA Goddard Space Flight Center, Greenbelt, MD 20771, USA. [10]Institute for Geophysics, Jackson School of Geosciences, University of Texas, Austin, TX 78758, USA. [11]Jet Propulsion Laboratory, California Institute of Technology, Pasadena, CA 91109, USA. [12]Department of Space Operations, Southwest Research Institute, Boulder, CO 80302, USA. [13]Department of Information Engineering, Electronics and Telecommunications, Sapienza University of Rome, 18-00184 Rome, Italy.

*To whom correspondence should be addressed. E-mail: roger@boulder.swri.edu
†Present address: Department of Geophysics, Colorado School of Mines, Golden, CO 80401, USA.

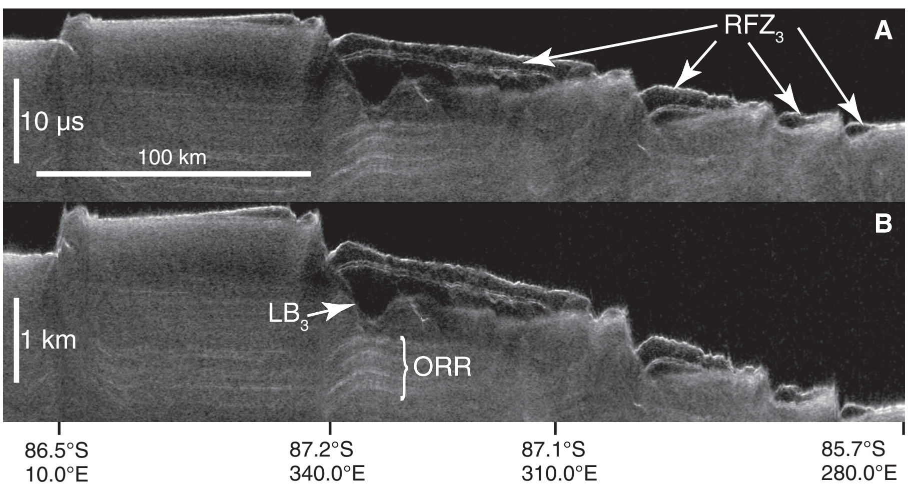

Fig. 1. SHARAD radargram 5968-01 traversing RFZ_3 terrain shown in original time-delay format (**A**) and converted to depth (**B**) by using the permittivity of water ice. Ground track location is shown in Fig. 3. ORR and LB_3 are indicated.

free subsurface zones (RFZ) extending downward from near the surface to depths approaching 1 km (fig. S1). The RFZs can be subdivided into four distinct types and locations (table S1) on the basis of their radar characteristics; here, we focus on RFZ$_3$, which is spatially coincident with the SPRC. Except for a commonly occurring thin layer that bisects the unit (Fig. 1), RFZ$_3$ is the most reflection-free volume that we have seen on Mars with SHARAD data: the signal level within approaches the background noise. Deeper reflectors passing beneath RFZ$_3$ brighten slightly more than expected on the basis of the change in thickness of typical SPLD material, implying that RFZ$_3$ deposits attenuate a radar signal less severely than these typical regions. Importantly, the low-power RFZ$_3$ radar return is thus not caused by strong scattering or absorption losses within the deposit.

To determine the real permittivity (ε′) of RFZ$_3$, we mapped key SHARAD reflectors for 79 MRO orbits (fig. S2). The lower boundary of RFZ$_3$, LB$_3$, is a highly irregular buried erosional surface that truncates subhorizontal reflectors. Extending several hundred meters beneath RFZ$_3$ is a zone of unorganized, weak radar reflectors that in turn is underlain by a coherent sequence of organized (layered) radar reflectors (ORR). By using the a priori assumption of a bulk water-ice composition (ε′ = 3.15) for the SPLD, we converted the vertical axis of radargrams from time delay to depth. The converted ORR sequence beneath LB$_3$ is typically offset from surrounding regions and exhibits significant topographic variations (Fig. 1B) that are strongly anticorrelated with LB$_3$ (Fig. 2A). This anticorrelation is unexpected because there is very likely no geological link between the earlier deposition of the ORR and the later erosion of the material above it that was subsequently filled with RFZ$_3$ material [see (*10*) for details]. On the basis of the argument that the anticorrelations are the fortuitous result of an incorrect choice of ε′ for RFZ$_3$, we found for each radargram the ε′ value that gave zero correlation between LB$_3$ and a test reflector (TR) in the ORR sequence (Fig. 2, B and C) (*10*). A second method (*10*) sought to minimize topographic perturbations and offsets on the TR by finding the ε′ value that obtained the smallest residuals to a linear regression on this interface (Fig. 2, D and E). Both methods tended to produce a relatively smooth and subhorizontal disposition to the TR, similar in nature to the likely extension of ORR observed by SHARAD in the Promethei Lingula region (*9*). Forty-one of the 79 radargrams were suitable for quantitative analyses using these procedures, and by using different strategies we found mean values for ε′ of the RFZ$_3$ volume in the range of 2.0 to 2.2, with standard deviations of 0.1 to 0.2 (*10*).

These permittivity estimates for RFZ$_3$ are unexpectedly close to a laboratory-measured value of low-porosity CO_2 ice of 2.12 ± 0.04 (*11*), similar to the well-known frequency-independent value of about 2.2 for bulk dry ice (*12*). The SHARAD-derived permittivity values are substantially lower than those of water ice (3.15) and CO_2 clathrate-hydrate ice (~2.85) (*13*), strongly supporting the hypothesis that RFZ$_3$ is a solid CO_2 deposit. An alternative view that RFZ$_3$ is porous water ice can be rejected on the basis of permittivity-thickness relationships (*10*).

With the permittivities estimated, we converted the time delays through RFZ$_3$ (using ε′ = 2.1) to thicknesses over each of the 79 radar traverses (fig. S3) and by interpolation constructed a continuous thickness distribution. Figure 3 shows this result placed over a geological map showing stratigraphic units in a portion of the SPLD (*14*, *15*). Of interest here are the largely overlapping horizontal extents of the AA$_3$ unit and the successively overlying water-ice (AA$_{4a}$) and CO_2-ice (AA$_{4b}$) units making up the SPRC. Also shown are the contacts (dashed) for unit AA$_3$, with the locations constrained well by exposures in troughs and by partial exposures beneath the SPRC. Where SHARAD data are available, there is a remarkable spatial correlation of RFZ$_3$ to the AA$_3$ unit except for the extremes of northward-extending lobes of the unit (*16*). Thus, we propose that the AA$_3$ unit is in fact RFZ$_3$, and its composition is dominated by CO_2 ice.

The AA$_3$ unit contains a system of large troughs, up to several km wide and typically <100 m deep, that do not cut older units (Fig. 3). In turn, smaller parallel aligned ridges, troughs, and elongate depressions mark some of these large troughs, and in places the depressions appear as coalescing or elongated pits (Fig. 4). Additionally, the westernmost outcrops of unit AA$_3$ (north of 87°S and near 240° to 270°E) include about 20 rimless circular pits (~300- to ~4000-m diameter), which do not occur in layers underlying unit AA$_3$ and do not display any rims or ejecta. All of these smaller troughs, depressions, and pits appear to result from erosion and removal of unit AA$_3$, with a strong component of sublimation and collapse. These features are not found elsewhere in the SPLD, and the CO_2-ice layer (AA$_{4b}$) of the SPRC is the only other perennial

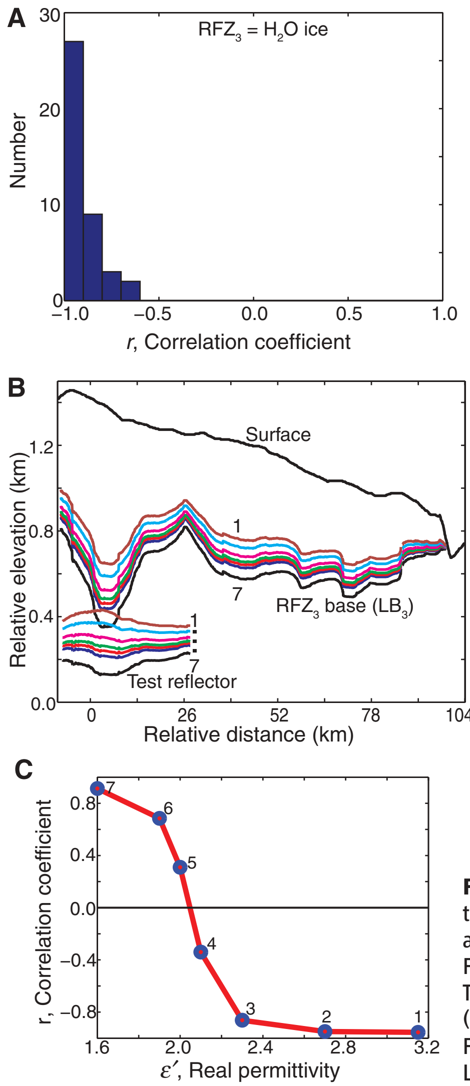

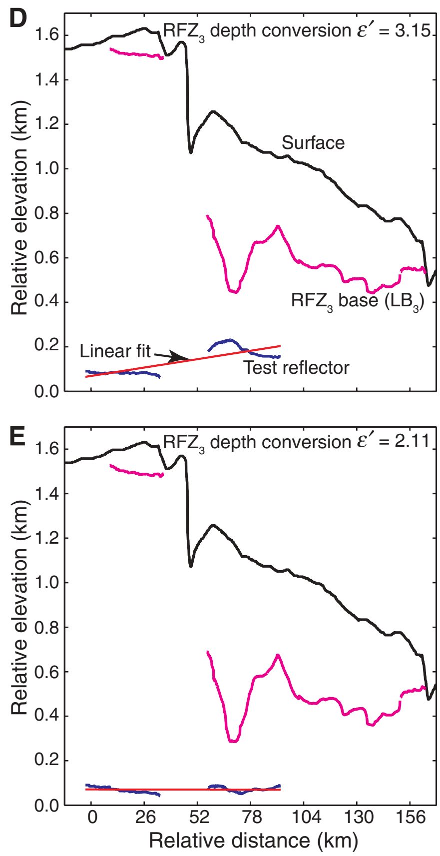

Fig. 2. (**A**) Distribution for 41 orbital observations of the correlation coefficients between LB$_3$ and the TR assuming RFZ$_3$ ε′ equals that of water ice, 3.15. (**B**) For observation 8104-01, the positions of LB$_3$ and TR as a function of RFZ$_3$ ε′. (**C**) The ε′ values used in (B) and the corresponding correlation coefficients. (**D**) For observation 8104-01, the positions of the surface, LB$_3$, and TR for RFZ$_3$ ε′ = 3.15. (**E**) Same as (D) except RFZ$_3$ ε′ = 2.11, which gives the best-fitting linear regression on TR.

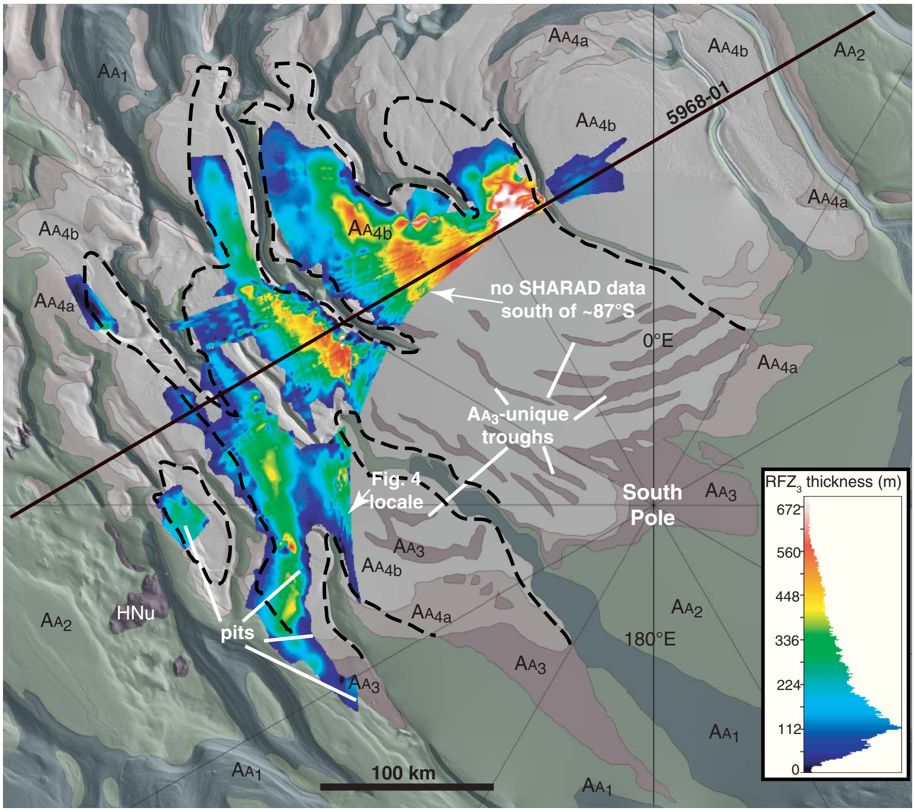

Fig. 3. Polar stereographic map of a portion of the SPLD, showing RFZ_3 thickness variations interpolated to a continuous volume for the 79 SHARAD ground tracks where RFZ_3 deposits were observed. Bright colors indicate deposit thicknesses calculated by using $\varepsilon' = 2.1$, and the histogram (**inset**) provides their relative occurrences. Base map (subdued colors) shows SPLD stratigraphy (*14*, *15*) with geologic units from oldest to youngest: HNu (substrate underlying SPLD); AA$_1$ (evenly bedded layers, up to 3.5 km thick); AA$_2$ (evenly bedded layers, <300 m thick); AA$_3$ (~300 m thick); and AA$_{4a}$ and AA$_{4b}$ (water-ice and CO_2-ice members, respectively, of the SPRC). The units are separated by unconformities, indicating episodes of erosion between them that resulted in retreat of the original lateral extents of the units and in development of local troughs and depressions. Dashed lines indicate boundaries of unit AA$_3$ where partially buried. Mars Orbiter Laser Altimeter (MOLA) shaded relief base at 115 m per pixel; because of spacecraft orbital inclinations, no SHARAD or MOLA data are available poleward of ~87°S. Ground track of observation 5968-01 (Fig. 1) is shown.

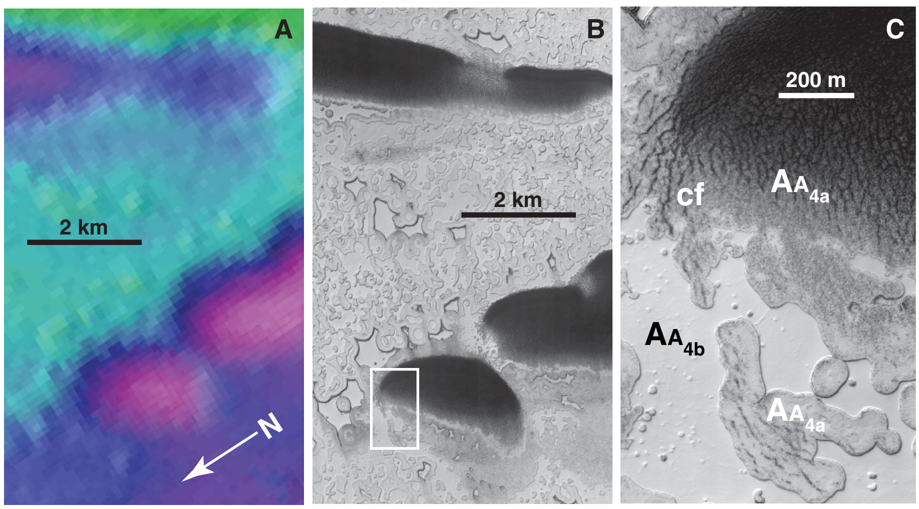

Fig. 4. MOLA topographic image (**A**) in the vicinity of 87°S, 268°E, showing linear depressions or troughs in the AA$_3$ unit. The total elevation range of the image is ~75 m from the lowest (pink) to the highest (green) surface. The troughs are associated with circular pits [(**B**), part of MRO HiRISE (High Resolution Imaging Science Experiment) image ESP_014342_0930] and are thinly buried by the SPRC (**C**), with unit AA$_{4b}$ (CO_2 ice) displaying sublimation windows into a fractured water-ice unit AA$_{4a}$ beneath (northwestern corner of a pit). The water-ice layer is completely exposed in the northeastern portion of this pit, where intense polygonal fracturing gives way to concentric fracturing on the pit rim (cf).

unit in the SPLD that exhibits clear (although different) morphological indicators of sublimation (*5*). The lack of sublimation features in exposures of the older units AA$_1$ and AA$_2$ indicate that CO_2, and not H_2O, is the sublimating material in the AA$_3$ unit, as might be expected given their relative volatilities. The AA$_3$ unit within pits distributed along the linear depressions is covered by a heavily fractured SPRC water-ice layer (AA$_{4a}$) that is overlain in places by the sublimating SPRC CO_2 layer (AA$_{4b}$) that formed after the fracturing (Fig. 4). The fracturing, not found in other SPLD units, may be a response to continuing unit AA$_3$ sublimation after the pits had first formed. The other three RFZs lack surface expressions of sublimation, but nondetection of sufficiently rugged lower boundaries precluded permittivity estimates.

Because we equate RFZ_3 to unit AA$_3$, we used the areal distribution of the geological unit to extrapolate the RFZ_3 volume poleward of ~87°S, achieving a total volume range (*17*) of ~9500 to 12,500 km^3 (*10*). In contrast, the volume of the CO_2-dominated SPRC is less than 380 km^3 (*3*), about 30 times less. The RFZ_3 thickness-independent permittivity values (*10*) imply a density close to that of bulk dry ice, 1500 to 1600 kg m^{-3} (*18*), which converts volume to an equivalent atmospheric pressure of 4 to 5 mbar, up to ~80% of the equivalent mass in the current atmosphere. The collapse features in the AA$_3$ unit suggest that the RFZ_3 mass has been waning, and an isolated patch of RFZ_3 (at ~345°E in Figs. 1 and 3) appears to be an erosional remnant. This suggests that the atmosphere has contained less than the present ~6 mbar of CO_2, hinting at past atmospheric collapse.

The lack of reflections in RFZ_3 apart from the bisecting layer can be interpreted as a lack of dust (*7*). Global climate models (GCMs) suggest (*19*) that, when the obliquity of Mars drops below a critical value, the atmosphere collapses onto the polar caps. At low obliquities, the ability of the atmosphere to lift dust is greatly diminished (*20*), possibly providing an explanation for the radar observations. Obviously, the CO_2 now buried in RFZ_3 was in the atmosphere at some time in the past. A plausible assumption is

that the RFZ_3 mass was largely in the atmosphere when the insolation at the south pole at summer solstice was at a maximum, which for the past one million years occurred about 600,000 years ago [obliquity = 34.76°, eccentricity = 0.085, longitude of perihelion = 259.4° (*21*)].

To assess the impact on some first-order climate parameters, we ran a fast version of the NASA/Ames Mars GCM (version 1.7.3) for these orbital conditions with a total exchangeable CO_2 inventory (atmosphere plus caps) equal to the present inventory (7.1 mbar) plus 5 mbar. We found that most of the additional 5 mbar of CO_2 ended up in the atmosphere. Surface pressures rose uniformly around the planet, with global-mean annually averaged pressures equaling 10.5 mbar. Annual mean cap masses increased by about 0.8 mbar, not accounting for the lost RFZ_3 mass. Surface temperatures, however, decreased slightly (~0.7 K) because the CO_2 ice was on the ground for a longer period, and this compensated the modest greenhouse effect.

There are two implications of these changes in the climate system. First, the increased CO_2 pressure expands the geographic locations where these pressures exceed the triple-point pressure of water, thereby permitting liquid water to persist without boiling (although it may still evaporate, as on Earth) (*22*). Second, higher surface pressures will lead to higher surface wind stresses, which will loft more dust in the atmosphere, leading to an increase in dust storm frequency and intensity. Given the complex interplay between the dust, water, and CO_2 cycles, additional changes in the climate system are very likely.

References and Notes

1. B. M. Jakosky, R. J. Phillips, *Nature* **412**, 237 (2001).
2. R. B. Leighton, B. C. Murray, *Science* **153**, 136 (1966).
3. P. C. Thomas, P. B. James, W. M. Calvin, R. Haberle, M. C. Malin, *Icarus* **203**, 352 (2009).
4. H. Kieffer, *J. Geophys. Res.* **84**, 8263 (1979).
5. S. Byrne, A. P. Ingersoll, *Science* **299**, 1051 (2003).
6. R. Seu *et al.*, *J. Geophys. Res.* **112**, E05S05 (2007).
7. R. J. Phillips *et al.*, *Science* **320**, 1182 (2008); 10.1126/science.1157546.
8. N. E. Putzig *et al.*, *Icarus* **204**, 443 (2009).
9. R. Seu *et al.*, *Science* **317**, 1715 (2007).
10. Materials and methods are available as supporting material on *Science* Online.
11. E. Pettinelli *et al.*, *J. Geophys. Res.* **108**, 8029 (2003).
12. R. Simpson, B. Fair, H. Howard, *J. Geophys. Res.* **85**, 5481 (1980).
13. D. C. Nunes, R. J. Phillips, *J. Geophys. Res.* **111**, E06S21 (2006).
14. E. J. Kolb *et al.*, "The residual ice cap of Planum Australe, Mars: New insights from the HRSC experiment." Paper presented at the 37th Lunar and Planetary Science Conference, League City, TX, 13 to 17 March 2006; www.lpi.usra.edu/meetings/lpsc2006/pdf/2408.pdf.
15. K. L. Tanaka, E. Kolb, C. Fortezzo, "Recent advances in the stratigraphy of the polar regions of Mars." Paper presented at the Seventh International Conference on Mars, Pasadena, CA, 9 to 13 July 2007; www.lpi.usra.edu/meetings/7thmars2007/pdf/3276.pdf.
16. RFZ_3 is seen discontinuously in radargrams here, but key reflectors could not be mapped with high confidence likely because of surface scattering interference, resolution limitations, and lack of coverage.
17. A lower value of ~4000 to 4500 km^3 is obtained with the unlikely assumption that RFZ_3 does not extend beyond SHARAD's data gathering locales, which are limited by MRO's orbital inclination. See (*10*).
18. R. C. Weast, *CRC Handbook of Chemistry and Physics* (CRC Press, Boca Raton, FL, ed. 55, 1974).
19. C. Newman, S. Lewis, P. Read, *Icarus* **174**, 135 (2005).
20. R. M. Haberle, J. R. Murphy, J. Schaeffer, *Icarus* **161**, 66 (2003).
21. J. Laskar *et al.*, *Icarus* **170**, 343 (2004).
22. R. Haberle *et al.*, *J. Geophys. Res.* **106**, 23317 (2001).

Acknowledgments: K. Herkenhoff and C. Fortezzo provided useful comments on an earlier version of the paper. Remarks by three anonymous referees were exceedingly helpful. Funding for this work was provided by the NASA MRO project. The radar and imaging data are available through NASA's Planetary Data System.

Supporting Online Material

www.sciencemag.org/cgi/content/full/science.1203091/DC1
Materials and Methods
SOM Text
Figs. S1 to S5
Tables S1 to S4
References

20 January 2011; accepted 23 March 2011
Published online 21 April 2011;
10.1126/science.1203091

Late Mousterian Persistence near the Arctic Circle

Ludovic Slimak,[1]* John Inge Svendsen,[2] Jan Mangerud,[2] Hugues Plisson,[3] Herbjørn Presthus Heggen,[2] Alexis Brugère,[4] Pavel Yurievich Pavlov[5]

Palaeolithic sites in Russian high latitudes have been considered as Upper Palaeolithic and thus representing an Arctic expansion of modern humans. Here we show that at Byzovaya, in the western foothills of the Polar Urals, the technological structure of the lithic assemblage makes it directly comparable with Mousterian Middle Palaeolithic industries that so far have been exclusively attributed to the Neandertal populations in Europe. Radiocarbon and optical-stimulated luminescence dates on bones and sand grains indicate that the site was occupied during a short period around 28,500 carbon-14 years before the present (about 31,000 to 34,000 calendar years ago), at the time when only Upper Palaeolithic cultures occupied lower latitudes of Eurasia. Byzovaya may thus represent a late northern refuge for Neandertals, about 1000 km north of earlier known Mousterian sites.

Most of the Russian Arctic was free of glacier ice throughout the past 50,000 years, including during the Last Glacial Maximum (LGM) (*1*). A varied herbivorous fauna existed in high Arctic areas that are presently wet tundra or almost barren Arctic deserts (*2*). Recent archaeological evidence demonstrates that Ice Age humans also at least temporarily lived and hunted in these northern landscapes beginning around 35,000 to 36,000 ^{14}C years before the present (yr B.P.) [≥40,000 yr B.P. in calibrated/calendar (cal) years] (*3*–*7*) (fig. S1). It has not been clear whether the early visitors were members of a fossil population [such as *Homo sapiens neanderthalensis* and affiliated groups (*8*, *9*)] or whether modern humans (*H. sapiens sapiens*) expanded northward into a previously uninhabited area.

This question is related to the Middle Palaeolithic (MP) to Upper Palaeolithic (UP) cultural transition in Eurasia. This transition, which has been considered to have taken place about 40,000 to 37,000 yr B.P. in most of Eurasia, saw the global extinction of the Neandertals and thus the end of their specific MP (Mousterian) culture. The Neandertals were replaced by modern humans, who were the bearers of all known UP cultures.

Here we describe lithic technology and age constraints from the Byzovaya site near the Polar Urals and show that humans bearing MP stone technology persisted to 32,000 to 34,000 cal yr B.P. in the Eurasian Arctic (Fig. 1). Byzovaya, which is among the northernmost known Palaeolithic sites, was previously considered to be an Early Upper Palaeolithic (EUP) site mainly on the basis of a few radiocarbon dates that suggested an age of about 27,000 ^{14}C years or younger.

The Byzovaya site (65°01′25″N, 57°25′12″E) is located on the right bank of the Pechora River, which flows northward across the lowland areas west of the Ural Mountains (Fig. 1). First described in 1965 by Guslitser *et al.* (*10*), the locality was investigated several times by Russian archaeologists (*11*); later by a Norwegian-Russian team, since 1996 (*6*, *12*); and by a French-Russian team since 2007. More than 300 stone artefacts and 4000 animal remains have been uncovered during the various excavations, which together cover an area of approximately 550 m^2.

[1]CNRS, UMR 5608, TRACES, Université de Toulouse le Mirail, Maison de la Recherche, 5 Allées Antonio Machado, 31058 Toulouse Cedex 9, France. [2]Department of Earth Science and Bjerknes Centre for Climate Research, University of Bergen, Allégaten 41, N-5007, Bergen, Norway. [3]CNRS, UMR 5199, PACEA, IPGQ, Université Bordeaux 1, Bâtiment B18, Avenue des Facultés, 33405 Talence Cedex, France. [4]CNRS, USR 3225 and UMR 7041, ArScAn, "Archéologies Environnementales," Maison de l'Archéologie et de l'Ethnologie René Ginouvès, CC023, 21, Allée de l'Université, 92023 Nanterre Cedex, France. [5]Department of Archaeology, Institute of Language, Literature and History, Komi Science Centre, Russian Academy of Sciences, Kommunisticheskaya Street 26, 167000 Syktyvkar, Komi, Russia.

*To whom correspondence should be addressed. E-mail: slimak@univ-tlse2.fr

The site is located in a paleo-gully that is incised into Triassic sandstone. The gully, which is about 250 m long and 300 m wide, starts from a shoulder in the river valley at an altitude of about 100 m above sea level (a.s.l.) and ends near the shore of the Pechora River about 44 m a.s.l. Artefacts are encased in a layer of sandy gravel up to 2.5 m thick that rests directly on the bedrock at the bottom of the paleo-gully. This layer crops out along the river cliff (Fig. 2 and fig. S7). The sediments that contain the archaeological finds accumulated during a series of successive debris flows. We were not able to determine whether there were breaks between each flow or if they all happened during one single event, although some individual flows are separated by thin layers of silt. Several meters of well-sorted windblown (aeolian) sand overlay and interfinger with the debris flow deposits (Fig. 2). Most of the bones and artefacts are well preserved. Both the excellent preservation of the bones and the inferred paleotopography indicate that the debris flows moved only a short distance, most likely less than a few tens of meters or so. The bones and artefacts occur throughout the gravelly layers. Several well-preserved mammoth bones and tusks were found on the surface of this formation, draped by the overlying windblown sand (fig. S8). Some bones and artefacts are concentrated within one of the mentioned silt horizons in the middle of the layer and may represent in situ deposits.

More than 97% of the identified faunal remains are from mammoth (*Mammuthus primigenius*) and represent at least 21 individuals. In addition, several other animals have been identified [supporting online material (SOM)]: woolly rhinoceros (*Coelodonta antiquitatis*), reindeer (*Rangifer tarandus*), musk ox (*Ovibos moschatus*), horse (*Equus callabus* sp.), brown bear (*Ursus arctos*), wolf (*Canis lupus*), and polar fox (*Alopex lagopus*). Many of the animal remains from the top deposit have cut marks that indicate processing by humans (figs. S10 and S11).

We obtained 33 ^{14}C dates from the bones (table S1). The mean age for all samples is 28,570 ± 1370 ^{14}C yr B.P., but 28,450 ± 820 when 12 dates with large uncertainties are omitted (SOM text). The distribution of the ^{14}C ages is almost Gaussian (fig. S2), and the simplest interpretation is that the spread of ages is mainly an artefact of random counting uncertainties and that all samples should therefore have a similar age. We conclude that the age of 28,450 ± 820 ^{14}C yr B.P. is the best age of the human occupation (fig. S2). Conversion of ^{14}C ages to sideral (cal) years is problematic for such old samples, but this age corresponds to the calibrated age intervals of 33,650 to 31,670 and 34,580 to 31,370 cal yr B.P. for the 68 and 95% confidence intervals, respectively, when using the IntCal09 (*13*) data set. As a further test, we obtained four optically stimulated luminescence (OSL) dates from the windblown sand draping the find-bearing strata. The ages were all between 30,000 and 33,000 yr B.P., with an uncertainty (1σ) of 2000 to 3000 years (Fig. 2 and table S2) and a mean of 32,000 ± 2000 yr B.P. The interfingering contact between the debris flow layer and the sand suggests that the ages of the layers are overlapping in time. Indeed, the OSL ages overlap with the calibrated ^{14}C ages of the bones.

These ages demonstrate that the human occupation of Byzovaya happened during the latter part of marine isotope stage (MIS) 3, well before the buildup of the Barents-Kara Ice Sheet during MIS 2. The age fits roughly into the period when the Bryansk soil developed on the Russian Plain farther to the south (*14*). This interstadial (31,000 to 24,000 ^{14}C yr B.P.) was slightly warmer than the preceding and following periods, but the climate was still much colder than at present. The radiocarbon chronology indicates that the human visits at Byzovaya took place a few hundred years after the mild Ålesund interstadial in Scandinavia, an interval that has been correlated with Greenland interstadial (GI) 8 to 7 (*15*). Taken at face value, the calibrated age of Byzovaya corresponds to the ice core interval GI 6 to 5.

A total of 313 lithic artefacts have been collected during the various excavations. The artefacts are mainly composed of local raw materials coming from the gravels of the Pechora River (table S3). These rocks are abundant on the river shore and also in thick glacial and glaci-lacustrine sediments in the river bank (*12*). Our experimental in situ knapping shows that the local raw materials are applicable for any kind of flaking technology.

This industry consists of flakes, 11 cores, and as many as 80 defined typological tools. End products are well represented for a collection of this size (80 out of 313). The cores were used exclusively for flake production. Four pieces are typical Levallois cores, a flaking method that is considered to be a distinctive feature in MP assemblages (Fig. 3, no. 2). This technology is also

Fig. 1. Map showing the location of the Byzovaya site, close to the northern Urals. Other sites mentioned in the text are also shown. The red stippled line circumscribes the area with known Neandertal sites; here only some selected young sites are marked. The maximum extent of the Eurasian Ice Sheet during the LGM (about 26,000 to 20,000 cal yr B.P.) is also shown (*1*).

represented by some well-defined Levallois flakes. The remaining seven cores are based on discoid (fig. S5, no. 3) and polyhedric flakings, which are a common combination in MP contexts. The applied stone technology is based on Levallois and discoid flake production. There are neither technological blades nor bladelets nor other elements that could be ascribed to the technical representation of UP technologies. We conducted experiments on the same raw materials and were able to make similar flakes only by direct hard hammer percussion. The preserved flakes could have been used to make side-scrapers of various types and sizes. Some flakes were directly used without any retouching, because some of their edges are worn (fig. S12).

None of the 313 artefacts reflects a tool production technology typical of UP cultures. Furthermore, diagnostic tools that are common in any UP industry of Eurasia such as burins, backed tools, pointed blades, or bladelets are not represented. There are 11 end-scrapers, but none of these were prepared from UP blades. Varieties of end-scrapers, prepared from flakes, are common elements in any European MP industry, known since the first Mousterian typological analysis (*16*). Typological tools are mainly members of the Mousterian group (*16*), dominated by distinctive side-scrapers made out of flakes (fig. S5, nos. 1 and 2) that are typical for MP industries (*17*) (fig. S6 and table S4). Six of these tools have been retouched to form a bifacial tool. Most of the bifacial tools are thick, with a plano-convex section: one face shaped by large flakes and the opposite face formed by a semi-abrupt retouch. This way of shaping has been used for producing so-called Keilmesser tools (plano-convex and backed bifacial tools, Fig. 3, no. 1), which are considered to be specific artefacts of some archetypical MP industries of Central and Eastern Europe (*18*–*20*). Two of the bifacial tools from Byzovaya present a thin regular transformation of their faces that illustrates the technological similarities between this industry and the Eastern European MP (*18*, *19*), where the so-called Blattspitzen (short foliate) tools occur frequently.

The lithic industry of Byzovaya is technically and typologically homogeneous and shows a combination of diagnostic features that belong exclusively to MP traditions from Central and Eastern Europe, previously known from sites dating from MIS 3 to 4 (*19*). All lithic tools and bones are stratigraphically associated, and 22 faunal remains show anthropogenic modifications. This is in accordance with the use wear of lithic tools related to butchering activities. Two of our dates are on a cut marked mammoth bone and a modified reindeer antler (table S1).

The EUP complexes that succeeded the MP complexes present specific archaeological features that distinguish them from the MP industries. Blades, bladelets, and projectile points constitute the lithic background for EUP assemblages in Eurasia. For example, at Kostenki 14, along the Don River in southern Russia (Fig. 1), these EUP elements appear in layer IV, dated to 45,000 to 41,000 cal yr B.P., which is about 10,000 years earlier than the human occupation at Byzovaya (*21*–*23*). At Zaozer'e, farther to the north and closer to Byzovaya, blades and bladelets were produced by humans sometime between 39,000 and 37,000 yr B.P. (Fig. 1) (*4*, *6*). Russian EUP sites that are more or less contemporaneous with Byzovaya, such as Sungir (*24*) and Garchi (*6*), are characterized by lithic triangular projectile points. A rich bone and ivory technology with spear points, figurines, ornaments, and beads is common in most EUP Eurasian sites where organic materials are well preserved (as at Byzovaya). It has been recently proposed that some of the Kostenki sites show some archaic traits resulting from a specialized tool kit made by UP hunters at a kill-butchery site (*25*). However, tools from the Gorotsovian and Streletskian layers at Kostenki do not resemble the Byzovaya assemblage but are dominated by typical UP traits reflecting their specific cultural associations (standardized triangular foliated spear points, in the Streletskian layers, and rich bone and ivory technologies in the Gorotsovian).

There is no evidence that the assemblage at Byzovaya can be explained by site-specific activities such as mammoth exploitation and butchering. At all well-dated sites with abundant mammoth remains, the artefacts that are found with the animal remains also reveal the cultural affiliation of the humans who made them. This is true for MP sites such as Mont-Dol (*26*) or Salzgitter-Lebenstedt (*27*) and for EUP Gravettian sites of Central Europe, such as Milovice in Moravia and Krakow-Spadzista in Poland (*28*, *29*). Theoretically, one may also wonder if the lack of some UP elements,

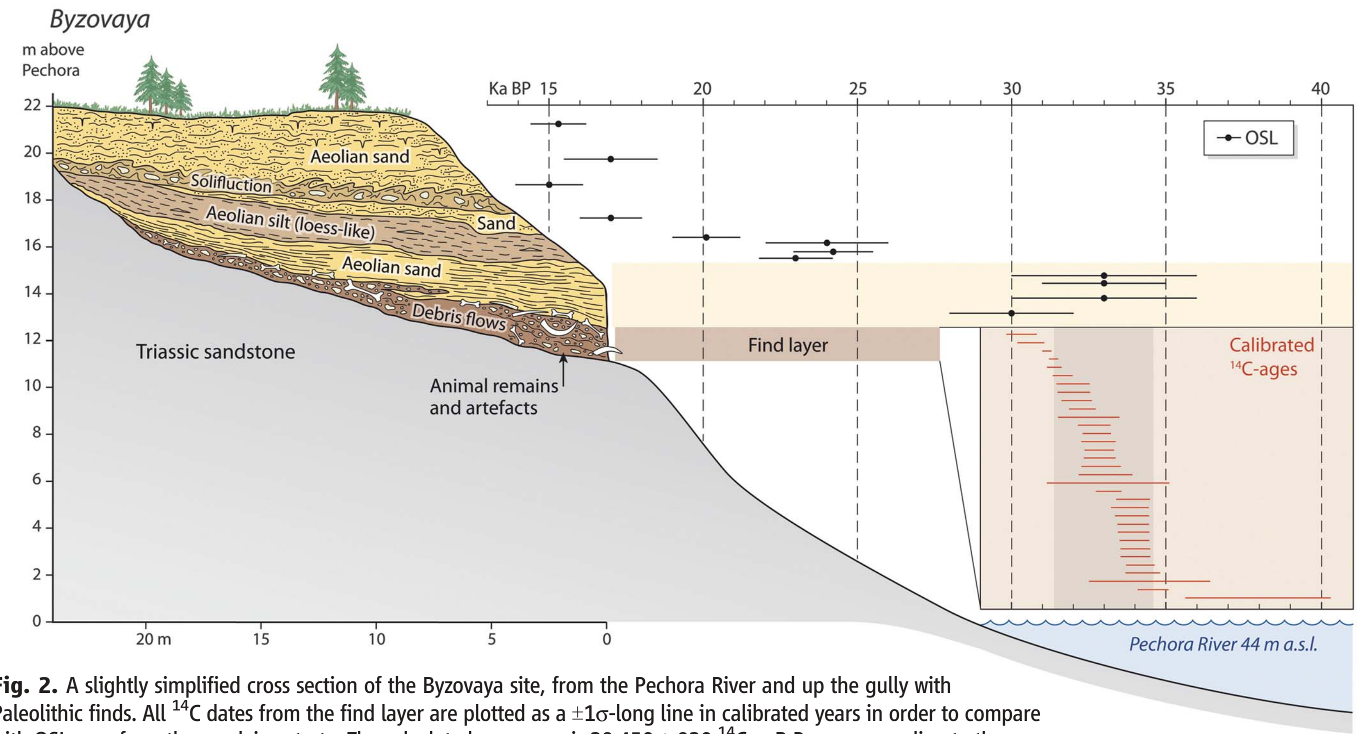

Fig. 2. A slightly simplified cross section of the Byzovaya site, from the Pechora River and up the gully with Paleolithic finds. All ^{14}C dates from the find layer are plotted as a $\pm 1\sigma$-long line in calibrated years in order to compare with OSL ages from the overlying strata. The calculated mean age is 28,450 ± 820 ^{14}C yr B.P., corresponding to the age interval 34,580 to 31,370 cal yr B.P. for the 95% confidence interval ($\pm 2\sigma$). This interval is marked by a vertical gray zone on the figure. All calculations are explained in the SOM text.

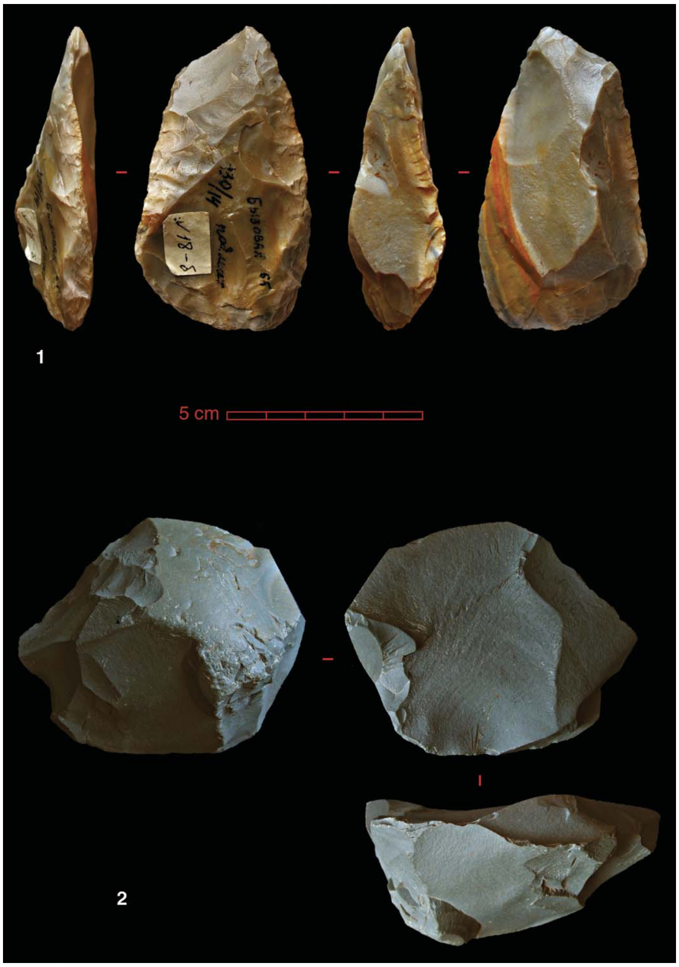

Fig. 3. Photographs of two stone artefacts from Byzovaya. 1, Keilmesser; 2, Levallois core, preferential method. [Photos by Hugues Plisson]

such as blades and bladelets, can be explained by the quality of the raw material at hand. However, various siliceous rocks of good quality were easily available and were also used for tool production at an adjacent Mesolithic site containing almost exclusively well-prepared and regular blades and bladelets.

Most researchers agree that classical Mousterian industries in Europe were exclusively produced by Neandertals (*30*, *31*). However, whether Byzovaya represents a Neandertal site or not cannot be demonstrated beyond doubt until human bones or DNA are found. If the Byzovaya artefacts were struck by modern humans, this would have major implications for understanding the MP-UP transition, as it would imply that these Arctic *H. sapiens* groups preserved older, traditional MP cultures far after the full expansion of UP modern societies in the rest of Eurasia.

Neandertal fossils and unambiguous MP industries are known from a large part of the Eurasian continent (fig. S1), stretching from the Atlantic Ocean to the Altai Mountains in the east (*32*). However, other unambiguous MP artefacts have not been reported from areas north of about 55°N latitude, which is about 1000 km south of Byzovaya (*33*). (Fig. 1). One of the most recent Neandertal remains is a skeleton found in Croatia (Vindija G1) and dated to ~32,000/33,000 ^{14}C yr B.P. (≥37 cal yr B.P.) (*34*). Younger Mousterian artefacts have been reported from the southern part of the Iberian Peninsula, including layer IV of Gorham's cave, Rock of Gibraltar, where 103 artefacts have been attributed to a late Mousterian culture between 33,000 and 24,000 ^{14}C yr B.P. (*35*). However, these ages have been debated (*36–38*).

If, like elsewhere in Europe, these technologies were realized by Neandertals, then such late persistence of Mousterian traditions at this high latitude as late as about 10,000 years after the UP first appearance at lower latitudes in Russia (Kostenki) would imply that the two human species coexisted over a longer time period than has been thought. In any case, the site shows that Neandertals or another relic population of humans with Mousterian technology were fully capable of coping with the cold climate and dark winters that prevailed at the highest latitudes. The site also challenges the hypothesis that there was a complete replacement of the MP societies in all of Europe as early as around 37,000 cal yr B.P. (*37*).

References and Notes

1. J. I. Svendsen *et al.*, *Quat. Sci. Rev.* **23**, 1229 (2004).
2. H. W. Hubberten *et al.*, *Quat. Sci. Rev.* **23**, 1333 (2004).
3. P. Pavlov, J. I. Svendsen, S. Indrelid, *Nature* **413**, 64 (2001).
4. J. I. Svendsen, P. Pavlov, in *The Chronology of the Aurignacian and the Transitional Technocomplexes: Dating, Stratigraphies, Cultural Implications*, J. Zilhao, F. d'Errico, Eds. (Trabalhos de Archaeologia, Lisboa, Portugal, 2003), pp. 109–120.
5. V. V. Pitulko *et al.*, *Science* **303**, 52 (2004).
6. J. I. Svendsen *et al.*, *Quat. Sci. Rev.* **29**, 3138 (2010).
7. P. Pavlov, W. Roebroeks, J. I. Svendsen, *J. Hum. Evol.* **47**, 3 (2004).
8. D. Reich *et al.*, *Nature* **468**, 1053 (2010).
9. J. Krause *et al.*, *Nature* **464**, 894 (2010).
10. B. I. Guslitser, V. I. Kanivets, Ye. M. Timofeyev, *Sovetskaya arkheologiya* **2**, 112 (1965) [in Russian].
11. P. Pavlov, *The Excavation of Byzovaya Upper Palaeolithic Site in 1983-1985* (*Pamiaatniki materialnoj kultyury na Evropeiskom severo-vostoke*) (Russian Academy of Sciences, Syktyvkar, Russia, (1986), pp. 7–16 [in Russian].
12. H. P. Heggen, J. I. Svendsen, J. Mangerud, *Boreas* **39**, 116 (2010).
13. P. Reimer *et al.*, *Radiocarbon* **51**, 1111 (2009).
14. A. A. Velichko, E. M. Zelikson, *Quat. Int.* **126-128**, 137 (2005).
15. J. Mangerud, S. Gulliksen, E. Larsen, *Boreas* **39**, 328 (2010).
16. F. Bordes, *Typologie du Paléolithique Ancien et Moyen* (Delmas, Bordeaux, France, 1961).
17. L. Slimak, thesis, Université de Provence, Aix-en-Provence, France (2004).
18. G. Bosinski, *Die Mittelpaläolithischen Funde im Westlichen Mitteleuropa* (Fundamenta A/4, Böhlau, Köln/Graz, Germany, 1967).
19. G. Bosinski, *Zephyrus* **53/54**, 77 (2001).
20. O. Jöris, *Ber. Römisch-Germanischen Komm.* **84**, 49 (2004).
21. A. A. Sinitsyn, J. F. Hoffecker, *Quat. Int.* **152-153**, 164 (2006).
22. M. V. Anikovich *et al.*, *Science* **315**, 223 (2007).
23. B. Giaccio *et al.*, *J. Volcanol. Geotherm. Res.* **177**, 208 (2008).
24. O. Bader, *Sungir Upper Palaeolithic Site* (Nauka, Moscow, 1978) [in Russian].
25. J. F. Hoffecker *et al.*, *J. Archaeol. Sci.* **37**, 1073 (2010).
26. P. Simonet, J. L. Monnier, *Quaternaire* **2**, 5 (1991).
27. E. W. Guenther, in *Der Altsteinzeitliche Fundplatz Salzgitter-Lebenstedt. Teil II. Naturwissenschaftliche Untersuchungen*, R. Busch, H. Schwabedissen, Eds. (Böhlau, Köln, Germany, 1991), pp. 101–147.
28. A. Brugère, L. Fontana, M. Oliva, in *In Search of Total Animal Exploitation. Case Studies from the Upper Palaeolithic and Mesolithic*, L. Fontana, F.-X. Chauvière, A. Bridault, Eds. (British Archaeological Reports International Series 2040, Oxford, 2009), pp. 45–69.
29. P. Wojtal, K. Sobczyk, *J. Archaeol. Sci.* **32**, 193 (2005).
30. J. J. Hublin, in *Rethinking the Human Revolution: New Behavioural and Biological Perspectives on the Origin and Dispersal of Modern Humans*, P. Mellars, K. Boyle, O, Bar-Yosef, C. Stringer, Eds. (McDonald Institute for Archaeological Research, Cambridge, 2007), pp. 235–248.
31. C. Stringer, *Philos. Trans. R. Soc. London Ser. B* **357**, 563 (2002).
32. J. Krause *et al.*, *Nature* **449**, 902 (2007).
33. J.-J. Hublin, W. Roebroeks, *C.R. Palevol.* **8**, 503 (2009).
34. T. Higham, C. B. Ramsey, I. Karavanić, F. H. Smith, E. Trinkaus, *Proc. Natl. Acad. Sci. U.S.A.* **103**, 553 (2006).
35. C. Finlayson *et al.*, *Nature* **443**, 850 (2006).
36. J. Zilhao, P. Pettitt, *Before Farming* **2006/3**, 95 (2006).
37. C. Barroso Ruiz, Ed., *El Pleistoceno Superior de la Cueva del Boquete de Zafarraya* (Arqueologia Monografias 15, Junta de Andalucia Sevilla, Spain, 2003).
38. S. P. E. Blockley, C. Bronk Ramsey, T. F. G. Higham, *J. Hum. Evol.* **55**, 764 (2008).

Acknowledgments: L.S., H.P., and A.B. analyzed the archaeological material; J.I.S, J.M., and H.P.H. performed the stratigraphic, paleoenvironmental, and chronological descriptions and interpretations; and P.Y.P. organized the archaeological field missions. All contributed to the writing of the paper. Supported by the Fondation des Maisons des Sciences de l'Homme, the French-Russian Center for Social and Human Sciences in Moscow, the French Ministry of Foreign and European Affairs, the Research Council of Norway, and Russian Foundation for

Humanitarian Research grant 08-01-94952a. Kh. A. Arslanov and S. Gulliksen performed the radiocarbon dating and A. Murray the OSL dating. We thank the Komi Scientific Centre in Syktyvkar; the museums of Pechora and of Syktyvkar; and the Institute of History of Material Culture of St. Petersburg, especially A. A. Sinitsyn and A. E. Matjuhin for access to their collections and N. N. Skakun for her help. We also thank E. Bjørseth for preparing Figs. 1 and 2 and figs. S1 and S2 and J. E. Lewis for improving the English.

Supporting Online Material
www.sciencemag.org/cgi/content/full/332/6031/841/DC1
SOM Text
Figs. S1 to S12
Tables S1 to S4
References *39* to *57*

4 February 2011; accepted 29 March 2011
10.1126/science.1203866

Experimental Evidence Supports a Sex-Specific Selective Sieve in Mitochondrial Genome Evolution

Paolo Innocenti,[1]* Edward H. Morrow,[1] Damian K. Dowling[2]*†

Mitochondria are maternally transmitted; hence, their genome can only make a direct and adaptive response to selection through females, whereas males represent an evolutionary dead end. In theory, this creates a sex-specific selective sieve, enabling deleterious mutations to accumulate in mitochondrial genomes if they exert male-specific effects. We tested this hypothesis, expressing five mitochondrial variants alongside a standard nuclear genome in *Drosophila melanogaster*, and found striking sexual asymmetry in patterns of nuclear gene expression. Mitochondrial polymorphism had few effects on nuclear gene expression in females but major effects in males, modifying nearly 10% of transcripts. These were mostly male-biased in expression, with enrichment hotspots in the testes and accessory glands. Our results suggest an evolutionary mechanism that results in mitochondrial genomes harboring male-specific mutation loads.

The mitochondrial-eukaryote union represents one of life's most important symbioses, equipping the eukaryotic cell with a highly efficient means of energy conversion. The upshot of this union is that contemporary metazoa harbor two obligate genomes. The genome located within the cell nuclei (nuclear genome) contains the vast majority of function-encoding genetic material (about 14,000 genes in *Drosophila melanogaster*) (*1*), whereas the mitochondrial genome (mtDNA) is diminutive in size, consisting of just 37 genes (13 protein-coding, 22 tRNA, and 2 ribosomal RNA) (*2*). Although few in number, mitochondrial genes serve an essential function, with both nuclear- and mtDNA-encoded proteins interacting within the mitochondria to perform cellular respiration. The tight coordination in gene expression necessary for organelle function is achieved by extensive signaling between mitochondrial and nuclear genomes, via anterograde and retrograde regulation (*3*).

Unlike their nuclear counterparts, mitochondrial genomes generally have solely maternal transmission, resulting in evolutionary dead ends for the mtDNA of males (*4*). As such, mtDNA should only be able to make a direct evolutionary response to selection through females [but see (*5*, *6*)]. This should pose no problem for traits with identical function across males and females. However, mutations in mtDNA that contribute to the expression of traits exhibiting different sex-specific optima (i.e., sexually dimorphic or sexually antagonistic traits) will be subject to a sex-specific selective sieve. This means that selection will fail to prevent the accumulation of mtDNA mutations that are deleterious when expressed in males, if the same mutations are only slightly deleterious (*4*), neutral (*7*), or beneficial (*8*, *9*) when expressed in females.

If a sex-specific selective sieve is important in mitochondrial genome evolution, then we predict that mitochondrial genomes should generally harbor a mutation load that is more pronounced in males. Also, the effect of the mutation load should increase with the degree of male-biased sexual dimorphism of the trait or tissue in question, because the benefits that males can salvage from relying on female-specific adaptation of mtDNA will diminish as the level of sex-biased expression increases and the intersexual genetic correlation erodes.

We tested these predictions on the basis of the facts that extensive signaling takes place between mitochondrial and nuclear genomes (*3*) and that polymorphisms in mtDNA typically exert their phenotypic effects through interactions with the nuclear genome (*10*). We explored genome-wide variation in nuclear gene expression across strains of *D. melanogaster* that differ only in the origin of their mitochondrial genomes by using GeneChip Drosophila Genome 2.0 microarrays (Affymetrix, Incorporated, Santa Clara, CA). We examined five distinct, naturally occurring mitochondrial genomes from around the globe [*Alstonville* (New South Wales, Australia), *Brownsville* (Texas, USA), *Dahomey* (Benin), *Japan*, and *Mysore* (India)]. An abundance of nonsynonymous and synonymous polymorphisms exists across the protein-coding sequences of these five genomes [supporting online material (SOM) text]. Each mitochondrial genome was coexpressed with the isogenic nuclear background, w^{1118}, in two replicates per strain. Replicates for each mtDNA strain were created as a safeguard to ensure that inferences regarding effects of mtDNA polymorphism were not confounded by cryptic genetic variation that might have accumulated in the nuclear background during the period in which the strains were created and assayed. No differential expression between replicates of any mtDNA strain was found ($P >$ 0.05 after multiple testing corrections in two-tailed *t* tests for all the transcripts, for each pair of replicate introgressions). Other environmental variables (e.g., food source, temperature, light, age, and mating status) were carefully controlled to minimize sources of variation.

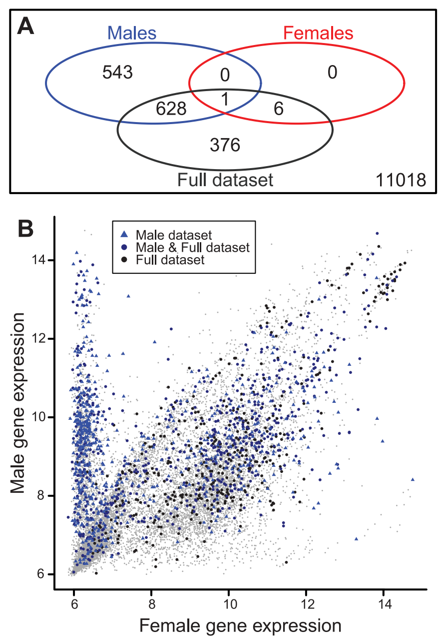

Fig. 1. Differentially expressed genes. (**A**) Venn diagram representing the intersections between the sets of nuclear genes showing a significant effect of mitochondrial strain in males (blue, top left), in females (red, top right), and in the full data set (black, bottom). (**B**) Expression levels (in $\log_2$ scale) of the same sets of genes (blue triangles and dark blue and black dots), in male and female adults of *D. melanogaster*. Gray dots in the background represent the expression level of non–differentially expressed genes.

[1]Department of Ecology and Genetics, Evolutionary Biology Centre, Uppsala University, Norbyvägen 18-D, 75236 Uppsala, Sweden. [2]School of Biological Sciences, Monash University, Clayton, Victoria 3800, Australia.

*These authors contributed equally to this work.
†To whom correspondence should be addressed. E-mail: damian.dowling@monash.edu

When male and female gene expression data were considered together, different mitochondrial strains significantly affected the expression of 1011 nuclear genes [8.0% of tested genes; $P < 0.05$ after a multiple testing correction was set as a cut-off for all contrasts (*6*)]. When male and female gene expression profiles were analyzed separately, the strain effect on males accounted for the differential expression of 1172 genes (9.3%), whereas only 7 genes (~0.06%) were significant for the strain effect on female gene expression. These results suggest that, in general, different mitochondrial strains have a large impact on nuclear gene expression and that this effect extends to a disproportionately larger number of genes in males than in females. The intersection of the three lists of genes (Fig. 1A) also indicates that most of the total variation in gene expression is driven by males (~62% of the genes showing an overall strain effect also show a significant strain effect in male gene expression). In total, 1554 nuclear genes were differentially expressed in at least one sex as a consequence of their coexpression with mitochondrial genomes of different origins.

We then examined the relationship between the significant genes and the levels of sexual dimorphism of the transcriptome. The nuclear genes with expression affected by the mitochondrial genomes were significantly more male-biased in expression than expected [two-tailed Fisher's exact test: odds ratio = 1.13, $P = 0.028$, mean-rank gene set enrichment test (*11*), MR-GSE, $P = 3.3 \times 10^{-22}$ (Fig. 1B)], and this effect was magnified when we considered only the transcripts that were differentially expressed in the male-only data set (Fisher's exact test: odds ratio = 1.56, $P = 1.1 \times 10^{-12}$, MR-GSE test, $P = 1.8 \times 10^{-52}$). To evaluate the likely impact of the mitochondrially affected genes on fitness, we tested their association with transcripts known to be associated with sex-specific fitness (*12*). Our set of 1554 significant genes was overrepresented among the genes associated with male fitness (MR-GSE test, $P = 4.19 \times 10^{-6}$) but not with female fitness (MR-GSE test, $P = 0.61$).

The pairwise correlations between the significant transcripts were used to compute modules of correlated expression and to cluster these genes into groups to determine whether they exhibit functional relationships. We identified 52 transcriptional modules containing from 1 to 275 genes. The largest modules [those containing more than 10 genes, $n = 18$ (Fig. 2)] were evaluated for their level of sexual dimorphism, tissue-specific enrichment, cross-tissue correlation, chromosomal distribution, association with functional categories (gene ontologies) and male fitness, female fitness and sexual antagonism (*12*) (SOM text, Table 1, tables S1 to S18, and figs. S1 to S18).

The two largest modules (12 and 16), together accounting for ~30% of the significant transcripts, also show the most male-biased expression. Module 12, containing 275 genes, is almost exclusively male-limited transcripts [mean intensity (x_m) = 9.7, SD = 1.2, x_f = 6.4, SD = 0.6; range of the whole data set, 5.7 to 15.1; Wilcoxon test: $W = 74553$, $P = 1.6 \times 10^{-86}$ (Fig. 3, A and B, and fig. S12B)], with expression largely limited to the male testes [Fisher's exact test: odds ratio = 107, $P = 2 \times 10^{-183}$; not significant in any other tissue (Fig. 3D and fig. S12F)]. Module 16 is represented by 185 genes

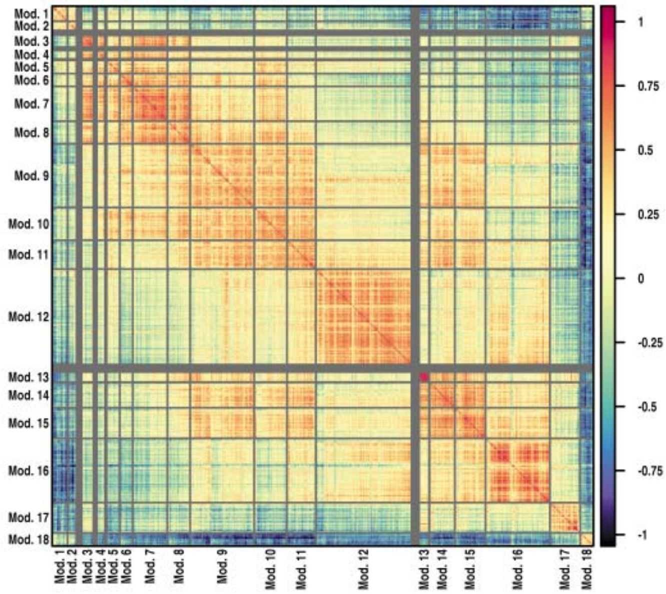

Fig. 2. Transcriptional modules. Level plot representing pairwise correlations between the 1554 differentially expressed genes. The correlation matrix has been used to compute modules of correlated expression. Modules are separated by gray lines (very small modules can be masked by overlapping dividers). The 18 modules with size greater than 10 are labeled.

Table 1. Main transcriptional modules. See (*6*) for details on the tests performed. Size indicates number of genes; Chr. dist., chromosomal distribution bias; GO, Gene Ontology; Associated with, module is overrepresented in lists of candidate male/female fitness-associated genes, published in (*12*); dash entries, not significant.

Module	Size	Overall sex bias	Tissue specificity	Chr. dist.	GO terms	Associated with
1	44	–	Spermatheca, midgut, fat body	–	Table S1	Male fitness, sexually antagonistic selection
2	26	–	–	–	Table S2	–
3	34	Male biased	Head, brain, eyes, thoracic ganglion, crop	–	Table S3	–
4	24	–	Brain, eyes, thoracic ganglion	4 (enriched)	Table S4	–
5	38	–	–	4 (enriched)	Table S5	Male fitness
6	37	Female biased	Ovary	–	Table S6	–
7	100	Female biased	Brain, eyes, thoracic ganglion, heart, ovary	X (enriched)	Table S7	–
8	65	–	–	–	Table S8	–
9	184	Female biased	–	–	Table S9	–
10	94	Female biased	Ovary	–	Table S10	–
11	83	Female biased	Ovary	–	Table S11	–
12	275	Male biased	Testes	2L (enriched)	Table S12	–
13	29	Female biased	–	–	Table S13	–
14	73	Female biased	–	–	Table S14	–
15	88	–	Accessory gland, ejaculatory duct, spermatheca, salivary gland	–	Table S15	–
16	185	Male biased	Accessory gland, ejaculatory duct	X (poor)	Table S16	Male fitness, sexually antagonistic selection
17	87	–	Heart, carcass	–	Table S17	Male fitness
18	38	–	–	–	Table S18	–

and is also mostly male-limited [x_m = 9.6, SD = 1.8, x_f = 6.8, SD = 1.2, Wilcoxon test: W = 31608, $P = 2.8 \times 10^{-46}$ (Fig. 3, E and F, and fig. S16B)], with expression primarily in the accessory gland (Fisher's exact test: odds ratio = 72, $P = 5 \times 10^{-144}$) and ejaculatory duct (Fisher's exact test: odds ratio = 7.8, $P = 1 \times 10^{-21}$) and relatively low or absent in the other tissues (Fig. 3H and fig. S16F).

Remarkably, the correlation in expression between these two clusters of genes in their respective male-limited tissues and other tissues is on average zero or even negative (Fig. 3, C and G), in stark contrast to the high levels of correlation typically observed among tissues for the whole transcriptome and subsets thereof (see, for example, figs. S7D, S8D, and S9D). Taken together, these data support the hypothesis that a large proportion of the observed differential effects attributable to the mitochondrial variants are driven by the accumulation of mutations in mtDNA that exert male-specific effects. That is, selection on mtDNA in females will presumably fail to screen genetic polymorphisms that are strongly male-biased, active only in male-limited tissues, and uncorrelated in their expression with other "shared" tissues.

A mitochondrial mutation load in the male reproductive tissues is expected to lead to a sharp decline in male fertility. This has been termed "mother's curse" (*13*) and has gained empirical support from studies in humans (*14*), hares (*15*), and beetles (*16*), which have documented associations between particular mitochondrial genetic variants and components of male fertility and reproductive fitness (*13*, *15*). Genetic polymorphisms within the cytoplasm leading to reductions or elimination of male fertility, via cytoplasmic male sterility in plants (*17*, *18*) and yeast (*19*) and via cytoplasmic incompatibility induced by intracellular parasites (e.g., *Wolbachia*) in arthropods (*20*, *21*), have long been documented. We purged the studied *Drosophila* lines of bacterial infection by using antibiotics and can conclude that the differential gene expression witnessed in our study is most likely driven by mtDNA polymorphisms (*6*). Indeed, males carrying one of the five mitochondrial haplotypes (*Brownsville*) used here are sterile when that haplotype is expressed alongside the w^{1118} isogenic background (*22*) but are fertile when the same haplotype is expressed alongside the coevolved natal background (*6*). The findings involving mtDNA polymorphism, and cytoplasmic genomes in general, indicate the profound scope by which cytoplasmic genomes affect male fertility. Existence of a sex-specific selective sieve in mtDNA is likely to exert strong selection on counteradaptations in the nuclear genome that restore lost male function (*10*, *23*, *24*).

Among the other clusters, we identified two broad groups whose characteristics suggest that they are involved in retrograde regulation of nuclear DNA transcription (*3*): genes in modules 6, 7, 10, and 11 (and to some extent 8 and 9) that are generally moderately expressed in every tissue but that show a peak in the ovary, suggesting a weak female bias in expression, and genes with a tendency to be highly correlated across tissues (figs. S6 to S11). Furthermore, Gene Ontology (www.geneontology.org)–enriched molecular functions mostly refer to proteins with enzymatic, adenosine triphosphate (ATP)–binding and trans-membrane transporter activity (tables S6 to S11), involved in metabolic and biosynthetic processes, macromolecule localization, and post-transcriptional modifications. The second group is characterized by transcripts specifically involved in mitochondrial functions (modules 1, 12, 14, and 17; see tables S1, S12, S14, and S17). Enriched gene ontologies for these modules explicitly refer to mitochondrial cellular structures (inner membrane, intermembrane space, matrix and ATP respiratory chain complex) and molec-

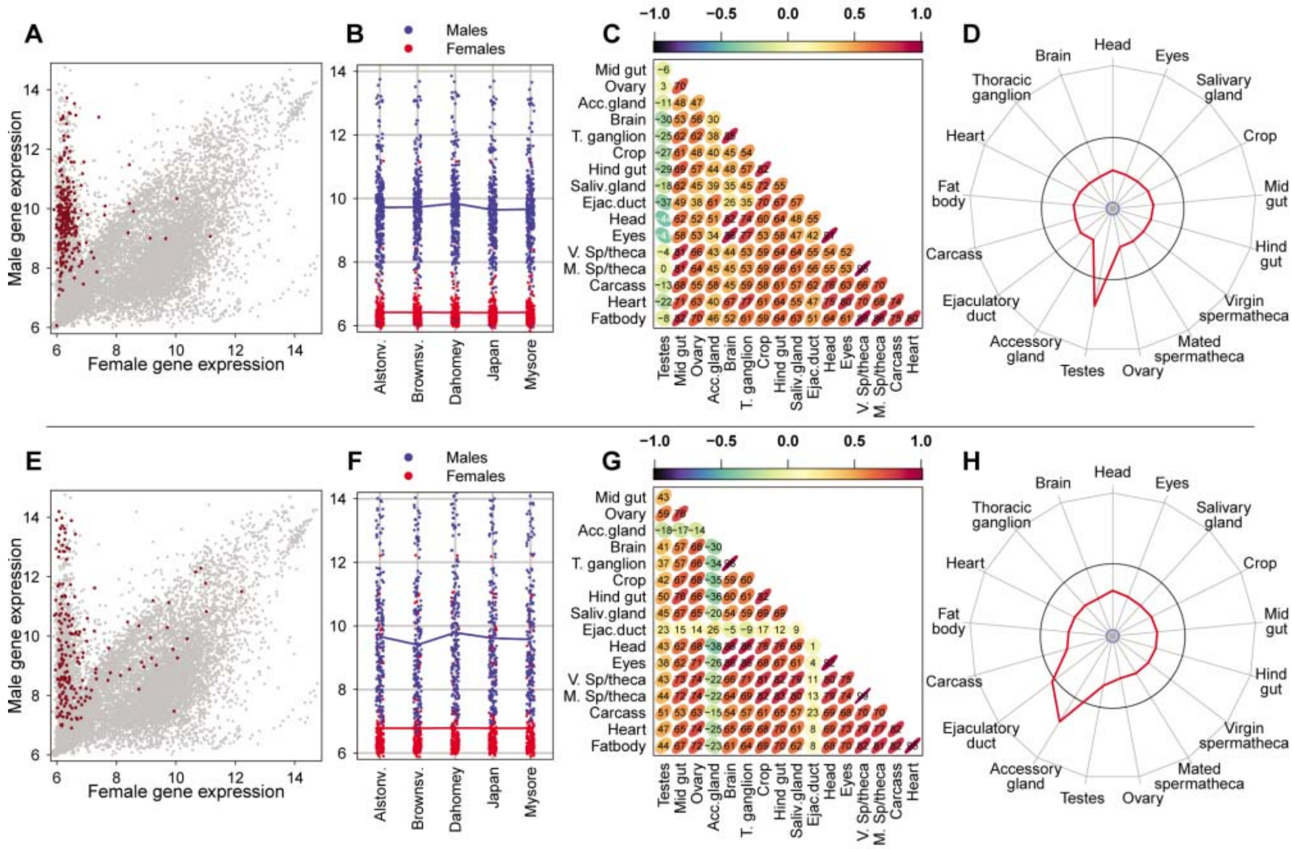

Fig. 3. Module 12 and 16. (**A** and **E**) Scatter plot representing sex bias in expression of the 275 genes in module 12 (A) and the 185 genes in module 16 (E). (**B** and **F**) Sex-specific expression of genes in module 12 (B) and module 16 (F) across the five mitochondrial haplotypes. Red and blue lines represent the within-line module average. (**C** and **G**) Correlation of the genes in module 12 (C) and module 16 (G) across the major tissues of *D. melanogaster*. (**D** and **H**) Average levels of tissue-specificity in expression for genes in module 12 (D) and 16 (H). The range of the data set is delimited by the center (minimum) and the external perimeter (maximum). The circular black line indicates the average expression in the whole body. The red line represents the expression in each tissue. Data on tissue-specific expression were obtained from FlyAtlas (*30*).

ular processes (oxidative phosphorylation, respiratory electron transport chain, ATP synthesis).

Population genetic models (*4*) suggest that mtDNA mutations that are slightly deleterious to females can be maintained at low frequencies under mutation-selection balance even when highly deleterious to males. Genetic drift will fix some of these mutations over time, as well as male-harming mutations that are totally neutral in females. This is because the efficiency of selection acting on mitochondrial genomes should be dampened, owing to their haploidy, maternal transmission, and a lack of recombination (*10*, *25*). In this sense, they are destined to accrue mutations in the same way that asexual organisms will via Muller's ratchet (*26*). Sexually antagonistic selection may also contribute to this mutation load, given that mutations of even slight benefit to female fitness will be selectively favored even if of catastrophic consequence to males. Under this scenario, the signal in nuclear gene expression induced by these mutations might simply be too subtle to detect within the nuclear transcriptome of females, if the phenotypic effects tied to the different mtDNA strains are much larger in males. Alternatively, the nuclear transcriptome might house modifiers (*17*, *27*), expressed within the male reproductive tissues, that have evolved to counter the negative effects of mtDNA mutations and that responded to the variance in mitochondrial genomes in our study. Although we cannot confidently ascribe which of the above processes is the major contributor to the male-specific mutation load that we have detected, they are all likely to have played some role. Lastly, we raise the possibility that the existence of large male-specific differences in nuclear gene expression across our experimental lines might occur if modifications to the expression of these nuclear transcripts are neutral to selection. However, this possibility seems unlikely given that (i) the differentially expressed transcripts are associated with male (but not female) fitness, (ii) one experimental mtDNA haplotype renders males sterile when expressed in the w^{1118} genetic background, whereas it does not have this effect in the nuclear background of origin, and (iii) mitochondrial genetic variation for male fertility has been previously documented (*14*–*16*). Moreover, if widespread differences in gene expression are neutral to selection, this phenomenon should also have been observed in females, short of assuming a generalized sex-specific difference in sensitivity to transcriptional levels.

In sum, mitochondrial genetic effects on male gene expression within the nuclear transcriptome were strong, affecting about 10% of all genes tested. Notably, these affected transcripts stretched well beyond those involved directly in bioenergetic processes of the mitochondria (oxidative phosphorylation and ATP production), demonstrating that retrograde signaling between the genomes is much more pervasive than previously considered. In this sense, there are parallels with the Y chromosome (*28*), which also houses a paucity of protein-coding genes and shows asymmetric transmission, but is nonetheless entwined in widespread regulatory control of the nuclear transcriptome (*28*, *29*). In contrast to the effects on males, mitochondrial effects on female-specific expression of the transcriptome were weak in magnitude and negligible in number. This discrepancy between the sexes is entirely consistent with the idea that the mitochondrial genetic polymorphisms involved have accrued under a sex-specific selective sieve.

References and Notes

1. M. D. Adams *et al.*, *Science* **287**, 2185 (2000).
2. D. L. Lewis, C. L. Farr, L. S. Kaguni, *Insect Mol. Biol.* **4**, 263 (1995).
3. J. D. Woodson, J. Chory, *Nat. Rev. Genet.* **9**, 383 (2008).
4. S. A. Frank, L. D. Hurst, *Nature* **383**, 224 (1996).
5. M. J. Wade, Y. Brandvain, *Evolution* **63**, 1084 (2009).
6. Materials and methods are available as supporting material on *Science* Online.
7. N. J. Gemmell, F. W. Allendorf, *Trends Ecol. Evol.* **16**, 115 (2001).
8. J. A. Zeh, D. W. Zeh, *Trends Genet.* **21**, 281 (2005).
9. D. K. Dowling, T. Meerupati, G. Arnqvist, *Am. Nat.* **176**, 131 (2010).
10. D. K. Dowling, U. Friberg, J. Lindell, *Trends Ecol. Evol.* **23**, 546 (2008).
11. J. Michaud *et al.*, *BMC Genomics* **9**, 363 (2008).
12. P. Innocenti, E. H. Morrow, *PLoS Biol.* **8**, e1000335 (2010).
13. N. J. Gemmell, V. J. Metcalf, F. W. Allendorf, *Trends Ecol. Evol.* **19**, 238 (2004).
14. E. Ruiz-Pesini *et al.*, *Am. J. Hum. Genet.* **67**, 682 (2000).
15. S. Smith, C. Turbill, F. Suchentrunk, *Mol. Ecol.* **19**, 36 (2010).
16. D. K. Dowling, A. L. Nowostawski, G. Arnqvist, *J. Evol. Biol.* **20**, 358 (2007).
17. P. Schnable, R. Wise, *Trends Plant Sci.* **3**, 175 (1998).
18. M. M. Rhoades, *Science* **73**, 340 (1931).
19. H. Y. Lee *et al.*, *Cell* **135**, 1065 (2008).
20. J. H. Werren, L. Baldo, M. E. Clark, *Nat. Rev. Microbiol.* **6**, 741 (2008).
21. S. Charlat, G. D. Hurst, H. Merçot, *Trends Genet.* **19**, 217 (2003).
22. D. J. Clancy, *Aging Cell* **7**, 795 (2008).
23. D. M. Rand, R. A. Haney, A. J. Fry, *Trends Ecol. Evol.* **19**, 645 (2004).
24. T. M. Majerus, M. E. Majerus, *PLoS Pathog.* **6**, e1000987 (2010).
25. M. Lynch, *Mol. Biol. Evol.* **14**, 914 (1997).
26. N. A. Moran, *Proc. Natl. Acad. Sci. U.S.A.* **93**, 2873 (1996).
27. V. C. S. de Moraes, F. Alexandrino, P. B. Andrade, M. F. Câmara, E. L. Sartorato, *Biochem. Biophys. Res. Commun.* **381**, 210 (2009).
28. B. Lemos, L. O. Araripe, D. L. Hartl, *Science* **319**, 91 (2008).
29. B. Lemos, A. T. Branco, D. L. Hartl, *Proc. Natl. Acad. Sci. U.S.A.* **107**, 15826 (2010).
30. V. R. Chintapalli, J. Wang, J. A. T. Dow, *Nat. Genet.* **39**, 715 (2007).

Acknowledgments: Funded by grants from the Australian Research Council (Discovery Project and Australian Research Fellowship, number DP1092897) and Monash University to D.K.D.; P.I. and E.H.M. were supported by the Swedish Research Council (grant 2008-5533 to E.H.M.). We thank D. Clancy for fly strains; U. Friberg for discussion; M. Norgate for sequencing; G. Arnqvist, U. Friberg, and J. Abbott for comments on the manuscript; and the Uppsala Array Platform. Microarray data have been deposited on the Gene Expression Omnibus database, accession no. GSE24729.

Supporting Online Material

www.sciencemag.org/cgi/content/full/332/6031/845/DC1
Materials and Methods
SOM Text
Figs. S1 to S18
Tables S1 to S18
References

2 December 2010; accepted 23 March 2011
10.1126/science.1201157

Role for piRNAs and Noncoding RNA in de Novo DNA Methylation of the Imprinted Mouse *Rasgrf1* Locus

Toshiaki Watanabe,[1,2]* Shin-ichi Tomizawa,[1,3] Kohzoh Mitsuya,[4] Yasushi Totoki,[5] Yasuhiro Yamamoto,[1,6] Satomi Kuramochi-Miyagawa,[7] Naoko Iida,[1,8] Yuko Hoki,[1,6] Patrick J. Murphy,[9] Atsushi Toyoda,[10] Kengo Gotoh,[7] Hitoshi Hiura,[11] Takahiro Arima,[11] Asao Fujiyama,[10,12] Takashi Sado,[1,6] Tatsuhiro Shibata,[5] Toru Nakano,[7] Haifan Lin,[2] Kenji Ichiyanagi,[1,6] Paul D. Soloway,[9] Hiroyuki Sasaki[1,6]*

Genomic imprinting causes parental origin–specific monoallelic gene expression through differential DNA methylation established in the parental germ line. However, the mechanisms underlying how specific sequences are selectively methylated are not fully understood. We have found that the components of the PIWI-interacting RNA (piRNA) pathway are required for de novo methylation of the differentially methylated region (DMR) of the imprinted mouse *Rasgrf1* locus, but not other paternally imprinted loci. A retrotransposon sequence within a noncoding RNA spanning the DMR was targeted by piRNAs generated from a different locus. A direct repeat in the DMR, which is required for the methylation and imprinting of *Rasgrf1*, served as a promoter for this RNA. We propose a model in which piRNAs and a target RNA direct the sequence-specific methylation of *Rasgrf1*.

Imprinted genes show parental origin–specific monoallelic expression, which is controlled by DNA methylation in the differentially methylated regions (DMRs) (*1*–*5*). Differential methylation of the DMRs is established in the parental germ line, passed to the zygote, and maintained in the somatic cells, which eventually leads to monoallelic expression. During fetal testis development, the DMRs are demethylated (imprint erasure) in primordial germ cells at 10.5 to 12.5

[1]Division of Human Genetics and Department of Integrated Genetics, National Institute of Genetics, Research Organization of Information and Systems, Mishima, Shizuoka, 411-8540, Japan. [2]School of Medicine, Yale University, New Haven, CT 06520, USA. [3]Laboratory of Developmental Genetics and Imprinting, The Babraham Institute, Cambridge, CB22 3AT, UK. [4]Center for Pregnancy and Newborn Research, Department of Obstetrics and Gynecology, University of Texas Health Science Center at San Antonio, 7703 Floyd Curl Drive, San Antonio, TX 78229–3900, USA. [5]Division of Cancer Genomics, National Cancer Center Research Institute, Tsukiji, Chuo-ku, Tokyo, 104-0045, Japan. [6]Division of Epigenomics, Medical Institute of Bioregulation, Kyushu University, 3-1-1 Maidashi, Higashi-ku, Fukuoka 812-8582, Japan. [7]Graduate School of Frontier Biosciences, Osaka Univ., Yamada-oka, Suita, Osaka 565-0871, Japan. [8]Division of Mutagenesis, Department of Molecular Genetics, National Institute of Genetics, Research Organization of Information and Systems, Mishima, Shizuoka, 411-8540, Japan. [9]Division of Nutritional Sciences, College of Agriculture and Life Sciences, Cornell University, Ithaca, NY 14853–5905, USA. [10]Comparative Genomics Laboratory, Center for Genetic Resource Information, National Institute of Genetics, Research Organization of Information and Systems, Mishima, Shizuoka, 411-8540, Japan. [11]Department of Informative Genetics, Environment and Genome Research Center, Tohoku University Graduate School of Medicine, 2-1 Seiryo-cho, Aoba-ku, Sendai 980-8575, Japan. [12]Principle Informatics Research Division, National Institute of Informatics, Hitotsubashi 2-1-2, Chiyoda-ku, Tokyo 101-8430, Japan.

*To whom correspondence should be addressed. E-mail: toshwatatoshiakiwatanabe@gmail.com (T.W.); hsasaki@bioreg.kyushu-u.ac.jp (H.S.)

days postcoitum (dpc) and de novo methylated (establishment) in prospermatogonia or gonocytes at 12.5 to 18.5 dpc (*2*, *3*, *5*–*7*), as retrotransposons (*1*–*3*, *5*). Of the three well-studied paternally methylated DMRs, the *Rasgrf1* DMR is unique in its requirement for the DNA methyltransferase Dnmt3b in both de novo methylation (*8*) and maintenance methylation (*9*). Intracisternal A-type particle (IAP) and long interspersed nucleotide element–1 (LINE1 or L1) retrotransposons also require Dnmt3b, as well as PIWI proteins and PIWI-interacting RNAs (piRNAs), for de novo methylation in the male germ line (*7*, *10*). piRNAs are 24- to 30-nucleotide (nt) small RNAs that bind to PIWI proteins. The PIWI-piRNA complexes

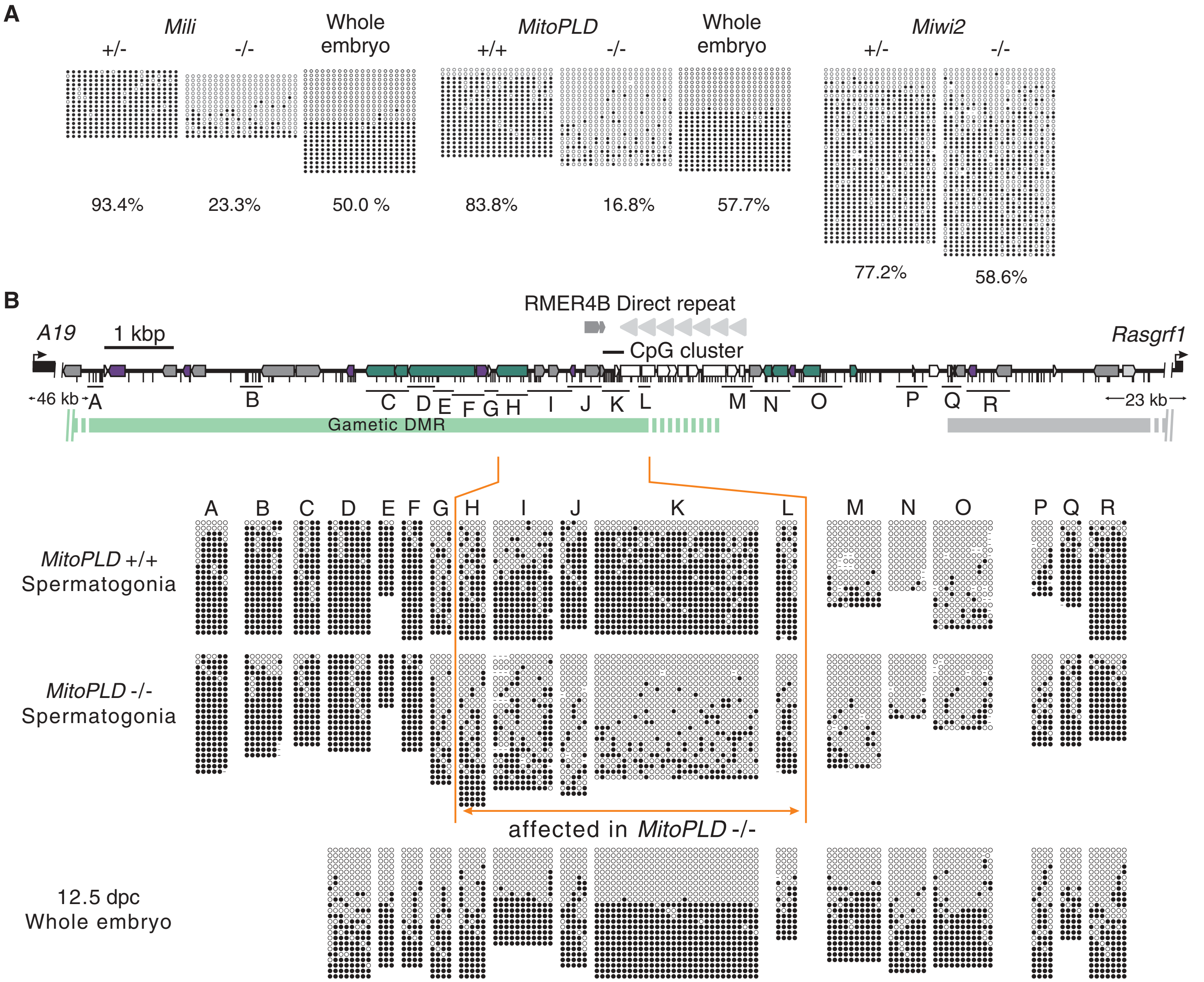

Fig. 1. DNA methylation of the imprinted *Rasgrf1* DMR is impaired in piRNA pathway mutants. (**A**) Methylation status of a portion of the *Rasgrf1* DMR [corresponding to a part of region K in (B)] in spermatogonia from *Mili*, *MitoPLD*, and *Miwi2* mutants revealed by bisulfite sequencing. Open and filled circles represent unmethylated and methylated cytosines, respectively. A result on 12.5-dpc wild-type whole-embryo DNA is also shown (control, 50% methylation expected). Percentage of methylation is shown below each panel. (**B**) Methylation status across the *Rasgrf1* DMR in *MitoPLD* mutants. The green and gray bars show the gametic DMRs (regions differentially methylated between oocyte and sperm) (*30*), of which the green one is important for imprinting. Positions of CpGs are indicated by short vertical bars. Repeat sequences identified by RepeatMasker are shown as colored boxes: green, LINE; purple, short interspersed nucleotide element (SINE); white, simple repeat; gray, LTR; light gray, DNA transposon. A direct repeat consisting of 40 copies of a 41-oligomer (*18*) and a copy of RMER4B solo LTR are also indicated.

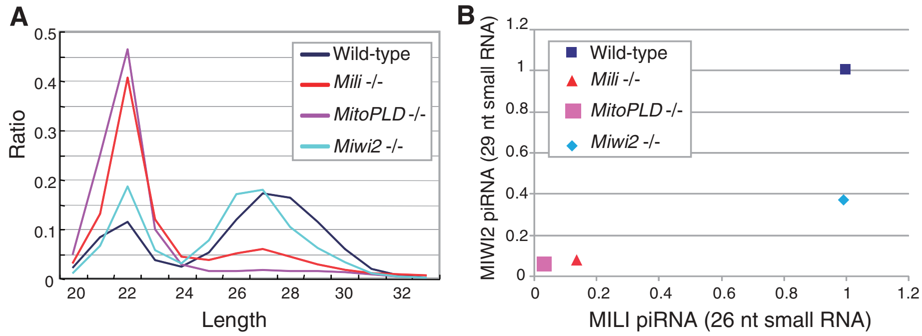

Fig. 2. Decreased piRNA levels in piRNA pathway mutants. (**A**) Size profiles are shown for small RNAs from wild-type (control), *Mili*$^{-/-}$, *MitoPLD*$^{-/-}$, and *Miwi2*$^{-/-}$ testes at 16.5 dpc. The peak at 22 nt represents miRNAs, and the other at 24 to 30 nt represents piRNAs. (**B**) Relative levels of Mili-bound (26-nt) and Miwi2-bound (29-nt) piRNAs compared with wild-type. The levels of miRNA were used to normalize the piRNA levels.

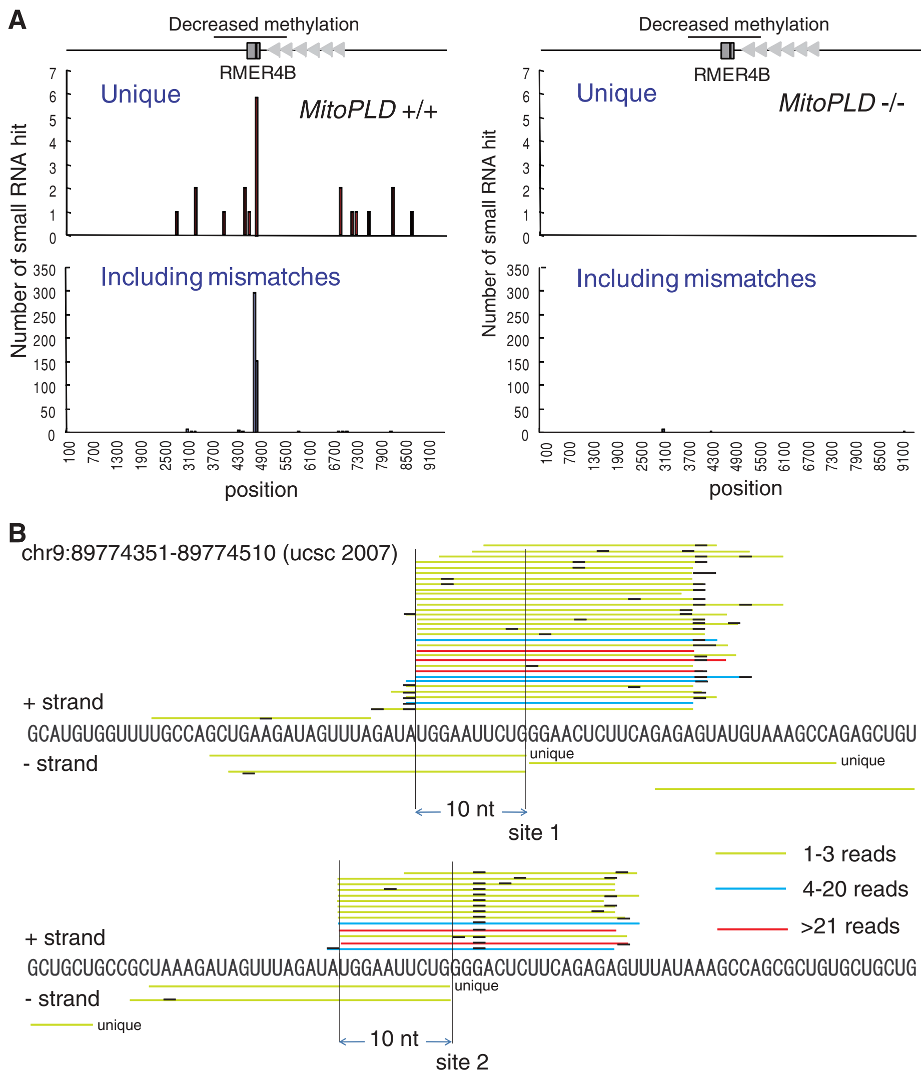

Fig. 3. An RMER4B sequence in the *Rasgrf1* DMR is targeted by piRNAs. (**A**) Numbers and locations of small RNAs from *MitoPLD*$^{+/+}$ (left) and *MitoPLD*$^{-/-}$ testes (right) at 16.5 dpc mapping to the *Rasgrf1* DMR (correspond to mm9 chr9: 89769659–89779158). Results for small RNAs with a unique hit (top) and those with mismatches (up to two mismatches including indels) are shown (bottom). (**B**) Detailed mapping of piRNAs in the RMER4B copy of the *Rasgrf1* DMR. piRNAs are represented by bars colored according to the number of sequence reads obtained. Plus strand hits are shown above the sequence, and minus strand hits are shown below it. Mismatches are represented by black portions of the bars. Unique hit piRNAs are indicated.

(PIWI-piRNAs) repress retrotransposons posttranscriptionally. Of the three mouse PIWI proteins, MILI and MIWI2 are expressed in fetal testes and MIWI in postnatal testes. Because DNA methylation of IAP and L1 retrotransposons is defective in the male germ line of *Mili* and *Miwi2* mutants (*7*, *10*, *11*), PIWI-piRNAs may also repress the retrotransposons transcriptionally through DNA methylation.

To determine whether PIWI-piRNAs are required for de novo methylation of the DMRs at imprinted loci, we studied mice with mutations in the piRNA pathway. MitoPLD/Zucchini is a protein with a phospholipase D/nuclease domain involved in primary piRNA production in both flies and mice (*12*–*15*). The *Mili*, *Miwi2*, and *MitoPLD* mutants show meiotic arrest during spermatogenesis. We analyzed the four paternally methylated DMRs (*H19*, *Dlk1*–*Gtl2*, *Gpr1*–*Zdbf2*, and *Rasgrf1*) in spermatogonia from *Mili*, *Miwi2*, and *MitoPLD* mutant pups by bisulfite sequencing (*16*). In the mutants, the *Rasgrf1* DMR showed reduced methylation (Fig. 1A), whereas the *H19*, *Dlk1*–*Gtl2*, and *Gpr1*–*Zdbf2* DMRs showed normal levels of methylation (figs. S1 and S2). At the *Rasgrf1* DMR, methylation was more severely affected in the *Mili* (23.3% methylation versus 93.4% methylation in control heterozygotes) and *MitoPLD* mutants (16.8% versus 83.8%) than in the *Miwi2* mutants (58.6% versus 77.2%). The *Rasgrf1* DMR is located on mouse chromosome 9 (chr9) between *Rasgrf1* and the *A19* noncoding RNA, both of which are imprinted (*17*, *18*). In the *MitoPLD* mutants, which showed the severest reduction in piRNAs, an ~2–kilobase (kb) region containing a cluster of CpGs was affected (region H to region L in Fig. 1B). A direct repeat in the *Rasgrf1* DMR is known to be essential for methylation and imprinting of *Rasgrf1* (*19*). In the sperm of the direct-repeat deletion mutants, the methylation status of the CpG cluster (corresponding to region K in Fig. 1B) is affected, whereas regions upstream and downstream of the cluster (regions upstream of region F and downstream of region Q in Fig. 1B) are unaffected (*19*, *20*). The extent and pattern of the defect in methylation in the *MitoPLD* mutants were essentially the same as those in the direct-repeat deletion mutants (*19*, *20*), which suggests that the methylation responsible for *Rasgrf1* imprinting is lost in the *MitoPLD* mutants.

To reveal the effect of the three mutations on piRNA expression, we analyzed small RNA libraries prepared from mutant fetal testes by Solexa deep sequencing (table S1). The relative abundance of 24- to 30-nt piRNAs decreased in all mutants compared with the wild-type control (Fig. 2A). It is known that MIWI2-bound piRNAs are larger in size than MILI-bound piRNAs. In the *MitoPLD* and *Mili* mutants, both 26-nt MILI-bound and 29-nt MIWI2-bound piRNAs were present at very low levels (3.4% and 3.5% of the wild-type control and 13.9% and 7.9% of the control, respectively)

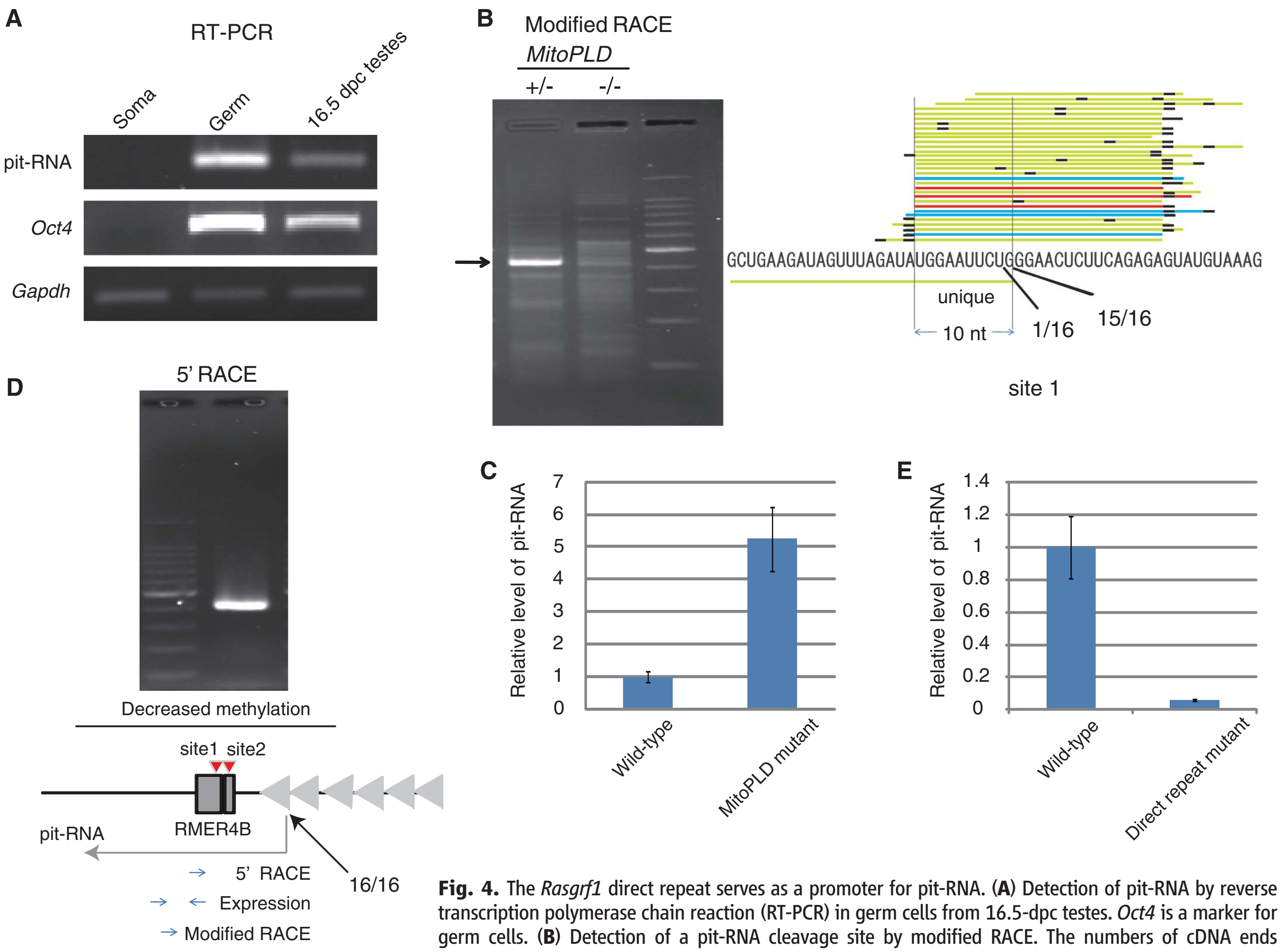

Fig. 4. The *Rasgrf1* direct repeat serves as a promoter for pit-RNA. (**A**) Detection of pit-RNA by reverse transcription polymerase chain reaction (RT-PCR) in germ cells from 16.5-dpc testes. *Oct4* is a marker for germ cells. (**B**) Detection of a pit-RNA cleavage site by modified RACE. The numbers of cDNA ends obtained by sequencing the recovered RACE products are also shown (right). (**C**) Transcription start-site analysis by 5′ RACE. The number of cDNA ends determined by sequencing the RACE products is shown with an arrow in the schematic representation of the region (bottom). The positions of the PCR primers for the analyses are also illustrated. (**D**) Quantitative PCR analysis of pit-RNA in wild-type and *MitoPLD*$^{-/-}$ testes at 16.5 dpc. Error bars represent standard deviation (n = 3). The level of *Oct4* mRNA was used as a reference. (**E**) Quantitative PCR analysis of pit-RNA in wild-type and direct repeat mutant testes at 16.5 dpc. Error bars represent standard deviation (n = 3). The level of *Oct4* mRNA was used as a reference.

(Fig. 2B). In the *Miwi2* mutants, 26-nt piRNAs were unchanged (99.2% of the control), whereas 29-nt piRNAs were reduced (36.7% of the control) (Fig. 2B). The extents of the defect in piRNA expression correlated with those in DNA methylation of the *Rasgrf1* DMR in the mutants (Fig. 1A).

To further explore the link between piRNA and *Rasgrf1* methylation, we identified 23- to 31-nt small RNAs mapping to the *Rasgrf1* DMR. Twenty-one small RNA reads from wild-type testes uniquely mapped to the DMR with perfect sequence matches (Fig. 3A and table S2), which showed that they are derived from this DMR. In *MitoPLD* mutants, these small RNAs were lost (Fig. 3A), which indicated that they are indeed piRNAs. When we allowed one or two mismatches, hundreds of piRNAs mapped to a narrow region annotated as an RMER4B sequence, located just upstream of the direct repeat. RMER4B is a solo long terminal repeat (LTR)–type retrotransposon found in a few thousand copies in the mouse genome. Most (95.2%) of these piRNAs also mapped to another RMER4B copy in a piRNA cluster on chr7 with perfect matches (fig. S3 and table S3). Furthermore, most (78.9%) of the chr7-matched piRNAs were unique (table S3), which suggested that they are generated from the chr7 piRNA cluster.

The *Rasgrf1*-derived piRNAs mapped to the minus strand of the *Rasgrf1* DMR (Fig. 3B), but the chr7-derived piRNAs predominantly mapped to the plus strand in two small regions (comprising sites 1 and 2 in Fig. 3B), which have similar sequences owing to a sequence duplication. In each mapped region, a 10-nt overlap was observed between the chr7-derived piRNAs and *Rasgrf1*-derived piRNAs (Fig. 3B), characteristic of the piRNA ping-pong cycle, which generates secondary piRNAs from target RNAs through cleavage by PIWI-piRNAs (*21*, *22*). These observations indicate that an RNA (or RNAs) transcribed from the *Rasgrf1* DMR is targeted by the chr7-derived piRNAs.

In a region immediately upstream of the RMER4B copy in the *Rasgrf1* DMR, we identified an RNA that was specifically expressed in prospermatogonia (Fig. 4A). Cleavage of a target RNA by PIWI-piRNAs creates a 5′ end with monophosphate. To map the cleavage sites in the newly identified RNA, we carried out modified RNA ligase–mediated 5′ rapid amplification of cDNA ends (modified RACE) (*23*). The most common 5′ end of the RNA fragments mapped precisely to site 1 (Figs. 3B and 4B), which was one of the two ping-pong signature sites. We could not detect fragments cleaved at site 2, probably because of the simultaneous cleavage at site 1, which was proximal to the primer site. The RNA fragments cleaved at site 1 disappeared in *MitoPLD* mutants, which confirmed that the RNA is targeted by piRNAs. Furthermore, the RNA was up-regulated ~5 times in the mutants (Fig. 4D). We named this RNA "piRNA-targeted noncoding RNA" (pit-RNA). The pit-RNA transcript was specifically expressed during the stage of de novo methylation (SOM text).

Rasgrf1 is imprinted in mice and rats but not in other rodent species (*18*). We found that the

RMER4B copies are conserved in the rat genome at both the *Rasgrf1* DMR and the piRNA cluster. Furthermore, it was reported that the direct repeat essential for the methylation and imprinting of *Rasgrf1* (*19*) is found in mice and rats but not in *Peromyscus* and rabbits (*18*). The 5′ end of pit-RNA determined by 5′ RACE indicated that its transcription is initiated within this direct repeat (Fig. 4C). It is therefore possible that the defect in *Rasgrf1* imprinting observed in the direct-repeat mutants (*19*) is a consequence of loss of pit-RNA. Consistent with this notion, pit-RNA was much reduced in testes of the mutants (Fig. 4E). It therefore appears that, through acquisition of the retrotransposon copies and direct repeat, *Rasgrf1* acquired imprinting to regulate postnatal growth (*24*), as explained by the "conflict hypothesis" (*25*). However, it is also possible that *Rasgrf1* imprinting is an inconsequential outcome of the importance of retrotransposon repression in the male germ line (i.e., *Rasgrf1* is an innocent bystander), as retrotransposon repression by the piRNA pathway is essential for spermatogenesis.

In the small interfering RNA (siRNA)–mediated transcriptional silencing systems of *Schizosaccharomyces pombe* and *Arabidopsis*, polymerase II (Pol II)–transcribed and Pol V–transcribed nascent RNAs, respectively, have been proposed to serve as scaffolds for recruitment of the silencing machinery through siRNA binding (*26*–*28*). In the *Rasgrf1* locus, the noncoding pit-RNA is targeted by piRNAs, and disruption of pit-RNA transcription results in a failure in de novo methylation. Furthermore, in mice heterozygous for the direct-repeat mutation, only the mutated allele loses methylation (*19*), which indicates that the repeat acts in cis for methylation. Therefore, although we cannot formally rule out an indirect effect of PIWI-piRNAs, these results together lead us to propose that targeting of nascent pit-RNAs by PIWI-piRNAs at the site of transcription is an important step in the sequence-specific methylation of the *Rasgrf1* DMR (fig. S4). In growing oocytes, transcription through the *Gnas* DMRs is required for their methylation (*29*), but in this case, involvement of the piRNA pathway is unlikely, because the offspring from *Mili*, *Miwi2*, and *MitoPLD* female mutants show no discernible phenotype (*7*, *10*, *11*, *15*). In prospermatogonia, however, a large proportion of piRNAs maps to retrotransposons, and it is likely that transcription through retrotransposon sequences has a role in shaping the epigenetic landscape of male germ cells. The methylation patterns established in this way are mostly reprogrammed in early embryos, but the *Rasgrf1* DMR is unique in that it maintains the parental origin–specific methylation (SOM text).

References

1. M. S. Bartolomei, *Genes Dev.* **23**, 2124 (2009).
2. H. Sasaki, Y. Matsui, *Nat. Rev. Genet.* **9**, 129 (2008).
3. W. Reik, *Nature* **447**, 425 (2007).
4. M. V. Koerner, F. M. Pauler, R. Huang, D. P. Barlow, *Development* **136**, 1771 (2009).
5. C. B. Schaefer, S. K. Ooi, T. H. Bestor, D. Bourc'his, *Science* **316**, 398 (2007).
6. A. A. Aravin *et al.*, *Mol. Cell* **31**, 785 (2008).
7. S. Kuramochi-Miyagawa *et al.*, *Genes Dev.* **22**, 908 (2008).
8. Y. Kato *et al.*, *Hum. Mol. Genet.* **16**, 2272 (2007).
9. R. Hirasawa *et al.*, *Genes Dev.* **22**, 1607 (2008).
10. A. A. Aravin, R. Sachidanandam, A. Girard, K. Fejes-Toth, G. J. Hannon, *Science* **316**, 744 (2007).
11. M. A. Carmell *et al.*, *Dev. Cell* **12**, 503 (2007).
12. A. Pane, K. Wehr, T. Schüpbach, *Dev. Cell* **12**, 851 (2007).
13. C. D. Malone *et al.*, *Cell* **137**, 522 (2009).
14. K. Saito *et al.*, *Nature* **461**, 1296 (2009).
15. T. Watanabe *et al.*, *Dev. Cell* **20**, 364 (2011).
16. Materials and methods are available as supporting material on *Science* Online.
17. A. de la Puente *et al.*, *Gene* **291**, 287 (2002).
18. R. S. Pearsall *et al.*, *Genomics* **55**, 194 (1999).
19. B. J. Yoon *et al.*, *Nat. Genet.* **30**, 92 (2002).
20. A. M. Lindroth *et al.*, *PLoS Genet.* **4**, e1000145 (2008).
21. J. Brennecke *et al.*, *Cell* **128**, 1089 (2007).
22. L. S. Gunawardane *et al.*, *Science* **315**, 1587 (2007).
23. C. Llave, Z. Xie, K. D. Kasschau, J. C. Carrington, *Science* **297**, 2053 (2002).
24. N. M. Drake, Y. J. Park, A. S. Shirali, T. A. Cleland, P. D. Soloway, *Mamm. Genome* **20**, 654 (2009).
25. T. Moore, D. Haig, *Trends Genet.* **7**, 45 (1991).
26. M. Bühler, A. Verdel, D. Moazed, *Cell* **125**, 873 (2006).
27. A. T. Wierzbicki, T. S. Ream, J. R. Haag, C. S. Pikaard, *Nat. Genet.* **41**, 630 (2009).
28. D. V. Irvine *et al.*, *Science* **313**, 1134 (2006).
29. M. Chotalia *et al.*, *Genes Dev.* **23**, 105 (2009).
30. S. Tomizawa *et al.*, *Development* **138**, 811 (2011).

Acknowledgments. We thank M. Kaneda, S. Chuma, V. Shteyn, and J. Peng for comments on the manuscript and H. Horiike, H. Furuumi, T. Ichiyanagi, Y. Amakawa, H. Chiba, and Y. Li for sample preparation. The accession number for the small RNA sequences is GSE20327. This work was supported in part by Grants-in-Aid from the Ministry of Education, Culture, Sports, Science, and Technology of Japan to H.S. and K.M.

Supporting Online Material

www.sciencemag.org/cgi/content/full/332/6031/848/DC1
Materials and Methods
SOM Text
Figs. S1 to S10
Tables S1 to S3
References

7 February 2011; accepted 5 April 2011
10.1126/science.1203919

Polarized *notum* Activation at Wounds Inhibits Wnt Function to Promote Planarian Head Regeneration

Christian P. Petersen[1]* and Peter W. Reddien[1,2,3]†

Regeneration requires initiation of programs tailored to the identity of missing parts. Head-versus-tail regeneration in planarians presents a paradigm for study of this phenomenon. After injury, Wnt signaling promotes tail regeneration. We report that wounding elicits expression of the Wnt inhibitor *notum* preferentially at anterior-facing wounds. This expression asymmetry occurs at essentially any wound, even if the anterior pole is intact. Inhibition of *notum* with RNA interference (RNAi) causes regeneration of an anterior-facing tail instead of a head, and double-RNAi experiments indicate that *notum* inhibits Wnt signaling to promote head regeneration. *notum* expression is itself controlled by Wnt signaling, suggesting that regulation of feedback inhibition controls the binary head-tail regeneration outcome. We conclude that local detection of wound orientation with respect to tissue axes results in distinct signaling environments that initiate appropriate regeneration responses.

How an organism determines what cells or tissues are missing for regeneration is poorly understood. Planarians are freshwater flatworms that can regenerate from nearly any injury (*1*). The head-versus-tail regeneration decision in planarians, known as regeneration polarity, is a paradigm for studying appropriate regeneration program specification (*2*). Wnt signaling controls regeneration polarity, with pathway components *β-catenin-1* (*3*–*5*) and *wnt1* (formerly called *wntP-1)* (*6*–*8*) required to prevent head regeneration and promote tail regeneration at posterior-facing wounds. *wnt1* expression is up-regulated near both anterior- and posterior-facing wounds (*6*, *8*, *9*). Therefore, how *wnt1* and *β-catenin* act to promote tail formation only at appropriate wounds is unknown.

We sought factors that inhibit Wnt signaling at anterior-facing wounds to promote head regeneration, and we identified a planarian homolog of *Drosophila notum* (*Smed-notum*) (fig. S1) (*10*). Notum proteins are secreted α/β-hydrolase family members (*11*, *12*), cleave glycosylphosphatidylinositol anchors of cell surface proteins (*13*), and can act on glypicans to modulate *Drosophila* Wnt signaling (*11*, *12*, *14*, *15*). Glypicans are cell surface, heparan-sulfate proteoglycans that participate in several signaling pathways (*16*). The roles of Notum proteins in development are unknown outside of *Drosophila*.

[1]Whitehead Institute for Biomedical Research, Cambridge, MA 02142, USA. [2]Department of Biology, Massachusetts Institute of Technology, Cambridge, MA 02138, USA. [3]Howard Hughes Medical Institute, 4000 Jones Bridge Road, Chevy Chase, MD 20815, USA.

*Present address: Department of Molecular Biosciences, Northwestern University, Evanston, IL 60208, USA.

†To whom correspondence should be addressed. E-mail: reddien@wi.mit.edu

notum was expressed at the planarian anterior pole (Fig. 1A). In contrast, *wnt1* is expressed oppositely, at the posterior pole (*3*, *6*). Early after head and tail amputation (6 to 24 hours), *notum* expression was highly up-regulated preferentially near anterior-facing wounds (Fig. 1B and fig. S2). *notum* expression was weaker and initiated later at posterior-facing wounds. Later after amputation (48 to 72 hours), anterior *notum* expression was

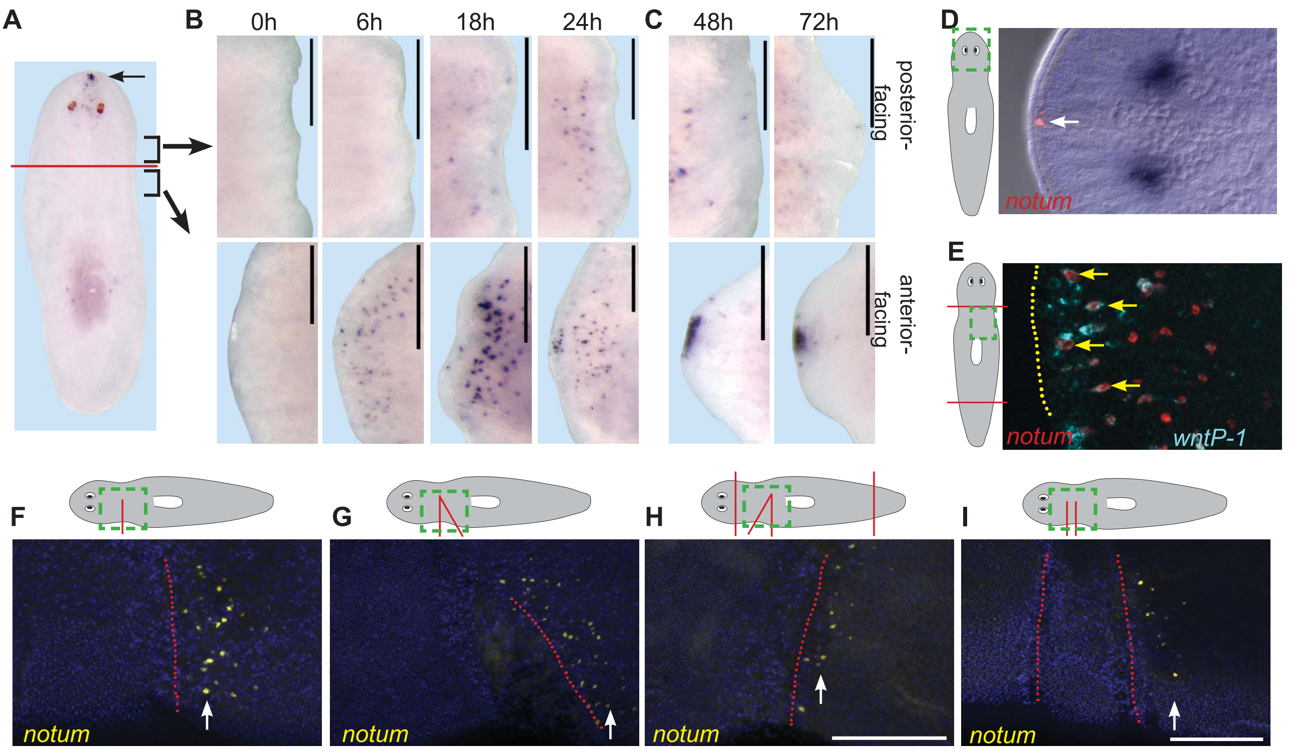

Fig. 1. *notum* is expressed at anterior-facing wounds. (**A** to **C**) *notum* in situ hybridizations: intact animals (A); regenerating head and trunk fragments over time (hours, h) [(B) and (C)]. Brackets shown in (A) indicate regions imaged in (B) and (C). (**D**) *notum* is expressed in anterior-pole, subepidermal cells (arrow). (D and E) The area highlighted by the dashed green box is enlarged in the right panels. (**E**) Double-fluorescence in situ hybridization (FISH); *notum* (red) and *wnt1* (blue) are coexpressed (arrows) at an anterior-facing wound (yellow dotted line) 18 hours after amputation. (**F** to **I**) FISH; *notum* expression 6 hours after incisions. (Top) The green box depicts the region that was imaged; red lines depict incisions. (Bottom) Dotted red lines show sealed wound location. In (G) and (H), triangular tissue was removed and the wound allowed to seal; tissue between incision sites (~200 μm apart) in (I) was not removed. Anterior to the left [(B) to (I)] or top (A); dorsal view, (A), 72 hours in (C) and (D); or ventral view (all other panels). Images represent ≥four of five animals per panel. Scale bars, 200 μm.

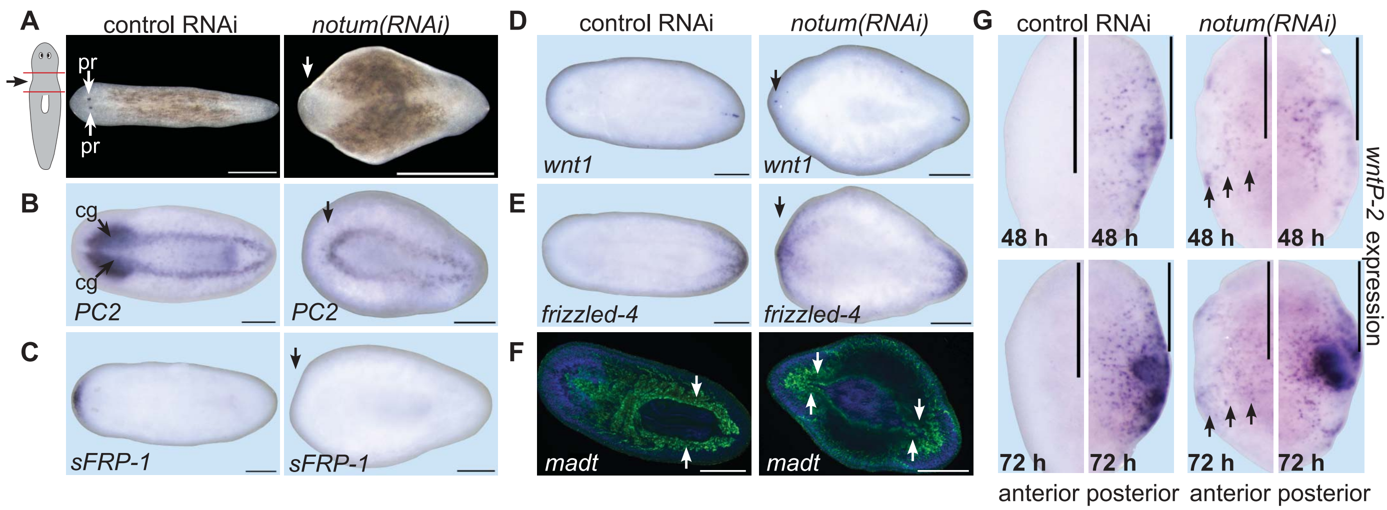

Fig. 2. *notum* is required for head-tail regeneration polarity. (**A**) *notum(RNAi)* fragments failed to regenerate a head by 14 days after amputation (47%, *n* = 133; controls were normal, 100%, *n* = 101). (**B** to **F**) Control or *notum(RNAi)*-regenerating animals lacking photoreceptors were probed for expression of (B) *PC2* (prohormone convertase 2, central nervous system marker), (C) *sFRP-1* (anterior-pole marker), (D) *wnt1*, (E) *fzd-4* (posterior markers), or (F) *madt* (gut marker, green). Blue, Hoechst stain. Arrows indicate lack of anterior marker [(B) and (C)], posterior marker presence [(D) and (E)], or posterior gut morphology (F) in *notum(RNAi)* animals. cg, cephalic ganglia; pr, photoreceptors. Images are representatives: (B) 9/11, (C) 8/25, (D) 7/24, and (E) 11/38 *notum(RNAi)* animals; other panels, 100%, $n \geq 7$. (**G**) Anterior- or posterior-facing wounds, probed for *wntP-2* expression. *wntP-2* has been proposed to be Wnt11-related with the name *wnt11-5* (*8*). Arrows indicate ectopic *wntP-2* expression. Images represent ≥five of six animals per panel. Anterior to the left. Scale bars, 500 μm (A); 200 μm (all other panels).

coalesced at the pole, whereas posterior expression remained low (Fig. 1C and fig. S2). *notum* was expressed in subepidermal cells (Fig. 1D) that, at wounds, resemble *wnt1*-expressing cells (*6*). Indeed, *notum* and *wnt1* were coexpressed in some cells at anterior-facing wounds (Fig. 1E).

To test whether wound-site *notum* expression is specific to head amputation, we incised animal sides without tissue removal. *notum* expression was detected specifically on the anterior-facing side of these sealed incisions (Fig. 1F). Therefore, asymmetric *notum* expression after wounding (greater at anterior-facing rather than posterior-facing wounds) does not require the loss of large tissue regions, such as the anterior pole. Asymmetric wound expression also occurred at sealed incisions diagonal to the main body axis (Fig. 1G) and was independent of anterior or posterior pole presence (Fig. 1H), indicating that local cues rather than signals from poles control *notum* expression asymmetry at wounds. We conclude that wounding elicits *notum* expression, dependent on wound-edge orientation with respect to the polarized primary body axis.

Posterior-facing wounds could be nonpermissive, and/or anterior-facing wounds could be specifically instructive, for *notum* expression. We therefore examined *notum* expression between two closely opposed wounds. Regions neighboring only an anterior-facing wound had more *notum*-expressing cells than did regions bordering both anterior- and posterior-facing wounds (11.0 ± 6.9 versus 1.6 ± 2.4 cells, respectively, *n* = 8 animals) (Fig. 1I). These data suggest that posterior-facing wounds suppress wound-induced *notum* expression, providing expression asymmetry.

The specificity of strong *notum* expression for anterior-facing wounds suggests that *notum* might control regeneration polarity. After head and tail amputation, *notum(RNAi)* animals [RNA interference (RNAi)] failed to regenerate a head with photoreceptors (47%, *n* = 113) and regenerated posterior-facing tails apparently normally (Fig. 2A). *notum(RNAi)* animals that did regenerate at least one photoreceptor did so aberrantly, possibly reflecting a weakly expressive *notum(RNAi)* phenotype (fig. S3). To characterize *notum(RNAi)* anterior blastemas lacking photoreceptors, we assessed axial marker expression (Fig. 2, B to F). *notum(RNAi)* anterior blastemas lacked cephalic ganglia and anterior-pole marker expression (*sFRP-1*) (Fig. 2, B and C). In contrast, *notum(RNAi)* anterior blastemas expressed the posterior markers *wnt1* and *frizzled-4* (Fig. 2, D and E). Furthermore, *notum(RNAi)* animals regenerated an anterior gut with posterior-specific morphology (two main branches) (Fig. 2F). We conclude that *notum* inhibition caused regeneration of an anterior-facing second tail after head and tail amputation. *notum* double-stranded RNA (dsRNA) delivery only after amputation also resulted in a regeneration polarity reversal (fig. S4), indicating a requirement for new *notum* expression after wounding.

wntP-2 [propsed to be Wnt11-related (*8*)] expression is up-regulated at posterior- and not anterior-facing wounds, and this requires *wnt1* and *β-catenin-1* (*6*). Therefore, *wntP-2* expression reflects an early readout (i.e., well before the majority of tissue forms) of *wnt1*/*β-catenin*–mediated polarity specification. *notum(RNAi)* fragments expressed *wntP-2* ectopically at anterior-facing wounds by 48 hours after injury (Fig. 2G), indicating that *notum* normally prevents activation of *β-catenin* targets at anterior-facing wounds.

The *notum(RNAi)* phenotype is similar to that caused by inactivation of APC, an intracellular β-catenin inhibitor (*4*). Additionally, *Drosophila notum* inhibits Wnt signaling in imaginal discs (*11*, *12*). Therefore, we performed double-RNAi experiments to assess the candidate pathway of action involving *notum*, *β-catenin-1*, and *wnt1*. *β-catenin-1* and *notum* double RNAi resulted in a polarity phenotype identical to that of *β-catenin-1* RNAi alone: anterior- and posterior-facing head regeneration (Fig. 3A). Similarly, *wnt1* inhibition suppressed the polarity phenotype caused by *notum* RNAi (Fig. 3A). *notum* RNAi efficiency was not reduced in double-RNAi animals (fig. S5), indicating that suppression of the *notum* phenotype by *wnt1* and *β-catenin-1* dsRNA is unlikely to be explained simply by competition with *notum* dsRNA for RNAi. These data suggest that the *notum(RNAi)* phenotype requires *wnt1* and *β-catenin* genes, supporting a model in which *notum* normally

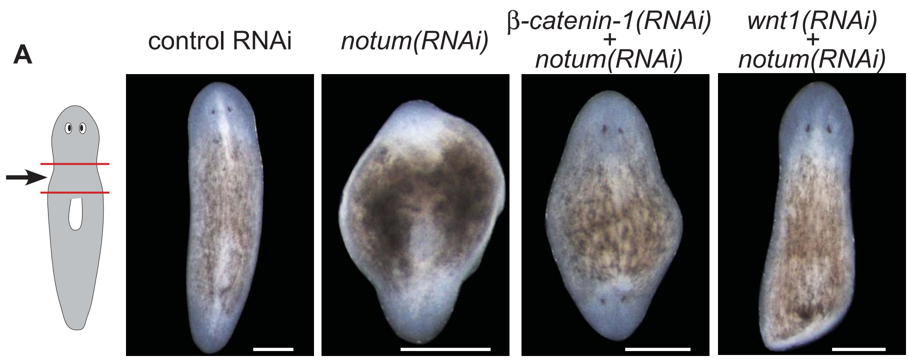

# PR in anterior blastema / RNAi condition	2 PR	1 PR	0 PR
control	100	0	0
notum	0	47	53
β-catenin-1 + *notum*	100	0	0
wnt1 + *notum*	100	0	0

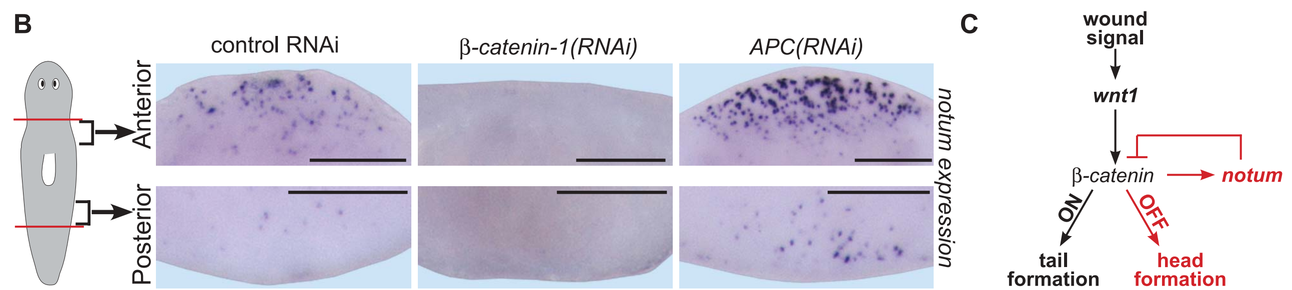

Fig. 3. *notum* is a Wnt signaling–dependent Wnt inhibitor that controls regeneration polarity. (**A**) Double RNAi between *notum* and Wnt signaling components. The chart shows phenotypes (PR, photoreceptor) as percentages of animals. *wnt1* RNAi can cause tail-regeneration failure and/or head regeneration at posterior-facing wounds (*6*–*8*). Competition between *wnt1* and *notum* dsRNA probably accounts for tail-regeneration failure rather than ectopic head regeneration in *wnt1(RNAi); notum(RNAi)* animals. (**B**) *β-catenin-1(RNAi)* reduced, and *APC(RNAi)* enhanced, *notum* expression 18 hours after amputation. *notum*-expressing cell numbers at anterior-facing wounds: controls, 102 ± 17 cells; *β-catenin-1(RNAi)*, 17 ± 23 cells ($P = 6.5 \times 10^{-8}$); *APC(RNAi)*, 186 ± 37 cells ($P = 8.1 \times 10^{-6}$). Number of *notum*-expressing cells at posterior-facing wounds: controls, 9 ± 5 cells; *β-catenin-1(RNAi)*, 1 ± 3 cells ($P = 0.003$); *APC(RNAi)*, 30 ± 24 cells ($P = 0.014$). Errors, standard deviations; *P* values, two-tailed *t* tests. Anterior to the top (A) or left (B). Scale bars, 200 μm. (**C**) Proposed pathway: selective feedback inhibition of wound-induced Wnt signaling by *notum* at anterior-facing wounds controls switchlike behavior of regeneration polarity.

inhibits *wnt1* and *β-catenin-1* function to allow head regeneration.

Hedgehog signaling affects planarian regeneration polarity (*9*, *17*), so we tested whether *notum* requires or influences Hedgehog signaling. *patched* RNAi overactivates Hedgehog signaling and increases *wnt1* wound expression; *hedgehog* inhibition reduces *wnt1* wound expression (*9*, *17*). In contrast, *notum(RNAi)* animals displayed normal *wnt1* expression after amputation (fig. S6A), suggesting that *notum* does not act in polarity by influencing Hedgehog activity. Second, *patched(RNAi)* animals regenerated anterior tails ($n = 3$ of 10 animals) but had normal asymmetric *notum* expression at wounds ($n = 8/8$) (fig. S6B), suggesting that Hedgehog signaling does not act in regeneration polarity to drive asymmetric *notum* expression at wounds.

notum can function as a *wingless* (Wnt) feedback inhibitor in *Drosophila* (*11*, *12*), so we tested whether Wnt signaling is required for wound-induced *notum* expression. *β-catenin-1* inhibition before amputation robustly reduced *notum* expression levels near wounds (Fig. 3B and fig. S7). Conversely, *APC* RNAi caused *notum* up-regulation near wounds (Fig. 3B and fig. S7, A to C). Therefore, Wnt signaling is necessary and can be sufficient at wounds for *notum* expression. Whether *Smed-notum* is a direct or indirect β-catenin transcriptional target is unknown, but *notum* is a direct target of Wnt signaling in cultured *Drosophila* and mammalian cells (*18*, *19*). Wnt signaling perturbation affected *notum* expression regardless of wound orientation (fig. S7, A and B), so we propose that some other process ensures asymmetric *notum* expression at wounds. Specifically, in *APC(RNAi)* animals, *notum* was up-regulated at wounds, but expression asymmetry remained. Because *Smed-notum* inhibits *β-catenin-1* activity and requires *β-catenin-1* for its effects, these results suggest that regulation of feedback inhibition controls the regeneration polarity decision (Fig. 3C).

Wnt signaling is used broadly in regeneration (*20*–*24*), and our results suggest that Notum proteins can be an important determinant of the outcome of Wnt expression in regeneration. Additionally, primary body-axis development involves anterior Wnt inhibition in many animals (*25*); *notum* is an ancient gene present in many metazoans (fig. S1), making it a candidate for controlling anterior identity broadly. Feedback inhibitors operate in many signaling pathways (*26*) and frequently simply attenuate pathway output. Here, we present evidence that a target and inhibitor of Wnt signaling, the secreted hydrolase NOTUM, controls the switchlike behavior of the head-versus-tail regeneration decision in planarians. These results raise the possibility that control of whether feedback inhibition occurs could, in general, be used to mediate binary developmental decisions.

In principle, decisions of which tissues to regenerate could be accomplished only by sensing the absence of particular structures. In contrast, our results indicate that regeneration programs elicited at wounds can involve local responses to tissue orientation regardless of the identity of missing tissue. We conclude that initiation of correct regeneration programs involves responses to wounding that depend on local tissue polarization, such as along a body axis.

References and Notes

1. P. W. Reddien, A. Sánchez Alvarado, *Annu. Rev. Cell Dev. Biol.* **20**, 725 (2004).
2. T. H. Morgan, *Arch. Entw. Mech. Org.* **7**, 364 (1898).
3. C. P. Petersen, P. W. Reddien, *Science* **319**, 327 (2008); 10.1126/science.1149943.
4. K. A. Gurley, J. C. Rink, A. Sánchez Alvarado, *Science* **319**, 323 (2008); 10.1126/science.1150029.
5. M. Iglesias, J. L. Gomez-Skarmeta, E. Saló, T. Adell, *Development* **135**, 1215 (2008).
6. C. P. Petersen, P. W. Reddien, *Proc. Natl. Acad. Sci. U.S.A.* **106**, 17061 (2009).
7. T. Adell, E. Salò, M. Boutros, K. Bartscherer, *Development* **136**, 905 (2009).
8. K. A. Gurley *et al.*, *Dev. Biol.* **347**, 24 (2010).
9. J. C. Rink, K. A. Gurley, S. A. Elliott, A. Sánchez Alvarado, *Science* **326**, 1406 (2009); 10.1126/science.1178712.
10. Materials and methods are available as supporting material on *Science* Online.
11. O. Gerlitz, K. Basler, *Genes Dev.* **16**, 1055 (2002).
12. A. J. Giráldez, R. R. Copley, S. M. Cohen, *Dev. Cell* **2**, 667 (2002).
13. A. Traister, W. Shi, J. Filmus, *Biochem. J.* (2007).
14. C. Han, D. Yan, T. Y. Belenkaya, X. Lin, *Development* **132**, 667 (2005).
15. J. Kreuger, L. Perez, A. J. Giraldez, S. M. Cohen, *Dev. Cell* **7**, 503 (2004).
16. D. Yan, X. Lin, *Cold Spring Harbor Perspect. Biol.* **1**, a002493 (2009).
17. S. Yazawa, Y. Umesono, T. Hayashi, H. Tarui, K. Agata, *Proc. Natl. Acad. Sci. U.S.A.* **106**, 22329 (2009).
18. D. S. Parker, Y. Y. Ni, J. L. Chang, J. Li, K. M. Cadigan, *Mol. Cell. Biol.* **28**, 1815 (2008).
19. Y. Torisu *et al.*, *Cancer Sci.* **99**, 1139 (2008).
20. H. Yokoyama, H. Ogino, C. L. Stoick-Cooper, R. M. Grainger, R. T. Moon, *Dev. Biol.* **306**, 170 (2007).
21. C. L. Stoick-Cooper *et al.*, *Development* **134**, 479 (2007).
22. W. Goessling *et al.*, *Dev. Biol.* **320**, 161 (2008).
23. G. Lin, J. M. Slack, *Dev. Biol.* **316**, 323 (2008).
24. J. B. Kim *et al.*, *J. Bone Miner. Res.* **22**, 1913 (2007).
25. C. P. Petersen, P. W. Reddien, *Cell* **139**, 1056 (2009).
26. O. Brandman, T. Meyer, *Science* **322**, 390 (2008).

Acknowledgments: We thank the Reddien Lab for discussions and S. Lapan for *hedgehog* constructs. P.W.R. is a Howard Hughes Medical Institute early career scientist. We acknowledge support by NIH R01GM080639, ACS RSG-07-180-01-DDC, the Keck Foundation, and an American Cancer Society postdoctoral fellowship to C.P.P. C.P.P. and P.W.R. are inventors on a pending patent on the use of Notum inhibitors to enhance regeneration.

Supporting Online Material
www.sciencemag.org/cgi/content/full/332/6031/852/DC1
Materials and Methods
Figs. S1 to S7
References

23 December 2010; accepted 23 March 2011
10.1126/science.1202143

Natural Microbe-Mediated Refractoriness to *Plasmodium* Infection in *Anopheles gambiae*

Chris M. Cirimotich,[1] Yuemei Dong,[1] April M. Clayton,[1] Simone L. Sandiford,[1] Jayme A. Souza-Neto,[1] Musapa Mulenga,[2] George Dimopoulos[1]*

Malaria parasite transmission depends on the successful transition of *Plasmodium* through discrete developmental stages in the lumen of the mosquito midgut. Like the human intestinal tract, the mosquito midgut contains a diverse microbial flora, which may compromise the ability of *Plasmodium* to establish infection. We have identified an *Enterobacter* bacterium isolated from wild mosquito populations in Zambia that renders the mosquito resistant to infection with the human malaria parasite *Plasmodium falciparum* by interfering with parasite development before invasion of the midgut epithelium. Phenotypic analyses showed that the anti-*Plasmodium* mechanism requires small populations of replicating bacteria and is mediated through a mosquito-independent interaction with the malaria parasite. We show that this anti-*Plasmodium* effect is largely caused by bacterial generation of reactive oxygen species.

Plasmodium parasites suffer considerable losses during their development in the mosquito midgut (*1*, *2*), where they encounter a hostile environment of human blood–derived factors, mosquito innate immune responses, and resident microbiota. However, escape of only a few parasites is sufficient to ensure onward transmission. Midgut bacteria play a key role in modulating *Plasmodium* infection of the *Anopheles* mosquito vector (*3*–*7*), but the mechanism(s) of bacterially mediated parasite inhibition has not been described, although the mosquito's innate immune responses to the microbiota and parasite challenge have been implicated in this phenomenon (*6*–*10*).

In the present study, we isolated bacteria from southern Zambian populations of *A. arabiensis*, an important malaria vector, during two collecting trips in two consecutive years (*11*). A majority of the captured mosquito's midguts contained bacteria, with an average concentration of 10^4 bacteria per non–blood-fed gut, similar to that observed for laboratory-reared *Anopheles* mosquitoes (*6*). Sixteen distinct bacterial strains were

[1]W. Harry Feinstone Department of Molecular Microbiology and Immunology, Bloomberg School of Public Health, Johns Hopkins University, 615 North Wolfe Street, Baltimore, MD 21205–2179, USA. [2]Malaria Institute at Macha, Choma, Zambia.

*To whom correspondence should be addressed: E-mail: gdimopou@jhsph.edu

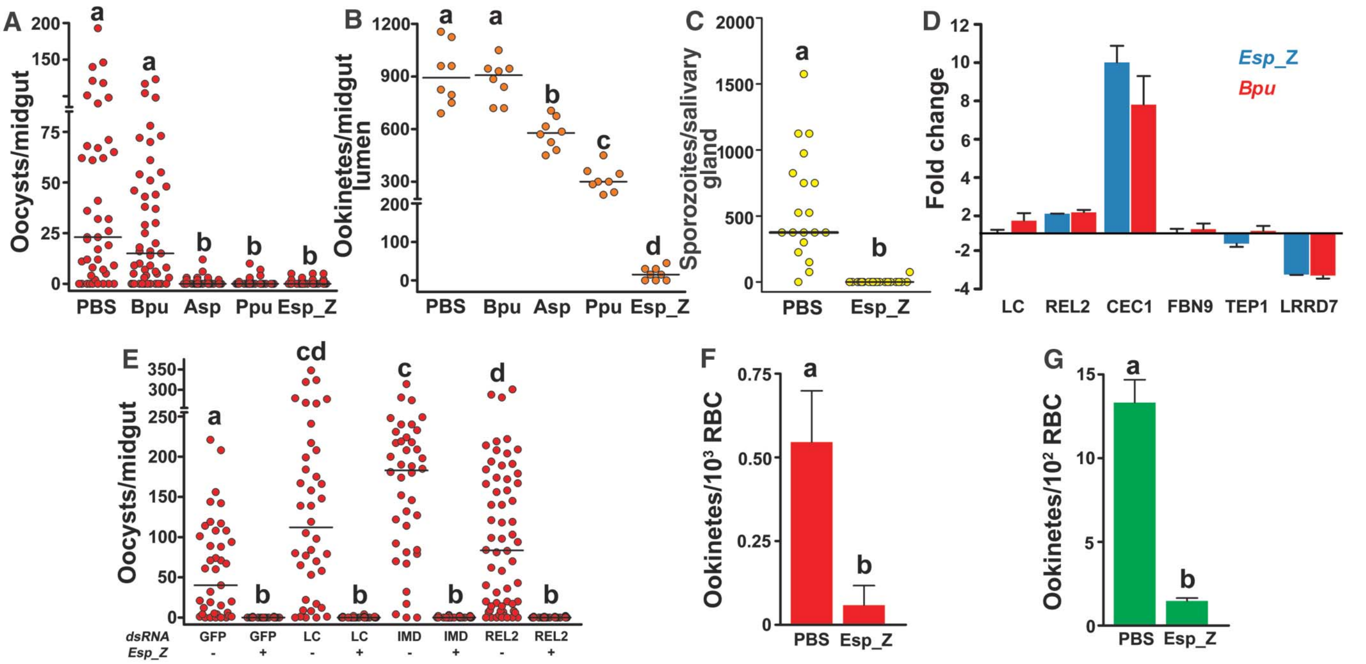

Fig. 1. Field bacteria–mediated inhibition of *Plasmodium* development. *P. falciparum* oocyst (**A**) and ookinete (**B**) loads in midguts of *A. gambiae* mosquitoes fed with both parasites and field-isolated bacteria. Bpu, *Bacillus pumilus*; Asp, *Acinetobacter* sp.; Ppu, *Pseudomonas putida*; Esp_Z, *Enterobacter* sp. (**C**) *P. falciparum* sporozoite loads in salivary glands of *A. gambiae* mosquitoes fed with both parasites and *Esp_Z*. For (A) to (C), circles represent the number of parasites from an individual mosquito and horizontal lines indicate the median number of parasites per tissue. (**D**) Midgut-specific transcript abundance of select genes at 8 hours after blood feeding with equal quantities of either the *Bpu* or *Esp_Z* isolate. Each column and error bar represent the fold-change ± standard deviation in transcript abundance when compared with PBS-fed controls. LC, PGRP-LC; CEC1, cecropin1; FBN9, fibrinogen immunolection 9; TEP1, thioester-containing protein 1; LRRD7, leucine-rich repeat–containing protein 7. (**E**) Oocyst loads in mosquitoes depleted of transcripts for IMD pathway molecules and cochallenged with *Esp_Z* and *P. falciparum*. The double-stranded RNA and absence (–) or presence (+) of *Esp_Z* are indicated below each column. Circles represent the same as in (A). (**F** and **G**) In vitro development of *P. falciparum* (E) and *P. berghei* (F) ookinetes cocultured with *Esp_Z* bacteria. Bars represent the mean and standard deviation in ookinetes. For all figures, statistical significance is represented by letters above each column, with different letters signifying distinct statistical groups [$P < 0.05$; Mann-Whitney test for (A) to (C) and (E); $P < 0.05$; unpaired *t* test for (F) and (G)].

identified based on 16*S* ribosomal DNA (rDNA) sequence, with similar genera isolated from both collections (table S1). Of these, some Gram-negative (G–) isolates reduced *P. falciparum* prevalence and intensity in the mosquito, whereas a Gram-positive (G+) isolate had no detectable effect on infection (Fig. 1A), in accordance with previous reports involving other *Plasmodium-Anopheles* models (*3*–*5*). The G– bacteria inhibited *P. falciparum* oocyst formation in the main African and Asian malaria vectors, *A. gambiae* and *A. stephensi*, respectively (Fig. 1A and fig. S1). To investigate the temporal specificity of parasite inhibition by G– bacteria, we monitored the development of the *Plasmodium* ookinetes in the presence of the field-isolated bacteria. Significantly fewer ookinetes developed with G– bacteria present, although the level of inhibition was bacterial species–dependent (Fig. 1B). The *Enterobacter* sp. (*Esp_Z*) bacterium inhibited ookinete, oocyst, and sporozoite development of a highly virulent laboratory *Plasmodium* strain by 98%, 99%, and 99%, respectively (Fig. 1, A to C), which led us to further investigate the mechanism of this inhibition.

The immune deficiency (IMD) innate immune pathway defends mosquitoes against *P. falciparum* in the gut tissue, and the microbiota has been shown to activate this pathway through the receptor protein peptidoglycan recognition protein-LC (PGRP-LC) (*6*–*8*); thus, we hypothesized that the refractory phenotype could be caused by *Esp_Z* activation of the IMD pathway. Two independent approaches showed that the mechanism of refractoriness is independent of the IMD pathway. First, although a general antibacterial response is mounted through the increased transcription of the antimicrobial peptide cecropin1 (*CEC1*), regulation of IMD pathway–controlled genes, including several potent anti-*Plasmodium* effector genes [fibrinogen immunolectin 9 (*FBN9*), leucine-rich repeat protein *LRRD7*, and thioester-containing protein 1 (*TEP1*) (*12*)] were similar in the midguts of mosquitoes challenged with *Esp_Z* or the non-inhibitory *Bacillus* bacterium (*Bpu*) (Fig. 1D). Second, RNA interference–mediated depletion of the key pathway molecules, PGRP-LC, Imd, and REL2, did not rescue *P. falciparum* oocyst development in the presence of *Esp_Z* (Fig. 1E).

Hence, we investigated the potential for parasite inhibition outside the mosquito. Although *P. falciparum* ookinete development was inefficient in vitro, coculture of *Esp_Z* with gametocytes inhibited ookinete formation by 89% (Fig. 1F). We observed a similarly strong in vitro inhibition of ookinete formation in the more-robust rodent malaria parasite *P. berghei* experimental model (Fig. 1G).

Inhibition of *P. falciparum* by *Esp_Z* in the mosquito was dose-dependent, with a threshold of 10^4 ingested bacteria providing near-complete protection against parasite infection (Fig. 2A). A remarkably low density of only 100 ingested bacteria was still able to significantly decrease oocyst intensity by 67% (Fig. 2A). In vitro ookinete development of *P. berghei* was also inhibited in a dose-dependent manner (Fig. 2B). *Esp_Z* populations in the midgut expanded by 100- to 1000-fold (Fig. 2C), which is within the range of microbial proliferation that normally occurs in the midgut lumen after a blood meal (*5*, *6*). The bacterial growth during the 24-hour period immediately after blood ingestion correlates with the time of parasite inhibition before ookinete formation (3 to 30 hours after ingestion) (*13*). Negative correlations were also observed with the timing of bacterial replication and inhibition of *P. berghei* ookinete development in vitro (correlation coefficient = –0.95 for 10^6 *Esp_Z* and –0.94 for 10^7 *Esp_Z*) (figs. S2 and S3), and taken together, these results indicated that active replication of the bacteria was required for parasite inhibition. Mosquito exposure to heat-inactivated (HIA) *Esp_Z* upon feeding on a *P. falciparum* gametocyte culture did not result in the same level of refractoriness that was observed with exposure to live bacteria (Fig. 2D). Because of an overlap in

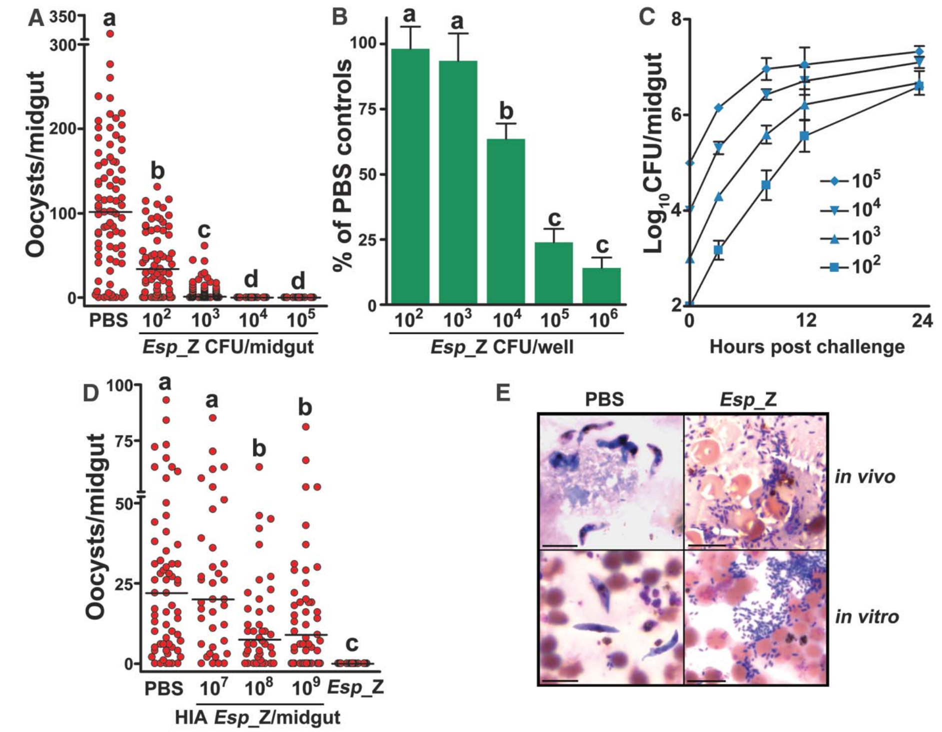

Fig. 2. Phenotypic analyses of *Esp_Z* modulation of *Plasmodium* development. (**A** and **B**) Effect of *Esp_Z* dosage on *P. falciparum* oocyst formation in mosquitoes (A) and *P. berghei* ookinete formation in vitro (B). Circles in (A) represent the number of oocysts in an individual mosquito midgut, and the horizontal lines indicate the median number of parasites per midgut. Bars in (B) represent the mean and the standard deviation in percentage of the number of ookinetes formed in bacteria-treated groups as compared with PBS-treated controls. (**C**) Temporal replication of *Esp_Z* in mosquito midguts after blood meal administration of different inoculating doses of bacteria. CFU, colony-forming unit. Bars represent the mean ± the standard deviation. (**D**) Effect of heat-inactivated *Esp_Z* bacteria on *P. falciparum* oocyst formation. Circles represent the same as in (A). For (A), (B) and (D), statistical significance is represented by letters above each column, with different letters signifying distinct statistical groups [$P < 0.05$; Mann-Whitney test for (A) and (D), unpaired t test for (B)]. (**E**) In vivo and in vitro *P. falciparum* development in the presence of *Esp_Z*. Scale bar, 10 μm.

antibacterial and anti-*Plasmodium* immune defenses in mosquitoes (*6*, *7*, *9*, *14*), the observed decrease in oocyst numbers with high concentrations of HIA bacteria (Fig. 2D) could also be interpreted as being caused by the induction of an antibacterial response in the mosquito gut, although physical inhibition of parasite infection by the killed bacteria is also plausible.

These observations, along with microscopy (Fig. 2E), indicated that *Esp_Z* inhibition of *Plasmodium* did not involve direct association between the bacteria and parasite and was mediated by diffusible bacterial factors produced during replication or by bacterial sequestration of mosquito factors that are essential for *Plasmodium* development. In subsequent assays, we observed that *Plasmodium* inhibition was independent of bacterial fatty acid metabolism (fig. S4) (*15*), xanthurenic acid (fig. S5), and iron (fig. S6) utilization by the parasite.

As the inhibitory effect did not appear to be dependent on the sequestration or acquisition of a molecule necessary for the parasite, we hypothesized that the bacteria were producing an anti-*Plasmodium* molecule. We tested this possibility by examining the in vitro development of *P. berghei*, first, in coculture with physically separated bacteria and, second, in filtered fresh supernatant of a bacterial culture. Separation of bacteria and parasites abolished bacteria-mediated inhibition of ookinete formation, except at very high bacterial concentrations (Fig. 3A). When parasites were cultured in filtered fresh supernatant from an *Esp_Z* culture, there was a 50% reduction in numbers of ookinetes formed (Fig. 3B). Together, these data indicated that the inhibitory activity was mediated by a short-lived molecule in a concentration-dependent manner. Reactive oxygen species (ROS) have a short half-life, kill *Plasmodium* (*16*–*19*), and can be generated by bacteria (*20*), so we tested the hypothesis that bacteria were inhibiting parasite development by producing ROS.

Among the field mosquito–derived bacteria, those lacking ookinete inhibitory activity (Fig. 1B) did not produce detectable levels of ROS, whereas cultures of the inhibitory *Esp_Z* did (table S2). To determine whether ROS was involved in the parasite inhibition, we supplemented the *P. berghei* culture with an antioxidant to neutralize free radicals formed. The addition of vitamin C (vitC) to in vitro cultures of *P. berghei*

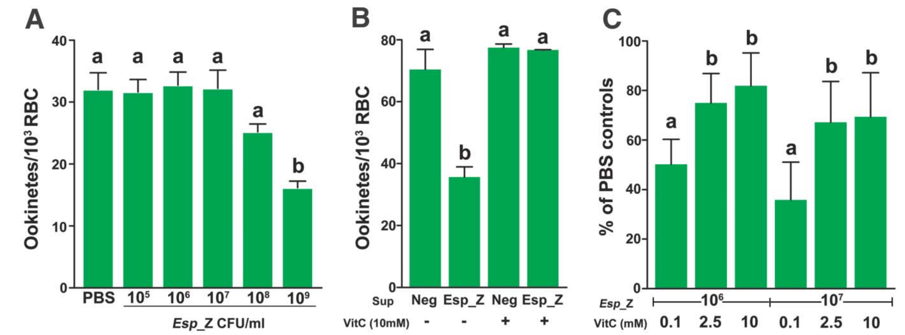

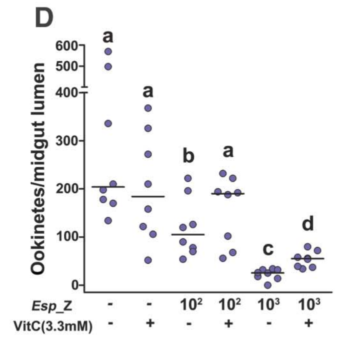

Fig. 3. Involvement of ROS generation by *Esp_Z* in inhibition of *Plasmodium* development. (**A**) Effect of physical separation of *Esp_Z* and parasites on *P. berghei* ookinete formation. (**B**) Effect of filtered culture supernatant and addition of vitamin C on *P. berghei* ookinete formation. Sup, supernatant; Neg, supernatant from a bacteria-negative culture; VitC, vitamin C. For (A) and (B), bars represent the mean and the standard deviation. (**C** and **D**) Effect of vitamin C addition on *P. berghei* ookinete formation in vitro (C) and *P. falciparum* ookinete formation in *A. gambiae* midguts (D). For (C), bars represent the means and the standard deviation in percentage of the number of ookinetes formed in bacteria-treated groups as compared with PBS-treated controls. For (D), circles represent the number of ookinetes from an individual mosquito, and horizontal lines indicate the median number of parasites per midgut. For all figures, statistical significance is represented by letters above each column, with different letters signifying distinct statistical groups [$P < 0.05$; unpaired t test for (A) to (C); Mann-Whitney test for (D)].

gametocytes rescued development of ookinetes to untreated control levels when grown in filtered *Esp_Z* culture medium (Fig. 3B), and parasite development in the presence of replicating *Esp_Z* was rescued by vitC in a dose-dependent fashion (Fig. 3C). Furthermore, reduced glutathione, another potent antioxidant, also rescued in vitro ookinete formation in the presence of *Esp_Z* (fig. S7). We showed that vertebrate leukocytes were not responsible for the observed in vitro ookinete inhibition (fig. S8). More important, supplementing an infectious blood meal with vitC did not affect parasite numbers in the absence of *Esp_Z* but rescued *P. falciparum* ookinete development twofold in the lumen of *A. gambiae* midguts when they were cofed with *Esp_Z* (Fig. 3D). The significant, yet incomplete, rescue of ookinete development with higher bacterial concentrations could be attributed to a variety of factors such as insufficient concentrations of antioxidant to neutralize the higher amount of bacterially produced ROS, excretion of substantial amounts of antioxidant by mosquito diuresis, an intimate association between bacteria and parasites that may not enable detoxification of ROS before parasite inhibition, or the loss of antioxidant activity from prolonged exposure in the digestive environment of the midgut. Antioxidant concentrations higher than 10 mM in the blood meal interfered with mosquito feeding propensity.

Genotypic analyses of laboratory and wild mosquito populations have suggested that a dominant refractory phenotype is associated with innate immunity and that *Plasmodium* infection is a result of immune failure (*21*–*23*). Our studies show a mechanism of *Plasmodium* inhibition that does not involve the mosquito-derived innate immune response, and they support the idea that the native microflora of *Anopheles* mosquitoes plays a crucial role in refractoriness to *Plasmodium* infection and will therefore influence transmission success to humans.

Bacteria of the genus *Enterobacter* have been isolated from many anopheline mosquito species in diverse geographic regions (*3*, *5*, *24*). We show that mosquitoes do not become infected with *Plasmodium* parasites when exposed to an *Enterobacter* bacterium isolated from wild mosquito populations in southern Zambia, and we show that inhibition of parasite development can be mediated by bacterial generation of ROS. Although *Esp_Z* was isolated from a single collection made during one rainy season, 25% of mosquitoes collected harbored the strain. It may be possible to manipulate the composition of the midgut microbial flora in wild mosquitoes to increase the prevalence of *Esp_Z* or other naturally inhibitory bacteria as part of an integrated malaria control strategy.

References and Notes

1. Y. Alavi *et al.*, *Int. J. Parasitol.* **33**, 933 (2003).
2. J. A. Vaughan, B. H. Noden, J. C. Beier, *Am. J. Trop. Med. Hyg.* **51**, 233 (1994).
3. L. Gonzalez-Ceron, F. Santillan, M. H. Rodriguez, D. Mendez, J. E. Hernandez-Avila, *J. Med. Entomol.* **40**, 371 (2003).
4. C. B. Pumpuni, M. S. Beier, J. P. Nataro, L. D. Guers, J. R. Davis, *Exp. Parasitol.* **77**, 195 (1993).
5. C. B. Pumpuni, J. Demaio, M. Kent, J. R. Davis, J. C. Beier, *Am. J. Trop. Med. Hyg.* **54**, 214 (1996).
6. Y. Dong, F. Manfredini, G. Dimopoulos, *PLoS Pathog.* **5**, e1000423 (2009).
7. S. Meister *et al.*, *PLoS Pathog.* **5**, e1000542 (2009).
8. L. S. Garver, Y. Dong, G. Dimopoulos, *PLoS Pathog.* **5**, e1000335 (2009).
9. Y. Dong *et al.*, *PLoS Pathog.* **2**, e52 (2006).
10. S. Kumar, A. Molina-Cruz, L. Gupta, J. Rodrigues, C. Barillas-Mury, *Science* **327**, 1644 (2010).
11. Materials and methods are available as supporting material on *Science* online.
12. C. M. Cirimotich, Y. Dong, L. S. Garver, S. Sim, G. Dimopoulos, *Dev. Comp. Immunol.* **34**, 387 (2010).
13. J. A. Vaughan, B. H. Noden, J. C. Beier, *J. Parasitol.* **78**, 716 (1992).
14. S. Meister *et al.*, *Proc. Natl. Acad. Sci. U.S.A.* **102**, 11420 (2005).
15. K. van Dijk, E. B. Nelson, *Appl. Environ. Microbiol.* **66**, 5340 (2000).
16. S. Kumar *et al.*, *Proc. Natl. Acad. Sci. U.S.A.* **100**, 14139 (2003).
17. S. Luckhart, Y. Vodovotz, L. Cui, R. Rosenberg, *Proc. Natl. Acad. Sci. U.S.A.* **95**, 5700 (1998).
18. A. Molina-Cruz *et al.*, *J. Biol. Chem.* **283**, 3217 (2008).
19. T. M. L. Peterson, A. J. Gow, S. Luckhart, *Free Radic. Biol. Med.* **42**, 132 (2007).
20. A. Mai-Prochnow *et al.*, *J. Bacteriol.* **190**, 5493 (2008).
21. S. A. Blandin *et al.*, *Science* **326**, 147 (2009).
22. O. Niaré *et al.*, *Science* **298**, 213 (2002).
23. M. M. Riehle *et al.*, *Science* **312**, 577 (2006).
24. O. Terenius *et al.*, *J. Med. Entomol.* **45**, 172 (2008).

Acknowledgments. This work has been supported by the National Institutes of Health/National Institute of Allergy and Infectious Disease R01AI061576 and a Johns Hopkins Malaria Research Institute (JHMRI) Pilot Grant (to G.D.), the Bloomberg Family Foundation, the Calvin A. and Helen H. Lang fellowship (to C.M.C.), a JHMRI postdoctoral fellowship (to J.S.-N.), and a fellowship from the NSF (to A.M.C.). The authors thank the mosquito collection team at the Malaria Institute at Macha, Zambia; the JHMRI Parasitology and Insectary Core facilities; Sanaria Inc.; E. Nelson (Cornell University) for providing mutant bacteria strains; and D. McClellan for editorial services. We performed all experiments according to Johns Hopkins Institutional Animal Care and Use Committee guidelines. Human landing catches were performed according to the approved protocol UNZA REC 011-02-04 with consent of participants. GenBank accession numbers generated for bacterial 16*S* rDNA sequences are listed in table S1, SOM.

Supporting Online Material

www.sciencemag.org/cgi/content/full/332/6031/855/DC1
Materials and Methods
Figs. S1 to S8
Tables S1 to S3
References and Notes

13 December 2010; accepted 6 April 2011
10.1126/science.1201618

Preserved Feedforward But Impaired Top-Down Processes in the Vegetative State

Melanie Boly,[1,2]* Marta Isabel Garrido,[2] Olivia Gosseries,[1] Marie-Aurélie Bruno,[1] Pierre Boveroux,[3] Caroline Schnakers,[1] Marcello Massimini,[4] Vladimir Litvak,[2] Steven Laureys,[1] Karl Friston[2]

Frontoparietal cortex is involved in the explicit processing (awareness) of stimuli. Frontoparietal activation has also been found in studies of subliminal stimulus processing. We hypothesized that an impairment of top-down processes, involved in recurrent neuronal message-passing and the generation of long-latency electrophysiological responses, might provide a more reliable correlate of consciousness in severely brain-damaged patients, than frontoparietal responses. We measured effective connectivity during a mismatch negativity paradigm and found that the only significant difference between patients in a vegetative state and controls was an impairment of backward connectivity from frontal to temporal cortices. This result emphasizes the importance of top-down projections in recurrent processing that involve high-order associative cortices for conscious perception.

The vegetative state (VS) is defined by preserved arousal, in the absence of any behavioral signs of awareness (*1*). In contrast, patients in a minimally conscious state (MCS) show nonreflexive and purposeful behaviors but are unable to communicate (*2*). Because the clinical diagnosis of these patients is extremely difficult (*3*), neuroimaging experiments have tried to establish accurate biomarkers of consciousness level in VS and MCS. These patients also provide a lesion-deficit model in the quest for neural correlates of consciousness in the human brain (*4*). The conscious perception of external stimuli requires activation of frontoparietal cortices, in addition to activity in low-level specialized cortices (*5*–*7*). However, frontoparietal activation can also be found during subliminal stimulus processing (*8*, *9*). Current evidence points to long-latency evoked event-related potential (ERP) components, involving frontoparietal cortices, as a reliable neu-

[1]Coma Science Group, Cyclotron Research Centre and Neurology Department, University of Liège and CHU Sart Tilman Hospital, 4000 Liège, Belgium. [2]Wellcome Trust Centre for Neuroimaging, Institute of Neurology, University College London, London WC1N 1PJ, UK. [3]Anesthesiology Department, University of Liège and CHU Sart Tilman Hospital, 4000 Liège, Belgium. [4]Department of Clinical Sciences, "Luigi Sacco," University of Milan, 20157 Milan, Italy.

*To whom correspondence should be addressed. E-mail: mboly@ulg.ac.be

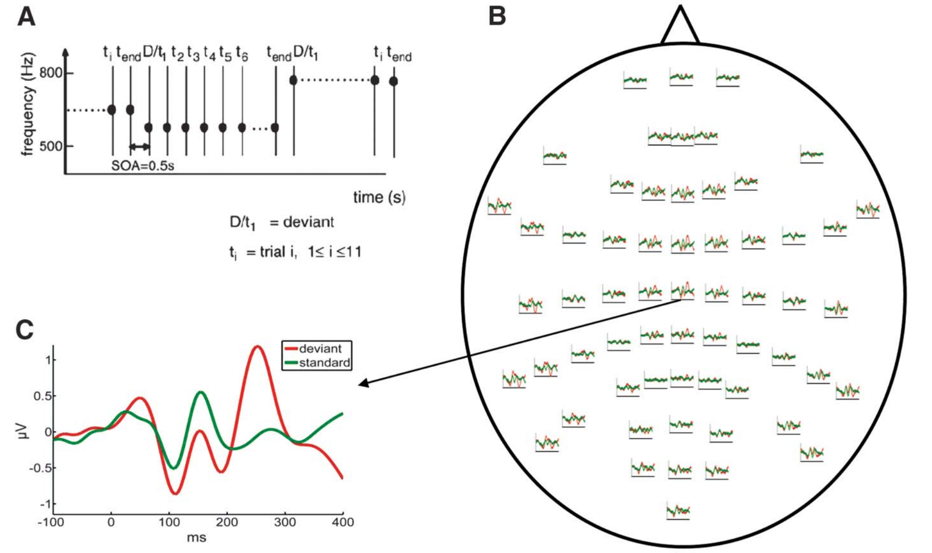

Fig. 1. Design and ERP responses elicited in a roving paradigm. (**A**) The experimental design used a sporadically changing standard stimulus (auditory tone). The first presentation of a novel tone is a deviant D = t_1 that becomes a standard, through repetition; $t_2,\ldots,t_{end}$. In this paradigm, deviants and standard have exactly the same physical properties. (**B**) Grand-mean (averaged over control subjects) ERP responses to the first and 11th tone presentations: the established "standard" (t_{11} in green) and deviant tone (t_1 in red) overlaid on a scalp map of 60 electroencephalogram electrodes. (**C**) ERP responses to standard and deviant tones at channel Cz (central). Deviant corresponds to responses elicited by the first tone presentation or to oddball events. Standard corresponds to the 11th repetition of the same tone. [Adapted from a figure in M. I. Garrido *et al*. (*22*), with permission from Elsevier]

ronal marker for conscious perception in healthy controls (*10*). Although feed-forward connectivity is sufficient to generate short-latency ERP components, long-latency components are mediated by backward connections (*11*). This suggests that the level of consciousness may rest on the integrity of backward (top-down) connectivity. We used a mismatch negativity (MMN) paradigm, which elicits well-characterized (preattentive) responses (*12*). The MMN correlates inversely with consciousness level during anesthesia (*13*) and with depth of sleep (*14*); although some studies report negative findings (*15*), MMN deficits have also been associated with the level of consciousness in MCS and VS (*16*) [see supporting online material (SOM) text]. We predicted that both long-latency components and backward connectivity would correlate with level of consciousness. We tested this hypothesis quantitatively, using Dynamic Causal Modeling (DCM), which allows for inferences about the neuronal architectures that generate hemodynamic or electromagnetic signals (*17*, *18*). DCM uses a generative model of how electrophysiological signals are produced at the neuronal level; it employs neural mass models and Bayesian statistics to infer the neuronal mechanisms (effective connectivity) underlying observed evoked electrophysiological responses (*19*, *20*). This method has been validated in a

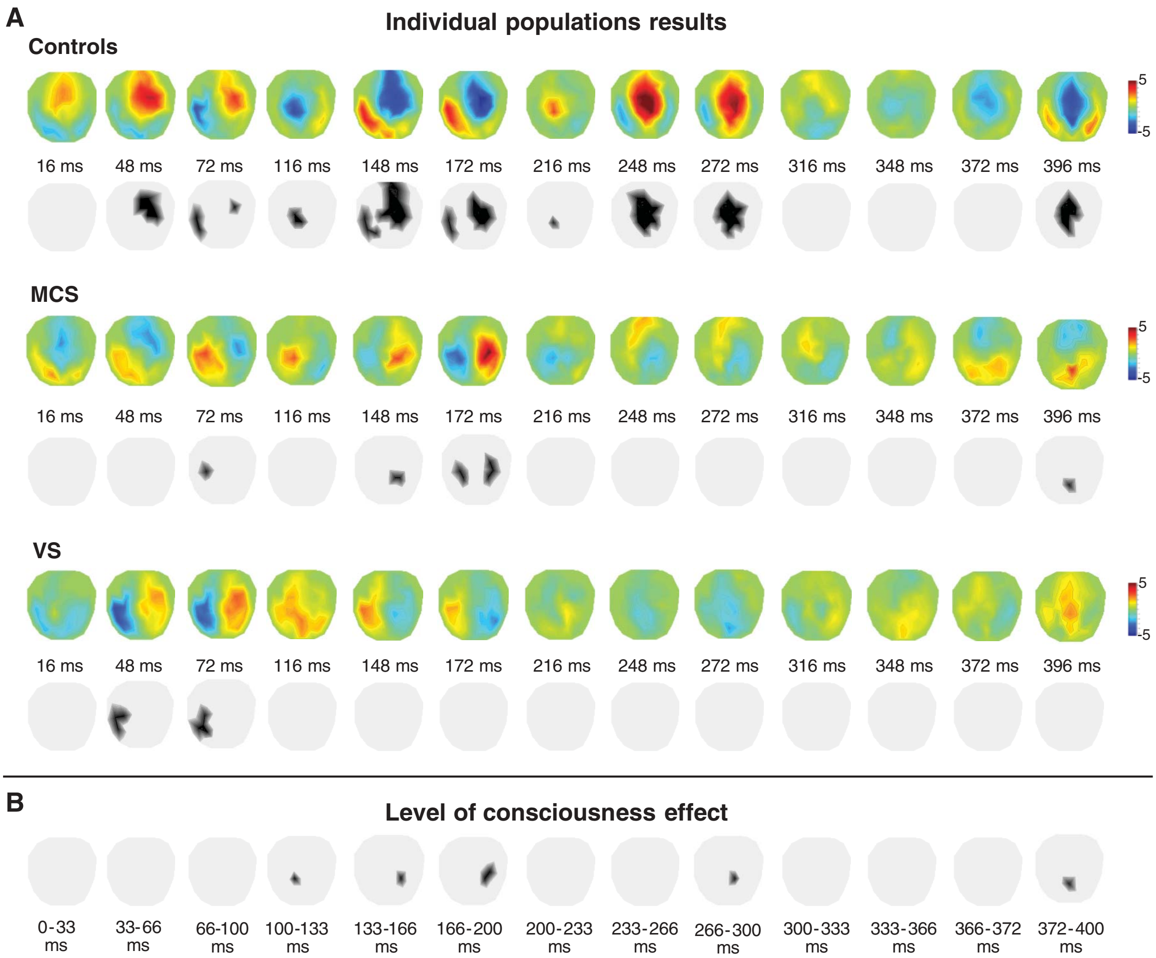

Fig. 2. Spatiotemporal grand-mean difference between standard and deviants correlates with the level of consciousness. The two-dimensional scalp topographies are interpolated from the 60 channels. (**A**) Statistical parametric maps of differential group responses in controls, MCS patients, and VS patients. For display purposes, instantaneous T maps are displayed without threshold and with threshold at $P < 0.001$ (uncorrected) in the three populations. Color scales correspond respectively to T values or to significant (in black) voxels. (**B**) Statistical parametric maps showing scalp regions where there is a significant interaction between response amplitude and consciousness level (with the threshold at $P < 0.05$; family-wise error corrected) over different time windows. Significant effects were found over temporal and frontal sensors in the range of 115 to 395 ms.

number of electrophysiological studies (*11*, *21*–*23*) and provides an efficient way to map from observed evoked potential patterns to causative neuronal mechanisms (*24*).

The present study used DCM of event-related potentials to quantify effective connectivity in backward and forward connections at two hierarchical cortical levels (i.e., in temporal and frontal cortices), during auditory processing in healthy subjects and MCS and VS patients. We used a roving oddball paradigm (Fig. 1), as in previous DCM studies (*22*, *23*) (SOM text). The functional anatomy engaged by this paradigm involves both forward and backward connections in a fronto-temporal cortical network (*22*). High-density ERP recordings were acquired in 21 brain-damaged patients (8 VS and 13 MCS) and 22 healthy controls (*25*). ERP data analysis, performed with statistical parametric mapping, tested the differential processing of standard and deviant sounds (*25*). Scalp-level group analyses detected long-latency components with a central topography in both controls and patients in a MCS ($P < 0.05$, family-wise error corrected). Peak latencies for the MMN were 170 ms in controls and 175 ms in patients in a MCS. Although the MMN was the most significant in MCS, the P3 component

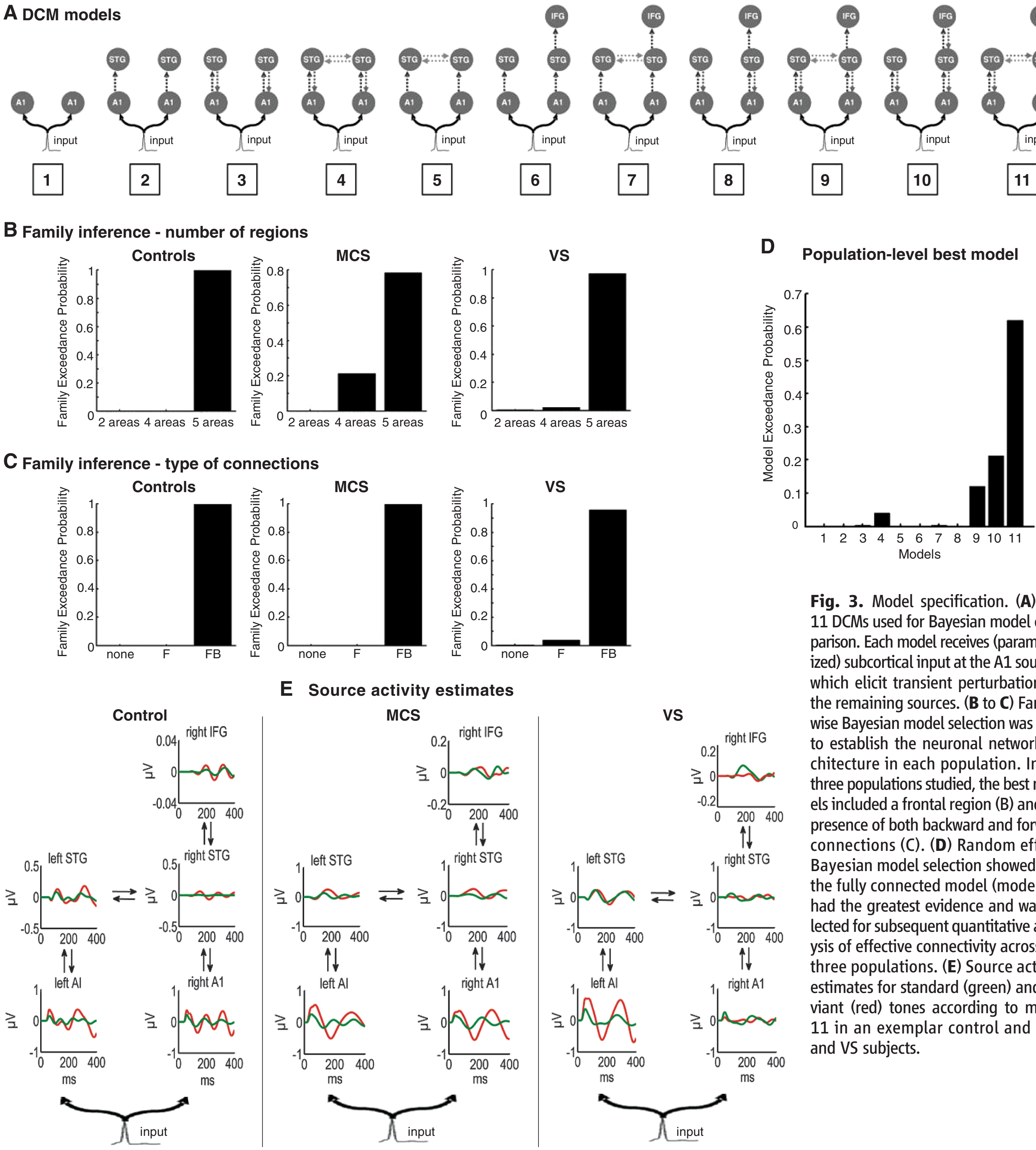

Fig. 3. Model specification. (**A**) The 11 DCMs used for Bayesian model comparison. Each model receives (parameterized) subcortical input at the A1 sources, which elicit transient perturbations in the remaining sources. (**B** to **C**) Family-wise Bayesian model selection was used to establish the neuronal network architecture in each population. In the three populations studied, the best models included a frontal region (B) and the presence of both backward and forward connections (C). (**D**) Random effects Bayesian model selection showed that the fully connected model (model 11) had the greatest evidence and was selected for subsequent quantitative analysis of effective connectivity across the three populations. (**E**) Source activity estimates for standard (green) and deviant (red) tones according to model 11 in an exemplar control and MCS and VS subjects.

(peak latency at 250 ms) was the most significant in controls. Only posterior early components (peak at 55 ms) could be seen in VS (Fig. 2). An analysis of covariance (ANCOVA) confirmed a significant interaction between level of consciousness and stimulus type on long-latency responses (peak latencies at 115, 175, 265, and 395 ms, $P < 0.05$, family-wise error corrected) across the three groups (Fig. 2).

Although the architecture of the network involved in the generation of MMN responses has been studied extensively in healthy volunteers (*26*) (SOM text), the involvement of frontal cortex, via its forward and backward connections, has yet to be established in brain-damaged patients. We thus performed a group-level Bayesian model comparison to identify the network architecture that best explained the responses of patients. Bayesian model selection (BMS) compared 11 models, which differed in the areas and connections involved (Fig. 3). Random effects family-level analysis showed that models including a frontal source with both forward and backward connections could best explain ERP responses in MCS and VS. For quantitative connectivity analysis, a second (random-effects) BMS procedure was applied to the 11 models, across all three groups (*25*). The fully connected model (model 11) had again the greatest evidence (Fig. 3). The corresponding source activity estimates in representative controls and MCS and VS subjects are also shown in Fig. 3. To assess differences between controls and patients, we compared the connectivity estimates (from the best model) using simple *t* tests (*25*). The only significant effect of the level of consciousness (differences between healthy volunteers, MCS subjects, and VS patient populations) was on the backward connection from frontal to superior temporal cortex (corrected $P = 0.012$), with no detectible differences in forward and backward processing in temporal cortex (Fig. 4). This backward connection was significantly impaired in VS patients as compared with controls ($P = 0.002$). MCS patients showed preserved top-down connectivity as compared with VS patients ($P = 0.001$) and were not significantly different from controls ($P > 0.05$) (Fig. 4).

Our main result is that, although the frontal cortex is still involved in the generation of the ERP in a VS, the main abnormality is in recurrent processing between higher-order cortices, owing to impaired backward connections from frontal to temporal cortices. Our analyses suggest that the (possibly diverse) pathophysiological causes of VS find a common expression in reducing top-down influences from frontal to temporal areas. Further research is required to establish the precise molecular or physiological mechanisms underlying these observations. In contrast to VS patients, MCS patients exhibited long-latency components in the scalp ERP and near-normal recurrent effective connectivity with higher-order cortices. This group difference cannot be attributable to differences in vigilance, as all patients were maintained in the same state of wakefulness throughout the experiment (*25*). Although forward connections are certainly needed for normal stimulus processing, these results suggest that the integrity of backward connections, or top-down processes, may be necessary for conscious perception. These findings stress the importance of recurrent processing in higher-order associative areas in the generation of conscious perception and do not support the view that recurrent processing in sensory cortex can be equated with consciousness (*27*). In contrast, our results suggest that recursive processing in high-order cortical areas is necessary for the generation of conscious perception (*5*). This would be mandated by the maintenance of high levels of integrated information, thought to be important for consciousness (*28*). A hierarchical recurrent cortical organization is also required by predictive coding formulations of the Bayesian brain hypothesis, which regards perception as inference on the causes of external stimuli (*29*). Under this perspective, VS patients are unable to elaborate (top-down) predictions of their sensorium, resulting (phenomenologically) in an impoverished percept and (physiologically) the absence of long-latency (endogenous) ERP components. Finally, our biologically plausible DCM shows that a selective impairment of a single (backward) connection accounts for widespread differences in the distributed responses we found between VS patients and healthy volunteers. This fits with the pervasive effects of recurrent processing on ERP amplitudes observed in healthy volunteers (a phenomenon referred to as "ignition") (*10*). Long-lasting slow ERP responses, such as K-complexes, can be observed during slow-wave sleep (*30*). Cortical connectivity analysis could be thus more specific than scalp-level analyses in terms of detecting the architectural correlates of conscious level. On the other hand, our analyses cannot say whether a failure of backward connectivity from the frontal region is a cause or consequence of processing that underlies consciousness (SOM text). What we can say is that a specific (top-down) failure of effective connectivity is implicated in consciousness and may play a necessary role.

In summary, our findings suggest that a selective disruption of top-down processes from high levels of a cortical hierarchy can lead to loss of consciousness in brain-damaged patients, and can clearly differentiate VS from MCS. In addition to its neuroscientific relevance, the present approach could constitute a new diagnostic tool to quantify the level of consciousness electrophysiologically at the patients' bedside. Further studies should also complement these findings in conditions such as sleep, epilepsy, or anesthesia-induced unconsciousness.

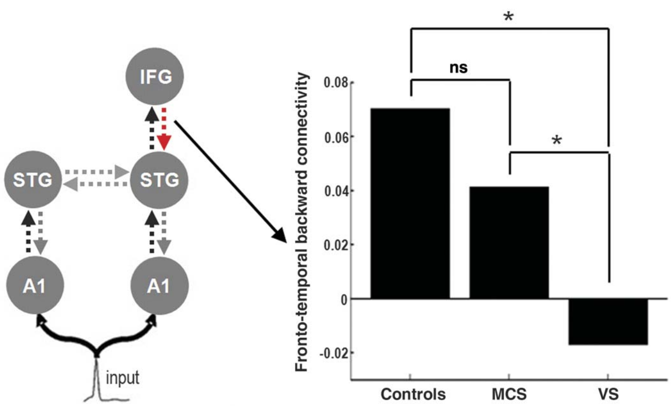

Fig. 4. Quantitative effective connectivity analysis revealed that the only significant difference between VS patients and controls was an impairment of backward connectivity from frontal to temporal cortex. MCS subjects showed significantly preserved connectivity compared with VS subjects and were not significantly different from controls.

References and Notes

1. S. Laureys, A. M. Owen, N. D. Schiff, *Lancet Neurol.* **3**, 537 (2004).
2. J. T. Giacino *et al.*, *Neurology* **58**, 349 (2002).
3. C. Schnakers *et al.*, *BMC Neurol.* **9**, 35 (2009).
4. S. Laureys, *Trends Cogn. Sci.* **9**, 556 (2005).
5. S. Dehaene, J. P. Changeux, L. Naccache, J. Sackur, C. Sergent, *Trends Cogn. Sci.* **10**, 204 (2006).
6. G. Rees, G. Kreiman, C. Koch, *Nat. Rev. Neurosci.* **3**, 261 (2002).
7. M. Boly *et al.*, *Arch. Neurol.* **61**, 233 (2004).
8. M. T. Diaz, G. McCarthy, *J. Cogn. Neurosci.* **19**, 1768 (2007).
9. Q. Luo *et al.*, *Cereb. Cortex* **19**, 1896 (2009).
10. A. Del Cul, S. Baillet, S. Dehaene, *PLoS Biol.* **5**, e260 (2007).
11. M. I. Garrido, J. M. Kilner, S. J. Kiebel, K. J. Friston, *Proc. Natl. Acad. Sci. U.S.A.* **104**, 20961 (2007).
12. R. Näätänen, P. Paavilainen, T. Rinne, K. Alho, *Clin. Neurophysiol.* **118**, 2544 (2007).
13. W. Heinke *et al.*, *Anesthesiology* **100**, 617 (2004).
14. P. Ruby, A. Caclin, S. Boulet, C. Delpuech, D. Morlet, *J. Cogn. Neurosci.* **20**, 296 (2008).
15. C. Fischer, J. Luaute, D. Morlet, *Clin. Neurophysiol.* **121**, 1032 (2010).
16. V. J. Wijnen, G. J. van Boxtel, H. J. Eilander, B. de Gelder, *Clin. Neurophysiol.* **118**, 597 (2007).
17. K. J. Friston, L. Harrison, W. Penny, *Neuroimage* **19**, 1273 (2003).
18. O. David *et al.*, *Neuroimage* **30**, 1255 (2006).
19. O. David, L. Harrison, K. J. Friston, *Neuroimage* **25**, 756 (2005).
20. S. J. Kiebel, M. I. Garrido, R. Moran, C. C. Chen, K. J. Friston, *Hum. Brain Mapp.* **30**, 1866 (2009).
21. M. I. Garrido, J. M. Kilner, S. J. Kiebel, K. E. Stephan, K. J. Friston, *Neuroimage* **36**, 571 (2007).
22. M. I. Garrido *et al.*, *Neuroimage* **42**, 936 (2008).
23. M. I. Garrido *et al.*, *Neuroimage* **48**, 269 (2009).
24. K. J. Friston, *Science* **326**, 399 (2009).
25. Materials and methods are available as supporting material on *Science* Online.
26. M. I. Garrido, J. M. Kilner, K. E. Stephan, K. J. Friston, *Clin. Neurophysiol.* **120**, 453 (2009).
27. V. A. Lamme, *Trends Cogn. Sci.* **10**, 494 (2006).
28. D. Balduzzi, G. Tononi, *PLOS Comput. Biol.* **4**, e1000091 (2008).
29. K. Friston, *Nat. Rev. Neurosci.* **11**, 127 (2010).
30. M. Roth, J. Shaw, J. Green, *Electroencephalogr. Clin. Neurophysiol.* **8**, 385 (1956).

Acknowledgments. This work was supported by the Belgian Fonds National de la Recherche Scientifique (FNRS), European Commission, Mind Science Foundation, McDonnell Foundation, French-Speaking Community Concerted Research Action (ARC 06/11-340), Fondation Léon Frédéricq, and National Institutes of Health. M.-A.B. and O.G. are Research Fellows, M.B. and C.S. Postdoctoral Fellows, and S.L. Senior Research Associate at the FNRS. M.I.G., V.L., and K.F. are supported by the Wellcome Trust.

Supporting Online Material
www.sciencemag.org/cgi/content/full/332/6031/858/DC1
Materials and Methods
SOM Text
Fig. S1
Table S1
References

22 December 2010; accepted 6 April 2011
10.1126/science.1202043

Improved Learning in a Large-Enrollment Physics Class

Louis Deslauriers,[1,2] Ellen Schelew,[2] Carl Wieman*†‡

We compared the amounts of learning achieved using two different instructional approaches under controlled conditions. We measured the learning of a specific set of topics and objectives when taught by 3 hours of traditional lecture given by an experienced highly rated instructor and 3 hours of instruction given by a trained but inexperienced instructor using instruction based on research in cognitive psychology and physics education. The comparison was made between two large sections (*N* = 267 and *N* = 271) of an introductory undergraduate physics course. We found increased student attendance, higher engagement, and more than twice the learning in the section taught using research-based instruction.

The traditional lecture approach remains the prevailing method for teaching science at the postsecondary level, although there are a growing number of studies indicating that other instructional approaches are more effective (*1*–*8*). A typical study in the domain of physics demonstrates how student learning is improved from one year to the next when an instructor changes his or her approach, as measured by standard concept-based tests such as the Force Concept Inventory (*9*) or the instructor's own exams. In our studies of two full sessions of an advanced quantum mechanics class taught either by traditional or by interactive learning style, students in the interactive section showed improved learning, but both sections, interactive and traditional, showed similar retention of learning 6 to 18 months later (*10*). Here, we compare learning produced by two contrasting instructional methods in a large-enrollment science course. The control group was lectured by a motivated faculty member with high student evaluations and many years of experience teaching this course. The experimental group was taught by a postdoctoral fellow using instruction based on research on learning. The same selected learning objectives were covered by both instructors in a 1-week period.

The instructional design for the experimental section was based on the concept of "deliberate practice" (*11*) for the development of expertise. The deliberate practice concept encompasses the educational ideas of constructivism and formative assessment. In our case, the deliberate practice takes the form of a series of challenging questions and tasks that require the students to practice physicist-like reasoning and problem solving during class time while provided with frequent feedback.

The design goal was to have the students spend all their time in class engaged in deliberate practice at "thinking scientifically" in the form of making and testing predictions and arguments about the relevant topics, solving problems, and critiquing their own reasoning and that of others. All of the activities are designed to fit together to support this goal, including moving the simple transfer of factual knowledge outside of class as much as possible and creating tasks and feedback that motivate students to become fully engaged. As the students work through these tasks, they receive feedback from fellow students (*12*) and from the instructor. We incorporate multiple "best instructional practices," but we believe the educational benefit does not come primarily from any particular practice but rather from the integration into the overall deliberate practice framework.

This study was carried out in the second term of the first-year physics sequence taken by all undergraduate engineering students at the University of British Columbia. This calculus-based course covers various standard topics in electricity and magnetism. The course enrollment was 850 students, who were divided among three sections. Each section had 3 hours of lecture per week. The lectures were held in a large theater-style lecture hall with fixed chairs behind benches grouping up to five students. The students also had weekly homework assignments, instructional laboratories, and tutorials and recitations where they solved problems; this work was graded. There were two midterm exams and a final exam. All course components were common across all three sections, except for the lectures, which were prepared and given independently by three different instructors.

During week 12, we studied two sections whose instructors agreed to participate. For the 11 weeks preceding the study, both sections were taught in a similar manner by two instructors (A and B), both with above average student teaching evaluations and many years experience teaching this course and many others. Both instructors lectured using PowerPoint slides to present content and example problems and also showed demonstrations. Meanwhile, the students took notes. "Clicker" (or "personal response system") questions (average 1.5 per class, range 0 to 5) were used for summative evaluation (which was characterized by individual testing without discussion or follow-up other than a summary of the correct answers). Students were given participation credit for submitting answers.

Before the experiment, a variety of data were collected on the students in the two sections

Table 1. Measures of student perceptions, behaviors, and knowledge.

	Control section	Experimental section
Number of students enrolled	267	271
Mean BEMA score (*13*) (week 11)	47 ± 1%	47 ± 1%
Mean CLASS score (*14*) (start of term) (agreement with physicist)	63 ± 1%	65 ± 1%
Mean midterm 1 score	59 ± 1%	59 ± 1%
Mean midterm 2 score	51 ± 1%	53 ± 1%
Attendance before experiment*	55 ± 3%	57 ± 2%
Attendance during experiment	53 ± 3%	75 ± 5%
Engagement before experiment*	45 ± 5%	45 ± 5%
Engagement during experiment	45 ± 5%	85 ± 5%

*Average value of multiple measurements carried out in a 2-week interval before the experiment. Engagement also varies over location in the classroom; numbers given are spatial and temporal averages.

[1]Carl Wieman Science Education Initiative, University of British Columbia, Vancouver, BC, Canada. [2]Department of Physics and Astronomy, University of British Columbia, Vancouver, BC, Canada.

*On leave from the University of British Columbia and the University of Colorado.

†To whom correspondence should be addressed. E-mail: gilbertwieman@gmail.com

‡This work does not necessarily represent the views of the Office of Science and Technology Policy or the United States government.

(Table 1). Students took two midterm exams (identical across all sections). In week 11, students took the Brief Electricity and Magnetism Assessment (BEMA), which measures conceptual knowledge (*13*). At the start of the term, students took the Colorado Learning Attitudes about Science Survey (CLASS) (*14*), which measures a student's perceptions of physics. During weeks 10 and 11, we measured student attendance and engagement in both sections. Attendance was measured by counting the number of students present, and engagement was measured by four trained observers in each class using the protocol discussed in the supporting online material (SOM) (*15*). The results show that the two sections were indistinguishable (Table 1). This in itself is interesting, because the personalities of the two instructors are rather different, with instructor A (control section) being more animated and intense.

The experimental intervention took place during the 3 hours of lecture in the 12th week. Those classes covered the unit on electromagnetic waves. This unit included standard topics such as plane waves and energy of electromagnetic waves and photons. The control section was taught by instructor A using the same instructional approach as in the previous weeks, except they added instructions to read the relevant chapter in the textbook before class. The experimental section was taught by two instructors who had not previously taught these students. The instructors were the first author of this paper, L.D., assisted by the second author, E.S. Instructor A and L.D. had agreed to make this a learning competition. L.D. and instructor A agreed beforehand what topics and learning objectives would be covered. A multiple-choice test (see SOM) was developed by L.D. and instructor A that they and instructor B agreed was a good measure of the learning objectives and physics content. The test was prepared at the end of week 12. Most of the test questions were clicker questions previously used at another university, often slightly modified. Both sections were told that they would receive a bonus of 3% of the course grade for the combination of participating in clicker questions, taking the test, and (only in the experimental section) turning in group task solutions, with the apportionment of credit across these tasks left unspecified.

In contrast to instructor A, the teaching experience of L.D. and E.S. had been limited to serving as teaching assistants. L.D. was a postdoctoral researcher working in the Carl Wieman (third author of this paper) Science Education Initiative (CWSEI) and had received training in physics education and learning research and methods of effective pedagogy while assisting with the teaching of six courses. E.S. had a typical physics graduate student background except for having taken a seminar course in physics education.

The instructional approach used in the experimental section included elements promoted by CWSEI and its partner initiative at the University of Colorado: preclass reading assignments, preclass reading quizzes, in-class clicker questions with student-student discussion (CQ), small-group active learning tasks (GT), and targeted in-class instructor feedback (IF). Before each of the three 50-min classes, students were assigned a three- or four-page reading, and they completed a short true-false online quiz on the reading. To avoid student resistance, at the beginning of the first class, several minutes were used to explain to students why the material was being taught this way and how research showed that this approach would increase their learning.

A typical schedule for a class was the following: CQ1, 2 min; IF, 4 min; CQ2, 2 min; IF, 4 min; CQ2 (continued), 3 min; IF, 5 min; Revote CQ2, 1 min; CQ3, 3 min; IF, 6 min; GT1, 6 min; IF with a demonstration, 6 min; GT1 (continued), 4 min; and IF, 3 min. The time duration for a question or activity includes the amount of time the students spent discussing the problem and asking numerous questions. There was no formal lecturing; however, guidance and explanations were provided by the instructor throughout the class. The instructor responded to student-generated questions, to results from the clicker responses, and to what the instructor heard by listening in on the student-student discussions. Students' questions commonly expanded upon and extended the material covered by the clicker questions or small-group tasks. The material shown on the slides used in class is given in the SOM, along with some commentary about the design elements and preparation time required.

At the beginning of each class, the students were asked to form groups of two. After a clicker question was shown to the class, the students discussed the question within their groups (which often expanded to three or more students) and submitted their answer using clickers. When the voting was complete, the instructor showed the results and gave feedback. The small-group tasks were questions that required a written response. Students worked in the same groups but submitted individual answers at the end of each class for participation credit. Instructor A observed each of these classes before teaching his own class and chose to use most of the clicker questions developed for the experimental class. However, Instructor A used these only for summative evaluation, as described above.

L.D. and E.S. together designed the clicker questions and small-group tasks. L.D. and E.S. had not taught this class before and were not familiar with the students. Before the first class, they solicited two volunteers enrolled in the course to pilot-test the materials. The volunteers were asked to think aloud as they reasoned through the planned questions and tasks. Results from this testing were used to modify the clicker questions and tasks to reduce misinterpretations and adjust the level of difficulty. This process was repeated before the second class with one volunteer.

During the week of the experiment, engagement and attendance remained unchanged in the control section. In the experimental section, student engagement nearly doubled and attendance increased by 20% (Table 1). The reason for the attendance increase is not known. We hypothesize that of the many students who attended only part of a normal class, more of them were captured by the happenings in the experimental section and decided to stay and to return for the subsequent classes.

The test was administered in both sections in the first class after the completion of the 3-hour unit. The control section had covered the material related to all 12 of the questions on the test. The experimental section covered only 11 of the 12 questions in the allotted time. Two days before the test was given, the students in both sections were reminded of the test and given links to the postings of all the material used in the experimental section: the preclass reading assignments and quizzes; the clicker questions; and the group tasks, along with answers to all of these. The students were encouraged by e-mail and in class to try their best on the test and were told that it would be good practice for the final exam, but their performance on the test did not affect their course grade. Few students in either section finished in less than 15 min, with the average being about 20 min.

The test results are shown in Fig. 1. For the experimental section, 211 students attended class to take the test, whereas 171 did so in the control section. The average scores were 41 ± 1% in the control section and 74 ± 1% in the experimental section. Random guessing would produce a score of 23%, so the students in the experimental section did more than twice as well on this test as those in the control section.

The test score distributions are not normal (Fig. 1). A ceiling effect is apparent in the experi-

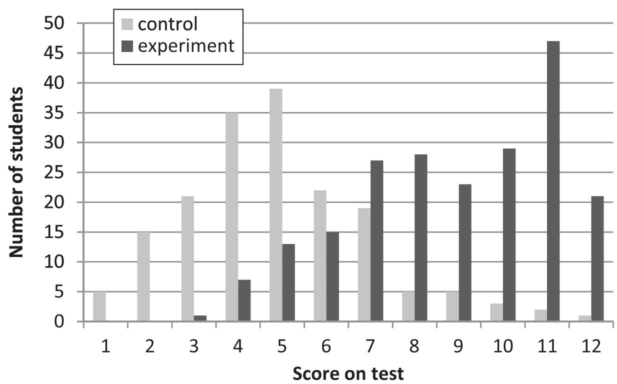

Fig. 1. Histogram of student scores for the two sections.

mental section. The two distributions have little overlap, demonstrating that the differences in learning between the two sections exist for essentially the entire student population. The standard deviation calculated for both sections was about 13%, giving an effect size for the difference between the two sections of 2.5 standard deviations. As reviewed in (*4*), other science and engineering classroom studies report effect sizes less than 1.0. An effect size of 2, obtained with trained personal tutors, is claimed to be the largest observed for any educational intervention (*16*).

This work may obtain larger effect sizes than in this previous work because of the design and implementation that maximized productive engagement. The clicker questions and group tasks were designed not only to require explicit expert reasoning but also to be sufficiently interesting and personally relevant to motivate students to fully engage. Another factor could be that previous work primarily used end-of-term tests, and the results on those tests reflect all the learning that students do inside and outside of class, for example, the learning that takes place while doing homework and studying for exams. In our intervention, the immediate low-stakes test more directly measured the learning achieved from preclass reading and class itself, in the absence of subsequent study.

We are often asked about the possible contributions of the Hawthorne effect, where any change in conditions is said to result in improved performance. As discussed in citations in the SOM, the original Hawthorne plant data actually show no such effect, nor do experiments in educational settings (*17*).

A concern frequently voiced by faculty as they consider adopting active learning approaches is that students might oppose the change (*18*). A week after the completion of the experiment and exam, we gave students in the experimental section an online survey (see SOM); 150 students completed the survey.

For the survey statement "I really enjoyed the interactive teaching technique during the three lectures on E&M waves," 90% of the respondents agreed (47% strongly agreed, 43% agreed) and only 1% disagreed. For the statement "I feel I would have learned more if the whole physics 153 course would have been taught in this highly interactive style." 77% agreed and only 7% disagreed. Thus, this form of instruction was well received by students.

In conclusion, we show that use of deliberate practice teaching strategies can improve both learning and engagement in a large introductory physics course as compared with what was obtained with the lecture method. Our study compares similar students, and teachers with the same learning objectives and the same instructional time and tests. This result is likely to generalize to a variety of postsecondary courses.

References and Notes

1. R. J. Beichner *et al.*, in *Research-Based Reform of University Physics*, E. F. Redish, P. J. Cooney, Eds. (American Association of Physics Teachers, College Park, MD, 2007).
2. C. H. Crouch, E. Mazur, *Am. J. Phys.* **69**, 970 (2001).
3. J. E. Froyd, "White paper on promising practices in undergraduate STEM education" [Commissioned paper for the Evidence on Promising Practices in Undergraduate Science, Technology, Engineering, and Mathematics (STEM) Education Project, The National Academies Board on Science Education, 2008]. www7.nationalacademies.org/bose/Froyd_Promising_Practices_CommissionedPaper.pdf
4. J. E. Froyd, "Evidence for the efficacy of student-active learning pedagogies" (Project Kaleidoscope, 2007). www.pkal.org/documents/BibliographyofSALPedagogies.cfm
5. R. R. Hake, *Am. J. Phys.* **66**, 64 (1998).
6. J. K. Knight, W. B. Wood, *Cell Biol. Educ.* **4**, 298 (2005).
7. M. Prince, *J. Eng. Educ.* **93**, 223 (2004).
8. L. Springer, M. E. Stanne, S. S. Donavan, *Rev. Educ. Res.* **69**, 21 (1999).
9. D. Hestenes, M. Wells, G. Swackhamer, *Phys. Teach.* **30**, 141 (1992).
10. L. Deslauriers, C. Wieman, *Phys. Rev. ST Phys. Educ. Res.* **7**, 010101 (2011).
11. K. A. Ericsson, R. Krampe, C. Tesch-Romer, *Psychol. Rev.* **100**, 363 (1993).
12. M. K. Smith *et al.*, *Science* **323**, 122 (2009).
13. L. Ding, R. Chabay, B. Sherwood, R. Beichner, *Phys. Rev. ST Phys. Educ. Res.* **2**, 010105 (2006).
14. W. K. Adams *et al.*, *Phys. Rev. ST Phys. Educ. Res.* **2**, 010101 (2006).
15. Materials and methods are available as supporting material on *Science* Online.
16. B. Bloom, *Educ. Res.* **13**, 4 (1984).
17. R. H. Bauernfeind, C. J. Olson, *Phi Delta Kappan* **55**, 271 (1973).
18. G. K. Allen, J. F. Wedman, L. C. Folk, *Innovative High. Educ.* **26**, 103 (2001).

Acknowledgments: This work was supported by the University of British Columbia through the Carl Wieman Science Education Initiative.

Supporting Online Material
www.sciencemag.org/cgi/content/full/332/6031/862/DC1
Materials and Methods
SOM Text
References

16 December 2010; accepted 5 April 2011
10.1126/science.1201783

CHN/O/S ANALYZER

The Model 440 Elemental Analyzer offers a wide linear range and is capable of routinely analyzing almost any sample type including organic compounds, pharmaceuticals, petrochemicals, polymers, refractory, environmental, or natural materials. Its unique horizontal furnace design, allowing for removal of residues between runs, prevents cross contamination, and allows for a greater number of samples between combustion column changes. Employing a unique combined static/dynamic combustion technology enables the Model 440 to precisely analyze the widest range of sample types from volatile to difficult to combust materials including nitrides, graphite fibers, ceramics, and even carbides with melting points of over 2,000°C. Offering unmatched operating accuracy and precision, the analyzer delivers simultaneous CHN analysis in less than five minutes, and oxygen and sulfur in only six minutes. Low gas and reagent consumption combined with high reduction tube life allows this model to deliver some of the lowest operating costs.

Exeter Analytical

For info: 800-440-7875 | www.exeteranalytical.co.uk

PRODUCTION-SCALE CELL CULTURE ACCESSORIES

New accessories for the Thermo Scientific Nunc EasyFill Cell Factory include a filling tubing set that connects a Nunc EasyFill Cell Factory directly to a media bag or other tube set; a universal adapter cap that can be used with one-half inch ID tubing or as a traditional Cell Factory port; quarter-inch and three-eighths inch barbed caps for the development of custom tubing sets; and filter assembly caps that expand the air-vent capability during fluid transfer(s). Each ready-to-use accessory is gamma radiated and individually packaged to save users time and money by eliminating cleaning and sterility validations. These accessories promote enhanced aseptic handling, improved air venting, and customizable tubing set solutions. The versatile Nunc EasyFill Cell Factories feature both a traditional and a large port, enabling users to fill via pouring, gravity, or peristaltic pumping.

Thermo Fisher Scientific

For info: 800-625-4327 | www.thermoscientific.com

NUCLEIC ACID/PROTEIN ELECTROELUTION

G-CAPSULE is a simple electroelution device which excises DNA or protein bands from agarose and polyacrylamide gels and elutes the sample to a final volume of ~30 µl. Electroelution through G-CAPSULE is a gentle method that eliminates the risk of damage to DNA or protein samples commonly encountered in use of glass milk, spin columns, binding columns, and other popular techniques. The G-CAPSULE method is simple to perform; eliminating additional steps involving washing, spinning, heating, or precipitation. G-CAPSULE has a simple two-part protocol: Simply pick up the protein or nucleic acid band with the G-Pick and assemble it with the G-Trap. The assembled G-CAPSULE is submerged in electrophoresis buffer on a horizontal electrophoresis system and the protein or nucleic acid is rapidly eluted into the G-Trap. The recovered DNA is high quality for use in molecular manipulations such as ligation, restriction enzyme digestion, sequencing, amplification, random priming, and other enzymatic reactions.

G-Biosciences

For info: 314-991-6034 | www.gbiosciences.com

microRNA PROFILING

The MiraMas Kit uses a novel approach for SYBR Green real-time polymerase chain reaction-based profiling of microRNAs and other small RNAs. This kit incorporates a convenient one-tube protocol to convert all of the microRNAs in a sample into cDNA, while offering researchers flexibility in terms of sample size and number of reactions performed. Using a highly efficient, proprietary 3′ ligation strategy, the MiraMas Kit allows researchers to produce cDNA libraries from up to 150 total or small RNA-enriched samples per kit. Using higher input amounts of RNA, hundreds of microRNA targets can be screened in up to 30 samples per kit. Using lower input amounts of RNAs allows more samples to be processed and screened for a smaller number of microRNA targets per sample. The microRNA targets are amplified using microRNA-specific Forward primers and the Universal Reverse primer included in the kit. The microRNA-specific Forward primers are designed using a simple algorithm that does not require modified nucleotides.

Bioo Scientific

For info: 888-208-2246 | www.biooscientific.com

REAGENT TROUGH

A new 25 ml trough is designed to reduce waste of valuable reagents in automated liquid handling applications. These troughs have a conical base design to minimize the liquid volume inaccessible to the liquid handling (LiHa) arm, reducing dead volume for conductive liquid level detection (cLLD) by a minimum of a third in comparison to Tecan's standard shaped troughs, and down to at least 500 µl for manual adjustment of tip positioning. Made of grey polypropylene, the new troughs are suitable for light-sensitive reagents, and can easily be sealed for convenient reagent transport. They are available in Tecan Pure standard—certified to be free from contamination by human DNA, RNase, DNase, and PCR inhibitors—making them ideal for molecular diagnostics, forensics, and genomics research applications.

Tecan

For info: +41-44-922-81-81 | www.tecan.com

HUMAN MTOR PROTEIN

The OriGene MTOR protein is the first commercially available full-length human MTOR protein with superior biological activity. MTOR is a serine/threonine protein kinase that regulates cell growth, cell proliferation, cell motility, cell survival, protein synthesis, and transcription. Purified, functional MTOR is highly desirable in high throughput functional screening assays and drug target discovery. Produced in mammalian cells, OriGene MTOR protein maintains the most authentic protein structure compared to truncated forms of the protein produced in bacterial or insect cells. When tested in a homogeneous time-resolved fluorescent (HTRF) assay, OriGene full-length MTOR demonstrated a high level of serine/threonine kinase activity.

OriGene Technologies

For info: 888-267-4436 | www.origene.com

Electronically submit your new product description or product literature information! Go to **www.sciencemag.org/products/newproducts.dtl** for more information.

Newly offered instrumentation, apparatus, and laboratory materials of interest to researchers in all disciplines in academic, industrial, and governmental organizations are featured in this space. Emphasis is given to purpose, chief characteristics, and availability of products and materials. Endorsement by *Science* or AAAS of any products or materials mentioned is not implied. Additional information may be obtained from the manufacturer or supplier.

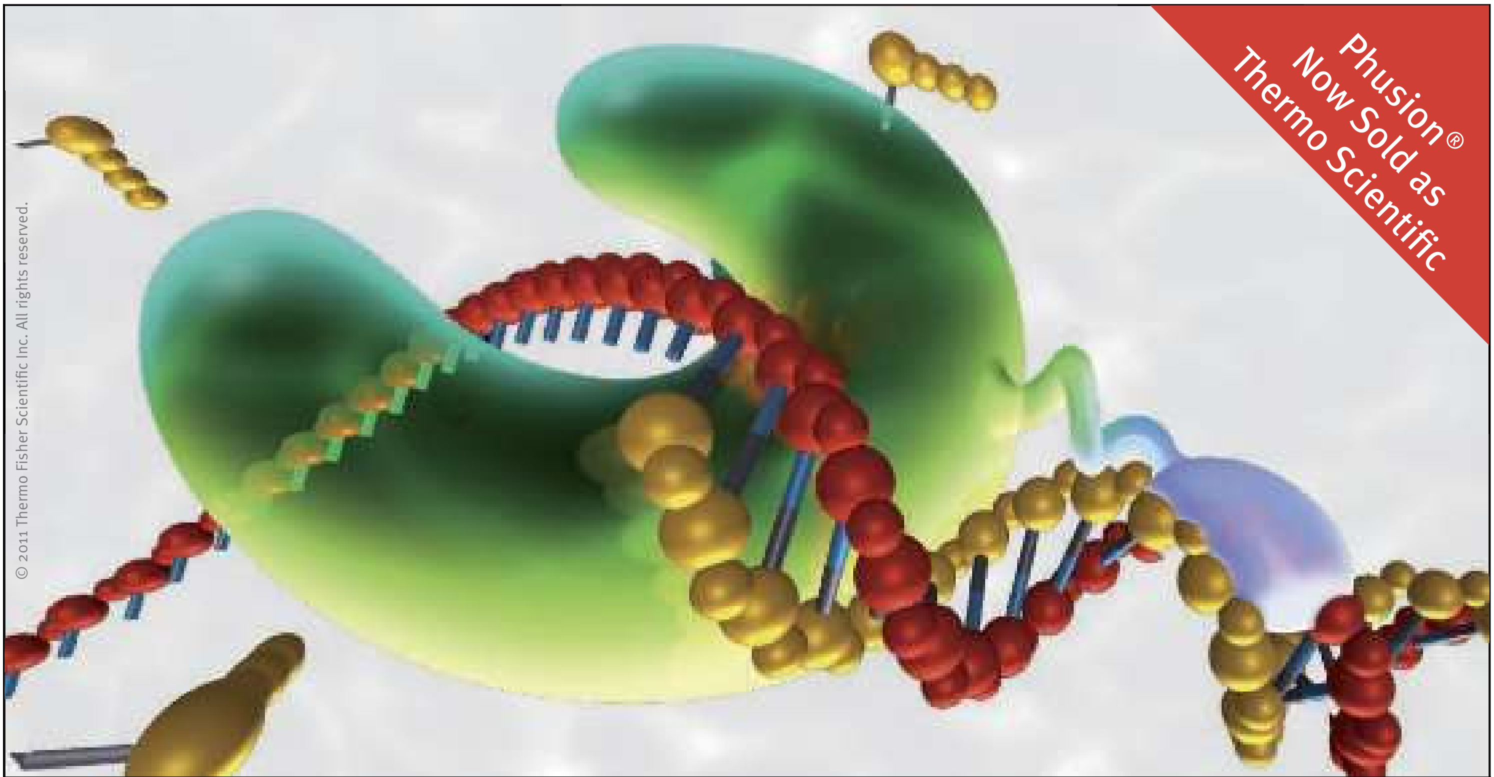

Best-In-Class High Fidelity DNA Polymerases.

Thermo Scientific Phusion High-Fidelity DNA Polymerases are the established standard for high-fidelity PCR. Phusion reagents were introduced in 2003 by Finnzymes, which is now part of Thermo Fisher Scientific. They are the first choice for several demanding PCR applications, including the creation of the first functional synthetic genome.

- **Accurate** – the highest fidelity of all thermostable DNA polymerases
- **Robust** – abundant yields with minimal reaction optimization
- **Fast** – high processivity allows short protocols
- **Specific** – hot start version minimizes non-specific amplification and primer degradation

All Finnzymes products including Phusion reagents are now sold under the Thermo Scientific brand.

Try Phusion today: **www.thermoscientific.com/phusionproducts**

Everything for PCR

Thermo Scientific PCR portfolio has everything you need for successful PCR including industry leading reagents, high-quality instruments and trusted plastic consumables.

Moving science forward

Thermo SCIENTIFIC

Part of Thermo Fisher Scientific

Submission deadline August 1

Your name here.

The GE & Science Prize for Young Life Scientists. Because brilliant ideas build better realities.

Imagine standing on the podium at the Grand Hotel in Stockholm, making your acceptance speech for the GE & Science Prize for Young Life Scientists. Imagine having your essay read by your peers around the world. Imagine discussing your work in a seminar with other prize winners and Nobel Laureates. Imagine what you could do with the $25,000 prize money. Now stop imagining. If you were awarded your Ph.D. in molecular biology in 2010, then submit your 1000-word essay by August 1, and you can make it a reality.

Want to build a better reality? Go to www.gescienceprize.org

GE & Science Prize for Young Life Scientists

* For the purpose of this prize, molecular biology is defined as "that part of biology which attempts to interpret biological events in terms of the physico-chemical properties of molecules in a cell".

(McGraw-Hill Dictionary of Scientific and Technical Terms, 4th Edition).

imagination at work

Science AAAS

GE Healthcare Bio-Sciences AB,
Björkgatan 30, 751 84 Uppsala, Sweden.

28-9402-06AB

PNAS Congratulates
2010 Cozzarelli Prize Recipients

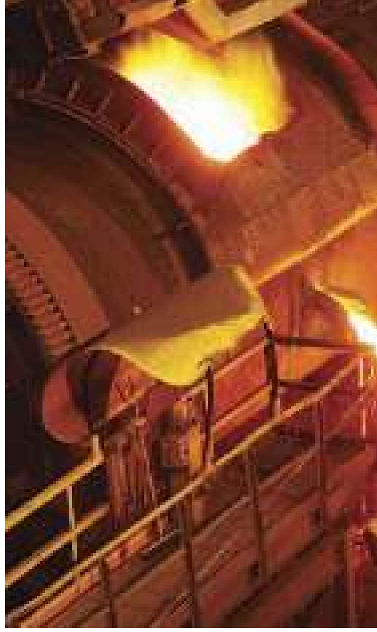

The *Proceedings of the National Academy of Sciences* (PNAS) has selected six outstanding articles for the 2010 Cozzarelli Prize, in recognition of their scientific excellence and originality. Winners were selected from the 3,700 research articles published in PNAS in 2010 and represent exceptional contributions to the six broadly defined classes under which the National Academy of Sciences is organized.

2010 Cozzarelli Prize Recipients

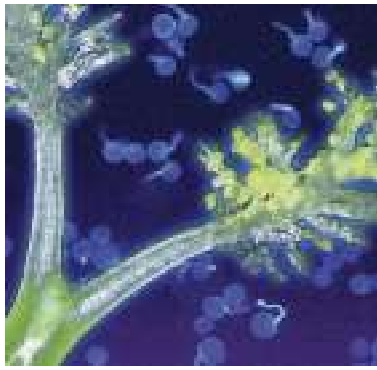

Class I: Physical And Mathematical Sciences
Detection of oxygen isotopic anomaly in terrestrial atmospheric carbonates and its implications to Mars
R. Shaheen, A. Abramian, J. Horn, G. Dominguez, R. Sullivan, and Mark H. Thiemens
(2010) PNAS 107:20213–20218

Class II: Biological Sciences
ATM signals to TSC2 in the cytoplasm to regulate mTORC1 in response to ROS
Angela Alexander, Sheng-Li Cai, Jinhee Kim, Adrian Nanez, Mustafa Sahin, Kirsteen H. MacLean, Ken Inoki, Kun-Liang Guan, Jianjun Shen, Maria D. Person, Donna Kusewitt, Gordon B. Mills, Michael B. Kastan, and Cheryl Lyn Walker
(2010) PNAS 107:4153–4158

Class III: Engineering and Applied Sciences
Entropy driven self-assembly of nonamphiphilic colloidal membranes
Edward Barry and Zvonimir Dogic
(2010) PNAS 107:10348–10353

Class IV: Biomedical Sciences
Influenza A virus-generated small RNAs regulate the switch from transcription to replication
Jasmine T. Perez, Andrew Varble, Ravi Sachidanandam, Ivan Zlatev, Muthiah Manoharan, Adolfo García-Sastre, and Benjamin R. tenOever
(2010) PNAS 107:11525–11530

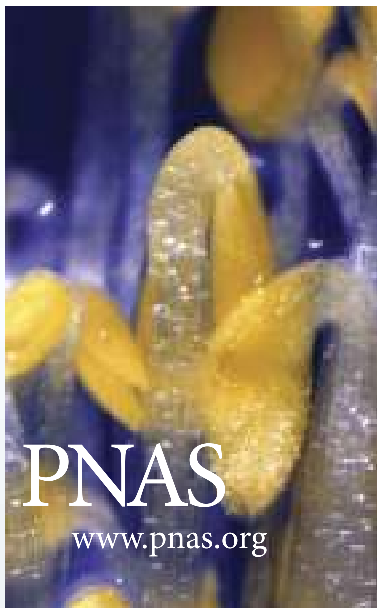

Class V: Behavioral and Social Sciences
Contingent cooperation between wild female baboons
Dorothy L. Cheney, Liza R. Moscovice, Marlies Heesen, Roger Mundry, and Robert M. Seyfarth
(2010) PNAS 107:9562–9566

Class VI: Applied Biological, Agricultural, and Environmental Sciences
Arsenic tolerance in *Arabidopsis* is mediated by two ABCC-type phytochelatin transporters
Won-Yong Song, Jiyoung Park, David G. Mendoza-Cózatl, Marianne Suter-Grotemeyer, Donghwan Shim, Stefan Hörtensteiner, Markus Geisler, Barbara Weder, Philip A. Rea, Doris Rentsch, Julian I. Schroeder, Youngsook Lee, and Enrico Martinoia
(2010) PNAS 107:21187–21192

Podcast interviews with the authors will be available at www.pnas.org/podcasts.

Who's helping you get more for your retirement?

Take the Fidelity Challenge: Put your savings and current retirement savings provider to the test. We're already helping thousands of higher education professionals like you take a fresh look at their investments.

THE FIDELITY CHALLENGE

- ☐ **Start with a plan.** One that gives you the flexibility to make adjustments as your needs change.
- ☐ **Find the right mix.** Determine how to divide up your portfolio to help you meet your goals.
- ☐ **Compare investments.** Evaluate what you own now and explore other choices to consider.

Take the Fidelity Challenge today

Schedule your one-on-one consultation with a Fidelity Planning and Guidance Consultant, and bring us your questions. You don't have to be a Fidelity client — and there's no cost or obligation. Let us help you feel more comfortable about your retirement.

Start now.

866.715.6111
Fidelity.com/challenge

Turn here®

Fidelity® INVESTMENTS

Keep in mind investing involves risk. The value of your investment will fluctuate over time and you may gain or lose money.

Although consultations are one on one, guidance provided by Fidelity is educational in nature, is not individualized, and is not intended to serve as the primary or sole basis for your investment or tax-planning decisions.

INTERNATIONAL SCIENCE & ENGINEERING
VISUALIZATION CHALLENGE

CALL FOR ENTRIES

ENTRY DEADLINE: SEPTEMBER 30, 2011

SCIENCE AND ENGINEERING'S MOST POWERFUL STATEMENTS ARE NOT MADE FROM WORDS ALONE

NEWS of exciting changes to this year's Challenge, coming soon!

Visualization in all its forms has the power to illuminate and educate. It explains and makes clear all aspects of the world around us. It feeds insight and provokes curiosity.

The National Science Foundation (NSF) and the journal *Science*, published by the American Association for the Advancement of Science, invite you to participate in this year's Challenge. The competition recognizes scientists, engineers, visualization specialists, and artists who produce innovative work in visual communication.

Winning entries will be published in *Science* and *Science Online*, and will be displayed on the NSF web site.

Award Categories

- Photography
- Illustrations
- Informational Posters and Graphics
- Videos
- Interactive Video Games

COMPLETE ENTRY INFORMATION:
www.nsf.gov/news/scivis

CHN/O/S ANALYZER

The Model 440 Elemental Analyzer offers a wide linear range and is capable of routinely analyzing almost any sample type including organic compounds, pharmaceuticals, petrochemicals, polymers, refractory, environmental, or natural materials. Its unique horizontal furnace design, allowing for removal of residues between runs, prevents cross contamination, and allows for a greater number of samples between combustion column changes. Employing a unique combined static/dynamic combustion technology enables the Model 440 to precisely analyze the widest range of sample types from volatile to difficult to combust materials including nitrides, graphite fibers, ceramics, and even carbides with melting points of over 2,000°C. Offering unmatched operating accuracy and precision, the analyzer delivers simultaneous CHN analysis in less than five minutes, and oxygen and sulfur in only six minutes. Low gas and reagent consumption combined with high reduction tube life allows this model to deliver some of the lowest operating costs.

Exeter Analytical

For info: 800-440-7875 | www.exeteranalytical.co.uk

PRODUCTION-SCALE CELL CULTURE ACCESSORIES

New accessories for the Thermo Scientific Nunc EasyFill Cell Factory include a filling tubing set that connects a Nunc EasyFill Cell Factory directly to a media bag or other tube set; a universal adapter cap that can be used with one-half inch ID tubing or as a traditional Cell Factory port; quarter-inch and three-eighths inch barbed caps for the development of custom tubing sets; and filter assembly caps that expand the air-vent capability during fluid transfer(s). Each ready-to-use accessory is gamma radiated and individually packaged to save users time and money by eliminating cleaning and sterility validations. These accessories promote enhanced aseptic handling, improved air venting, and customizable tubing set solutions. The versatile Nunc EasyFill Cell Factories feature both a traditional and a large port, enabling users to fill via pouring, gravity, or peristaltic pumping.

Thermo Fisher Scientific

For info: 800-625-4327 | www.thermoscientific.com

NUCLEIC ACID/PROTEIN ELECTROELUTION

G-CAPSULE is a simple electroelution device which excises DNA or protein bands from agarose and polyacrylamide gels and elutes the sample to a final volume of ~30 µl. Electroelution through G-CAPSULE is a gentle method that eliminates the risk of damage to DNA or protein samples commonly encountered in use of glass milk, spin columns, binding columns, and other popular techniques. The G-CAPSULE method is simple to perform; eliminating additional steps involving washing, spinning, heating, or precipitation. G-CAPSULE has a simple two-part protocol: Simply pick up the protein or nucleic acid band with the G-Pick and assemble it with the G-Trap. The assembled G-CAPSULE is submerged in electrophoresis buffer on a horizontal electrophoresis system and the protein or nucleic acid is rapidly eluted into the G-Trap. The recovered DNA is high quality for use in molecular manipulations such as ligation, restriction enzyme digestion, sequencing, amplification, random priming, and other enzymatic reactions.

G-Biosciences

For info: 314-991-6034 | www.gbiosciences.com

microRNA PROFILING

The MiraMas Kit uses a novel approach for SYBR Green real-time polymerase chain reaction-based profiling of microRNAs and other small RNAs. This kit incorporates a convenient one-tube protocol to convert all of the microRNAs in a sample into cDNA, while offering researchers flexibility in terms of sample size and number of reactions performed. Using a highly efficient, proprietary 3′ ligation strategy, the MiraMas Kit allows researchers to produce cDNA libraries from up to 150 total or small RNA-enriched samples per kit. Using higher input amounts of RNA, hundreds of microRNA targets can be screened in up to 30 samples per kit. Using lower input amounts of RNAs allows more samples to be processed and screened for a smaller number of microRNA targets per sample. The microRNA targets are amplified using microRNA-specific Forward primers and the Universal Reverse primer included in the kit. The microRNA-specific Forward primers are designed using a simple algorithm that does not require modified nucleotides.

Bioo Scientific

For info: 888-208-2246 | www.biooscientific.com

REAGENT TROUGH

A new 25 ml trough is designed to reduce waste of valuable reagents in automated liquid handling applications. These troughs have a conical base design to minimize the liquid volume inaccessible to the liquid handling (LiHa) arm, reducing dead volume for conductive liquid level detection (cLLD) by a minimum of a third in comparison to Tecan's standard shaped troughs, and down to at least 500 µl for manual adjustment of tip positioning. Made of grey polypropylene, the new troughs are suitable for light-sensitive reagents, and can easily be sealed for convenient reagent transport. They are available in Tecan Pure standard—certified to be free from contamination by human DNA, RNase, DNase, and PCR inhibitors—making them ideal for molecular diagnostics, forensics, and genomics research applications.

Tecan

For info: +41-44-922-81-81 | www.tecan.com

HUMAN MTOR PROTEIN

The OriGene MTOR protein is the first commercially available full-length human MTOR protein with superior biological activity. MTOR is a serine/threonine protein kinase that regulates cell growth, cell proliferation, cell motility, cell survival, protein synthesis, and transcription. Purified, functional MTOR is highly desirable in high throughput functional screening assays and drug target discovery. Produced in mammalian cells, OriGene MTOR protein maintains the most authentic protein structure compared to truncated forms of the protein produced in bacterial or insect cells. When tested in a homogeneous time-resolved fluorescent (HTRF) assay, OriGene full-length MTOR demonstrated a high level of serine/threonine kinase activity.

OriGene Technologies

For info: 888-267-4436 | www.origene.com

Electronically submit your new product description or product literature information! Go to **www.sciencemag.org/products/newproducts.dtl** for more information.

Newly offered instrumentation, apparatus, and laboratory materials of interest to researchers in all disciplines in academic, industrial, and governmental organizations are featured in this space. Emphasis is given to purpose, chief characteristics, and availability of products and materials. Endorsement by *Science* or AAAS of any products or materials mentioned is not implied. Additional information may be obtained from the manufacturer or supplier.

Science Careers

From the journal *Science* AAAS

Science Careers Advertising

For full advertising details, go to ScienceCareers.org and click For Employers, or call one of our representatives.

Tracy Holmes
Worldwide Associate Director
Science Careers
Phone: +44 (0) 1223 326525

UNITED STATES & CANADA

E-mail: advertise@sciencecareers.org
Fax: 202-289-6742

Tina Burks
Midwest/West Coast/
South Central/Canada
Phone: 202-326-6577

Elizabeth Early
East Coast & Industry
Phone: 202-326-6578

Marci Gallun
Sales Administrator
Phone: 202-326-6582

Online Job Posting Questions
Phone: 202-326-6577

EUROPE & REST OF WORLD

E-mail: ads@science-int.co.uk
Fax: +44 (0) 1223 326532

Alex Palmer
Phone: +44 (0) 1223 326527

Susanne Kharraz
Phone: +44 (0) 1223 326529

Dan Pennington
Phone: +44 (0) 1223 326517

Lisa Patterson
Phone: +44 (0) 1223 326528

JAPAN

ASCA Corporation
Jie Chin
Phone: +81-3-6802-4616
Fax: +81-3-6802-4615
E-mail: careerads@sciencemag.jp

CHINA & TAIWAN

Ruolei Wu
Phone: +86-1367-1015-294
E-mail: rwu@aaas.org

All ads submitted for publication must comply with applicable U.S. and non-U.S. laws. *Science* reserves the right to refuse any advertisement at its sole discretion for any reason, including without limitation for offensive language or inappropriate content, and all advertising is subject to publisher approval. *Science* encourages our readers to alert us to any ads that they feel may be discriminatory or offensive.

UK
UNIVERSITY OF KENTUCKY
College of Medicine

Chair and Professor

Department of Microbiology, Immunology and Molecular Genetics

The University of Kentucky College of Medicine is seeking a new Chair of the Department of Microbiology, Immunology and Molecular Genetics. We are searching for a scientist of international stature with a record of sustained grant support and visionary leadership skills. The new Department Chair is expected to lead an active research program in a department with 25 full-time faculty, promote faculty development and student education, and foster interactions within the Department and throughout the University of Kentucky. Current research strengths in the Department focus on microbial pathogenesis (bacterial, protozoan, fungal and viral), host responses to infection, and Cellular Immunology. The Department is home to the transgenic mouse and flow cytometry Core Facilities. The Department is part of an Integrated Biomedical Sciences (IBS) Program, which fosters the recruitment and education of doctoral candidates for the basic science departments in the College of Medicine.

Successful candidates must possess a PhD and/or MD; UK offers competitive compensation based on rank and experience and an excellent benefits package.

Located at the heart of Central Kentucky's famed scenic Bluegrass Region, Lexington is an economically thriving and vibrant midsized city offering many cultural and recreational activities.

To apply, please send curriculum vitae, statements of research interests and goals as Department Chair, and names of three references to:

Greg Gerhardt, PhD
Chair, Search Committee
c/o Cheryl Songer
138 Leader Avenue
Lexington, KY 40506

Visit us online to learn more about the University and the Department.
www.mc.uky.edu/microbiology

Upon offer of employment, successful applicants must pass a pre-employment drug screen and undergo a national background check as required by University of Kentucky Human Resources. The University of Kentucky is an equal opportunity employer and encourages applications from minorities and females.

PRESIDENT AND CHIEF EXECUTIVE OFFICER LIBERTY SCIENCE CENTER

Following upon the distinguished leadership of Dr. Emlyn Koster, who is retiring after a 15-year tenure, Liberty Science Center is seeking its next President and Chief Executive Officer. Located in historic Liberty State Park in New Jersey, Liberty Science Center is a major educational facility offering exceptional science learning experiences to a broad public of all ages. The position of President and Chief Executive Officer offers an outstanding opportunity for an individual with the requisite vision and leadership abilities to assure a vibrant future for an institution poised to play an increasingly important role in the area of STEM education in the State, the region, and the nation.

Liberty Science Center recently completed a $109 million expansion and renovation and offers an unparalleled facility, a wide array of educational programs and exhibitions, a talented and experienced team of professionals, and an exciting location situated at the heart of the greater New York/New Jersey metropolitan region.

The President and Chief Executive Officer reports to the Liberty Science Center Board of Trustees and is charged with providing creative leadership to all aspects of the institution, including: the provision of strong direction to the articulation and implementation of its mission; rigorous oversight of its administration; articulate and persuasive advocacy of its purposes; vigorous engagement in raising the resources necessary to its operation from government, corporate and individual donors, and operations; a committed presence in the communities it serves; willing collaboration with the wide range of educational and cultural institutions in the region; and, assuring its effectiveness in making the study and understanding of science accessible to people of all backgrounds.

Qualifications for appointment to the position of President and Chief Executive Officer of Liberty Science Center include the following: at least 10 years of increasingly responsible and relevant leadership experience; proven administrative and management skills, including rigorous budget management; a profound understanding of the sciences and of the role of science in society; a demonstrated commitment to the purposes of education; proven abilities as a fundraiser; superb communication skills; strong interpersonal skills and presence as a public figure; and, the ability to build and galvanize a talented team of professionals.

Nominations and applications for the position, enclosing a letter, current resume, and list of references, may be made to the Chair of the Search Committee:

Dr. Susan A. Cole, President
Montclair State University
1 Normal Avenue
Montclair, New Jersey 07043
Attention of: Mr. Michael G. Owen

Or electronically to:
lscsearch@mail.montclair.edu

FROM THE LAB TO THE CLINIC AND BACK:

TRANSLATIONAL RESEARCH TRAINING AND CAREERS

Translational research programs bring together physicians, bench scientists, bioengineers, epidemiologists, patent experts, and more. The goal is learning to communicate across disciplines to achieve advances in health care. By Chris Tachibana

Liz Broussard

A translational scientist should be able to move an idea all the way from basic research to a clinical application and back to the lab to inform more basic science.

"The way I treat cancer today is completely different from 10 years ago because of translational research," says **Mary** (**Nora**) **Disis,** oncologist and principal investigator of the Institute of Translational Health Sciences at the University of Washington. Look at drugs like Gleevec, Avastin, and Herceptin, she says. All are examples of translational researchers converting molecular knowledge about specific cancer cells into effective, targeted therapies. The efficient movement of basic science discoveries into clinical applications—often described as "bench to bedside" work—is the goal of translational research. Disis thinks the field is so promising she hopes her kids grow up to work in it.

FLUENT IN MANY LANGUAGES, COMFORTABLE IN MANY CULTURES

Future translational researchers of all ages must be adaptable, lifelong learners, says Disis. "They have to be highly curious about a lot of different things, collecting data and ideas from the basic literature and creatively applying these to disease solutions. This means being outside your comfort zone, reading literature that is way outside your field." "Translating" is exactly what these scientists do—taking information from one domain and expressing it in another, and communicating daily with people who speak different scientific languages: laboratory scientists, clinicians, patent and regulatory experts, biostatisticians, epidemiologists, and patients. A translational scientist should be able to move an idea all the way from basic research to a clinical application and back to the lab to inform more basic science. Handing off projects from one expert to another doesn't work, says Disis. Success requires someone who understands the idea intimately, and who can build a multidisciplinary team to guide it along the translational path.

It's a long journey with physical hurdles, since basic and clinical research labs usually reside in separate departments. There are also intellectual and cultural barriers. Basic science starts with a hypothesis and designs experiments that validate or reject it, with the goal of acquiring knowledge. Translational science starts with a health need and looks for scientific insights or tools to address that need. Its goal is improving health, explains **Barry Coller,** vice president for medical affairs and physician-in-chief at Rockefeller University, in a 2008 *Mount Sinai Journal of Medicine* article. The successful translational researcher needs to be comfortable in both of these cultures, be fluent in many fields, and thrive on collaboration.

For those with medical training, this might mean learning about hypothesis-driven science and designing experiments and assays. For those with a research background, it could mean learning clinical study design and the bioethics of human research. In either case, the goal is becoming competent to interpret, evaluate, and discuss different types of research, rather than conducting it all yourself, says **Doris Rubio,** professor of medicine, biostatistics, nursing, and clinical and translational science at the University of Pittsburgh. In her translational science training program, she says, "I have a bioengineer who can now design a clinical trial. I love that he can do that, and he says it gives him a deeper understanding of his own research." Formalized training is important because translational science is so complex and getting exposure to all the elements is difficult outside of a specific program, says Rubio.

BEING A MULTIDISCIPLINARY TEAM PLAYER

Training options include a Ph.D., Master's degree, or certificate in translational science. For those who already have an M.D. or Ph.D., career development awards can provide support during the training period. Classes explain the basics of study design and methods, biostatistics, and bioethics. Because developing a new drug, device, or procedure is a team project, coursework might include team dynamics and management. However, for most trainees, the most valuable aspects of a training program are mentoring and hands-on experience in multidisciplinary research. continued »

UPCOMING FEATURES

Biotech and Pharma: Moving Up the Industry Ladder—June 17

BS/MS Scientists: Careers in Bioprocess (online only)—July 15

Postdoc Survey—August 26

CREDIT: (LIZ BROUSSARD): ROCKY YEH; ISTOCKPHOTO.COM

"I hope to provide some concrete recommendations for cost-effective, straightforward lifestyle choices that can preserve quality-of-life as people get older, not necessarily increasing their lifespan, but their health span."
—Ian Lanza

In the United States, most training opportunities are through the Clinical and Translational Science Awards (CTSAs), which were launched in 2006 based on the 2003 National Institutes of Health (NIH) Roadmap for Medical Research. This set of guidelines encourages cross-disciplinary, team-based research as a way to overcome obstacles to turning scientific discoveries into health solutions. Currently, CTSAs have been granted to 55 institutions, with a plan to fund 60 institutions by 2012. The goal is to fund the consortium of award recipients with approximately $500 million annually. The NIH continues to promote translational research with the creation of the National Center for Advancing Translational Sciences (NCATS) as a "bold, new, focused center systematically engineered to accelerate translation." The CTSAs will be the cornerstone of the NCATS. However, NCATS has been controversial for the speed at which the center is being created and the effect of reorganization on other programs currently housed with the CTSAs under the NIH National Center for Research Resources.

The Howard Hughes Medical Institute also funds translational science training through its Med into Grad Initiative, which has awarded various institutions a total of $16 million as of 2010. The programs introduce elements of clinical training into basic science graduate work. They vary by institute, but range from Ph.D. programs in translational research to mentoring opportunities that pair graduate students with a physician advisor.

M.D.-Ph.D. degrees train individuals in clinical and basic research, but translational research programs strive to integrate these two sides of medical science by connecting people and building networks. **Liz Broussard** is a gastroenterologist who is finishing a University of Washington Institute of Translational Health Sciences training program. "There's absolutely no way a junior researcher could launch a translational research career without this training," she says, pointing out the benefits of everyday experience in a multidisciplinary team of scholars. "My first year, we had a psychiatrist, a surgeon, a social worker, a cardiologist, and a pharmacist in the program." A particularly useful activity, she says, is weekly discussions of project ideas and works in progress. These are guided by senior faculty, who also give advice on "their career trajectory, resources, funding mechanisms, partnerships that were successful—essentially life experience, and teaching us how to succeed in research." For a physician, Broussard said the value of a training program is lessons in research methods and thinking scientifically, and learning to ask whether the story in your project and funding application makes sense and has logically supported specific aims.

For a bench scientist, a background in translational research turns the medical objective that is often written into a grant application into a real and achievable goal. **Ian Lanza** earned a Ph.D. in kinesiology, and is now a senior research fellow in the Mayo Clinic CTSA Mentored Career Development Program. This gives him both a postdoctoral research opportunity and guidance towards his long-term goal: "That my research has a high impact on public health." Lanza's project involves collaborating with an endocrinologist and a radiologist, and he says, "It has been very seamless working with both, with a lot of collegiality between the departments." In fact, one way that translational science programs integrate disciplines is to have students and young investigators act as liaisons between senior faculty in different departments. In turn, says Lanza, trainees benefit from having established clinical researchers as mentors and from working with experienced investigators from several disciplines. Lanza's project illustrates another aspect of translational research: It's not always about designing the next cancer drug. It can be traditional bench work with an eye toward how the results might be applied to everyday health care. Lanza is not currently planning any clinical trials for his work on muscle mitochondrial physiology and function, but looking ahead, says, "I hope to provide some concrete recommendations for cost-effective, straightforward lifestyle choices that can preserve quality-of-life as people get older, not necessarily increasing their lifespan, but their health span."

To get a sense of the variety and diversity of translational research and the educational options, look through the online offerings hosted by each CTSA-funded site. Depending on the institution, these include online case studies, podcasts and webcasts of seminars, and continuing medical education courses on topics such as statistical methods, or engaging the community in research. These web-based resources also extend the network of translational research into the global scientific community.

INTERNATIONAL AND INTERDISCIPLINARY

Translational research is not just multidisciplinary, it's multinational. "Translational research is an emerging field in China," says **Depei Liu,** president and professor of the Chinese Academy of Medical Sciences and Peking Union Medical College in Beijing. "For now there are no classes called 'translational research,' although related skills and experience are widely taught." Formal training includes an option at some medical schools including Peking Union Medical College that provides eight months of research training after the clinical program. Another program allows qualified medical school graduates to earn a Master's degree in a basic research field. Informally, "doctors are encouraged to do basic research, to apply for funding and to publish papers and collaborate with specialists in genetics and molecular biology, and doctors and basic researchers often hold meetings together. In addition, there are many short courses and training programs in the fields of basic research and clinical continued »

FEATURED PARTICIPANTS

Chinese Academy of Medical Sciences
www.cams.ac.cn

European Commission
www.ec.europa.eu/index_en.htm

Institute of Translational Health Sciences at the University of Washington
www.iths.org

Mayo Clinic
www.mayoclinic.com

Peking Union Medical College
english.pumch.cn/english

Rockefeller University
www.rockefeller.edu

University of Pittsburgh
www.pitt.edu

Wellcome Trust
www.wellcome.ac.uk

"We've embedded clinical researchers and facilities in academic hospitals, with close links to the research environment around them, including access to technology for 'omics and imaging."
—John Williams

WEB RESOURCES

Clinical and Translational Science Awards
ncrr.nih.gov/ctsa

Howard Hughes Medical Institute Med into Grad Initiatives
www.hhmi.org/grants/office/graduate/gradstudent/medintograd_opportunities.html

Marie Curie Actions
ec.europa.eu/mariecurieactions

research," says Liu. Translational research centers have been established in major research cities, he says, for example the SIBS-Novo Nordisk Translational Research Center for Pre-Diabetes in Shanghai. Current government support includes Chinese National Science Foundation funding for applied medical research, broad support for science and technology projects from the National Basic Research (973) Program, and Science and Technology Special Projects support for basic research in drug discovery and infectious disease.

In Europe, one opportunity for translational research training is the Marie Curie Actions, part of the European Union (EU) Seventh Framework Programme for Research and Technological Development. Project support is available at the doctoral, postdoctoral, and career development level as well as for partnerships between industry and academia and for multisite studies. In keeping with the translational science goals of building networks, collaborations between countries are a focus, as is researcher mobility from one EU country to another. The budget for translational health research since 2007 has been 12 million euros, representing 3% of health research training programs for the Marie Curie Actions, according to **Georges Bingen,** the European Commission's head of unit for the Marie Curie Actions People Programme.

In the United Kingdom, another stakeholder—the pharmaceutical industry—is involved in translational science training. The Translational Medicine and Therapeutics Programmes were established two years ago at University of Cambridge, University of Newcastle, Imperial College London, and a consortium of Scottish institutions. Funding is in the form of 11 million pounds from the Wellcome Trust, a London-based foundation that supports research on animal and human health, and contributions to individual institutions from companies such as GlaxoSmithKline, Pfizer, Roche, AstraZeneca, Sanofi-Aventis, Sirtris Pharmaceuticals, and PTC Therapeutics. "We recognized a need to train a new type of researcher who is comfortable in the creative space between academics and pharma," says **John Williams,** head of clinical activities and head of neuroscience and mental health for the Wellcome Trust. "To do this, we partnered institutions with high-quality academics and health care facilities with world-class pharmaceutical companies." Training programs can be individualized, but usually guide physicians through a Ph.D. project with an emphasis on teamwork, group support, and mentoring. Currently, 6 to 10 fellowships are awarded per year. Bidirectional communication between the lab and the clinic is facilitated by physical proximity. "We've embedded clinical researchers and facilities in academic hospitals, with close links to the research environment around them, including access to technology for 'omics and imaging," says Williams. "This allows subject phenotyping and tissue sampling to be brought into research labs to do the high-technology work that reflects today's bioscience."

Regardless of the geographic setting, the goals and challenges of translational research are the same, says Liu: Getting funding and infrastructure support from the government, training young investigators, creating a multidisciplinary community of researchers who can effectively communicate with each other, and finding ways to systematically implement translational research results into clinical practice.

A GROWING FIELD IN A SHIFTING BACKGROUND

Scientists beginning a career in translational science also need to consider the changing emphasis of medical research, particularly in the United States, where health care reform is currently under way. Doris Rubio says, "we're seeing a shift to personalized medicine and medicine that's more evidence-based. The field is also expanding into patient-centered outcomes research, so not just comparing drug A with a placebo, but drug A versus drug B." In spite of the uncertainties, she says, "It's an exciting time because we have a lot to learn."

Changes in the business sector also affect the translational researcher. John Williams of the Wellcome Trust says, "Pharma is looking to change its discovery models, and as painful as that retrenchment may be, it creates wonderful opportunities in the space between pharma and academia. We hope it will inspire the most creative minds to participate in this exciting time in biomedical and translational research."

Even in the changing health research landscape, postdoctoral fellow Ian Lanza is positive about his career path. He sees the field as growing, and feels that the NIH generally supports young investigators. Gastroenterologist Liz Broussard says although she could make five times as much money in clinical practice, this would probably mean "doing colonoscopies eight hours a day," and she finds her work on a colon cancer vaccine much more inspiring. "I enjoy the clinical work I do now," she says, "but ultimately, translational research can affect patients by changing the current standard of care. I am optimistic about it because I can see myself doing a small part to advance science. It's exciting and, despite funding woes, that keeps me going."

Chris Tachibana is a science writer based in Seattle, USA, and Copenhagen, Denmark.

DOI: 10.1126/science.opms.r1100103

CREDIT: WELLCOME IMAGES

Announcing:

The MedImmune Postdoctoral Program

Postdoctoral Fellowships in Research and Development

MedImmune
www.medimmune.com/careers

We are now accepting applications for our Postdoctoral Program where you will have an opportunity to develop your professional potential and gain valuable experience from some of the top minds in the biopharmaceutical industry.
We are seeking PhD talent for a 3-year assignment. Positions are available in **Gaithersburg, Maryland; Santa Clara and Mountain View, California; and Cambridge, UK.**

Explore our Fellowship opportunities in areas of biotechnology discovery and product development including:

- **Infectious Disease**
- **Respiratory & Inflammation**
- **Translational Science**
- **Oncology**
- **Biopharmaceutical Development**
- **Protein Engineering**

World-class mentoring • Competitive salary and benefits, 401(k), and bonus potential!

Learn much more at: **www.medimmune.com/careers**

Click on the Postdoctoral box on the home page, or on the link under "Our Opportunities".

Advancing Science and Medicine to Help People Live Better Lives

ETH
Eidgenössische Technische Hochschule Zürich
Swiss Federal Institute of Technology Zurich

Professor of Disease Genetics / Epigenetics

The Department of Biology (www.biol.ethz.ch) at ETH Zürich invites applications for a position of Associate or Full Professor in the area of Disease Genetics/Epigenetics.

Candidates are expected to build a strong and independent research program in molecular genetics or epigenetics aimed at studying the relationship between the genome/epigenome and mammalian organ function in health and disease. In his or her hypothesis-driven research the successful applicant should combine molecular/biochemical approaches and advanced genetics and functional genomics technologies with functional studies based on viral vectors, RNA interference, transgenesis or knockout technology using the mouse as a model system. He or she should complement the research in the area of Molecular Health Sciences performed at the Department of Biology, with a strong focus on the understanding of disease mechanisms and on the development of the scientific foundations for personalized medicine. Candidates integrating a translational research program are particularly welcome.

The new Professor will be a member of the Department of Biology of ETH Zurich and strengthen the research focus in Molecular Health Sciences. ETH Zurich offers state-of-the art technology platforms and outstanding opportunities to participate in interdisciplinary research programs. Involvement in the teaching programs in Biology and Molecular Health Sciences is expected. She or he will be expected to teach undergraduate level courses (German or English) and graduate level courses (English).

Please apply online at **www.facultyaffairs.ethz.ch**. Your application should include your curriculum vitae, a list of publications, and a detailed research plan. The letter of application should be addressed **to the President of ETH Zurich, Prof. Dr. Ralph Eichler. The closing date for applications is 31 August 2011**. With a view towards increasing the number of women in leading academic positions, ETH Zurich specifically encourages women to apply.

MFPL Max F. Perutz Laboratories

Vienna International Post-Doctoral Training in Molecular Life Sciences

With support from the Austrian Ministry of Science and Research and the City of Vienna, the Max F. Perutz Laboratories offer a unique post-doctoral training programme, the Vienna International Post-Doctoral Training in Molecular Life Sciences (VIPS).

Join the VIPS

Application Deadline 30th of June 2011

www.mfpl.ac.at/vips

Our Mission:
To promote Post-Docs on their way to scientific independence

Our Offer:

- 3-5 years Post-Doctoral training
- Independent research budget
- Travel money
- Mentoring and Coaching
- Career development
- Grant writing support
- Child care

Our profile:
MFPL is part of the Vienna Biocenter Campus, a center for world class research. We offer a broad coverage of research areas, ranging from Biochemistry, Cellular Biology, Immunobiology to Organismal Biology, Bioinformatics, Structural Biology and Neurosciences.

Spend your post-doctoral training in a thriving scientific environment in one of the most liveable cities of the world!

Contact: Gabriele Permoser, e-mail: vips@mfpl.ac.at

City of Vienna

NIEHS National Institute of Environmental Health Sciences, National Institutes of Health

Director, Clinical Research Program

Research Triangle Park, North Carolina

The National Institute of Environmental Health Sciences of the National Institutes of Health is searching for a senior investigator qualified for tenured appointment to direct its Clinical Research Program, which includes an on-site Clinical Research Unit in Research Triangle Park and components at the Clinical Research Center in Bethesda, Maryland. NIEHS supports and conducts research that contributes to the basic understanding of biological and chemical processes, the contributions of environmental agents to human disease and dysfunction, and the underlying mechanisms of environmentally associated diseases. The Director, Clinical Research Program, is responsible for the development, administration, coordination and oversight of investigator-initiated clinical research; provides general advice to the Director and Scientific Director, NIEHS, on matters relating to human and clinical studies; supervises the Office of Research Compliance; and develops policies and programs for the execution of clinical research at NIEHS. For additional information concerning the duties, go to niehs.nih.gov and click on Jobs at NIEHS.

Candidates must have an established and nationally or internationally recognized record in the conduct and supervision of clinical research in a discipline relevant to the environmental health sciences. Candidates should also have an established record of experience with clinical training, institutional review boards, and compliance with current clinical safety and regulatory issues. Candidates must have a Doctor of Medicine or Doctor of Osteopathy degree from a school in the United States or Canada accredited by the Liaison Committee on Medical Education (LCME) in the year of the applicant's graduation. Candidates with a Doctor of Medicine or equivalent degree from a non-LCME accredited medical school must be certified by the Educational Commission for Foreign Medical Graduates (ECFMG) or hold a Fifth Pathway certificate issued prior to December 31, 2009. Candidates must be board certified or board-eligible in a medical specialty approved by the American Board of Medical Specialties (ABMS), and have the ability to obtain medical licensure in the U.S. To apply, submit a cover letter with plans for directing and conducting a clinical and translational research program, Curriculum Vitae and bibliography and the names and addresses (including e-mail addresses and phone numbers) of three references to the following address by **June 13, 2011**. Salary is commensurate with level of experience.

Ms. Stephanie Jones (Vacancy Number DIR 11-03)
National Institutes of Health
Office of Human Resources
P.O. Box 12233, Maildrop K1-01
Research Triangle Park, NC 27709
E-mail **collinsonj@od.nih.gov**

U.S. DEPARTMENT OF HEALTH AND HUMAN SERVICES
National Institutes of Health

DHHS and NIH are Equal Opportunity Employers
We are dedicated to building a diverse community in our training and employment programs

---

LOYOLA MEDICINE
Loyola University Chicago Stritch School of Medicine

Scientific Program Leaders Oncology Institute Cardinal Bernardin Cancer Center

Loyola University Chicago Stritch School of Medicine (SSOM) is recruiting scientific program leaders for its Oncology Institute, the basic and translational research arm of its Cardinal Bernardin Cancer Center. The primary areas of focus are:

1. Stem cell biology
2. Signal transduction and experimental therapeutics
3. Gene regulation and epigenetics
4. Immunotherapy

Successful candidates will: (a) Lead a basic and translational scientific program in one of the designated research areas; (b) Develop synergistic research collaborations spanning clinical domains of hematologic, breast, GU, GI and/or skin malignancies; and (c) Provide mentorship and assistance to junior faculty within their programs. Our highly interactive research environment provides opportunities for translational research in association with the Cancer Center's strong clinical oncology program. It is expected that applicants will have evidence of sustained academic productivity and grant support. Individuals with a Ph.D., M.D., and/or equivalents at any academic rank are welcome to apply for these full-time, 12-month, tenure-track faculty appointments. Recruitment slots for additional faculty will be provided in addition to a generous start up package and laboratory space. Rank of academic appointment, salary and startup will be commensurate with credentials.

Interested candidates should send a current CV, letter of interest and a list of at least three professional references to:

Paul C. Kuo, M.D.
Director, Oncology Institute
Loyola University Stritch School of Medicine
pkuo@lumc.edu

Loyola University Chicago is an Equal Opportunity and Affirmative Action Employer, and provides a smoke-free and drug-free environment.

Jennifer - Research Scientist for Lilly

Senior and Associate Scientists in Biotechnology Discovery and Development – Indianapolis and San Diego

For more than 130 years, Lilly has been dedicated to meeting the health care needs of people in the United States and around the world. We address these needs primarily by developing innovative medicines and investing a higher percentage of our sales in research and development than any other major pharmaceutical company.

Due to a strategic commitment to the growth of biotherapeutics within the Lilly portfolio, multiple opportunities are currently available within Biotechnology Discovery Research, Bioproduct Research and Development, and Drug Disposition. These are multidisciplinary organizations, focused on the discovery and development of novel therapeutic proteins and peptides through the optimization of their molecular properties. These programs are synergized by the collaborative efforts of scientists at our Indianapolis and San Diego sites, who take full advantage of our excellence in protein science, molecular engineering and optimization, biology and pharmaceutical development, in the context of an integrated operational infrastructure that seamlessly combines the biotherapeutic discovery and development organizations.

We are looking for several Senior and Associate level Scientists with expertise in molecular and cellular biology, protein chemistry, protein characterization, biophysical chemistry, protein formulation, PK/PD of biologics, biochemical engineering, protein purification process design and scale-up for biologics. To be considered for these positions, please visit www.lilly.com/careers and search for opportunities in science.

Lilly

LILLY IS AN EQUAL OPPORTUNITY EMPLOYER.

Georgia Health Sciences University

VASCULAR BIOLOGY CENTER

ASSISTANT/ASSOCIATE/FULL PROFESSORS
TENURE-TRACK

Applications are invited from qualified applicants for available faculty positions at all ranks. The Vascular Biology Center is a department-like unit of the Georgia Health Sciences University that presently includes 14 tenured/tenure-track core faculty, and a total of 110 staff (research faculty, Pre- and Post-doctoral Fellows, Research Assistants, etc.) in recently renovated, well-equipped 20,000+ square feet laboratory space. The existing faculty are highly collaborative with extramural grant awards in excess of $11 million. The Center directs the PhD program in Vascular Biology, and Pre- and Post-doctoral Institutional NIH Training Programs.

The successful applicants will have excellent communication skills and research interest in some aspect of vascular biology. Associate/Full Professors should have established NIH-funded programs. Preference will be given to applicants with interests complementing those of existing faculty; **http://www.georgiahealth.edu/centers/vbc/vbc_corefaculty.html**.

Competitive salaries and start-up packages are available. Inquiries and applications (including full CV, letter of research interests/career plans, and three letters of reference) should be addressed to **Dr. John D. Catravas (jcatrava@georgiahealth.edu)** or **Dr. David Fulton (dfulton@georgiahealth.edu)**.

The Georgia Health Sciences University is an Equal Opportunity and Equal Access Institution, AA/EEO/Equal Access or AA/EEO/Equal Access/ADA Employer. Applications from women and under represented minorities are particularly encouraged. On-Line Application http://www.georgiahealth.edu/facultyjobs reference #5404, #5405, or #5406 Vascular Biology Center.

MDA Muscular Dystrophy Association
Fighting Muscle Disease

Director - Research Development

The Muscular Dystrophy Association is searching for a new member to join our research and advocacy teams. Based in Washington DC in MDA's advocacy office, the Director - Research Development will lead MDA's effort to promote high-impact research designed to find the causes of and treatments for neuromuscular diseases. Working closely with the research department at MDA national headquarters in Tucson, AZ and reporting to the Vice President – Research, this individual is expected to represent MDA's research priorities and develop collaborative opportunities with partners in government and federal agencies, industry, and other non-profit agencies, enhance the visibility of MDA's research enterprise, and further leverage MDA's research program and infrastructure to accelerate therapy development for neuromuscular diseases .

Strong candidates will have a doctoral degree (or equivalent) in a relevant field, research experience, and a working understanding of federal research and regulatory agencies (exceptional non-doctoral candidates with appropriate experience will also be considered). Experience in neuromuscular disease, with a focus on the translational research pipeline is preferred. Candidates should also have the ability to think broadly across scientific disciplines; be innovative and resourceful; have demonstrated ability to communicate complex scientific concepts to a wide array of audiences including the lay public, policy makers, members of Congress and Congressional staff; have comfort with public speaking; and have knowledge of regulatory practices as they pertain to therapeutic development and industry.

MDA is a leading advocate for neuromuscular disease research and actively sponsors basic and translational research with the goal of developing new therapies. Based in Tucson, Arizona, MDA maintains some 200 MDA funded medical clinics, a $40 million/year research program, and a national grassroots network of service providers.

Salary and benefits will be highly competitive and commensurate with experience. Interested individuals should contact:

Sanjay Bidichandani, M.B.B.S., Ph.D.
MDA Vice President – Research
E-mail: researchinfo@mdausa.org

Burnett School of Biomedical Sciences College of Medicine

Endowed Chair in Cardiovascular Science

The Burnett School of Biomedical Sciences, College of Medicine, seeks to fill Florida Hospital Foundation Endowed Chair in Cardiovascular Science. The chair holder is expected to be an accomplished scientist with a well-funded research program who will be a tenured full professor. This position will provide an opportunity to lead the Cardiovascular Science program, one of the four areas chosen for emphasis in this school. He/she is expected to lead recruiting of new faculty members and develop cooperative research programs with the Heart and Vascular Institute and Cardiothoracic Transplant Division in Florida Hospital that does one of the largest number cardiovascular surgical procedures in the US as well as other institutions interested in cardiovascular science in Central Florida.

A competitive salary, startup package and laboratories in the new 198,000 sq.ft. Burnett School of Biomedical Sciences building with 24,000 sq.ft. state of the art vivarium and shared core facilities at Lake Nona will be provided. Access to the substantial core facilities at the Sanford-Burnham medical Research Institute building in the adjacent site at Lake Nona will be available. The VA Hospital and Nemours Children's hospital under construction in the neighboring sites at Lake Nona will provide additional opportunities for collaborative research.

The University of Central Florida has over 56,000 students and an outstanding technology-based infrastructure. It is located in Orlando, a dynamic and progressive metropolitan region, a major player in high-tech industry, and adjacent to a top ranked Research park and a great place to live and work. Review of candidates will begin on June 1, 2011. Please apply to by submitting a curriculum vitae, a two page summary of research plans and contact information for three or more references to **biomedcardiochair@ucf.edu** .

University of Central Florida

The University of Central Florida is an equal opportunity, equal access, and affirmative action employer. As a member of the Florida State University System, all application materials and selection procedures are available for public review.

DEPARTMENT OF THE NAVY
USN ONR
Science & Technology

DIRECTOR – WARFIGHTER PROTECTION & APPLICATIONS DIVISION

(Pharmacologist, Physiologist, or Biologist)

The Office of Naval Research is seeking a qualified individual to serve as the Director of the Warfighter Protection & Applications Division in the Warfighter Performance Science & Technology (S&T) Department. The incumbent is responsible for managing and directing extensive activities in fostering, administering, and executing an integrated program of basic research, applied research, and advanced technology development in the fields of biology, physiology, pharmacology, and research psychology. Sponsored efforts are conducted principally at U.S. universities and industry or Federal laboratories. This is a Civil Service position at the NP-IV level ($105,211 – $155,500) depending on individual qualifications.

The position requires a world-class scientist with knowledge and experience in the fundamental theories, concepts, and current-state-of-the art research and/or technology development in the broad areas of biology, physiology, pharmacology, and research psychology, and has a proven track record in carrying out research and development at a level that has garnered respect in the highest levels of academia.

For information on qualifications and how to apply, see the Job Announcement via the link posted at http://www.onr.navy.mil/en/career-job-opportunity/job-listing.aspx. Applications must be submitted to the job announcement by close of business 20 May 2011 or postmarked as of 20 May 2011.

U.S. CITIZENSHIP REQUIRED • AN EQUAL OPPORTUNITY EMPLOYER

National Aeronautics and Space Administration

NASA AMES RESEARCH CENTER
Research Scientist Position

WORK WITH NASA AMES TO DEFINE THE FIELD OF SPACE SYNTHETIC BIOLOGY

Building on decades of cutting edge scientific achievements, NASA Ames Research Center is creating a new, interdisciplinary, research effort to use synthetic biology as an enabling technology to explore our solar system.

As a recognized expert and leader, you will establish a Center for Space Synthetic Biology and play a key role in defining the field. You will direct start-up funds (subject to appropriation) intended to fund your salary, lab equipment, graduate students, and post-doctoral students, and grow research capabilities to build this center into a world-renowned establishment. You will recruit and lead research teams, compete for grants, and collaborate with others within and outside of NASA.

The Center for Space Synthetic Biology at NASA Ames Research Center is being created to harness biology in reliable, robust, engineered systems to support NASA's exploration and science missions, to improve life on Earth, and to help shape NASA's future.

At NASA, your research could change the world, and enable exploration of new ones.

US Citizenship is required.

Interested applicants should apply directly to USAJobs to vacancy number AR11B0066 at
http://jobsearch.usajobs.gov/ftva.asp?opmcontrol=2240258

NASA Ames Research Center does not discriminate in employment on the basis of race, color, religion, sex, national origin, political affiliation, sexual orientation, gender identity, marital status, disability and genetic information, age, membership in an employee organization, or other non-merit factor.

Call for applications for the positions of

Chief Scientist

RIKEN Advanced Science Institute, JAPAN

RIKEN Advanced Science Institute (ASI) is applying its integrated and interdisciplinary resources and autonomous atmosphere to strengthen various interdisciplinary research fields. ASI is now planning to establish a laboratory headed by Chief Scientist who is capable of implementing original research in the interface between chemistry and biology, to establish functional strategies over the medium and long terms. The new laboratory is expected to stand at the forefront of chemistry, e.g. in creating innovative substances, and develop a new research field through construction of higher order biological complexes, dynamic analysis of living systems, and so forth.

The post is a permanent appointment, subject to RIKEN's mandatory retirement age of 60. RIKEN expects that the successful applicant will be able to take up this position on April 1, 2012.
Applicants should send a full curriculum vitae and photograph; list of publications; one copy each of five key publications; a statement (about five pages A4 sized paper) explaining former research experience and proposals for research at RIKEN; and the names and addresses of three referees. Further details are available from the address below. **All applications should reach RIKEN by August 15, 2011**.

Applicants should address all correspondence to:
Dr. Yukishige Ito, Head of the Chief Scientist Nominating Committee, RIKEN Advanced Science Institute, 2-1 Hirosawa, Wako, Saitama, 351-0198, JAPAN

For more information, please visit:
http://www.riken.go.jp/engn/r-world/info/recruit/k110316_s_asi.html

---

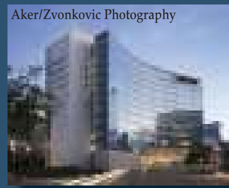

Our World-Class Research Institute Is Looking for Scientific Leaders

Since its inception, The Methodist Hospital Research Institute has challenged the notion of "by-the-book" medical research. Led by Mauro Ferrari, Ph.D., President and CEO, the Research Institute is a 440,000-square-foot research enterprise for The Methodist Hospital System in Houston, TX, and is affiliated with the Weill Cornell Medical College in New York City. Methodist is transforming medicine with emerging techniques, and a staff that is developing real treatments and cures every day. Our laboratories are equipped with advanced technology and facilities that include a cyclotron, pre-clinical and clinical imaging, flow cytometry and microscopy, small and large animal vivariums; and a GMP facility for nanoparticles, contrast agents, vaccines, and therapeutic molecules.
Our facility is a vertically integrated state-of-the-art laboratory for translational and clinical research where translational researchers and physician scientists bring ideas to clinical applications.

We are now searching for research professionals to serve in a variety of capacities.

Program leaders in the fields of:

- *Neurodegenerative Diseases and Repair of the Nervous System (Methodist Neurological Institute)*
- *Cardiovascular Science (Methodist DeBakey Heart & Vascular Center)*
- *Cancer Biology (Methodist Cancer Center)*

Senior scientists in the fields of:

- *Diabetes and Metabolic Disorders (Methodist Center for Diabetes, Obesity and Lipids)*
- *Transplant Immunology (Methodist Transplant Center)*

Candidates should be nationally and internationally recognized leaders with an outstanding track record of scientific discovery, funded research, programmatic leadership and academic mentorship. We will provide you with a position in the epicenter of medical research. You'll discover an excellent research environment, state-of-the-art equipment, and the chance to follow your research from discovery to clinical application in a single facility.
Applicants should submit a Statement of Scientific Interest, a Curriculum Vitae, and the names of three references to: Tong Sun, Director of Central Research Administration, The Methodist Hospital Research Institute, 6670 Bertner St., M.S. R2-216, Houston, TX 77030, or email facultyapplications@tmhs.org (please specify applying field in the subject line of email). Our success as an organization is due to the diversity of our team. We are an equal opportunity employer.

www.tmhri.org **www.MethodistHealth.com**

Methodist® The Methodist Hospital Research Institute®

Houston, TX

LEADING MEDICINE®

The Methodist Hospital System is the official health care provider of the Houston Texans, Houston Astros, Houston Dynamo, Rice Athletics, Houston Ballet, Houston Grand Opera and Houston Symphony.

Postdoctoral Associates

Stony Brook University's Department of Physiology and Biophysics is seeking Postdoctoral Associate's. The positions are available for those holding PhD/D.Sc., or equivalent in the biological sciences (required) with 0 to 2 years of prior postdoctoral training (preferred). The Wnt signaling cascade controlling development will be explored at the cellular level using molecular and cell biological as well as proteomic strategies, focusing on studies performed in embryonic stem cells. Read-outs include gene expression, protein-protein interactions in live cells, and expression of developmentally important markers. Prior experience in research techniques central either to developmental or to molecular biology and /or Wnt signaling preferred. Prior experience in embryonic stem cell propagation and use welcomed.

For a full position description, application procedures, or to apply online, visit *www.stonybrook.edu/jobs* (Job Reference #: HS-R-6793-11-05-S) or email cover letter and C.V. to: Dr. Hsien-yu Wang, Stony Brook University, Physiology and Biophysics, Stony Brook, NY 11794-8661 wangh@pharm.stonybrook.edu

Stony Brook University/SUNY is an equal opportunity, affirmative action employer.

STONY BROOK
STATE UNIVERSITY OF NEW YORK

ETH

Eidgenössische Technische Hochschule Zürich
Swiss Federal Institute of Technology Zurich

Professor of Sustainable Agroecosystems

The future Department of Environmental Systems Science at ETH Zurich invites applications for a Professor to develop and lead a research group in Sustainable Agroecosystems. The new Professor will be expected to develop an internationally recognized research program in agroecosystem science. His or her research will lead to new tools and concepts to assess and manage agroecosystems at the farm to landscape scale. The overall goal in this professorship will be to increase the resource efficiency of food production while minimizing the negative impacts of agricultural production on the environment.

The new colleague will be expected to engage in extensive research and teaching collaborations with other professorships sharing similar interests at ETH Zurich, within the ETH domain and with relevant institutions. The new professor will be expected to teach undergraduate level courses (German or English) and graduate level courses (English) in the field of agroecosystems science.

Please apply online at **www.facultyaffairs.ethz.ch**. Your application should include your curriculum vitae, a list of publications, a statement of your research and teaching interests, and the names and contact information of three possible referees. The letter of application should be addressed **to the President of ETH Zurich, Prof. Dr. Ralph Eichler. The closing date for applications is 31 August 2011.** With a view towards increasing the number of women in leading academic positions, ETH Zurich specifically encourages women to apply.

Assistant/Associate Professor of Veterinary Anatomic Pathology (tenure track)

UCDAVIS
School of Veterinary Medicine

Applications are desired from candidates who have enthusiasm for investigative or translational research in areas that integrate within existing research strengths at the University of California, Davis and the concepts of "One Health". Veterinarian with advanced training in anatomic pathology is required as well as publication in high quality journals and a PhD or equivalent. Eligibility for certification by the American or European College of Veterinary Pathology is required. However, board certification is preferred. Candidates are expected to have or to establish and maintain a strong extramurally funded research program. Candidates must possess excellent interpersonal and communication skills and a demonstrated ability to work with others in a collegial team atmosphere. Candidates with a demonstrated aptitude/experience in professional and/or graduate education would best complement the diverse curriculum at UC Davis. Postdoctoral research experience is preferred. Office and laboratory space are available in a new, state-of-the-art facility (Veterinary Medicine 3A, opened in 2007). The department's research and teaching programs interdigitate with other campus-wide programs, and resources in the Schools of Medicine and Veterinary Medicine, the California National Primate Research Center, and the Cancer Center.

To receive fullest consideration, applications must be received by **September 1, 2011**; position opened until filled. Submit applications with letter of interest, curriculum vitae, concise statement of present and future research plans, summary of teaching experience, and names of three references (including addresses, telephone numbers and e-mail addresses) to: **Linda Potoski, Department of Pathology, Microbiology and Immunology, School of Veterinary Medicine, University of California, Davis, CA 95616**.

The University of California is an Equal Opportunity/Affirmative Action Employer.

The Norwegian University of Science and Technology (NTNU) in Trondheim represents academic eminence in technology and the natural sciences as well as in other academic disciplines ranging from the social sciences, the arts, medicine, architecture to fine art. Cross-disciplinary cooperation results in innovative breakthroughs and creative solutions with far-reaching social and economic impact.

Faculty of Medicine

Professorship
in Medicine (Nanomedicine)

The Faculty of Medicine at the Norwegian University of Science and Technology (NTNU) announces a vacancy for a Professor in Medicine (Nanomedicine). The professorship is part of NTNU's strategic effort in the field of nanotechnology.The successful applicant will benefit from a strong existing infrastructure at NTNU NanoLab (www.ntnu.no/nanolab).The new St. Olav's Hospital is a fully integrated university hospital with offices and laboratories located inside the clinical centers. This provides an excellent arena for translational and inter-disciplinary research involving medicine, technology and the natural sciences. We seek a candidate with solid experience in organizing and leading an independent research group and attracting international funding. The successful candidate excels in nanomedicine as proven by a strong record of scientific publications.

For further information about the application process see www.jobbnorge.no or contact Professor Olav Haraldseth, E-mail: olav.haraldseth@ntnu.no, Tel. +0047 7359 8249. See also http://www.medisin.ntnu.no/eng/ Application deadline: 31 July 2011.

Jobbnorge.no

NTNU
Norwegian University of Science and Technology

POSITIONS OPEN

DEPARTMENT HEAD
Veterinary and Microbiological Sciences
North Dakota State University

The North Dakota State University (NDSU) Department of Veterinary and Microbiological Sciences is currently recruiting for a Head. Our faculty train undergraduate and graduate students in core areas of veterinary and microbiological sciences. In addition, the department has well-equipped laboratories and nationally recognized areas of research. The Head will foster excellence in research, teaching, and service within the department. In collaboration with faculty, the Head will lead the development and articulation of the departmental vision. In addition, the Head will develop and maintain productive, collegial working relationships with the university, scientific communities, and the public as well as livestock and companion animal constituencies. (S)he will manage the department's human, financial, and physical resources, which will include conducting performance evaluations, preparing and submitting administrative reports, administering merit-based pay increases, and providing oversight of budgets and physical facilities. The Head will recruit and retain outstanding students, staff, and faculty; will promote an environment that fosters diversity, collegiality, and teamwork; and will actively seek resources for the support of academic and service programs including extramural funding and endowments. It is anticipated that the Head will contribute to academic and/or service programs as is commensurate with his/her administrative responsibilities.

For a complete list of minimum and preferred qualifications and instructions to apply, please visit **website: http://jobs.ndsu.edu/postings/438.**

NDSU is an Equal Opportunity /Affirmative Action Employer. NDSU is an ADVANCE Institution.

FACULTY POSITION ASSISTANT PROFESSOR in Nutrition and Cancer
The University of Texas at Austin

The Department of Nutritional Sciences, School of Human Ecology, College of Natural Sciences, invites applications for a tenure-track faculty position at the rank of Assistant Professor. For this position, we are seeking candidates with a focus on nutrition and cancer. Candidates with research on nutrition in relation to pediatric cancers are especially encouraged to apply. Specific research areas related to nutrition and cancer and of particular interest include inflammation, epigenetics, metabolism/metabolomics, and early life exposures; however, qualified candidates in other research areas may also be considered. The successful candidate will have, and is expected to maintain, a strong, externally funded research program. Candidates should also have a strong interest in teaching at the undergraduate and graduate levels. Individuals must have a Ph.D., M.D., or M.D.-Ph.D. in a relevant field and a strong record of teaching, research productivity, and federal funding. Applicant Instructions: Interested candidates should submit a letter of interest, curriculum vitae, a research statement, and a list of five references (who will not be contacted without the consent of the candidate). Applications and letters should be sent to the attention of: **Dr. John DiGiovanni, Chair-Search Committee, Department of Nutritional Sciences, The University of Texas at Austin, Dell Pediatric Research Institute, R1800, 1400 Barbara Jordan Boulevard, Austin, TX 78723** or **e-mail: jdigiovanni@mail.utexas.edu.** *Background check conducted on applicant selected. The University of Texas at Austin is an Affirmative Action/Equal Opportunity Employer.*

ASSISTANT/ASSOCIATE PROFESSOR
Harvard Medical School
Beth Israel Deaconess Medical Center

Department of Obstetrics and Gynecology. The candidate should be a Ph.D. committed to research in one of the followings areas: Reproductive Biology, Reproductive Endocrinology, or Gynecologic Oncology. Attractive opportunity for the candidate to establish a new program in an outstanding and vibrant environment. Send inquiries and curriculum vitae to: **John Yeh, M.D.,** Professor and Chairman, Obstetrics and Gynecology, Beth Israel Deaconess Medical Center, Harvard Medical School, Boston, MA. **E-mail: jyeh1@bidmc.harvard.edu.**

POSITIONS OPEN

FACULTY POSITION
Department of Pharmaceutical Sciences
University of Pittsburgh

The Department of Pharmaceutical Sciences of the School of Pharmacy is seeking candidates at all levels for a tenured/tenure-stream position.

The department's faculty have diverse research interests: biochemical pharmacology, molecular biology and genetics; drug discovery, development and delivery; and etiology of drug abuse disorders (**website: http://www.pharmacy.pitt.edu/about/departments/pharmsciences.html**). The faculty interacts through their associations with the school's Center for Pharmacogenetics, Center for Education and Drug Abuse Research and Center for Translational Research, and the University of Pittsburgh Drug Discovery Institute, the University of Pittsburgh Clinical and Translational Science Institute, the University of Pittsburgh Cancer Institute, and the VA Pittsburgh Healthcare System.

Applicants whose research interests complement existing areas of strength are particularly encouraged to apply. Applicants should have a Ph.D., PharmD, M.D., or equivalent and a record of experience and scholarship consistent with the rank sought. The successful applicant will be expected to contribute significantly to the School's Ph.D. and PharmD programs.

The Department of Pharmaceutical Sciences is located on the Oakland campus of the University of Pittsburgh along with the other Health Sciences Schools and the School of Arts and Science. This close proximity, along with affiliation with the University of Pittsburgh Medical Center, provides unique intellectual opportunities for research collaboration, as well as access to extensive research resources. The University of Pittsburgh continuously ranks in the top ten among all universities in research support from the National Institutes of Health. For information on the Pittsburgh area, see **website: http://www.coolpgh.pitt.edu/.**

Applicants should send PDF files containing a letter describing their interest in the position, a description of their current and/or future research interests, a complete curriculum vitae, and the names of at least four individuals who will serve as references to: **Ms. Michele Chamberlain** at **e-mail: mrc6@pitt.edu.** Applications will be reviewed starting July 1.

The University of Pittsburgh is an Affirmative Action/Equal Opportunity Employer.

POSTDOCTORAL POSITION
Johns Hopkins University
Membrane Transport Program

William B. Guggino, Ph.D., professor and director of Physiology in the School of Medicine seeks outstanding individuals to study transport proteins using electrophysiological approaches. Suitable candidates must have a Ph.D. and a proven record of research achievements in the study of transport proteins. Presently, the laboratory has a wide range of interests in basic transport physiology with a particular emphasis on transport related diseases such as Cystic Fibrosis and Polycystic Kidney Disease. Further information about the Physiology Department is available at **website: http://physiology.bs.jhmi.edu/,** and the Guggino laboratory **website: http://www.guggino.org.** Applicants will be assessed on an ongoing basis until July 30, 2011 and should send one electronic (PDF) document including curriculum vitae, a statement of research plans, and copies of any relevant publications, to **e-mail: gugginolabrecruitment@jhmi.edu.** At least two letters of recommendation should be sent directly from the supporters to the same e-mail above with the applicant's name in the subject heading.

The Johns Hopkins University is an Equal Opportunity/Affirmative Action Educator and Employer.

POSTDOCTORAL POSITION
GERMLINE STEM CELLS

Studies include culture, differentiation, and gene activity of male germline stem cells. See *Science* **316**:404, 2007 and *PNAS* **106**:21672, 2009. Send curriculum vitae, names of three references, and a letter describing research experience to: **R. L. Brinster,** School of Veterinary Medicine, University of Pennsylvania. **E-mail: cpope@vet.upenn.edu.**

POSITIONS OPEN

FACULTY POSITION
Section of Endocrinology
Tulane School of Medicine

Research or tenure-track position, **ASSISTANT** or **ASSOCIATE PROFESSOR** level. Section focus is on diabetes. Funded candidates with molecular and/or clinical pathophysiology are encouraged to apply. Research and teaching responsibilities. Adjunct appointment(s) with Physiology, Biochemistry, and Pharmacology are also possible. Section has strong clinical research/clinical trials program. Clinical samples/materials available for collaborative clinical/translational research. Section also involved in epidemiology studies and a pilot program of clinical translation of stem cell therapy in diabetes. Send curriculum vitae, research and teaching goals, and three references to **e-mail: vfonseca@tulane.edu.** Search open until qualified applicant is identified.

Affirmative Action/Equal Opportunity Employer. Women and minorities are invited to apply.

MARKETPLACE